DISSERTATION

POLYOXOMETALATES AND THEIR INTERACTION
WITH ORGANIC MOLECULES AND INTERFACES

University of Regensburg

Faculty for Chemistry and Pharmacy

„Zur Erlangung des Doktorgrades der Naturwissenschaften (Dr. rer. nat.)
der Fakultät für Chemie und Pharmazie der Universität Regensburg"

Submitted by

THOMAS BUCHECKER

from Augrub

June 2018

"Skibadee Skibadanger, I am the rearranger."

- *Hans Peter Geerdes alias H.P. Baxxter*

Acknowledgement

THANK YOU!

The practical work was performed from October 2015 until April 2018 at the Institute of Inorganic Chemistry at the University of Regensburg in the working group of Prof. Dr. Arno Pfitzner.

This work was supervised by Prof. Dr. Arno Pfitzner.

Submission of the PhD: June 25, 2018

Date of the oral exam: July 25, 2018

Examination Committee:

Chairman: Prof. Dr. Frank-Michael Matysik

1. Examiner: Prof. Dr. Arno Pfitzner

2. Examiner: Dr. Pierre Bauduin

Further examiner: Prof. Dr. Werner Kunz

Scientific contributions

Publications

[1] T. Buchecker,† S. Krickl,† R. Winkler, I. Grillo, P. Bauduin, D. Touraud, A. Pfitzner and W. Kunz: The impact of structuring of hydrotropes in water on the mesoscale solubilisation of a third hydrophobic component. *Phys. Chem. Chem. Phys.*, **2017**, *19*, 1806-1816.

[2] T. Buchecker, X. Le Goff, B. Naskar, A. Pfitzner, O. Diat and P. Bauduin: Polyoxometalate/polyethylene glycol interactions in water: From nano-assemblies in water to crystal formation by electrostatic screening. *Chem. Eur. J.* **2017**, *23*, 8434 -8442, **Cover Page**:

Cover Picture:
P. Bauduin et al.
Polyoxometalate/Polyethylene Glycol Interactions in Water:
From Nanoassemblies in Water to Crystal Formation by Electrostatic Screening

[3] S. Krickl,† T. Buchecker,† A. Meyer, I. Grillo, D. Touraud, P. Bauduin, B. Koenig, A. Pfitzner and W. Kunz: A systematic study of the influence of mesoscale structuring on the kinetics of a chemical reaction. *Phys. Chem. Chem. Phys.* **2017**, *19*, 23773—23780.

[4] S. Friesen, T. Buchecker, A. Cognigni, K. Bica, and R. Buchner: Hydration and Counterion Binding of [C12MIM] Micelles, *Langmuir*, **2017**, *33*, 9844–9856.

[5] R. Winkler, T. Buchecker, F. Hastreiter, D. Touraud and W. Kunz: PPh$_4$Cl in aqueous solution – the aggregation behaviour of an antagonistic salt. *Phys. Chem. Chem. Phys.*, **2017**, *19*, 25463 - 25470

[6] T. Buchecker, P. Schmid, S. Renaudineau, A. Proust, O. Diat, A. Pfitzner and P. Bauduin: Polyoxometalates in the Hofmeister series. *Chem. Commun.*, **2018**, *54*, 1833-1836, **Cover page**:
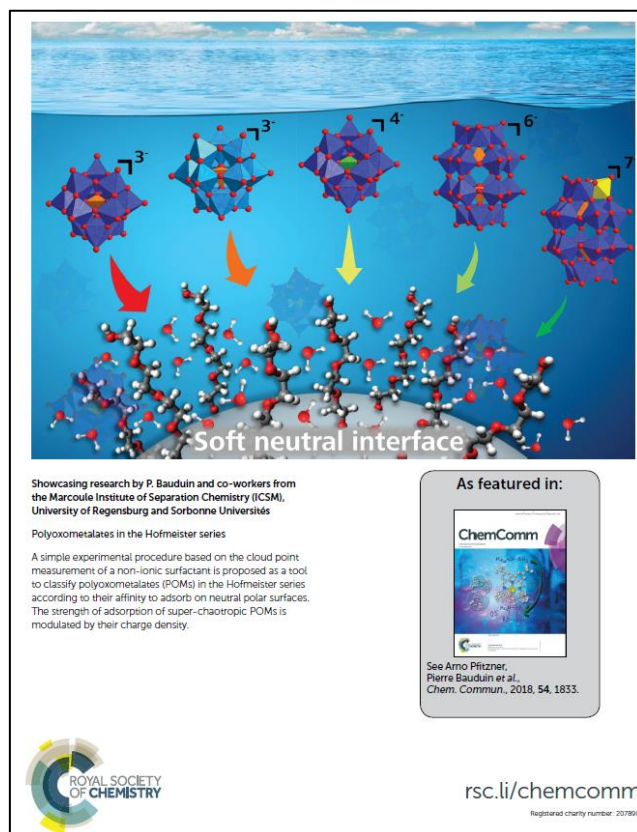
[7] T. Buchecker, P. Schmid, M. Röhrl, S. Stemplinger, O. Diat, P. Bauduin and A. Pfitzner: Visible light mediated Single-crystal to Single Crystal transition of a polyoxometalate-ethylene glycol hybrid crystal, *manuscript in preparation*.

[8] T. Buchecker, P. Schmid, I. Grillo, S. Prévost, T. Zinn, M. Drechsler, O. Diat, A. Pfitzner and P. Bauduin: Self-assembly of short chain Poly-*N*-isopropylacrylamid (PNIPAM) to Stimuli Responsive Globules and Nano-Sheets induced by the α-H$_3$PW$_{12}$O$_{40}$ Keggin Polyoxometalate, *manuscript in preparation*.

[9] S. Krickl,† T. Buchecker,† Max Hahn,† L. Jurko, S. Mandl, G. Jošt, D. Touraud, P. Bauduin, A. Pfitzner and W. Kunz: Role of Hydrogen bond donor- and hydrogen bond acceptor functionality on the occurrence of mesoscale inhomogeneities in surfactant-free microemulsions, *manuscript in preparation*.

[10] T. Buchecker, O. Diat and P. Bauduin: POM surface activity induced by a self-assembly process with ethers: On the origin of the mystery of the "POM-etherate", *manuscript in preparation.*

†: *split first authors who contributed equally to the scientific work and to writing the paper*

Oral Presentations

Thomas Buchecker, Olivier Diat, Pierre Bauduin and Arno Pfitzner
The adsorption of Polyoxometalates on polar micellar surfaces visualized by SAXS
7th Russian German Travelling seminar – Physics and Chemistry of Nanomaterials and Synchrotron Radiation, **2015**, Berlin, Rostock, Lund, Kopenhagen, Hamburg, Leverkusen, Köln, Koblenz.

Thomas Buchecker, Olivier Diat, Pierre Bauduin and Arno Pfitzner
The influence of mesoscale structuring on a chemical reaction
The fourth international conference "Advances in Synthesis and Complexing", **2017**, Moscow.

Thomas Buchecker, Olivier Diat, Pierre Bauduin and Arno Pfitzner
The impact of solvent structuring on a polyoxometalate catalysed reaction
254th ACS international conference **2017**, Washington, USA.

Thomas Buchecker, Olivier Diat, Pierre Bauduin and Arno Pfitzner
Polyoxometalates and their interaction with uncharged interfaces
During a Research stay **2017**, Nikolaev Institute of Inorganic Chemistry, Novosibirsk.

Thomas Buchecker, Olivier Diat, Pierre Bauduin and Arno Pfitzner
The interaction of Polyoxometalates with uncharged molecules and the formation of light-responsive hybrid materials
During a Research stay **2017**, University of Jekaterinburg, Jekaterinburg.

Thomas Buchecker, Olivier Diat, Pierre Bauduin and Arno Pfitzner
Design of POM based hybrid materials by non-specific interactions
International Conference on Coordination Chemistry (ICCC), **2018**, Sendai, Japan.

Table of Contents

1   Introduction

1.1   Specific ion effects

Already in the 19th century, much emphasis was put upon the investigation of how salts influence solution behaviour of macromolecules and living tissue. The Hofmeister series, which was shaped by Franz Hofmeister almost 120 years ago, describes the ability of salts to precipitate proteins from aqueous solution.[1] Back then, salts were evaluated according to their water ordering series, *i.e.* kosmotropic (water network structuring) and chaotropic (water network breaking). F. Hofmeister discovered that weakly hydrated soft cations with a low charge density and highly hydrated hard anions with a high charge density behaved similar with respect to their protein denaturation behaviour. The qualitative order of cations and anions is displayed in **Figure 1.1**. It should be noted, that in the Hofmeister series only ions are considered, whereas in aqueous solutions salts should rather be considered.
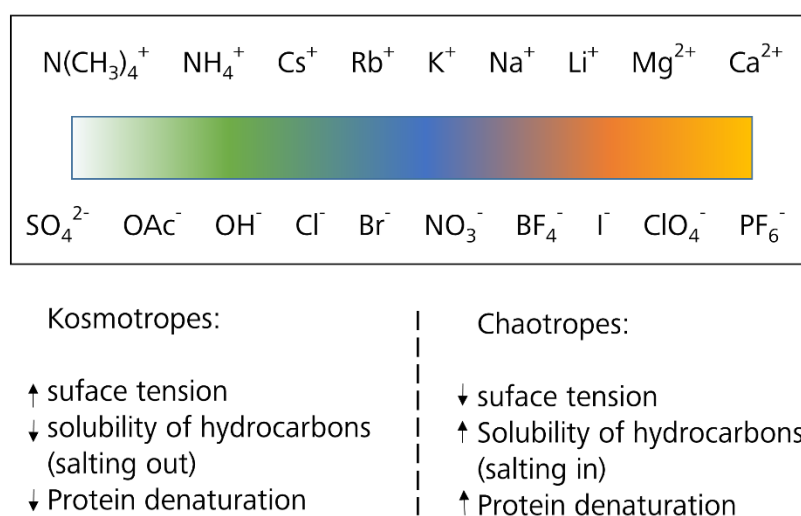
Figure 1.1: Classification of ions in the Hofmeister series and their specific impact on aqueous solutions/biological media. Image adapted and redesigned from W. Kunz.[2]

Kosmotropes are highly hydrated and cause proteins to precipitate (salt out) from aqueous solution. Owing to their high charge density, kosmotropes exhibit low polarizability and can be considered as hard ions. Chaotropes, on the contrary, unveil loosely bound hydration water molecules which can be easily shed off. They are much more polarizable and can be considered as soft ions.

The impact of the Hofmeister series on biological matter and specific organic molecules goes beyond the precipitation of proteins. It plays a critical role in a broad variety of chemical and physical phenomena, ranging from cloud points of non-ionic surfactants, colloidal stability and zeta potential to molecular forces and critical micellar concentrations of surfactants (CMCs).[3] The impact of salts on

aqueous solutions and aqueous solutions containing a third component is nowadays rather well known and exploited in many fields. Nevertheless, the mode of interaction of ions with organic molecules and interfaces at a molecular level is not completely understood. For a long time, it was assumed that Hofmeister effects (salting in, salting out, *etc.*) were related to the capability of various ions to make or break bulk water structure.[4–6] Theoretical and experimental investigations of Batchelor *et al.* and Omta *et al.* contract this theory and revealed that the water network is not perturbed by the solubilisation of ions in aqueous media. They showed that at least for monovalent ions, water structure is not affected beyond the first hydration shell.[7,8] It is often proposed that Hofmeister effects should be treated as an interfacial phenomenon.[9–11] Direct interactions of ions with macromolecules and interfaces and interfacial water structure is considered to be the origin of specific ion effects.[12]

Tobias *et al.* and Jungwirth *et al.* revealed by means of molecular dynamics (MD) simulations that kosmotropes are repelled from an interface, whereas soft ions are attracted to them.[13,14] Large ions, especially anions with a low inherent charge density, exhibit a strong propensity to enrich at the top most layer of interfaces. These calculations are in agreement with surface tension measurements of aqueous solutions containing salts.[12,15,16] Many attempts have been made to deduce specific ion effects from their inherent properties like size, charge and energy of hydration. These parameters play a crucial role, but do not take into account the interface. In order to predict specific ion effects in solution, more parameters have to be considered: *(i)* the overall charge density of ions, which also correlates with the ion polarizability and associated dispersion forces which are often proposed to be the origin of specific ion effects,[17,18] and *(ii)* the interface, especially water structuring around interfaces. And of course *(iii)* further parameters, *e.g.* salt concentration dependence, *pH*, the chemical structure (overall agglomeration, π-stacking, *etc.*) and the particular environment including the solvent or counter ions or *e.g.* head groups of ionic surfactants as counter ions in vicinity play a major role on specific ion effects.[19] Only by conceding all of these interactions, the effect of *e.g.* electrolytes on the surface tension of water/air or *e.g.* on bubble coalescence can be outlined properly.[2]

All in all, specific ion effects result in a subtle balance between competing ion-water/water-surface interactions that likely involve the charge density, polarizability, hydrophobic effects and the particular environment of the ion. Furthermore, there are specific ion effects beyond Hofmeister chemistry which are responsible for the impact of ions on various biological functionalities. In such cases, Hofmeister-type interactions can even be overruled by particular steric arrangements in various ion binding sites of macromolecules.[20]

A very simple model to predict ion behaviour, in specific ion association in solution, was provided by Kim Collins, namely the concept of matching water affinities.[21] In this theory, Collins considers ions as spheres with a point charge in the centre. Ions with a high inherent charge density are

considered to be highly hydrated and are referred to as kosmotropic, whereas large ions with a low inherent charge density are considered to be poorly hydrated (chaotropic). The hydration shell of the latter is bound loosely. A second reasonable assumption in his theory is that charges of opposite sign attract each other strongly via Coulomb attraction, see **Figure 1.2**.
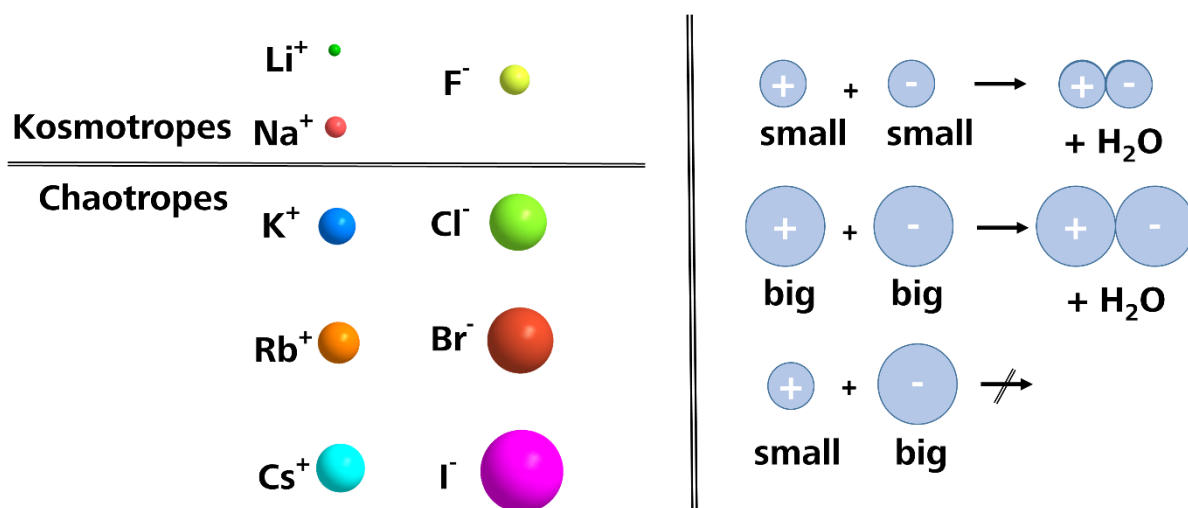
Figure 1.2: Division of alkali metal cations and halides between kosmotropes and chaotropes on the left-hand side. Usually Cl^- and K^+ delineate the border between kosmotropic and chaotropic ions. The anions and cations are depicted in their relative size ratio (size excerpted from Shannon *et al.*[22]) On the right-hand side: Contact ion pair formation only occurs between ions with a similar free energy of hydration and a similar affinity to water. Image adapted and redesigned from K.D. Collins.[21]

Collins concludes that two small ions with a high charge density attract each other and can overcome their free energy of hydration. These ions expel water from their hydration shell and entropy is gained resulting in a final competition between electrostatic forces, entropy and hydration energy.[21]

In case of two big ions, the Coulomb attraction is weaker, but the effect is the same: due to the fact that the hydration shell is only loosely bound, hydration water can be removed easily. Therefore, big, polarizable ions attract each other. However, in case of the interaction of two differently hydrated ions, the electrostatic force is too small to overcome the hydration energy of the kosmotropic ion. Hence, both ions remain separated in solution and do not form a close contact ion pair. Therefore, Collins' concept of matching water affinities is again a concept based on the very powerful concept "like seeks like". Note that this concept was also successfully extended to the interaction behaviour of charged head groups of surfactants with counter ions.[19]

Collins' concept was applied for predicting the interaction of charged moieties. However, the interaction between polar interfaces and charged moieties is different to the one between two charged

particles as pure electrostatic interactions do not come into play. Nevertheless, Leontidis *et al* proposed that the affinity of anions for hydration water is a good hint for predicting the propensity of ions to interact with and adsorb on uncharged interfaces.[10] Leontidis *et al.* made the transition from the interaction of two charged particles (Collins' concept) to the interaction of ions with hydrophobic surfaces. It is worth to note that a surface can be considered as hydrophobic when the charge density of the surface or the molecule tends to zero. Leontidis *et al.* investigated the effect of ions (salt) on phospholipids and they described the general process of ion adsorption as *"an ion-lipid battle for hydration water and interfacial sites"*. They proposed that the propensity of chaotropic anions to adsorb on lipid interfaces results from the big size of the anion, which affects in different ways the hydration free energy terms of the anion and the organic interface.[10] Furthermore, Schwierz *et al.* and Horinek *et al.* investigated modelling approaches toward anion specificity at surfaces of varying charge and polarity.[11,23] In contrast to the work of Leontidis *et al.* dealing with the interaction of phospholipid interfaces and chaotropic anions and the work of Schwierz *et al.* and Horinek *et al.*, the interaction of super-chaotropic anions with polar interfaces and molecules was studied in the present thesis.

> *In the framework of this PhD thesis, the general question occurred: to what extent can the general concept of contact ion pair formation (Collins concept) or ion adsorption (conclusions from Schwierz et al. and Horinek et al.) at charged/hydrophobic interfaces or molecules (conclusions from Leontidis et al.) be applied to predict the adsorption of charged ions, in specific nanometer-sized polyoxometalates, at polar but uncharged(!) interfaces?*

By taking into account the accomplishments of Collins' concept of matching water affinities and the recent progress of Leontidis *et al.* regarding the general competition of anions and lipids for hydration water, the interaction between chaotropic anions and polar but uncharged(!) interfaces could also be explained with a general competition of anions and polar interfaces/molecules for hydration water. If a large anion with a very low charge density and a polar interface/molecule have comparable affinities towards water, an adsorption of this ion at the polar interface/molecule could be favoured, *i.e.* an entropically driven process without considering specific interactions, including for example ion polarizability. Here, non-specific interactions are considered to be very weak interactions without the formation of discrete donor-acceptor complexes between the chaotropic anion and the polar surface or molecule. The adsorption process of ions on polar interfaces or molecules would be similar to the formation of contact ion pairs between two ions. Hence, this assumption would also be an extension of the famous and successful concept "like seeks like" as proposed by Pearson and Collins.[21,24]

Investigations of this concept were performed in the first four chapters of this thesis using a class of anions, namely polyoxometalates (POMs) as representatives of super-chaotropic anions. POMs

provide access to the super-chaotropic side of the Hofmeister series of anions.[25] These anions feature a big size with a low inherent charge density implying a very loose hydration in terms of Collins' or Hofmeister's concept. This class of ions was shown to interact with loosely hydrated polar interfaces (ethylene glycol or glucoside decorated surfaces) as shown by the work of Naskar *et al.*[25] In their work, POMs-based surfactants were formed spontaneously through noncovalent and nonspecific interactions in water by mixing nonionic surfactants with POM.

1.2 Polyoxometalates - a general overview

In the present work, the main focus was laid upon the investigation of super-chaotropic polyoxometalates (POMs) and their interaction with uncharged polar interfaces and molecules. POMs, complex polyoxoanions, mostly consist of oxygen atoms surrounding an early transition metal octahedrally (V, Nb, Mo, Ta, W), with V, Mo and W being by far the most representative transition metals in POMs.[26,27] If *p*-block elements are incorporated (B, Al, Si, P, Ge, As, Sb, Te, I) in the centre of the anions, these POMs are called heteropolyanions, otherwise they are referred to as homopolyanions. Back in the days when Berzelius discovered the element Mo, he already commented on remarkable properties of POMs.[28] Even before, Scheele mentioned the famous POM-molybdenum blue in 1778.[29] In the 20th century a broad variety of heteropolyoxometalates emerged: by applying X-ray diffraction methods in the early 1930s, Keggin was the first to report the structure of the most famous representative of the POMs, namely the so called Keggin anion $PW_{12}O_{40}^{3-}$ (PW^{3-}), see **Figure 1.3(a)**.[30] Besides the almost spherical Keggin structure, several other POM architectures exist, *e.g.* the prolate spheroidal Dawson type POMs, see **Figure 1.3(b)**, Lindquist POMs, Anderson POMs (both not shown as they were not used in this PhD thesis), *etc*.
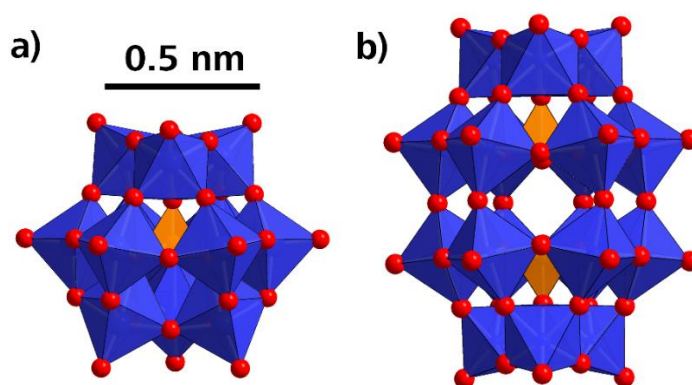
Figure 1.3: Structure of the most common polyoxometalate anions of (a) Keggin's type, $PW_{12}O_{40}^{3-}$ (PW^{3-}), and (b) Dawson's type, $P_2W_{18}O_{62}^{6-}$, in polyhedral representation. Oxygen atoms form octahedra surrounding tungsten atoms. The octahedra are linked by their edges and vertices. In the centre of these anions a *p*-block element (here an oxoanion containing phosphorous as central atom) is located.

The electronic versatility, the blend of p-bock elements, transitions metals and differently bound oxygen atoms (terminal and bridging) grant POMs innumerable special properties resulting in a broad field for applications such as catalysis,[31,32] material science,[33,34] biology[35,36] and medicine.[37] POMs were shown to have great applications as catalysts in organic chemistry (photocatalysts,[38] epoxidation catalysts,[39] oxidation catalysts[40]), exhibit antiviral[41,42] and anticancer activity[43] and are used as ion complexing agents for nuclear waste treatment.[44]

Due to their outstanding variety of applications and fascinating properties mentioned in this section, they emerged as model representatives for large, highly chaotropic anions with a very low charge density to investigate their interaction with polar molecules or interfaces. Note that owing to their spherical shape and delocalized charge, Keggin-type POMs are also favourable for theoretical calculations.[45,46]

Table 1.1: Calculated charge densities of common spherical anions. Values for the crystal ionic radii were excerpted from Shannon *et al.* [22] and the radius of $PW_{12}O_{40}^{3-}$ and $SiW_{12}O_{40}^{4-}$ was obtained by SAXS fits from Naskar *et al.*[25] e is the elementary charge.

	Ion radius [Å]	Ion surface [Å^2]	Ion volume [Å^3]	(Excess) charge density [e/nm^3]
F^-	1.3	21.2	9.2	108.7
Cl^-	1.8	40.7	24.4	41.7
Br^-	2.0	50.2	33.5	29.9
I^-	2.2	60.8	44.6	22.4
$SiW_{12}O_{40}^{4-}$	4.4	243.3	356.8	11.2
$PW_{12}O_{40}^{3-}$	4.6	265.9	407.7	7.4

The comparison of the geometrical properties and charge densities of POMs with the ones of conventional halides in **Table 1.1** informs on the molecular geometries and the very low charge density of POMs and therefore indicates the super-chaotropy of this class of anions. Keggin type POMs have more than twice the ionic radius of I^- and more than five times the surface area of I^- (which itself is considered a strong chaotrope), see **Table 1.1**. The charge density (the elementary charge(s) per volume) decreases by a factor of ~15 by comparing F^- and PW^{3-}. Another feature of POMs is the isostructural relation between $SiW_{12}O_{40}^{4-}$ (SiW^{4-}) and PW^{3-}. This fact allows the tuning of the overall charge without changing the total number of electrons or the shape of the POM.

All in all, it appears from **Table 1.1** that POMs represent a class of highly polarizable anions, because their charge density (in case of PW^{3-}) amounts to merely one quarter of the charge density of I^-.

Therefore, it is expected that the right-hand side of the Hofmeister can be expanded to a super-chaotropic range, see **Figure 1.4**.
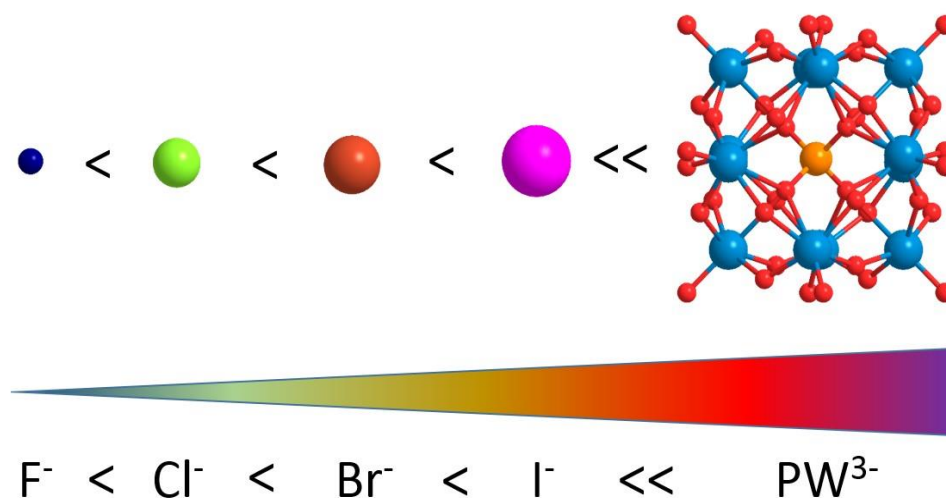
Figure 1.4: Extension of the classical Hofmeister series of anions. The anions are depicted in their relative size scale. The crystal ionic radii were taken from Shannon *et al.* [22] and the radius of PW^{3-} was taken from Naskar *et al.*[25] Image adapted from Naskar *et al.*[25]

1.3 The super-chaotropy of POMs and its implications

The group of Pierre Bauduin and Olivier Diat proved in a recent study the super-chaotropy of Keggin type POMs.[25] Coming up from a physicochemical point of view in solution chemistry, they found that POMs exhibit a very strong affinity to interact with and adsorb on interfaces covered with polar but uncharged(!) groups, such as sugar and ethylene oxide (EO_x) groups. Hence, the expansion of the Hofmeister series for anions by POMs to a super-chaotropic side is indeed possible. The super-chaotropic nature of POMs results in a general, non-specific adsorption of POMs on interfaces covered with polar groups, which was demonstrated to not be sensitive on the curvature of the interface. This non-specific adsorption is also confirmed by simulations, which predict the adsorption of polarizable anions at the water/air surface.[10,47,48] The arising key question at the beginning of this PhD thesis was:

What is the nature and the driving force for an adsorption of polarizable anions on polar interfaces?

Naskar *et al.* proposed that the explanation for the strong interaction of POMs with organic molecules and interfaces is again a competition of the anionic POM and uncharged molecules located at

the interface for hydration water. Remember that this was previously also proposed by Leontidis *et al.* for the interaction of ions with phospholipids or as it is the case for two charged particles in Collins' concept of matching water affinities and is further supported by the work of Schwierz *et al.* and Horinek *et al.*[10,11,21,23,49,50] Due to their large size, their low charge density and twelve terminal and 28 bridging oxygen atoms - being all potential hydrogen bond acceptors - POMs are highly hydrated with comparably weak hydrogen bonds to hydration water molecules. Hence, it should be possible to break such hydrogen bonds and release hydration water molecules to the water bulk phase – such a process would be associated to a large gain of entropy. For the sake of clarity, this process is depicted in **Figure 1.5**.
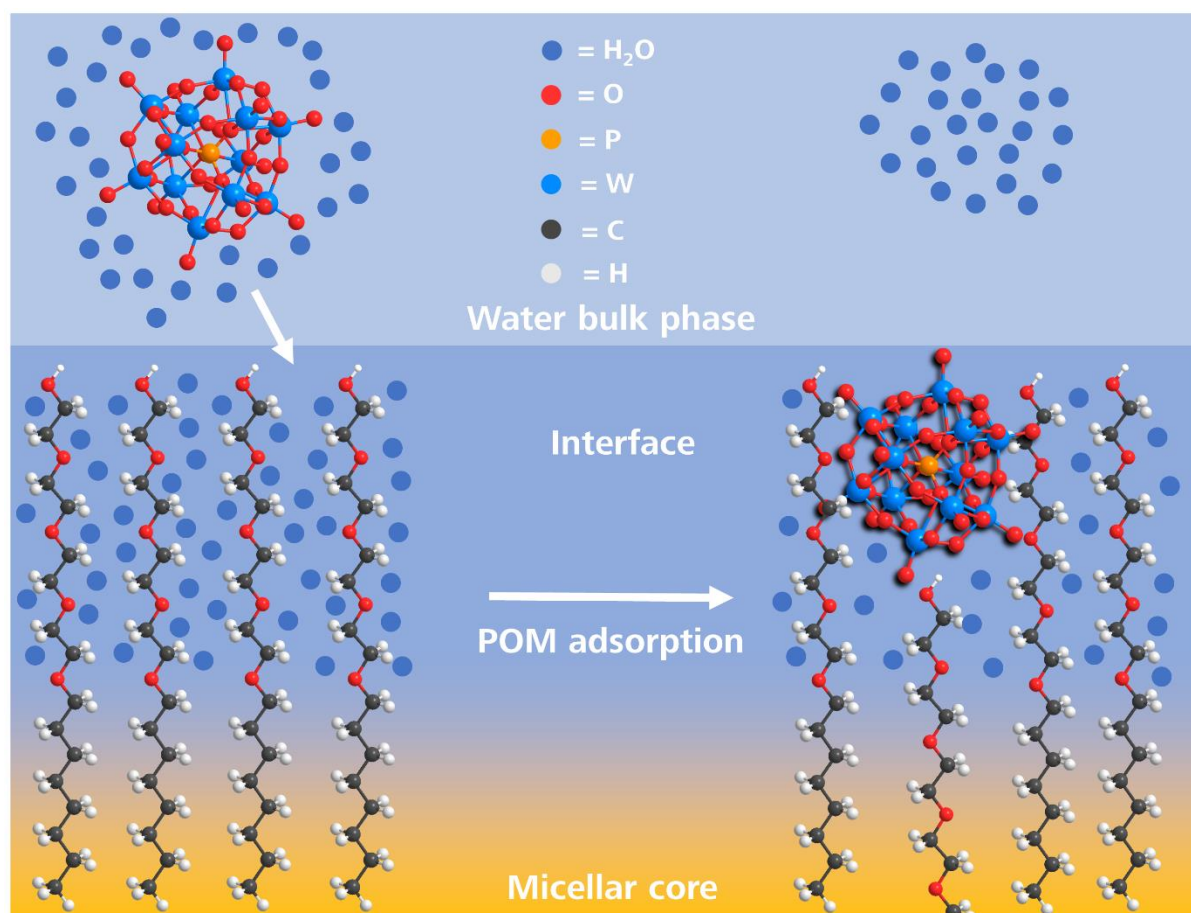
Figure 1.5: Entropy gain upon the adsorption of a hydrated POM on hydrated polar interfaces (here: ethylene glycol moieties, C_8**EO$_4$**). Water molecules stemming from the hydration of the POM and from the hydration of EO_x moieties are released to the water bulk phase. The image was adapted and redesigned from Naskar *et al.*[25]

Hence, the adsorption is considered to be non-specific (no strong and directing bonds and without the formation of energetically favourable donor acceptor complexes between the anion and the polar surface or molecule) and entropically driven by the release of water molecules to the water

bulk phase. Convenient solvent approaches with a continuum model and an overall dielectric constant (Debye-Hückel theory or other Poisson-Boltzmann approaches) do not adequately capture these specific ion effects of POMs on hydrated organic molecules or interfaces. Only recently, Malinenko *et al.* addressed a very intriguing question: *Are Keggin's POMs Charged Nanocolloids or Multicharged Anions?*[51] Multicharged anions are usually treated by the Debye-Hückel theory (therein, the solutes are treated as dissociated point charges, are not polarizable by applying an external field and the solvent is only treated as a continuum with a given permittivity). The interaction of colloids on the other hand is usually expressed with the Derjaguin-Landau-Verwey-Overbeek (DLVO) theory. The DLVO theory explains aggregation phenomena in aqueous dispersions quantitatively and describes the forces taking place between charged surfaces of colloids interacting through a liquid medium. It combines the effects of the van-der-Waals attraction (dispersion forces) of larger objects and the electrostatic repulsion of charged surfaces with a given surface charge density. On the other hand, the DLVO theory neglects specific ion effects. By combining dynamic light scattering (DLS) and static small angle X-ray studies (SAXS) Malinenko *et al.* came to the conclusion that POMs behave as both, nanocolloids (because POMs can be described by a classical colloidal approach by DLS and SAXS) as well as multicharged anions since they adsorb on neutral polar surfaces like chaotropic anions. Hence, Keggin POMs are indeed at the frontier between nanocolloids and multicharged anions.[51]

1.4 Bibliography

[1]   F. Hofmeister, *Arch. Exp. Pathol. Par.* **1888,** *24,* 1-30.

[2]   W. Kunz, *Curr. Opin. Colloid Interface Sci.* **2010**, *15*, 34–39.

[3]   W. Kunz, P. Lo Nostro, B. W. Ninham, *Curr. Opin. Colloid Interface Sci.* **2004**, *9*, 1–18.

[4]   X. Chen, T. Yang, S. Kataoka, P. S. Cremer, *J. Am. Chem. Soc.* **2007**, 12272–12279.

[5]   R. J. Clarke, C. Lüpfert, *Biophys. J.* **1999**, *76*, 2614–2624.

[6]   P. H. Von Hippel, T. Schleich, *Acc. Chem. Res.* **1969**, *2*, 257–265.

[7]   J. D. Batchelor, A. Olteanu, A. Tripathy, G. J. Pielak, *J. Am. Chem. Soc.* **2004**, *126*, 1958–1961.

[8]   A. W. Omta, M. F. Kropman, S. Woutersen, H. J. Bakker, *Science* **2003**, *301*, 347–349.

[9]   C. Calero, J. Faraudo, D. Bastos-González, *J. Am. Chem. Soc.* **2011**, *133*, 15025–15035.

[10]   E. Leontidis, M. Christoforou, C. Georgiou, T. Delclos, *Curr. Opin. Colloid Interface Sci.* **2014**, *19*, 2–8.

[11]   N. Schwierz, D. Horinek, R. R. Netz, *Langmuir* **2010**, *26*, 7370–7379.

[12]   Y. Zhang, S. Furyk, D. E. Bergbreiter, P. S. Cremer, *J. Am. Chem. Soc.* **2005**, *127*, 14505–14510.

[13]   M. Lund, L. Vrbka, P. Jungwirth, *J. Am. Chem. Soc.* **2008**, *130*, 11582–11583.

[14]   L. Vrbka, M. Mucha, B. Minofar, P. Jungwirth, E. C. Brown, D. J. Tobias, *Curr. Opin. Colloid Interface Sci.* **2004**, *9*, 67–73.

[15]   W. Melander, *Arch. Biochem. Biophys.* **1977**, *183*, 200–215.

[16]   P. Weissenborn, P. Robert, *J. Colloid Interface Sci.* **1996**, *184*, 550–563.

[17]   B. W. Ninham, V. Yaminsky, *Langmuir* **1997**, *13*, 2097–2108.

[18]   W. Kunz, *Specific Ion Effects*, World Scientific, **2010**.

[19]   N. Vlachy, B. Jagoda-Cwiklik, R. Vácha, D. Touraud, P. Jungwirth, W. Kunz, *Adv. Colloid Interface Sci.* **2009**, *146*, 42–47.

[20]   H. I. Okur, J. Hladílková, K. B. Rembert, Y. Cho, J. Heyda, J. Dzubiella, P. S. Cremer, P. Jungwirth, *J. Phys. Chem. B* **2017**, *121*, 1997–2014.

[21]   K. D. Collins, *Methods* **2004**, *34*, 300–311.

[22]   B. Y. R. D. Shannon, M. H, N. H. Baur, O. H. Gibbs, M. Eu, V. Cu, *Acta Crystallogr. A* **1976**, *32*, 751.

[23]   D. Horinek, A. Serr, D. J. Bonthuis, M. Boström, W. Kunz, R. R. Netz, *Langmuir* **2008**, *24*, 1271–1283.

[24]   R. G. Pearson, *Chemical Hardness*, Wiley Online Library, **1997**.

[25]   B. Naskar, O. Diat, V. Nardello-Rataj, P. Bauduin, *J. Phys. Chem. C* **2015**, *119*, 20985–20992.

[26]   J. J. Borrás-Almenar, E. Coronado, A. Müller, M. Pope, *Polyoxometalate Molecular Science*, Springer Netherlands, **2012**.

[27]   M. T. Pope, A. Müller, *Angew. Chemie - Int. Ed.* **1991**, *30*, 34–48.

[28]   J. J. Berzelius, *Ann. Phys.* **1826**, *82*, 369–392.

[29]   P. Gouzerh, M. Che, *Actual. Chim.* **2006**, *298*, 9–22.

[30]   J. W. Illingworth, J. F. Keggin, *J. Chem. Soc.* **1935**, 575–580.

[31]   C. L. Hill, *Comprehensive Coordination Chemistry II:From Biology to Nanotechnology*, Elsevier, Oxford, **2004**.

[32]   S. S. Wang, G. Y. Yang, *Chem. Rev.* **2015**, *115*, 4893–4962.

[33]   A. Proust, B. Matt, R. Villanneau, G. Guillemot, P. Gouzerh, G. Izzet, *Chem. Soc. Rev.* **2012**, *41*, 7605.

[34]   H. N. Miras, J. Yan, D.-L. Long, L. Cronin, *Chem. Soc. Rev.* **2012**, *41*, 7403.

[35]   B. Hasenknopf, *Front. Biosci.* **2005**, *10*, 275.

[36]   H. Stephan, M. Kubeil, F. Emmerling, C. E. Müller, *Eur. J. Inorg. Chem.* **2013**, 1585–1594.

[37]   L. Fu, H. Gao, M. Yan, S. Li, X. Li, Z. Dai, S. Liu, *Small* **2015**, *11*, 2938–2945.

[38]   D. K. Lyon, W. K. Miller, T. Novet, P. J. Domaille, E. Evitt, D. C. Johnson, R. G. Finke, *Am. Chem. Soc.* **1991**, *113*, 7209–7221.

[39]   L. Leclercq, A. Mouret, A. Proust, V. Schmitt, P. Bauduin, J. M. Aubry, V. Nardello-Rataj, *Chem. - A Eur. J.* **2012**, *18*, 14352–14358.

[40]   M. V. Vasylyev, R. Neumann, *J. Am. Chem. Soc.* **2004**, *126*, 884–890.

[41]   M. Fukuma, Y. Seto, T. Yamase, *Antiviral Res.* **1991**, *16*, 327–339.

[42]   J. T. Rhule, C. L. Hill, D. a. Judd, R. F. Schinazi, *Chem. Rev.* **1998**, *98*, 327–357.

[43]   R. Prudent, V. Moucadel, B. Laudet, C. Barette, L. Lafanechère, B. Hasenknopf, J. Li, S. Bareyt, E. Lacôte, S. Thorimbert, et al., *Chem. Biol.* **2008**, *15*, 683–692.

[44]   M. T. Pope, *Polyoxometalates for Radioactive Waste Treatment - Final Report - 06/15/1996 - 09/14/2000*, **2000**.

[45]   A. Chaumont, G. Wipff, *J. Phys. Chem. C* **2009**, *113*, 18233–18243.

[46]   A. Chaumont, G. Wipff, *Phys. Chem. Chem. Phys.* **2008**, *10*, 6940–6953.

[47]   A. P. Santos, Y. Levin, *Langmuir* **2012**, *28*, 1304–1308.

[48]   A. P. dos Santos, Y. Levin, *Faraday Discuss.* **2013**, 75–87.

[49]   K. D. Collins, G. W. Neilson, J. E. Enderby, *Biophys. Chem.* **2007**, *128*, 95–104.

[50]   T. Zemb, E. Leontidis, *Curr. Opin. Colloid Interface Sci.* **2014**, *19*, 1.

[51]   A. Malinenko, A. Jonchère, L. Girard, S. Parrès-Maynadié, O. Diat, P. Bauduin, *Langmuir* **2018**, *34*, 2026–2038.

2   Goals of this work and abstract of this PhD thesis

2.1   Part 1: The interaction of POMs with organic molecules and oligomers

As the following chapters are already published as full papers or communications in different renown scientific journals, a short abstract and a central theme of the present PhD thesis is given in this chapter.

> *The general goal of the first part of this PhD thesis is to study in depth the interaction of POMs with different type of interfaces in order to (i) investigate the general concept of super-chaotropy and to (ii) establish how general this concept is.*

Therefore, the first part of this work directly follows the contribution of Naskar *et al.* who investigated the interaction of the two most prominent Keggin-type POMs, *i.e.* $H_3PW_{12}O_{40}$ and $H_4SiW_{12}O_{40}$ (PW^{3-} and SiW^{4-}), with C_8EO_4 and C_8G_1 surfactants at the micellar- and the H_2O/air surface. They found that PW^{3-} and SiW^{4-} strongly adsorb on *uncharged* but polar tetra-ethylene glycol mono-octyl ether (C_8EO_4) and n-octyl-β-D-monoglucoside (C_8G_1) surfactants. They claimed that this adsorption is entropically driven: the partial dehydration of hydrated POMs and the partial dehydration of hydrated interfaces (C_8EO_4 or C_8G_1) leads to an increase of "free bulk water" concomitant with an entropic gain of the system.

As a continuation of this study, the work of Naskar *et al.* was extended in **chapter 3 "Polyoxometalates and the Hofmeister series"** to yield information on the decisive molecular parameters of POMs which influence the strength of POM adsorption on C_8EO_4 micelles. If the POM adsorption is really entropically driven, POMs with low charge densities should display a stronger adsorption on C_8EO_4 micelles than POMs with a higher charge density, since the dehydration process should be facilitated. Furthermore, if the process was really entropically driven, the shape of the POM, *i.e.* Keggin- or Dawson type POMs, should not play much of a role in the adsorption process. Therefore, a parametric study of different Keggin- and Dawson type POMs, *i.e.* different POM sizes, charges, structures, compositions and counter ions, was performed to rank POMs according to their ability to increase the cloud point (CP) of C_8EO_4. A pronounced increase of the CP of C_8EO_4 is considered to be the result of a stronger adsorption of POMs on C_8EO_4 micelles as C_8EO_4 micelles become formally charged upon the adsorption of POMs leading to a higher water solubility of C_8EO_4.

Chapter 4 "From nano-assemblies in water to crystal formation by electrostatic screening" deals with the interaction of PW^{3-} with ethylene glycol oligomers (EO_x, $1 < x < 400$) which is similar to the bare hydrophilic head of the C_8EO_4 surfactant. The main focus of this study was to investigate

if a C_8EO_4 micelle – H_2O and the H_2O/air interface is needed to promote an adsorption of POMs as studied in **chapter 3 "Polyoxometalates and the Hofmeister series"** and to answer the question if POM adsorption on hydrated surfaces is only an interfacial effect. We show that POMs also adsorb on single hydrated organic oligomers in aqueous solution to yield POM-oligomer nano-assemblies which are stabilized by electrostatic repulsion between the negatively charged POMs. Addition of NaCl, aiming at screening the inter-nano-assembly repulsions, induces aggregation and formation of hybrid crystalline materials. This new method to build POM-organic composite materials without covalent or electrostatic grafting of the POM and an organic molecule was called *"the electrostatic screening method"*. The combination of a single-crystal X-ray study with small angle X-ray and small angle neutron scattering (SAXS/SANS) and ^{1}H-nuclear magnetic resonance (NMR) experiments allowed relating the structure of the POM-oligomer nano-assemblies solubilized in aqueous solution to the structure model of the single crystal.

Chapter 5 "Single crystal to single crystal transformation in a POM based composite crystal" treats of the application of this *"electrostatic screening method"* described in **chapter 4 "From nano-assemblies in water to crystal formation by electrostatic screening"** to build *new functional POM based hybrid materials* with $PMo_{12}O_{40}^{3-}$ - EO_5/EO_6 - $3Na^+$. Since $PMo_{12}O_{40}^{3-}$ is a well-known visible light active photocatalyst in aqueous catalysis, catalytic activity could also be expected in hybrid crystals composed of $PMo_{12}O_{40}^{3-}$ and ethylene glycol. Upon irradiation of these crystals with visible light, it is indeed demonstrated that $PMo_{12}O_{40}^{3-}$ - EO_5/EO_6 - $3Na^+$ crystals undergo an irreversible single crystal to single crystal (SCSC) transformation concomitant with *(i)* a decrease of the unit cell volume of $PMo_{12}O_{40}^{3-}$ - EO_5/EO_6 - $3Na^+$ crystals and *(ii)* a change of the crystal colour from bright yellow to blueish black. Upon irradiation of $PMo_{12}O_{40}^{3-}$ - $EO_{5/6}$ - $3Na^+$ crystals, the visible light active photocatalyst $PMo_{12}O_{40}^{3-}$ catalyses the oxidation of a terminal hydroxyl function -CH_2-OH of ethylene glycol to the corresponding aldehyde -CH=O in the solid state. The formation of the well-known reduced heteropolyblue-polyoxometalate $PMo_{12}O_{40}^{4-/5-}$ goes along with a change of the crystal colour from yellow to black.

To further explore the interaction of POMs with water soluble oligomers, the **"Interaction of POMs with poly-N-isopropylacrylamide (PNIPAM) oligomers (PNIPAMx000, x = 2, 5, 7, 10)"** was studied in **chapter 6**. In contrast to EO_x oligomers whose interaction with POMs was studied in **chapter 4 "From nano-assemblies in water to crystal formation by electrostatic screening"** PNIPAM provides a different chemical repeating motif. Furthermore, PNIPAM is well known for its subtle molecular hydrophilic-hydrophobic balance resulting in a lower critical solubilisation temperature (LCST) at 33 °C (*i.e.* good solubility of PNIPAM polymers in H_2O below 33 °C and a liquid-liquid

phase separation of PNIPAM and H_2O above 33 °C). The goal was to investigate the interaction/adsorption of POMs on PNIPAM to find out whether the adsorption of POMs on oligomers is restricted to specific chemical groups (only ethylene glycol groups or also other repeating motifs of oligomers) and a second goal was to alter the LCST of PNIPAM upon the addition of super-chaotropic POMs. We show for the first time that PNIPAM polymers - probably the most studied among thermo- and stimuli-responsive "smart" polymers - self-assemble to stimuli responsive *(i)* discrete globules and to *(ii)* 2D nano-sheets upon the adsorption of PW^{3-}, PMo^{3-} and SiW^{4-}.

2.2 Part 2: POMs as photocatalysts in mesoscopically structured solvents

The second part of this PhD thesis deals with the application of $H_5PMo_{10}V_2O_{40}$ as photocatalyst in mesoscopically structured solvents. The idea was to extend the adsorption of POMs on oligomers/polymers and well-defined interfaces to *interfaces of ill-defined, highly fluctuating surfactant free microemulsions* (SFME). The POM photocatalyst should ideally adsorb on an ill-defined H_2O/benzyl alcohol interface stabilized by alcohol molecules (ethanol, EtOH, isopropyl alcohol, IPA, *N*-propanol, NPA, and *tert*-butanol, TBA) analogous to "micellar catalysis". Note that in "micellar catalysis", the catalyst is located at the surface of micelles which incorporate the non-water-soluble reactant. A close vicinity of the catalyst and the organic molecule should then preferably lead to fast reaction rates. In the present case, the visible light active POM photocatalyst $H_5PMo_{10}V_2O_{40}$ is supposed to adsorb on benzyl alcohol/alcohol clusters solubilized in water (surfactant free microemulsion, SFME) and should catalyse the oxidation of benzyl alcohol to the corresponding benzyl aldehyde. In case of a close proximity of $H_5PMo_{10}V_2O_{40}$ and benzyl alcohol the initial reaction rate should be higher compared to a statistically distributed $H_5PMo_{10}V_2O_{40}$ benzyl alcohol mixture where the contact probability of $H_5PMo_{10}V_2O_{40}$ and benzyl alcohol should be lower.

In **chapter 7 "Structuring of Hydrotropes in water"**, the structuring of binary mixtures of primary and secondary alcohols with H_2O is first linked to the solubilisation of poorly water miscible compounds (primarily benzyl alcohol which should be oxidized by $H_5PMo_{10}V_2O_{40}$). This study allowed to determine whether the solvent mixture H_2O/alcohol/benzyl (alcohol = EtOH, IPA, NPA, TBA) is mesoscopically structured or not. Ideally, very pronounced structuring (benzyl alcohol – alcohol droplets in a continuous water phase with $PMo_{10}V_2O_{40}^{5-}$ adsorbed at the interface) should lead to high reaction rates. Therefore, we have chosen a series of short-chain alcohols as hydrotropes and benzyl alcohol, limonene and a hydrophobic azo-dye (Disperse Red 13) as organic compounds to be solubilised. Very weak pre-structuring is found for binary EtOH/H_2O and NPA/H_2O mixtures. Structuring of H_2O/alcohol mixtures is most developed for binary NPA/H_2O and TBA/H_2O mixtures making them a suited binary solvent for the $PMo_{10}V_2O_{40}^{5-}$ catalysed reaction according to the present considerations. Besides these findings we additionally found that pre-structuring of binary H_2O/TBA

mixtures leads to a high solubilisation power for poorly water miscible components compared to non-structured mixtures H_2O/EtOH or H_2O/IPA. This difference in solubilisation power was linked to *(i)* the formation of mesoscale structures in case of EtOH and IPA and to *(ii)* the extension of pre-structures in case of NPA and TBA. Furthermore, three different solubilisation mechanisms could be identified: bulk solubilisation, interface solubilisation and the combination of both.

In **chapter 8 "The impact of hydrotrope structuring on a polyoxometalate catalysed reaction"**, we finally link the mesoscopic structuring of the most structured binary solvent mixture H_2O/*tert*-butanol (TBA) to the kinetics and the efficacy of the oxidation of benzyl alcohol (BA) to the corresponding aldehyde catalysed by $PMo_{10}V_2O_{40}^{5-}$. We demonstrate that the obtained yields of benzyl aldehyde depend on the type of mesoscopic structuring of the binary solvent H_2O/TBA. An elevated catalytic performance of at least 100% is found for unstructured binary mixtures H_2O/TBA compared to compartmented binary mixtures H_2O/TBA. Although it was shown that $PMo_{10}V_2O_{40}^{5-}$ adsorbs on well-defined surfaces of *e.g.* Brij L23 ($C_{12}EO_{23}$) micelles, $PMo_{10}V_2O_{40}^{5-}$ does not adsorb on ill-defined, highly fluctuating H_2O/benzyl alcohol interfaces stabilized by TBA molecules. We conclude that compartmentation of both benzyl alcohol and $PMo_{10}V_2O_{40}^{5-}$ in TBA and water-rich micro phases is unfavourable for the catalytic efficacy.

3 Polyoxometalates and the Hofmeister series

3.1 Preface and Abstract

Showcasing research by P. Bauduin and co-workers from the Marcoule Institute of Separation Chemistry (ICSM), University of Regensburg and Sorbonne Universités

Polyoxometalates in the Hofmeister series

A simple experimental procedure based on the cloud point measurement of a non-ionic surfactant is proposed as a tool to classify polyoxometalates (POMs) in the Hofmeister series according to their affinity to adsorb on neutral polar surfaces. The strength of adsorption of super-chaotropic POMs is modulated by their charge density.

As featured in:

ChemComm

See Arno Pfitzner, Pierre Bauduin et al., Chem. Commun., 2018, **54**, 1833.

rsc.li/chemcomm

Registered charity number: 207890

Figure 3.1: Inside Back Cover Artwork of the published article in Chemical Communications.

This chapter was published in the peer-reviewed Journal *Chemical Communcations* of the publisher Royal Society of Chemistry (DOI:10.1039/C7CC09113C, this is also where the electronic supplementary information (ESI) can be found). It is worth to mention that this work was highlighted as an **Inside Back Cover** of the respective issue. Several other people also contributed to this work:

- Philipp Schmid contributed with experimental work during a Bachelor thesis.
- Séverine Renaudineau synthesized the three Dawson type Polyoxometalates used in this study.
- Dr. Olivier Diat, Prof. Dr. Anna Proust and Prof. Dr. Arno Pfitzner contributed with fruitful discussions and supervised the experimental work and improved the manuscript (MS).
- Dr. Pierre Bauduin performed the SAXS fitting, contributed with fruitful discussions, supervised the experimental work and corrected/improved the MS.
- Thomas Buchecker performed the experimental work (cloud point measurements and SAXS measurements), designed the figures, wrote and improved the MS.

Abstract: We propose a simple experimental procedure based on the cloud point measurement of a non-ionic surfactant as a tool for *(i)* estimating the super-chaotropic behaviour of polyoxometalates (POMs) and for *(ii)* establishing a classification of POMs according to their affinity towards polar surfaces.
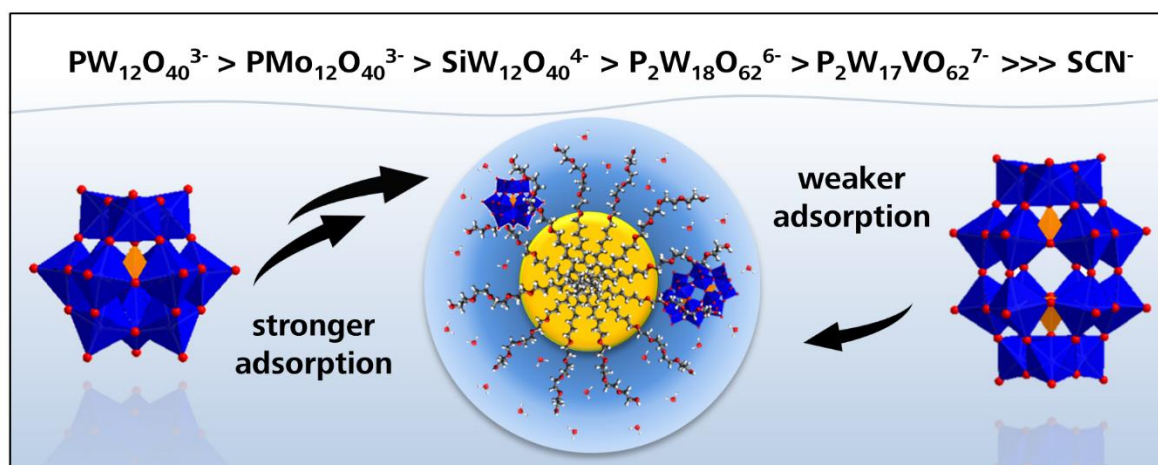
Figure 3.2: Table of contents visualizing of the adsorption and ranking of POMs on a micellar surface according to their adsorption strength.

3.2 Introduction

Polyoxometalates (POMs) are discrete nanometer sized anionic oxo-metal clusters that consist of early transition metals, especially V, Mo, and W and often incorporate a heteroatom.[1,2] Due to their unique structural and electronic versatility, POMs find many applications in biology,[3-6] as a phasing

tool in protein crystallography,[7] as (photo)-catalytically active oxidants[8,9] and in molecular materi-als.[10-13]

According to Hofmeister's classification of ions, chaotropic or salting-in anions are hydrated, highly polarizable, with low charge density and have the propensity to weakly adsorb on polar inter-faces.[14-18] Furthermore, they are usually referred to as soft anions. Recently, Naskar *et al.* showed that POMs are super-chaotropes compared to classical chaotropic anions, such as iodide or thiocy-anate, mostly due to their large size and delocalized charge.[19] Naskar *et al.* also highlighted that the super-chaotropic character of POMs was related to their strong propensity to adsorb on electri-cally neutral surfaces covered with polar groups such as $-(O-CH_2-CH_2)_x-OH$ or glucoside groups.[19] The POM adsorption process is considered to be entropically driven by partial dehydration of both the surfaces and POMs. It was further shown that the adsorption of super-chaotropic POMs is not specific towards polar surfaces but can be generalized to neutral and hydrated oligomers or poly-mers such as (poly-)ethylene glycol.[20] In most of the applications of POMs surface effects are in-volved as in catalysis,[21] materials science,[22] in micrography[23] and in the fabrication of electrodes.[24] Therefore, a deep understanding and characterization of the ability of POMs to adsorb spontane-ously on surfaces is essential for further innovative developments.

In this contribution, we propose a simple experimental procedure to classify POMs according to their propensity to adsorb on polar surfaces. The classification of POMs was made by investigating the cloud point (CP) increase of a non-ionic ethylene glycol (EO_x)-based surfactant, tetraethylene glycol octyl ether (C_8EO_4), upon the addition of POMs of different sizes, charges, structures and compositions, see **Figure 3.3**.
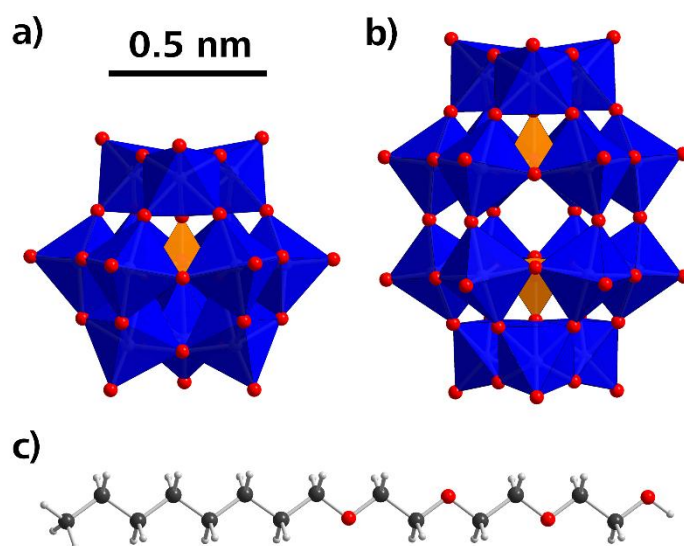
Figure 3.3: Representative structures of (a) an *α*-Keggin-type POM anion (here $PW_{12}O_{40}^{3-}$, PW^{3-}, $PMo_{12}O_{40}^{3-}$, PMo^{3-}, $SiW_{12}O_{40}^{4-}$, SiW^{4-}), (b) a Dawson-type POM anion (here $P_2W_{18}O_{62}^{6-}$, KP2W and HP2W, and $P_2W_{17}VO_{62}^{7-}$, HP2WV) and (c) the structure of tetraethylene glycol monooctyl ether (C_8EO_4).

The term cloud point (CP) generally refers to a liquid-liquid phase separation upon heating an aqueous solution containing a thermosensitive polymer or a surfactant.[25,26] The CP increase of a thermo-responsive molecule by adding a salt has been previously used as a tool to evaluate the adsorption strength/association constant of polarizable anions to the thermo-responsive molecule.[26,27] Naskar *et al.* showed that a pronounced increase of the CP of C_8EO_4 upon the addition of POMs was related to the strong adsorption of $PW_{12}O_{40}{}^{3-}$ and $SiW_{12}O_{40}{}^{4-}$ anions onto the micellar surface.[19] This approach is extended here to a series of POMs in order to highlight the pertinent parameters that influence the super-chaotropic behaviour of POMs. In a recent work by Kobayashi *et al.* a partial ranking of POMs according to their chaotropic nature was made based on the effect of POMs on the surface pressure isotherm of ionic and zwitterionic lipids. They concluded that POM's effects result from hydrophobic and electrostatic interactions between polyoxometalates and lipid mono-layers.[28] The present work investigates the effect of POMs on non-ionic systems which allows excluding the role of pure electrostatic interactions in the adsorption of POMs at surfaces. Moreover, the role of the hydrophobic effect is also likely to be negligible in the surface adsorption of POMs as they do not show any surface activity at water–alkane interfaces.

3.3 Experimental

CP measurements. Solutions containing 60 mM C_8EO_4 and a distinct amount of POM were placed into a thermostat (Thermomix_1460, B.Braun Melsungen AG) and were heated from 24 °C to 97 °C with a rate of 1 °Cmin^{-1}. The CP was detected by visual inspection with an uncertainty of $\pm$ 1 °C.

SAXS. SAXS/WAXS experiments were performed at the TRUSAXS beamline (ID02) at the ESRF in Grenoble, France. The instrument uses a pin-hole collimated monochromatic incident beam with a wavelength λ = 0.1 nm (12.4 keV). The SAXS detector (Rayonix MX-170HS) was set to a sample-to-detector distance of 1.2 m and WAXS data is simultaneously recorded with a Rayonix LX170HS detector placed in air 14 cm away from the sample. This setting allows to cover a broad q-range from 0.06 to 6.5 nm^{-1} with $q = 4\pi/\lambda \sin(\theta)$, the scattering vector defined by the scattering angle 2θ. The magnitude of the q vector for the WAXS was calibrated with the Bragg-reflections of a Para Bromo Benzoic Acid (PBBA) standard. The flux of the incident X-ray beam was $6\cdot10^{12}$ photons/s. Samples were contained in quartz capillaries with a diameter of 2.0 mm and a wall thickness of 0.01 mm. Measured 2D scattering pattern were normalized to absolute scale (in mm^{-1}) after instrumental corrections and azimuthally averaged to obtain the scattered intensity as a function of q. The normalized cumulative background of water, sample cell and instrument were subtracted to obtain I(q). Note that the beam polarization was not taken into account during the data reduction.

3.4 Results and Discussion

The cloud point (CP) increase of C_8EO_4 (60 mM) is plotted in **Figure 3.4** as a function of POM concentration and compared to the effect of classical Hofmeister anions (data for salts are taken from Naskar *et al.*[19]). $H_3PW_{12}O_{40}$ (H_3PW) demonstrates the strongest CP increase followed by $H_3PMo_{12}O_{40}$ (H_3PMo) depicting a similar but slightly less pronounced CP increase for c(H_3PW/ H_3PMo) < 5 mM. For c(H_3PW/ H_3PMo) > 5 mM, a precipitate is obtained confirming the stronger attractive interactions of these two POMs with the micellar surface, compared to the other investigated POMs. The CP increase by H_4SiW is even less prominent than the one by H_3PW and H_3PMo. Interestingly, $K_6P_2W_{18}O_{62}$ (KP2W) and $H_6P_2W_{18}O_{62}$ (HP2W), two Dawson-type POMs, increase the CP almost similarly but much less than the Keggin-type POMs. $K_7P_2W_{17}VO_{62}$ KP2WV displays the least pronounced effect. It is shown here for the first time that POMs of Dawson's type increase the CP of a thermosensitive molecule. The CP increase by lowly charged Keggin-type POMs, *i.e.* H_3PW, H_3PMo and H_4SiW, is more pronounced than by highly charged Dawson-type POMs, i.e. KP2W, HP2W and KP2WV. Moreover, it should be remarked that the CP increase by POMs is much more pronounced than by chaotropic anions in the classical Hofmeister's series. For example, sodium thiocyanate, NaSCN, increases the CP only by 5.3 °C for c(NaSCN) = 50 mM,[19] compared to 10–60 °C for c(POM) = 4 to 8 mM depending on the POM. The ranking according to the absolute CP increase is therefore as follows: H_3PW > H_3PMo > H_4SiW > KP2W ≈ HP2W > KP2WV >>> NaSCN.
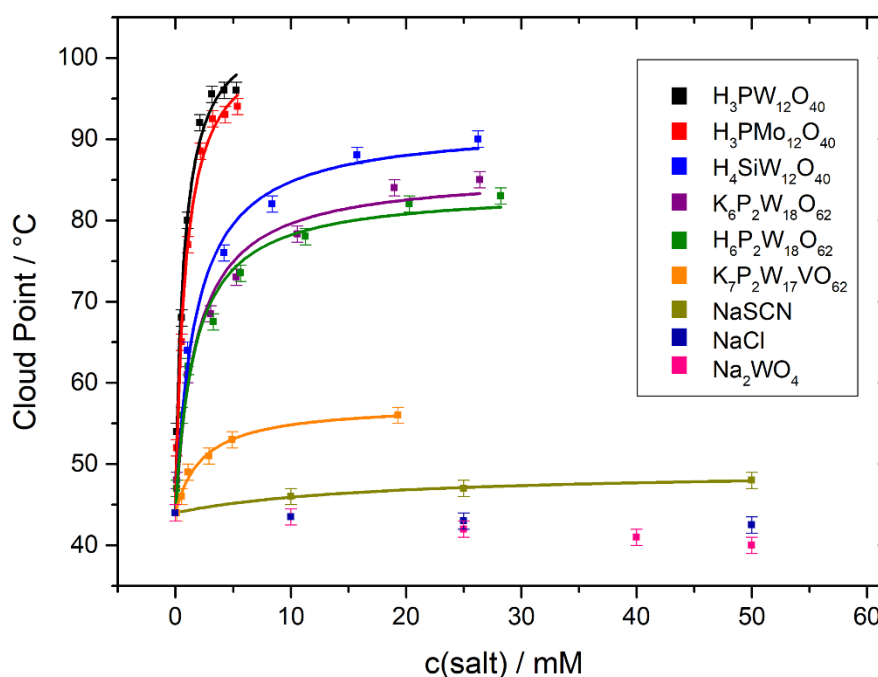
Figure 3.4: CP of 60 mM C_8EO_4 as a function of increasing POM (or salt) concentration. The solid lines represent Langmuir fits of the CP increase. Error bars represent the error of the CP by detection with visual inspection, $\pm$ 1 °C. The CP values for salts were taken from Naskar *et al.*[19]
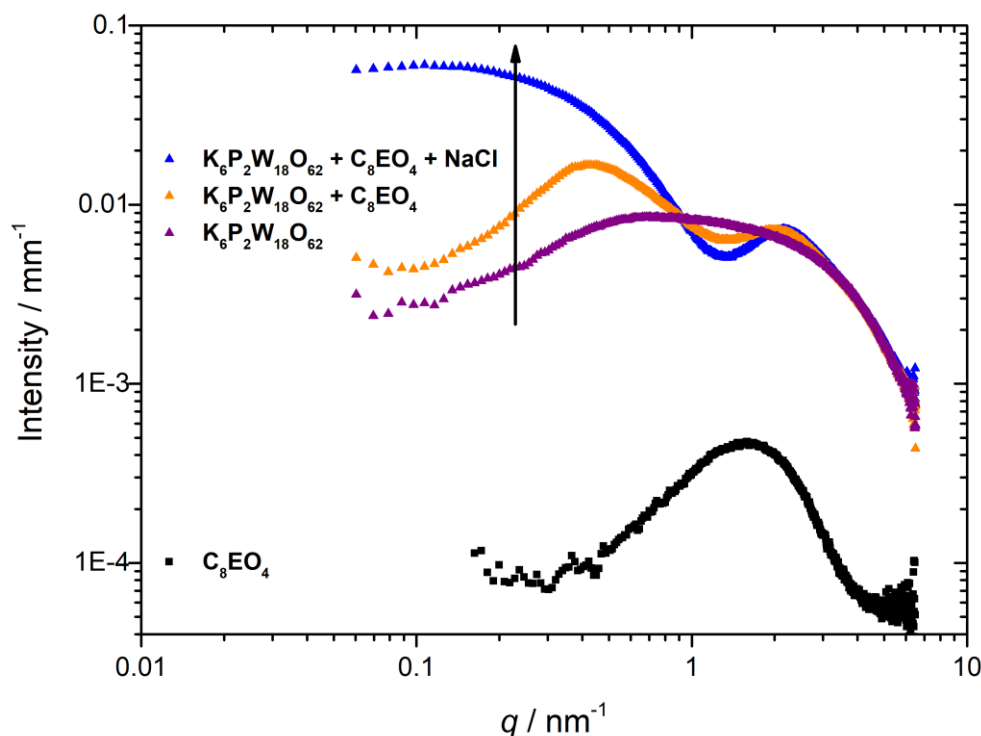
Figure 3.5: SAXS spectra of 60 mM C_8EO_4 (with and without 100 mM NaCl),1 mM $K_6P_2W_{18}O_{62}$ and their mixtures (1 mM $K_6P_2W_{18}O_{62}$–60 mM C_8EO_4 and 1 mM $K_6P2W_{18}O_{62}$–60 mM C_8EO_4–100 mM NaCl) in aqueous solution.

Small angle X-ray scattering measurements (SAXS) were performed on C_8EO_4, POMs and their mixtures to investigate the adsorption of POMs on the micellar surface, see the results for C_8EO_4–KP2W in **Figure 3.5**.

The scattered intensity of 60 mM C_8EO_4 is very low, as expected from the very low contrast of micelles compared to water.[19] The large oscillation, centred at around 1.5 nm^{-1}, originates mainly from an electron density excess in the micellar shell due the presence of EO groups providing a high electron density compared to the micellar core (octyl chains) and water. KP2W displays the scattering signature of dispersed prolate spheroidal objects in aqueous solution with electrostatic repulsions as indicated by the decay of the scattered intensity for $q < 0.5$ nm^1. The SAXS spectrum of the mixtures of 60 mM C_8EO_4 and 1 mM KP2W displays a much higher scattered intensity and a typical pattern of a core–shell structure with a large electron density excess in the shell, *i.e.* C_8EO_4 micelles with POMs adsorbed in the micellar shell.[19] Strong inter-micelle and inter-POM repulsions account for the depression of the scattered intensity for $q < 0.4$ nm^{-1}. The addition of 100 mM NaCl to a solution containing 60 mM C_8EO_4 and 1 mM KP2W, aiming at screening electrostatic interactions, leads to an increase in the scattering intensity for $q < 0.4$ nm^{-1}. Such a SAXS pattern therefore shows

the strong adsorption of POMs onto the surface of C_8EO_4 micelles as shown previously by Naskar *et al.* for H_4SiW–C_8EO_4 in comparable compositions.[19] The adsorption of POMs onto the surface of C_8EO_4 micelles leads to a strong increase in micelle–micelle repulsions leading to an increased CP of C_8EO_4 in the presence of POMs. A similar conclusion is made for all POMs under discussion since they produce a similar scattering pattern as depicted in **Figure 3.5**, see Fig. S4 (ESI†). The adsorption of POMs in the micelle's corona is confirmed by the fitting of the SAXS spectra using a core–shell model, as described previously.[19] The fitting results, see Table S1 (ESI†), suggest a large increase in electron density subsequent to the POM adsorption. Specific details on the fitting procedure are given in the ESI†.

Considering that POMs adsorb on the micellar surface, the CP increase as shown in **Figure 3.4** resembles a general evolution of an adsorption isotherm. Hence, the CP curves were fitted with a Langmuir model modified by a scaling parameter B_{max} corresponding to the extent of the CP increase:

Equation 1: $CP = CP(C_8EO_4) + (B_{max} \cdot K_A \cdot c(POM)) / (1 + K_A \cdot c(POM))$

with $CP(C_8EO_4)$ being the cloud point of C_8EO_4 in pure water and K_A the equilibrium association constant of the adsorption in units of mM^{-1}. This latter parameter is mostly dependent on the steepness of the CP increase at low POM concentrations whereas B_{max} describes the maximum extent of the CP increase. At this point we want to emphasize that the CP evolution does not meet the requirements of a classical Langmuir isotherm model as it *(i)* implies an adsorption process that is based on a well-defined flat monolayer under isothermal conditions with *(ii)* identical and equivalent adsorption sites and *(iii)* excluding (electrostatic) interactions and steric hindrance between POMs on adjacent adsorption sites. Despite the apparent non-applicability of this model on the system studied here, B_{max} and K_A values can be extracted from the best fits of the experimental data, see the fits represented by full lines in Fig. 2. B_{max} and K_A values corresponding to the best fits are listed in Table 1. Both B_{max} and K_A values provide an estimation of the chaotropic behaviour of each POM, *i.e.* the higher the B_{max} and K_A values the stronger the super-chaotropic behaviour. It should be noted that B_{max} values are more reliable than K_A values to estimate the relative chaotropic behaviour of POMs. K_A values values are tainted with a large error, typically 0.1 mM^{-1}, due to the steep increase in the CP for low POM concentrations observed for all POMs, except for KP2WV which shows a significantly lower B_{max} values. Nevertheless, the low K_A values obtained here – in the mM^{-1} range – show a strong general affinity of the POMs towards the micelle surface. Note that the K_A value for thiocyanate (SCN^-), a classical chaotropic Hofmeister anion, obtained from a similar fitting procedure, is much weaker than that for the (super-chaotropic) POMs, see **Table 3.1**.

Table 3.1: Fitting parameters (R^2 always larger than 98.3%) obtained from a modified Langmuir model of the CP increase. The volume charge density ρ is obtained by dividing the excess charge, $n \cdot e$ by the volume of Keggin type POMs (0.46 nm^3) and Dawson type POMs (0.68 nm^3) extracted from S. Hermann.[31]

	B_{max}	K_A	Charge	ρ
	°C	mM^{-1}	e	$e \cdot$nm^{-3}
$H_3PW_{12}O_{40}$	61.2	1.41	3	6.5
$H_3PMo_{12}O_{40}$	59.6	1.16	3	6.5
$H_4SiW_{12}O_{40}$	47.8	0.58	4	8.7
$K_6P_2W_{18}O_{62}$	42.0	0.56	6	8.8
$H_6P_2W_{18}O_{62}$	39.8	0.61	6	8.8
$K_7P_2W_{17}VO_{62}$	13.4	0.42	7	10.3

In the following an attempt was made to rationalize the series of POMs obtained according to their super-chaotropic behavior. In general, the chaotropic/kosmotropic behavior of ions follows their size/charge and polarizability where large anions of low charge density and high polarizability show the most pronounced chaotropic character.[29] Therefore, the volume charge density of POMs, ρ, expressed in number of charges per volume unit, see **Table 3.1**, was chosen as a criterion to characterize the chaotropic behaviour of POMs as ρ is related to their charge and size. It should be noted that for small ions (Cl$^-$, Br$^-$, SCN$^-$, *etc.*) such a calculation is much trickier since their ion radius in aqueous solutions is not well defined. This leads to huge errors in the estimation of the ionic volume. For this reason, hydrated volumes obtained from density measurements are usually considered as a size criterion to compare ions in solution.[30] As POMs are well defined nano-building units their volumes were calculated from their size in the crystal structure. The Keggin type POMs were considered to be oblate spheroids, almost spherical, with dimensions of 0.82 nm x 1.03 nm x 1.03 nm resulting in a volume of 0.46 nm^3 and Dawson type POMs were considered as prolate spheroids with dimensions of 1.22 nm x 1.03 nm x 1.03 nm resulting in a volume of 0.68 nm^3. These size values were taken from ref. [31], with H$_3$PW taken as a representative of a Keggin anion and HP2W as a representative of a Dawson anion. The substitution of tungsten by molybdenum has a negligible influence on the volume of the POM resulting in a similar ρ value for PMo^{3-} and PW^{3-}.

It appears here that the ρ values of POMs are related to the CP increase and to their chaotropy, *i.e.* the lower the ρ the higher the B_{max}, see **Table 3.1**. Indeed, ρ *vs.* B_{max} shows a roughly linear evolution, with a coefficient of determination of $R^2 = 0.85$ (see Fig. S5, ESI†). This result suggests that the charge density is a major feature of POMs that controls their chaotropic behaviour. It is generally assumed that a higher ρ leads to stronger hydration, *i.e.* water molecules bind more strongly to POMs with a higher charge density. Consequently, partial dehydration of POMs, taking place along

with the adsorption process, is associated with a higher energy cost for POMs with a higher p. It is interesting to remark that the type of the POM counterion is negligible on B_{max} when compared to KP2W and HP2W. Therefore, the counter ion has nearly no influence on the super-chaotropic behaviour of POMs. Moreover, this result is a direct proof that (i) the CP increase of C_8EO_4 by adding POMs is not related to the acidity of different POMs and that (ii) the high acidity does not lead to protonation of the surfactant and formation of an anionic (POM)-cationic (protonated surfactant) complex. PW^{3-} is found to be slightly more chaotropic than PMo^{3-}, see **Table 3.1** and **Figure 3.4**. PMo^{3-} and PW^{3-} only differ with respect to their polarizability, as they have an almost identical size and the same charge. Indeed, PW^{3-} is known to be more polarizable than PMo^{3-},[32] as expected from the higher number of electrons of a W atom ($Z_W = 74$) compared to a Mo atom ($Z_{Mo} = 42$). Highly polarizable ions adjust their charge distribution to minimize the electrostatic self-energy cost during adsorption at an interface.[33] Hence, the polarizability of POM nano-ions also influences the chaotropic behaviour and adsorption propensity of POMs towards polar molecules or surfaces but much less pronounced than their charge density.

3.5 Conclusion

In an attempt to draw general conclusions, it appears that the super-chaotropic behaviour of anions emerges from different features: the anion should have delocalized charges and should be large enough, typically at least in the nm range (nano-ions), to provide a high entropic gain associated with the surface adsorption process. This major entropic contribution to adsorption is associated with the release of hydration water molecules from the nano-ion (and from the surface) to the water bulk phase. The strength of the super-chaotropic behaviour is related to the volume charge density, p of the anion, i.e. the lower the p the higher B_{max}. A stronger anion hydration, due to a higher p, leads to a less efficient dehydration (lower entropy gain) during the adsorption process because a smaller number of water molecules is released, see PW^{3-} vs. SiW^{4-} or PW^{3-} vs. $P2W^{6-}$. The anion polarizability influences the chaotropic tendency of POMs (PMo^3 vs. PW^{3-}) to a much smaller extent as they scale with dispersion forces which are often proposed to be the driving force of specific ion effects.[29] In this context, our conclusions are also an extension of Collins concept of matching water affinities, observed between two oppositely charged particles (ions),[34] to the interaction of charged particles (here POMs) with uncharged but hydrated/polar molecules or surfaces. The procedure described here for POMs can be extended to other types of nanoions, such as boron clusters: dodecaborate, which was recently described as a super-chaotrope[35] or metallacarboranes.[36]

3.6 Bibliography

[1]   J. J. Borrás-Almenar, E. Coronado, A. Müller and M. Pope, *Polyoxometalate Molecular Science, Springer*, Netherlands, **2012**.

[2]   M. T. Pope and A. Müller, *Angew. Chem., Int. Ed.,* **1991**, *30,* 34–48.

[3]   B. Hasenknopf, *Front. Biosci.,* **2005**, *10,* 275.

[4]   J. T. Rhule, C. L. Hill, D. A. Judd and R. F. Schinazi, *Chem. Rev.,* **1998**, *98,* 327–357.

[5]   H. Stephan, M. Kubeil, F. Emmerling and C. E. Müller, *Eur. J. Inorg. Chem.,* **2013**, 1585–1594.

[6]   M. Aureliano, G. Fraqueza and C. A. Ohlin, *Dalton Trans.,* **2013**, *42,* 11770.

[7]   A. Bijelic and A. Rompel, *Coord. Chem. Rev.,* **2015**, *299,* 22–38.

[8]   S. Krickl, T. Buchecker, A. U. Meyer, I. Grillo, D. Touraud, P. Bauduin, B. König, A. Pfitzner and W. Kunz, *Phys. Chem. Chem. Phys.,* **2017**, *19,* 23773–23780.

[9]   C. L. Hill, *Comprehensive Coordination Chemistry II: From Biology to Nanotechnology*, Elsevier, Oxford, **2004**.

[10]   J. M. Clemente-Juan, E. Coronado and A. Gaita-Arino, *Chem. Soc. Rev.,* **2012**, *41,* 7464.

[11]   G. Izzet, F. Volatron and A. Proust, *Chem. Rec.,* **2017**, *17,* 250–266.

[12]   Y.-F. Song and R. Tsunashima, *Chem. Soc. Rev.,* **2012**, *41,* 7384.

[13]   H. N. Miras, J. Yan, D.-L. Long and L. Cronin, *Chem. Soc. Rev.,* **2012**, *41,* 7403.

[14]   E. Leontidis, M. Christoforou, C. Georgiou and T. Delclos, *Curr. Opin. Colloid Interface Sci.,* **2014**, *19,* 2–8.

[15]   T. Zemb and E. Leontidis, *Curr. Opin. Colloid Interface Sci.,* **2014**, *19,* 1.

[16]   N. Schwierz, D. Horinek and R. R. Netz, *Langmuir,* **2010**, *26,* 7370–7379.

[17]   W. Kunz, *Curr. Opin. Colloid Interface Sci.,* **2010**, *15,* 34–39.

[18]   F. Hofmeister, *Zur Lehre von der Wirkung der Salze,* **1888**, *vol. 24.*

[19]   B. Naskar, O. Diat, V. Nardello-Rataj and P. Bauduin, *J. Phys. Chem. C,* **2015**, *119,* 20985–20992.

[20]   T. Buchecker, X. LeGoff, B. Naskar, A. Pfitzner, O. Diat and P. Bauduin, *Chem. − Eur. J.,* **2017**, *23,* 8434–8442.

[21]   G. Bernardini, A. G. Wedd, C. Zhao and A. M. Bond, *Proc. Natl. Acad. Sci. U. S. A.,* **2012**, *109,* 11552–11557.

[22]   S. Polarz, S. Landsmann and A. Klaiber, *Angew. Chem., Int. Ed.,* **2014**, *53,* 946–954; V. Jallet, G. Guillemot, J. Lai, P. Bauduin, V. Nardello Rataj and A. Proust, *Chem. Commun.,* **2014**, *50,* 6610–6612.

[23]   S. Brenner and R. W. Horne, *Biochim. Biophys. Acta,* **1959**, *34,* 103–110.

[24]   C. Rong and F. C. Anson, *Inorg. Chim. Acta,* **1996**, *242,* 11–16.

[25]   M. Heskins and J. E. Guillet, *J. Macromol. Sci., Part A: Pure Appl. Chem.,* **1968**, *2*, 1441–1455.

[26]   H. Schott and A. E. Royce, *J. Pharm. Sci.,* **1984**, *73*, 793–799.

[27]   Y. Zhang, S. Furyk, D. E. Bergbreiter and P. S. Cremer, *J. Am. Chem. Soc.*, **2005**, *127,* 14505–14510.

[28]   D. Kobayashi, H. Nakahara, O. Shibata, K. Unoura and H. Nabika, *J. Phys. Chem. C*, **2017**, *121*, 12895–12902.

[29]   W. Kunz, *Specific ion effects,* World Scientific, **2010**; B. W. Ninham and V. Yaminsky, *Langmuir,* **1997**, *13,* 2097–2108.

[30]   Y. Marcus, *Ions in Solution and their Solvation,* John Wiley & Sons, **2015**.

[31]   S. Herrmann, *New synthetic routes to polyoxometalate containing ionic liquids: an investigation of their properties,* Springer, **2015**.

[32]   C. G. Liu, W. Guan, P. Song, Z. M. Su, C. Yao and E. B. Wang, *Inorg. Chem.,* **2009**, *48,* 8115–8119.

[33]   Y. Levin, *Phys. Rev. Lett.*, **2009**, *102,* 1–4.

[34]   K. D. Collins, *Methods,* **2004**, *34,* 300–311.

[35]   K. I. Assaf, M. S. Ural, F. Pan, T. Georgiev, S. Simova, K. Rissanen, D. Gabel and W. M. Nau, *Angew. Chem., Int. Ed.,* **2015**, *54,* 6852–6856.

[36]   P. Bauduin, S. Prevost, P. Farras, F. Teixidor, O. Diat and T. Zemb, *Angew. Chem., Int. Ed.,* **2011**, *50,* 5298–5300.

4 From nano-assemblies in water to crystal formation by electrostatic screening

4.1 Preface and Abstract

Figure 4.1: Back Cover Artwork of the published article in Chemistry – A European Journal.

This chapter was published in the peer-reviewed Journal *Chemistry – A European Journal* of the publisher Wiley (DOI: 10.1002/chem.201700044, this is also where the electronic supplementary information (ESI) can be found). It is worth to mention that this work was highlighted as a **Back Cover** of the respective issue and was marked as a **HOT PAPER**. Several other people also contributed to this work:

- Dr. Xavier LeGoff performed the single-crystal X-ray study for PW^{3-} - EO_6/EO_5 - $3Na^+$ crystals.
- Dr. Bappaditya Naskar was the first one who observed the formation of ethylene glycol – polyoxometalate crystals
- Dr. Olivier Diat and Prof. Dr. Arno Pfitzner contributed with fruitful discussions and supervised the experimental work and improved the manuscript (MS)
- Dr. Pierre Bauduin simulated SAXS spectra, contributed with practical work for SANS measurements, contributed with fruitful discussions, supervised the experimental work and wrote/corrected the MS
- Thomas Buchecker performed the practical work, performed the single-crystal X-ray study for PW^{3-} - EO_{11} - $K^+H^+H^+$ crystals, designed the figures, wrote and improved the MS.

Abstract: In the last decade organic-inorganic hybrid materials have become essential in material science as they combine properties of both building blocks. Nowadays the main routes for their synthesis involve electrostatic coupling, covalent grafting and/or solvent effects. In this field, poly-oxometalates (POMs) have emerged as interesting inorganic functional building blocks due to their outstanding properties. In the present work we show that the well-known α-Keggin polyoxometalate, α-$PW_{12}O_{40}{}^{3-}$ (PW^{3-}), can form hybrid crystalline materials with industrial (neutral) poly-ethylene glycol oligomers (PEG) under mild conditions, *i.e.* in aqueous medium and at room temperature. The formation of these materials originates from the spontaneous self-assembly of PW^{3-} with EO_x, with at least four EO units ($x > 4$). The PW^{3-}-PEG nano-assemblies, made of a POM surrounded by about two PEG oligomers, are stabilized by electrostatic repulsions between the negatively charged PW^{3-} anions. Addition of NaCl, aiming at screening the inter-nano-assembly repulsions, induces aggregation and formation of hybrid crystalline materials. Single crystal analysis showed a high selectivity of PW^{3-} towards EO_5-EO_6 oligomers from PEG200, which is made of a mixture of EO_{3-8}. Therefore, a general "soft" route to produce POM - organic composites is proposed here by the control of electrostatic repulsions between spontaneously formed nano-assemblies in water. The methodology developed here, which is based on the electrostatic screening between pre-formed organic-inorganic EO_x-PW^{3-} nano-assemblies, can be extended to other kind of water soluble oligomers that interact with POMs in solution as shown for composite materials consisting of $PW^{3-} - EO_{11}$ - K^+ - H^+ - H^+, *i.e.* different (mixed) cations, different EO_x chain lengths and different number of ethylene glycol chains (EO_5/EO_6 *vs.* EO_{11}). This rational design of new POM hybrid (crystalline) materials with

hydrophilic blocks using such a simple mixing procedure of the components however implies a deep understanding of the molecular interactions.
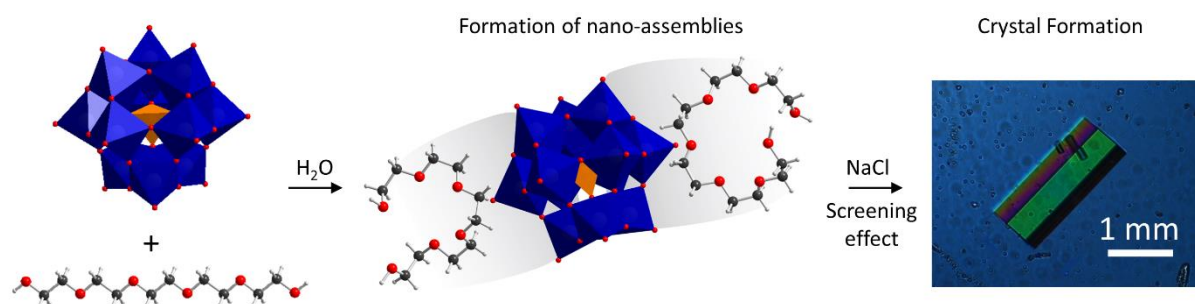
Figure 4.2: Come together: The screening of the electrostatic repulsions between spontaneously formed ethylene glycol-polyoxometalate nano-assemblies promotes the formation of a crystalline hybrid material.

4.2 Introduction

Polyoxometalates (POMs) are anionic metal-oxygen clusters consisting of oxo-linked MO_x polyhedra of early transition metals in their highest oxidation state.[1] Their electronic versatility and the blend of *p*-bock elements, transitions metals and differently bound oxygen atoms (terminal and bridging) grant special properties resulting in a broad field for applications such as catalysis,[2,3] material science,[4,5] biology[6,7] and medicine.[8–10] For most of these applications the understanding of the interactions between inorganic POM clusters and organic entities is essential.

In this context, much effort has been made to the design and building of POM-organic hybrid assemblies. Many examples on such hybrid POM systems are provided in recent comprehensive reviews for example by Proust *et al.*[11] and Cronin *et al.*[12] The design of POM-organic composite materials is mostly based on two approaches: an electrostatic coupling between an anionic POM with an organic cation and a covalent coupling with the POMs chemically grafted to organic moieties. POMs fixed at electrodes,[13] embedded in polymers[14] and organized in a hierarchical self-assembly[15–22] are examples that meet the former case. In a recent contribution of Izzet *et al.* hierarchical self-assembly of POM hybrids has been achieved by using an approach that combines electrostatics interactions and metal coordination of a POM chemically grafted building block.[18] Interestingly, the self-assembly process in this latter system, from discrete assembly to nano-aggregate, was tuned by changing the type of solvent. On the other hand, covalent grafting has been used to immobilize POMs on surfaces or interfaces,[23] in mesoporous materials[24,25] and in the synthesis of POM based surfactants to form either microemulsion systems[26] or smart electrochemically responsive materials.[27]

Recently, the strong propensity of α-Keggin based POMs, phospho- and silico-tungstate (α-SiW$_{12}$O$_{40}^{4-}$ and α-PW$_{12}$O$_{40}^{3-}$), to adsorb on neutral soft interfaces covered with polar organic moieties, such as sugar and ethylene oxide (EO) groups, was highlighted.[28] POMs were indeed shown to adsorb at the micellar surface of *e.g.* tetraehtyleneglycol mono-octyl ether (C$_8$EO$_4$) and octyl beta-glucoside (C$_8$G$_1$), without disrupting the micellar assembly. It was also shown that the adsorption of POMs is not restricted to the micelle-water interface but it also takes place at the water-air surface covered by these two surfactants. These findings give an opportunity to the formation of hybrid POM materials by another approach that is neither based on pure electrostatic or covalent grafting but that takes advantages of weak intermolecular forces between POMs and polar organic functional groups in aqueous solution.

Consequently, the aim of this work was first to study more specifically the role of the supramolecular POM-(poly-)ethylene oxide (PEG) interaction previously observed at the micelle-water and water-air interface covered by PEG based non-ionic surfactants and second to investigate the potential to use POM-PEG interactions to build up highly ordered hybrid POM based materials. This work is restricted to the investigation of weak interactions, *i.e.* neither electrostatic nor covalent bonds, acting between POM and polar organic functional groups. These interactions were probed in the most "green" solvent, *i.e.* water, without using polar organic solvents classically used in POM chemistry such as acetonitrile or DMSO.
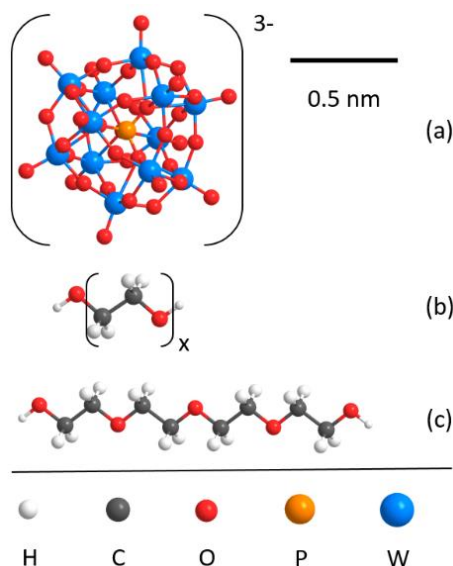
Figure 4.3: Optimized structures of (a) α-PW$_{12}$O$_{40}^{3-}$ (PW^{3-}), (b) the EO$_x$ oligomer repeating unit and (c) the main component in PEG200, *i.e.* EO$_4$. PW^{3-}-EO$_x$ interactions were investigated as a function of its ratio, EO$_x$ chain length and EO$_x$ concentration. Polydisperse PEG chemicals (PEG200, PEG300, PEG400 and PEG20000) were used to cover a broad range of EO$_x$ oligomer chain lengths.

The strategy applied here was to simplify the chemical systems by investigating the interactions in water between POM, α-PW$_{12}$O$_{40}^{3-}$ (PW^{3-}), see **Figure 4.3**, and the polar head of PEG based non-ionic surfactants, *i.e.* simple oligomeric PEG chains see **Figure 4.3**. Therefore, only the POM-PEG

interactions without surface effects were probed in the present contribution. POMs and PEG chains are not expected to interact in water as *(i)* they are anionic and electrical neutral, respectively, and as *(ii)* they are both highly hydrophilic/water-soluble.

PEGs receive an outstanding importance in medicine as well as in chemistry, biology and industry due to their low price and high biocompatibility.[29,30] They are widely applied in product and drug formulations, chemical reactions and in advanced functional materials.[31–34] Hence, composite materials of POM and EO_x oligomers face a long history as the combination of both the catalytic performance of POMs and above mentioned benefits of PEG could lead to advantageous materials with superior performances. Therefore, lots of work has already been performed on this subject.[35–39] Already in 1989, Neumann *et al.* observed an elevated catalytic activity of POMs in the presence of PEG.[39] In material science, layered PEG-POM structures consisting of PEG chains covalently grafted to a POM, have been constructed.[36,37] Only recently, non-covalently bound POM-(long) PEG composites were produced via a hydrothermal route and characterized as intermediate temperature proton conductors.[38]

In the present work, PEG-PW^{3-} interactions were probed in water at room temperature and at low concentrations (< 100 mM), much below the solubility limits of the components, by varying the chain length of PEG for a series of compounds from pure EO_1 to EO_4. Longer EO_x were tested as well but as they are difficult to obtain with a pure grade, industrial mixtures were used: PEG200 (equivalent in average to EO_4), PEG300 (~ EO_6), PEG400 (~ EO_8) and PEG20000 (~ EO_{400}). Industrial grade PEG_x show dispersity in their chain lengths, *i.e.* in their number of EO units. PEG200 for example covers a range EO_x from $x = 3$ to 8 without a majority (around 90%) being EO_4, EO_5 and EO_6, as analyzed by mass-spectroscopy, see SI.

PW^{3-}-EO_x interactions were studied by combining several techniques with different focus. Small angle X-ray scattering (SAXS) experiments were performed as a function of POM/EO_x ratios to obtain information on electron density inhomogeneity coming mainly from the POM and the surrounding medium composed of water and EO_x. Small angle neutron scattering (SANS) measurements were performed in deuterated water in order to gain structural and supramolecular information on the hydrogenated EO_x oligomers. Furthermore ^{1}H-NMR was used to yield information at a molecular level on the chemical environment of the hydrogen atoms of EO_x in the presence of POM.

Since from a previous investigation[28] the addition of excess salt is known to screen electrostatic interactions between negatively charged POM anions,[28] the impact of salt addition on the EO_x-POM mixtures was also investigated. The formation of a solid phase and the formation of crystals consisting of EO_x-PW^{3-} composites were investigated by SAXS as well as by single crystal-XRD. An attempt was made here to correlate interactions taking place between PW^{3-} and EO_x in aqueous solution with the highly ordered structure obtained in the solid state.

4.3 Experimental

Materials. Phosphotungstic acid hydrate (H_3PW, MW = 2898 g/mol, $H_3PW_{12}O_{40} \cdot H_2O$, 99.995% purity) was purchased from Sigma Aldrich. The maximum solubility of H_3PW in water is 900 mM, the diameter of PW^{3-} is 0.95 nm, providing a volume of 0.54 nm^3 per PW^{3-}. This molecular volume corresponds to a maximum volume fraction of 27% of a concentrated PW^{3-} solution. TGA measurements revealed, that purchased PW^{3-} contains up to 5 wt% of water. This was not taken into account for sample preparation. PEG200, PEG300, PEG400, were purchased from Sigma Aldrich and were of reagent grade. The molecular weights of EO_x with x = 1 is 62 g/mol and 44 g/mol per every further repeating $-CH_2-CH_2-O-$ (EO) unit. PEG 200 means, that the molecular weight average of PEG amounts to 200 g/mol^{-1}, therefore having an average in the size distribution at 4 EO units (PEG300: 6 EO units, PEG400: 8 EO units). This is due to the fact, that PEG polymers consist of mixtures with a distribution on the number of the EO units, for example PEG 200 is composed of a mixture of PEG_n = 3,4,5,6 EO units, see SI. Pure ethylene oxide (EO_1, 99%), diethylene oxide (EO_2, 99%), triethylene oxide (EO_3, 99%) and tetraethylene oxide (EO_4, 99%) were purchased from Sigma Aldrich. In contrast to PEG_x compounds, those chemicals do not exhibit a distribution in their chain length, but have a distinct chain length. Sodium chloride (NaCl, 99.5%), potassium chloride (KCl, 99%), were purchased from Sigma Aldrich, hydrochloric acid (HCl, 37% for analysis) was purchased from Carlo Erba reagents. Milli-Q water was used with a conductivity lower than 10.5 μS/cm and a total organic carbon content of max. 400 ppb.

Sample preparation. Crystals were prepared along the same following procedure: An aqueous solution containing EO_x/PEG_x and salt/acid (HCl, LiCl, NaCl) (solution 1) was cooled down to 4 °C in the refrigerator. A second aqueous solution containing PW^{3-} and the same amount of salt/acid (solution 2) was also cooled down to 4°C. Solution 2 was poured gently to solution 1 and left in the refrigerator for 3 days. Then a microscopy analysis was performed to see if crystals were formed or not.

SAXS. SAXS measurements using Mo radiation (λ = 0.071 nm) were performed on a bench built by XENOCS. The scattered beam was recorded using a large online scanner detector (diameter: 345 mm, from MAR Research). A large q-range (0.2 to 40 nm^{-1}) was covered with an off-center detection. The collimation was applied using a 12:$\propto$ multilayer Xenocs mirror (for Mo radiation) coupled to two sets of scatter less FORVIS slits providing a 0.8 × 0.8 mm X-ray beam at the sample position. Pre analysis of data was performed using FIT2D software. The scattered intensities are expressed versus the magnitude of scattering vector q = [(4π)/λ]sin(θ/2), where λ is the wavelength of incident radiation and θ the scattering angle. 2 mm quartz capillaries were used as sample containers for the solutions. Usual corrections for background (empty cell and detector noise) subtractions and intensity normalization using high density polyethylene film as a standard were applied. Experimental

resolution was $\Delta q/q = 0.05$. Silver behenate in a sealed capillary was used as the scattering vector calibration standard.

SANS. SANS spectra were recorded at the V16-TOF beamline at the HZB Berlin. The q-range from 0.6 nm^{-1} to 7 nm^{-1} was accessed which corresponds to sizes from around 0.9 to 10.5 nm in real space. All spectra were corrected from instrumental background and empty cell and from the incoherent scattering, mainly due to hydrogen atoms of the PEG$_x$. The small contribution of PW^{3-} (constant scattering over the whole q-range) was also subtracted. The scattered intensity was calibrated with water and therefore data are shown in absolute values (cm^{-1}).

NMR. All NMR spectra were measured at room temperature using a Bruker Avance 300 (300 MHz for ^{1}H) NMR spectrometer. All chemical shifts are reported in δ-scale as parts per million (ppm) (multiplicity, coupling constant J, number of protons) relative to the solvent residual peak (D$_2$O) as the internal standard.

4.4 Results and Discussion

A concentration of 50 mM EO$_1$-EO$_4$ and PEG (200, 300, 400, 20000) in aqueous media of H$_3$PW, the acidic form of PW^{3-}, provides clear isotropic solutions at any proportion without the formation of any precipitate visible at the macroscopic level.
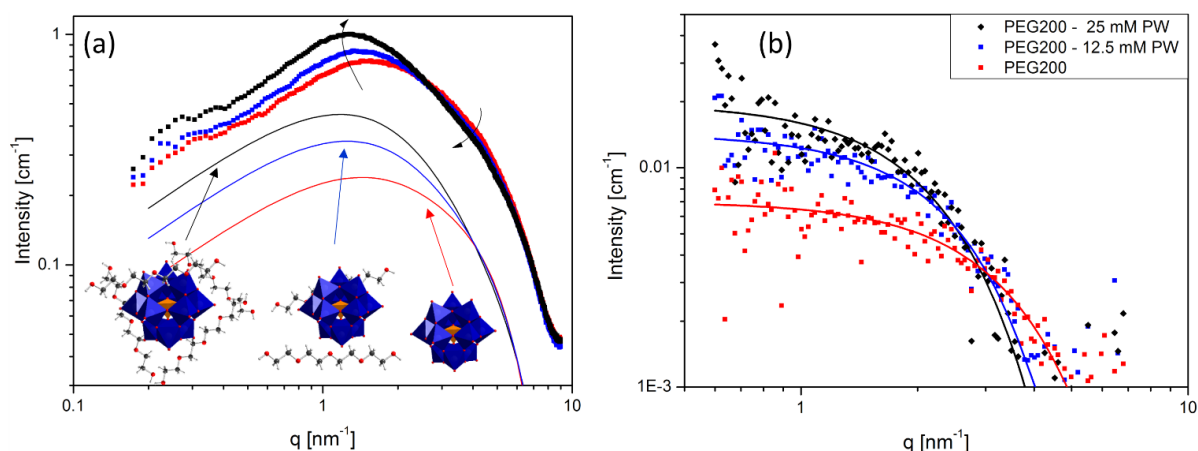
Figure 4.4: The interaction of EO$_x$/PEG – POM monitored on a molecular level. (a) SAXS spectra of 0 mM (red), 50 mM (blue) and 100 mM PEG200 (black) in the presence of 25 mM H$_3$PW. The scattering pattern of PEG200 in water is not shown as c(PEG200) < 100 mM does not produce a detectable signal compared to the spectrum of neat water. Theoretical simulations (solid lines) of SAXS spectra for hypothetical molecular arrangements of PW^{3-}-PEG assemblies: PW^{3-} alone (red), PW^{3-} with two EO$_4$ oligomer in a fully extended conformation (blue) , PW^{3-}-2(EO$_4$), (blue) and PW^{3-} with four EO$_4$ oligomers in a fully extended conformation PW^{3-}-4(EO$_4$), (black). For the sake of clarity, the simulated spectra are shifted in intensity from the experimental spectra. (b) SANS spectra of 50 mM PEG200 as representative model for EO$_x$ oligomers in the presence of 0, 12.5 and 25 mM H$_3$PW.

4.4.1 PW^{3-}/EO$_x$ nano-assemblies by small angle X-ray scattering (SAXS).

The SAXS spectra of 25 mM PW^{3-} in pure water and in the presence of 50 and 100 mM PEG200 are depicted in **Figure 4.4**. All spectra overlap in the high q-regime ($q > 5$ nm^{-1}) where the scattered intensity comes mainly from the PW^{3-}, *i.e.* its form factor and its concentration. At low q values ($q < 0.5$ nm^{-1}) where inter-molecular sub-molecular distances are concerned, all spectra show a decreased intensity indicating strong repulsive interactions between negatively charged POMs.[28] The spectra of PEG – PW^{3-} show excess scattering in the low q-range ($q < 4$ nm^{-1}) compared to pure PW^{3-}. The excess scattering increases and shows a maximum value that is shifting to lower q values, *i.e.* larger distances, with increasing PEG200 concentration. These two last features observed in the spectra by adding PEG200 can be attributed to an excess of electron density (compared to water) around the POM and to the formation of a structure larger than the POM alone (~ 1 nm in size), respectively. Therefore, the SAXS spectra can be interpreted by the formation of POM-PEG self-assemblies with the POM decorated by PEG oligomers, which has an electron density higher than the one of water.

This type of structure for the nano-assemblies was validated by simulations of the SAXS spectra for different hypothetical computer built PW^{3-}-(EO$_4$)$_x$ molecular arrangements. PW^{3-}-(EO$_4$)$_x$ nano-assemblies were designed in-silico and their SAXS spectra were calculated from their spatial atomic positions by using the CRYSOL software.[40] Snapshots of the different molecular arrangements, the simulated curves and the details on the procedure to produce the simulated spectra are given in SI. The simulated spectra for PW^{3-} and for PW^{3-}-EO$_4$ nano-assemblies with 1:2 and 1:4 ratios, *i.e.* PW^{3-}-2(EO$_4$) and PW^{3-}-4(EO$_4$), (see solid lines in **Figure 4.4**) have shapes similar to the experimental spectra obtained for PW^{3-}-PEG200 at different PEG concentrations. Both the shift to lower q values and the increase in the excess scattered intensity are reproduced in the simulations. The consistency between the experimental and simulated spectra suggests that PEG oligomers bind with PW^{3-} in water and that PW^{3-} are getting more and more surrounded by PEG oligomers with increasing PEG/PW^{3-} ratio.

In a previous investigation, Keggin POMs were found to adsorb on the surface of micelles of non-ionic PEG/sugar based surfactants.[28] In order to ensure that such a structure, formed by PEG(s) surrounded by POMs, does not form in PEG/PW^{3-} mixtures, simulations of PW^{3-}-PEG$_x$ nano-assemblies made of a core of many PEG$_x$ oligomer(s) surrounded with several PW^{3-}, were investigated, see Figure S1. Such hypothetical molecular arrangements give SAXS spectra with a strong oscillation in the mid q-range, at around 2 nm^{-1}, originating from strong POM-POM repulsions. Such an oscillation was never observed in the experimental spectra confirming that PW^{3-}-PEG assemblies consist of single POMs decorated with PEG oligomers.

In order to get a deeper understanding of PW^{3-}-PEG interactions in water, EO$_1$ – EO$_4$ and PEG300/PEG400/PEG20000 were also investigated by SAXS in the presence of PW^{3-}, see Figure S2.

Scattering spectra of $EO_1 - EO_4$ / PW^{3-} mixtures overlap the spectrum of pure PW^{3-} in water over the whole q-range, suggesting that no assembly is formed. The spectra of PEG300/PEG400/PEG20000 – PW^{3-} clearly show excess scattering in the low q-range ($q < 4$ nm^{-1}) compared to the PW^{3-} spectrum; the same holds for PEG200. By increasing the length of PEG, the excess scattering and the maximum of the scattered intensity, respectively, becomes more pronounced and is shifted to lower q values. Considering that electrostatic repulsions between the aggregates take place, the size of the PW^{3-}/PEG_x assemblies cannot be estimated by applying a Guinier analysis. As a rough estimation, the intensity decrease in the q-range $1 < q < 3$ nm^{-1} indicates that aggregates with an average radius of 0.6 to 1 nm are formed. Comparing these average radii to the hydrodynamic radii of pure PW^{3-} in water, *i.e.* 0.5 nm see Figure S3, also confirms the presence of nano-assemblies of PW^{3-}/PEG. Moreover, this scattering signal is shifted to smaller q values from PEG300 to PEG400 to PEG20000 indicating that larger nano-assemblies are formed with increasing EO_x chain lengths. The comparison of the experimental and simulated spectra, see Figure S1, indicates that PEG300-PW^{3-} and PEG400-PW^{3-} assemblies produce similar scattering patterns as the ones of PW^{3-} surrounded by 3 and 7 EO_4 oligomers, respectively. Therefore, it can be concluded that the extent of excess scattering and the shift of the q_{max} values depend on the absolute number of EO_x oligomers around PW^{3-}. The change in the conformation of the EO_4 oligomer, from an extended to a U-shaped conformation, alters only slightly the simulated SAXS scattering pattern of EO_x decorated PW^{3-} assemblies. Therefore, no configurational information can be derived from SAXS.

From these scattering experiments we can deduce that the formation of PW^{3-}/EO_x assemblies is mostly promoted by longer EO_x oligomers $x \geq 4$ and that the size of these assemblies increases with the length of the EO_x oligomer, once a critical EO_x chain length is reached, *i.e.* for $x > 4$.

4.4.2 PW^{3-}/EO_x nano-assemblies by small angle neutron scattering (SANS).

SAXS gives a first proof of the PW^{3-}/EO_x interactions taking place in water and leading to their self-assembly. The scattering contrast in SAXS originates here from inter and intra correlation of POM which has a very high electron density due to the presence of tungsten atoms. In order to investigate further the PW^{3-}-EO_x self-assembly, SANS experiments were performed on PEG200-PW^{3-} mixtures in D_2O. The advantage of performing SANS in the present system is that PW^{3-} produces almost no contrast with D_2O and a constant scattered intensity is observed over the whole q-range. For the sake of clarity this spectrum is not shown in **Figure 4.4(b)**. Therefore, only the hydrogenated PEG200 contributes to the coherent scattered intensity. **Figure 4.4(b)** shows the SANS spectra of PEG200 at 50 mM in D_2O for different PW^{3-} concentrations: 0, 12.5 and 25 mM, corresponding to PEG/PW^{3-} molar ratios of 1/0, 4/1 and 2/1. The spectrum of 50 mM PEG200 shows the typical scattering of globular objects. Addition of PW^{3-} leads to *(i)* an increase of the forward scattering, $I(0)$, and to *(ii)* a slight shift of the scattering spectra towards lower q, which indicates the formation of

larger scattering objects. However, the difference between the spectra at 12.5 and 25 mM remains weak.

The spectra could be well fitted with a Guinier model, $I(q) = I(0) \, exp(-q^2 R_g/3)$, yielding mean radii of gyration (R_g) of the aggregates from 0.5 (for 0 mM PW^{3-}), 0.7 (for 12.5 mM PW^{3-}) to 0.8 nm (for 25 mM PW^{3-}), confirming the increasing size of the scattering object when adding PW^{3-}. Furthermore, the $I(0)$ values were analysed by assuming the scattering of isotopically distributed objects as:

Equation (1): $\qquad\qquad I(0) = nV^2(\Delta\rho)^2$

with n being the concentration of the scattering objects, V their Volume, and $\Delta\rho$ the scattering length density difference between D$_2$O and the scattering objects. By assuming that (i) PEG200 oligomers only contribute to the scattered signal in SANS and that (ii) PEG200 is mostly composed of EO$_4$, then the forward scattered intensity can be rewritten as:

Equation (2): $\qquad I(0) = [EO]_4 \cdot N_{agg} \cdot V^2([EO]_4) \cdot (\rho(D_2O) - \rho(EO_4))^2$

with [EO$_4$] the PEG200 number concentration, N_{agg} the aggregation number of EO$_4$ in EO$_x$/PW^{3-} assemblies, $V^2([EO]_4)$ the molecular volume of EO$_4$ and ρ the scattering length densities of D$_2$O and EO$_4$. The experimental spectra were fitted by adjusting only N_{agg} as the other parameters are known. The N_{agg} values obtained by this approach are 1.0, 2.0 and 2.2 for 0, 12.5 and 25 mM PW^{3-} and correspond to averaged aggregation numbers with an error estimated to be at least 0.5. Only averaged N_{agg} values can be estimated as the PEG can be present in solution as a mixture of un-associated oligomers and PW^{3-} associated oligomers (PW^{3-}-EO$_4$, PW^{3-}-2(EO$_4$), PW^{3-}-3(EO$_4$) *etc.*). From the SANS results it can be concluded that (i) PEG200 is in monomeric form, *i.e.* non-aggregated at 50 mM in pure water and that (ii) addition of PW^{3-} leads to PEG200 aggregation. By combining the SAXS/SANS results, it can be stated that PW^{3-}-PEG200 nano-assemblies consist of a POM surrounded by in average two PEG oligomers.

4.4.3   Molecular interactions in the nano-assemblies probed by NMR.
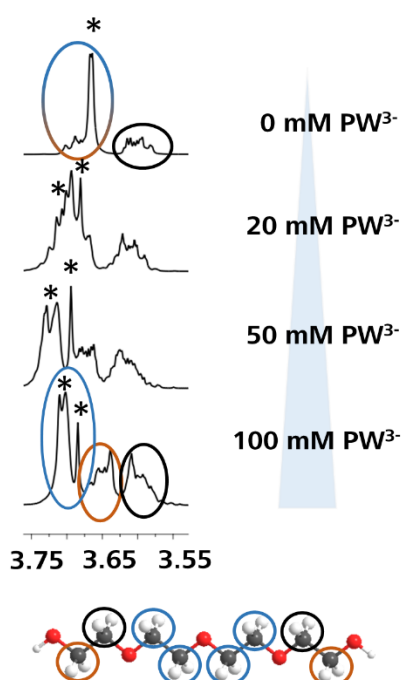
Figure 4.5: NMR resonance signals of 100 mM PEG200 in the presence of 0, 25, 50 and 100 mM PW^{3-} (from top to bottom) and qualitative assignment of the protons of the main component of PEG200, *i.e.* EO$_4$, to the resonance signals. The stars indicate the change in intensity of the resonance signal stemming from the inner protons (blue circles) and the emergence of a doublet of PEG200, which represents PEG200 adsorbed on PW^{3-}.

^{1}H-NMR was performed to probe the change in the local environment of the EO$_x$ oligomers caused by their adsorption on PW^{3-}. Previous studies have shown that NMR is an efficient technique to probe molecular interactions of PEG for example with zeolithe[41] or proteins.[42]

PEG200 was chosen as a EO$_x$ representative as SAXS and SANS experiments clearly showed the presence of PW^{3-}/PEG200 nano-assemblies. Hence, ^{1}H-NMR spectra of 100 mM PEG200 solutions in D$_2$O were collected for different PW^{3-} concentrations (0, 20, 50, 100 mM), see **Figure 4.5**. The spectrum for 0 mM PW^{3-} depicts three resonance signals: a multiplet from 3.55 to 3.62 ppm, a multiplet from 3.65 to 3.70 ppm and a sharp singlet at 3.65 (marked with *). By considering EO$_4$ (C$_8$O$_5$H$_{18}$), the main component of PEG200, hydrogen atoms can be assigned by using Shoolery's rules for the NMR increment of -CH$_2$- groups.[43] The multiplet overlapping with the large singlet at 3.65 to 3.70 ppm is assigned to the -CH$_2$-**CH$_2$**-OH (brown). The large singlet is assigned to the magnetically equivalent inner -O-**CH$_2$**-**CH$_2$**-O- groups (blue)[41,44] and the multiplet from 3.55 to 3.62 ppm is assigned to the CH$_2$ groups connected to the terminal -CH$_2$OH groups -**CH$_2$**-CH$_2$-OH (black). The O-H protons of the terminal hydroxyl groups are not visible in this NMR setup due to their fast intermolecular exchange with the solvent.[45]

Addition of PW^{3-} to PEG200 produces two main effects on the spectra, it yields to *(i)* a shift of the large singlet to the deep-field and to *(ii)* an intensity decrease of the singlet and the emergence of a doublet which increases in intensity with increasing PW^{3-} concentration (marked with *). This last trend as a function of PW^{3-} concentration indicates that the singlet and the emerging doublet correspond respectively to the un-associated and associated form of the PEG in solution. Therefore, the progressive formation of the nano-assemblies by increasing PW^{3-} concentration is monitored. For 100 mM PW^{3-} the three signals are well separated and can therefore be integrated separately giving a hydrogen ratio of 8:4:4. A detailed integration of the multiplets is shown in Figure S4. The multiplet at 3.57 ppm can still be attributed to the terminal $-CH_2-$ groups (red) as it remains almost constant with increasing PW^{3-} concentration. The multiplet initially at 3.67 ppm also remains almost constant. Only the singlet corresponding to the inner hydrogen atoms of EO_4 shifts to the deep-field upon addition of PW^{3-}. Therefore, NMR suggests that the hydrogen atoms of the two inner EO units strongly interact with PW^{3-} whereas CH_2 groups in the two terminal EO moieties do not take part in the self-assembly between PW^{3-} and EO_x oligomers, see **Figure 4.6**. Note, that for NMR experiments higher PW^{3-} concentrations were chosen compared to SAXS/SANS experiments in order to highlight the trend of the splitting and shifting of the resonance signals. Furthermore, additional NMR experiments on the pure EO_4 compound, *i.e.* tetraethylene glycol, were performed to obtain further information on the adsorption process for shorter chain EO_x oligomers, see Figure S5. Indeed, a shift of an intense singlet to the deep-field was observed (as it was the case for PEG200). However, *(i)* no splitting of the singlet and *(ii)* no changes in the relative intensities of the resonance signals were observed. Furthermore, the relative chemical shift, δ Δppm, upon addition of PW^{3-} is smaller compared to the relative chemical shift of PEG200 upon PW^{3-} addition. Therefore, it can be concluded that pure EO_4 also interacts with PW^{3-}, but at only at higher concentrations of PW^{3-} in comparison to PEG200.

In order to prove that the shift of the singlet and the emergence of the doublet do not originate from a classical salt effect or from the acidic protons of H_3PW^{3-}, NMR spectra of PEG200 were collected in the presence of various salts and for similar acidity using HCl. These tests did not result in significant changes of the shape and the shift of the resonance peaks, see Figure S6 and S7. Consequently, the changes observed on the ^{1}H-NMR spectra by increasing PW^{3-} concentration can be attributed to the formation of PW^{3-}-EO_x nano-assemblies in water. It should be noted that the NMR signal of PEG200 is interpreted to come from its main component, *i.e.* EO_4, because the integration of the three ^{1}H-NMR signals gave the ratio 8/4/4 for H atoms of inner and outer EO moieties. This assumption is however validated by the average number of EO unit in PEG200 which is generally considered to be 4, as deduced from its average molar mass. The complexity of the NMR spectra showing many overlapping peaks may arise from the polydispersity of PEG200 which is composed of a mixture of EO_x oligomers with x ranging from 3-8 as measured by electro-spray ionization-mass

spectroscopy (ESI-MS), see Figure S8. From the qualitative assignment of NMR resonance signals of the PEG200 compound, it can be concluded that *(i)* PW^{3-} interacts with EO_x oligomers and that *(ii)* PW^{3-} interacts preferentially with the inner protons of the EO_x oligomer, as shown in the sketch of the nano-assembly in **Figure 4.6**.
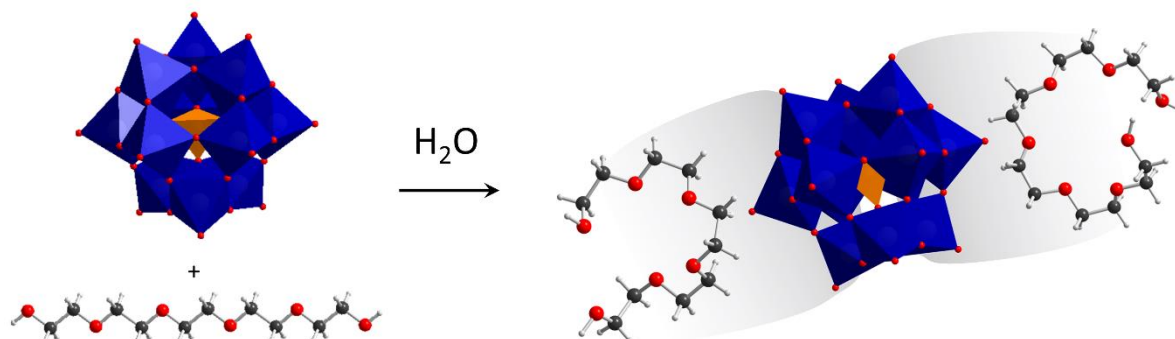
Figure 4.6: Schematic representation of the PW^{3-}-PEG nano-assemblies in aqueous solution. Scattering methods (SAXS, SANS) and NMR revealed an accumulation of roughly two PEG oligomers in a loop shape configuration around one PW^{3-} anion. SAXS/SANS provides information on the type of supramolecular assemblies, *i.e.* a PW^{3-} surrounded by PEG oligomers, and NMR informs on the special interaction of the inner $-CH_2-$ groups of EO_x with PW^{3-} supporting the loop shape model of EO_x in PW^{3-}/EO_x nano-assemblies.

4.4.4   From nano-assembly in water to crystal formation by electrostatic screening

In a previous study it was shown by SAXS that addition of salts, such as NaCl, to POM aqueous solutions leads to the screening of electrostatic repulsions between the POM anions.[28] A salt induced screening effect was previously observed also between non-ionic micelles decorated by POMs.[28] In the following, the screening of electrostatic repulsions in the PW^{3-}-$(EO)_x$ mixtures was investigated for a fixed PW^{3-} concentration of 25 mM by adding 100 mM NaCl, which is sufficient to screen most of the electrostatic repulsions.[28]

In the case of EO_1, EO_2, EO_3 and EO_4, the solutions stayed clear in the presence of NaCl in the concentration range of $[EO_x]$ from 5 to 500 mM and no changes in the SAXS spectra were observed compared to the spectrum of pure PW^{3-} (25 mM) with NaCl (100 mM), see Figure S9. On the contrary for PEG200, PEG300 and PEG400, white crystalline precipitates were formed instantly after mixing PEG-NaCl and PW^{3-}-NaCl solutions. For the much longer EO_x oligomers, *i.e.* PEG20000, the solution became cloudy after mixing with PW^{3-}/NaCl and streak like- or coacervate like structures, were formed, see the optical microscope images in Figure S10. Consequently, precipitation only takes place when PW^{3-}-PEGs nano-assemblies are present in solution suggesting that the precipitates originate from the aggregation of the nano- assemblies caused by a screening of electrostatic repulsions between the nano-assemblies. To gain further insight into the structure of the PEG (200, 300, 400) - PW^{3-} composite materials, crystal growth conditions have been optimized to obtain large crystals suitable for single crystal analysis. The experiments focused on the concentration variation

of PEG (200, 300, 400) from 12.5 mM up to 100 mM. The concentration of PW^{3-} was varied between 25 mM and 50 mM and the concentration of NaCl was kept constant at 100 mM. It has to be mentioned that the PW^{3-} concentration was much below its solubility limit in water (> 900 mM). As a general trend, crystal size decreases with increasing PEGx00 concentration and with increasing x. For PEG200, millimeter size crystals with a hexagonal habitus were obtained. These crystals were sufficiently large to be investigated by single crystal X-ray diffraction. The largest crystals were obtained by using 50 mM PEG200, 50 mM PW^{3-} and 100 mM NaCl, see microscopy images in Figure S11 and S12. The single crystal analysis reveals a monoclinic crystal system and a primitive lattice, space group $P2_1/c$, with the parameters given in Table S1 in the SI. The asymmetric unit of the unit cell consists of one PW^{3-} anion and three sodium cations entangled by two EO_x oligomer chains (one EO_5 and one EO_6), see **Figure 4.7**. Sodium cations counterbalance the charge of the PW^{3-} anion, and almost all oxygens of polydental EO_x oligomers coordinate Na^+, see **Figure 4.7** and **Figure 4.8**. Four water molecules per asymmetric unit are incorporated into the crystal structure. The latter also coordinate towards Na^+ and link two of the three Na^+ cations. Further detailed information on the parameters of the single crystal structure analysis can be found in Table S1 and an IR characterization of the compound can be found in Figure S.13.
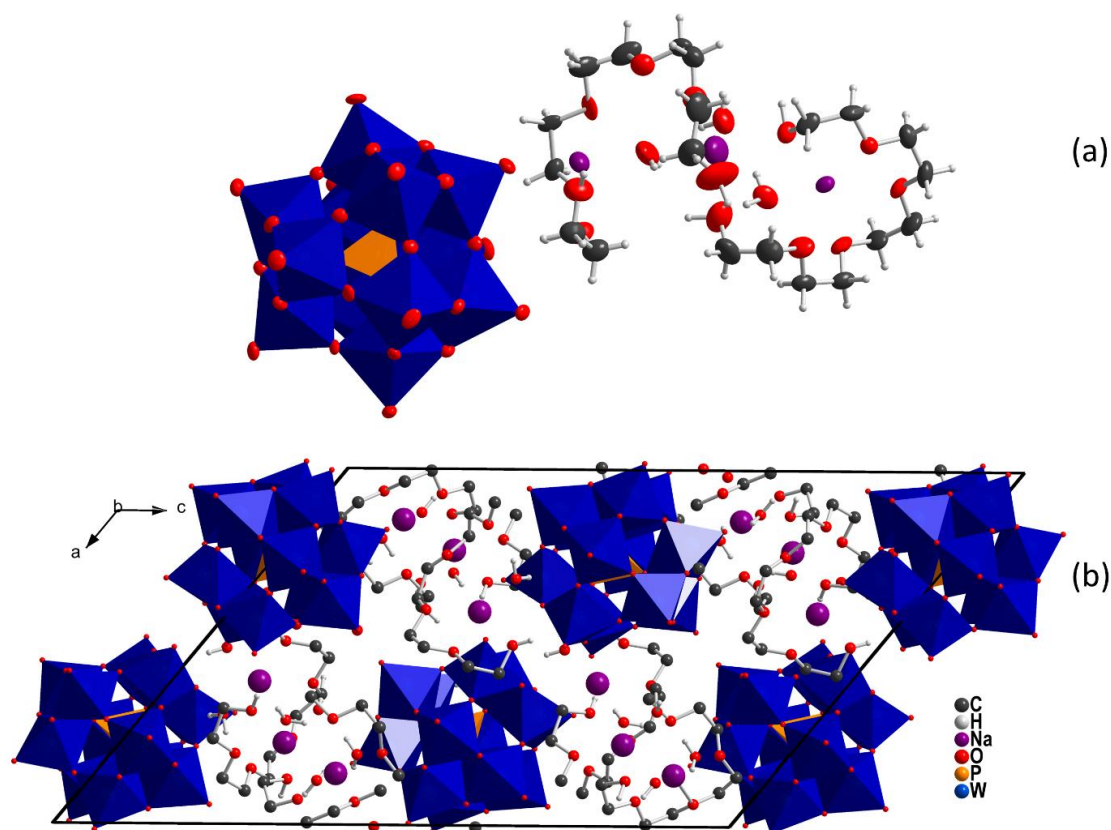
Figure 4.7: (a) Asymmetric unit of the structure model of $C_{22}H_{56}Na_3O_{57}PW_{12}$ represented with displacement ellipsoids (probability factor 70%). Split positions are not shown in this representation. (b) Packing of the elementary cell projected along [010]. For the sake of clarity, atoms are not displayed with displacement ellipsoids and hydrogen atoms connected to carbon are omitted.

A powder diffraction pattern was calculated from the single crystal data and was compared to an experimental pattern of the precipitate obtained by using 50 mM PEG200, 25 mM H_3PW and 100 mM NaCl. Both powder patterns coincide almost perfectly in most of the reflections indicating that the structure model obtained is representative for all crystals, see Figure S14.

Surprisingly, two oligomers, one EO_5 and one EO_6, are embedded in the crystal structure. Hence, salt addition promotes the selective precipitation of EO_5-EO_6 from an aqueous PEG200 solution, which is composed of a mixture of EO_x oligomers with x ranging from 3-8 (see ESI-MS, SI). This implies that EO_x oligomers with $x < 5$ and $x > 6$ remain in the mother liquor. The two oligomers, EO_5 and EO_6 are almost perfectly ordered. Only one $-CH_2$-O-CH_2 fragment of the EO_6 chain is disordered and had to be refined with split positions in the structure model refinement (not shown in **Figure 4.8** but indicated with a black circle). The EO_6 oligomer forms a nearly full helix around two Na^+ ions. Na1 is fully buried in the EO_6 helix and is in an octahedral coordination of oxygen atoms from a terminal oxygen of PW^{3-}, two water molecules and three oxygen atoms of the EO_6 chain.
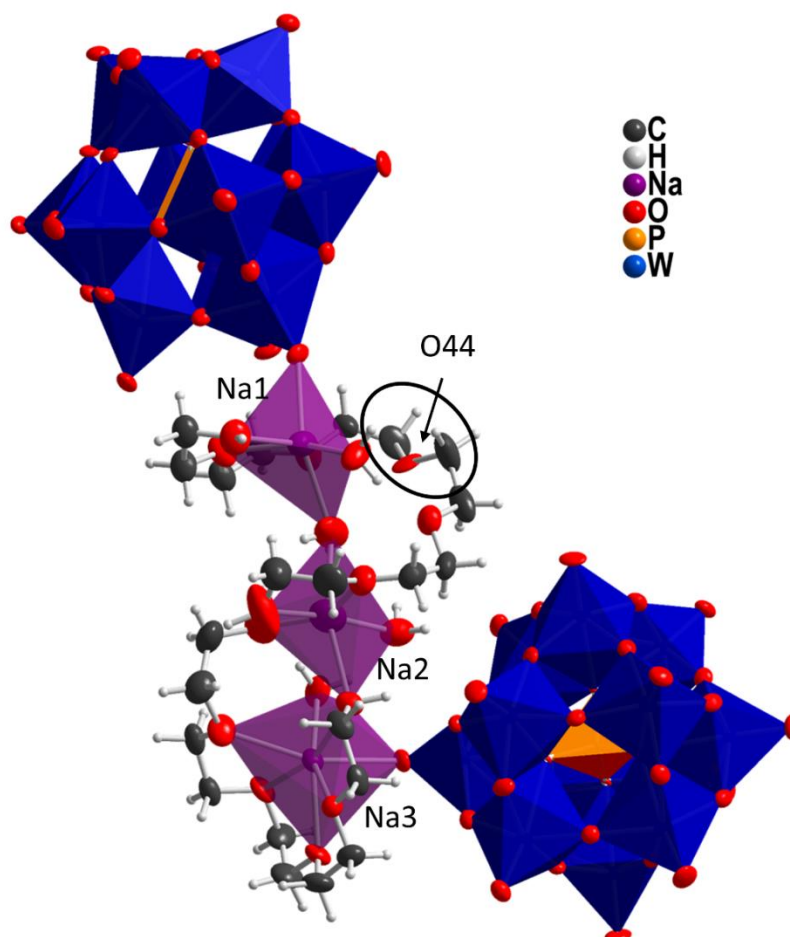
Figure 4.8: Representation of the coordination polyhedra of Na^+ (Na1: distorted octahedron, Na2: distorted octahedron and Na3: distorted pentagonal bipyramide). The black circle marks the disordered fragment of the EO_6 chain in the crystalline compound due to a long interatomic distance d(O44A-Na1) = 2.77 Å and d(O44B-Na1) = 3.25 Å, respectively. This fragment was refined with split positions; only the major contribution is shown here.

Note, that the disorder of the $-CH_2-O-CH_2$ fragment may originate from the non-coordinating behaviour of O44 to Na1 due to a long interatomic distance d(O44A-Na1) = 2.77 Å and d(O44B-Na1) = 3.25 Å, respectively, for the two positions of O44). Na2 is coordinated by two oxygen atoms stemming from the EO_6 chain, two water molecules and the terminal -OH functions of the EO_5 chain resulting in a slightly distorted octahedral coordination. Na3 is fully buried in the EO_5 chain surrounded by in total seven coordinating oxygen atoms, hence a distorted pentagonal bipyramidal coordination. Note that the EO_5 chain is too short to form a full helix; it has a loop or U-shape conformation.

EO_x chains are well known to adopt a helical conformation in the solid state, which is usually referred to as a 7/2 helix, as seven monomer units form two helical turns.[46,47] Here, EO_6 is long enough to adopt a helical conformation, as found previously in self–assembled monolayers.[48] In the compound under discussion, the presence of sodium in the helical structure produces a larger helix with 6-7 EO units required to form one full helical turn. The value of 3 EO units per sodium cation in the complexes is very common in EO_x-metal alkali complexes, for example with K^+.[49] Here, 9 EO units out of 11 which are available ($EO_5 + EO_6$), are involved in the complexation of the Na^+ cations. Hence, two short EO oligomers are present in the crystal structure in order to provide about 3 EO units per sodium ion. In PEG200, the concentration of EO_9 (or longer EO_x oligomers), which would be long enough to coordinate 3 sodium ions, is negligible. Therefore, it is not observed in the present crystals. For the longer PEGs, PEG300/400, the powder patterns indicate the formation of a different crystalline material, which likely contains EO_x oligomers with $x > 6$, see Figure S15 and S16. This is topic of ongoing investigations. Moreover, PEG300/400 produce smaller crystals as compared to PEG200. This is expected for longer oligomers which have more conformational freedom and therefore prevent crystal growth. The helical structure of PEG was previously observed in isobutryic acid/water mixtures, whereas only the coil conformation is formed in pure water.[50]

NMR investigations in water have shown that the internal EO units of EO_x oligomers interact strongly with PW^{3-}. This implies that the EO_x oligomers adopt a loop or a U-shape conformation in the EO_x-PW^{3-} nano-assemblies. The internal EO units coordinate towards the PW^{3-} and the more hydrophilic terminal EO units ($-CH_2-CH_2-OH$) coordinate towards the water phase. Compared to the nano-assemblies in water (NMR results), no interaction between CH_2 groups and PW^{3-} can be observed in the crystal structure, which rather shows a strong complex between Na^+ and O atoms from the PEGs. In aqueous phase, it is expected that EO_x oligomers adsorbed at the PW^{3-} surface are still highly flexible and have many degrees of freedom to change their conformation. The addition of NaCl to the nano-assemblies promotes the crystallization. During this process, PEG chains must rearrange, as entropic and enthalpic contributions lead to the coordination of the PEG-oxygens to Na^+ to counterbalance its electron deficiency in the final crystal. Therefore, it appears that the nano-assemblies, formed at low concentrations in water, play the role of nuclei for the crystallization

process once NaCl (Na$^+$) is added. Therefore, the results presented herein strongly suggest that *(i)* PW^{3-} - EO$_5$/EO$_6$ - 3Na$^+$ crystals are in an equilibrium with nano-assemblies spontaneously preformed in water and that *(ii)* the addition of salt (here NaCl) promotes crystallization of PW^{3-}-EO$_x$ nano-assemblies with a subtle reorganization of EO$_x$ chains from the liquid to the crystal.

4.4.5   The versatility of the "electrostatic screening method"

To show the versatility of the "electrostatic screening method" to construct POM-ethylene glycol based hybrid materials, different POM/PEG composite materials were also synthesized by varying the length of the EO$_x$ oligomeric mixtures (PEG200, PEG300, PEG400) and by using different salts, *i.e* LiCl, NaCl, KCl. Therefore, a cooled (4 °C) solution *(i)* containing POM (c(POM) = 25 and 50 mM) and the additional salt was mixed with a solution *(ii)* containing PEGx00 (x = 2,3,4) and the additional salt without stirring (all combinations were tried). The mixture was left for crystallization at 4 °C in a dark refrigerator.

Precipitates (small crystals < 10 μm) were obtained for the following mixtures (final concentrations are provided):

- 25 mM H$_3$PW$_{12}$O$_{40}$ – 12.5 mM PEG300 – 100 mM LiCl
- 25 mM H$_3$PW$_{12}$O$_{40}$ – 12.5 mM PEG400 – 100 mM LiCl
- 50 mM H$_3$PW$_{12}$O$_{40}$ – 12.5 mM PEG300 – 100 mM LiCl
- 50 mM H$_3$PW$_{12}$O$_{40}$ – 100 mM PEG300 – 100 mM LiCl
- 25 mM H$_3$PMo$_{12}$O$_{40}$ – 25 mM PEG300 – 100 mM LiCl
- 25 mM H$_3$PMo$_{12}$O$_{40}$ – 50 mM PEG300 – 100 mM LiCl
- 50 mM H$_3$PMo$_{12}$O$_{40}$ – 12.5 mM PEG300 – 100 mM LiCl
- 50 mM H$_3$PMo$_{12}$O$_{40}$ – 25 mM PEG300 – 100 mM LiCl
- 50 mM H$_4$SiW$_{12}$O$_{40}$ – 6.25 mM PEG400 – 100 mM KCl
- 50 mM H$_3$PW$_{12}$O$_{40}$ – 50 mM PEG400 – 6.25 mM KCl
- 25 mM H$_3$PW$_{11}$VO$_{40}$ – 50 mM PEG400 – 100 mM NaCl

Only in case of 50 mM H$_3$PW$_{12}$O$_{40}$ – 6.25 mM PEG400 – 6.25 mM KCl suitable crystals for a single crystal analysis were obtained. It can be expected that it is possible to grow larger crystals suited for a single crystal analysis from the mixtures provided above by changing the component ratio and by optimizing the crystallization process (especially by variation of the salt, *i.e.* LiCl, NaCl, KCl concentration).

4.4.6 $PW^{3-} - EO_{11} - K^+ - H^+ - H^+$ composite crystals

Composite crystals consisting of PW^{3-} - EO_{11} - K^+ - H^+ - H^+ were prepared upon mixing a solution containing 100 mM PEG400 - 6.25 mM KCl with a solution containing 100 mM H_3PW and 6.25 mM KCl. After three months in a dark refrigerator at 4 °C, only three crystals were obtained. A suitable crystal was selected and measured on a single source Cu K_α (λ = 1.54184 Å) SuperNova diffractometer equipped with an Atlas detector. The crystal was kept at 123(1) K during data collection. The CrysAlisPro 1.171.39.37b[51] software was used for data reduction and a numerical absorption correction based on gaussian integration over a multifaceted crystal model was performed. Using the Olex2 graphical user interface,[52] the structure was solved with the ShelXT[53] structure solution program using Intrinsic Phasing and refined with the ShelXL[54] refinement package using Least Squares minimisation. The single crystal analysis reveals a triclinic crystal system, space group P-1 (space group no. 2) with the following parameters: a = 11.7384(2) Å, b = 16.0179(3) Å, c = 16.5804(3) Å, α = 92.64(1)°, β = 95.34(2)°, γ = 90.47(2)° and V = 3100.4(1) Å^3. Further parameters are provided in **Table 4.1.**

The structure model consists of one PW^{3-} anion, one potassium cation entangled by one EO_{11} oligomer chain and six crystal water molecules, see **Figure 4.9**. Note that the three-fold negative charge of PW^{3-} cannot be counterbalanced by one K^+. Therefore, it is assumed that two further H^+ cations are incorporated in the structure model whose exact atomic positions cannot be resolved in this single crystal X-ray experiment as their electronic contrast is too weak for X-rays.

Table 4.1: Crystallographic data for PW^{3-} - EO_{11} - K^+ - H^+ - $H^+ \cdot 6\ H_2O$ hybrid crystals. Crystal water molecules are renounced in the crystal name hereafter.

	PW^{3-} - EO_{11} - K^+ - H^+ - $H^+ \cdot 6\ H_2O$ hybrid crystals
Sum formula	' $C_{22}\ H_{58}\ K\ O_{58}\ P\ W_{12}$'
Molecular weight / g mol^{-1}	3526.95
Crystal habit	colourless block
Crystal dimensions / mm^3	$0.087 \times 0.044 \times 0.042$
Crystal system	triclinic
Space group	P-1
a / Å	11.7384(2)
b / Å	16.0179(3)
c / Å	16.5804(3)
α / °	92.64(1)
β / °	95.34(2)
γ / °	90.47(2)
V / Å^3	3100.4(1)
Z	2
d / g cm^{-3}	3.778
F(000)	3152
μ / mm^{-1}	41.835
Absorption correction	gaussian
Diffractometer	SuperNova
Radiation	Cu K_α (λ = 1.54184 Å)
T / K	123(1)
Index ranges	$-14 < h < 14$; $-20 < k < 20$; $-20 < l < 20$
Reflections collected	58271
Independent reflections	12851 [R_{int} = 0.0605, R_σ = 0.0386]
Data/restraints/parameter	12854/0/867
Final R indices [$I \geq 2\sigma(I)$]	R_1 = 0.0383, wR_2 = 0.0976
Final R indices	R_1 = 0.0425, wR_2 = 0.1007
GooF	1.047
difference peak / hole (e Å^{-3})	2.23 / -3.90
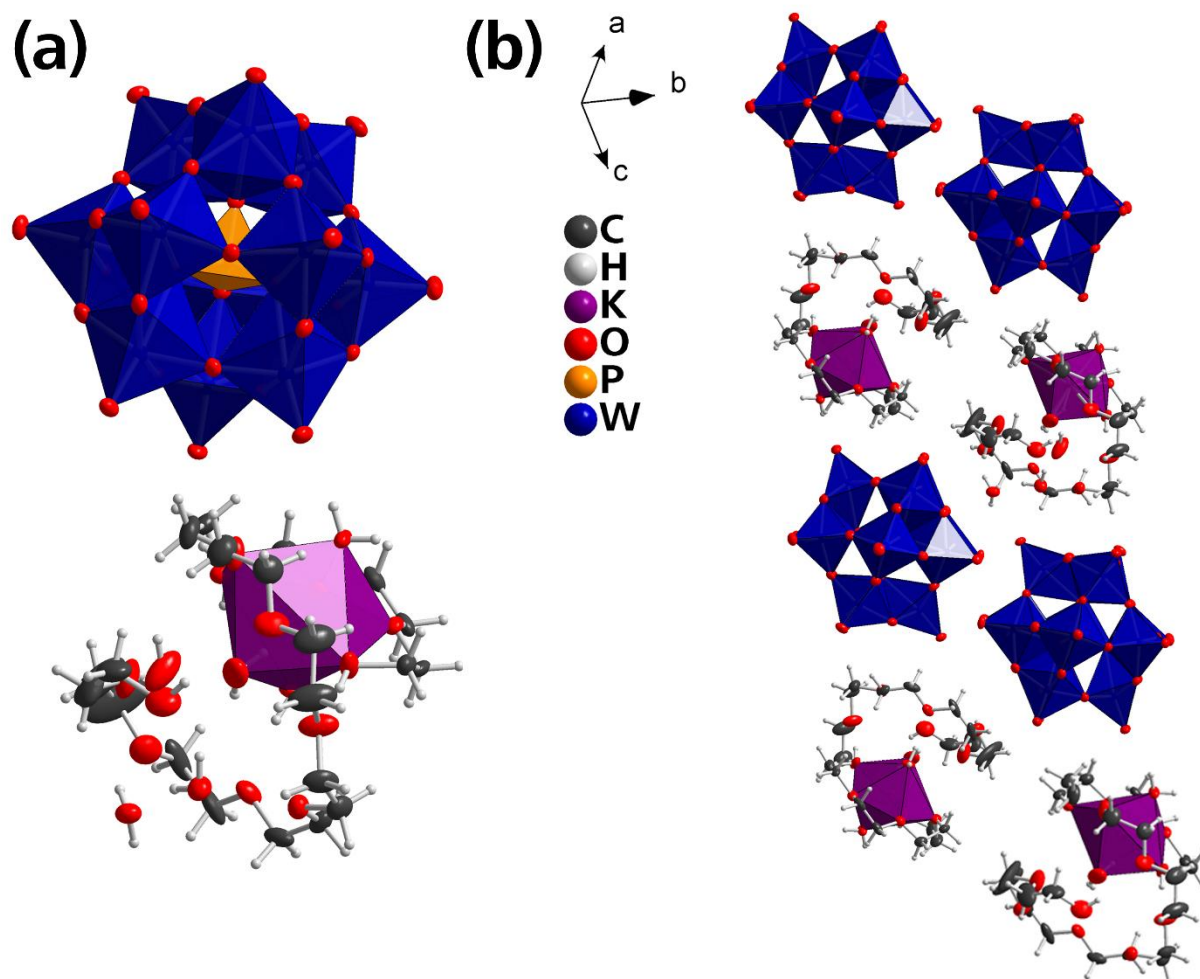
Figure 4.9: (a) Structure model of PW^{3-} - EO_{11} - K^+ - H^+ - H^+ hybrid crystals and (b) packing of four structure model units represented with displacement ellipsoids (probability factor 50%) and coordination polyhedra around K^+, W^{6+} and P^{5+}.

PW^{3-} forms distorted close packed layers (2D) with an **A** - **B** - **A** - **B** sequence, see **Figure 4.10**. Note that layers A and B do not form a hexagonal dense packing as PW^{3-} anions from layers **A** and **B** superimpose (eclipsed arrangement). K^+ cations (and H^+ cations) including the EO_{11} chain (not shown in **Figure 4.10**) *(i)* act as spacer between layers of PW^{3-} and *(ii)* lead to a distortion of the close packed layer of PW^{3-}.
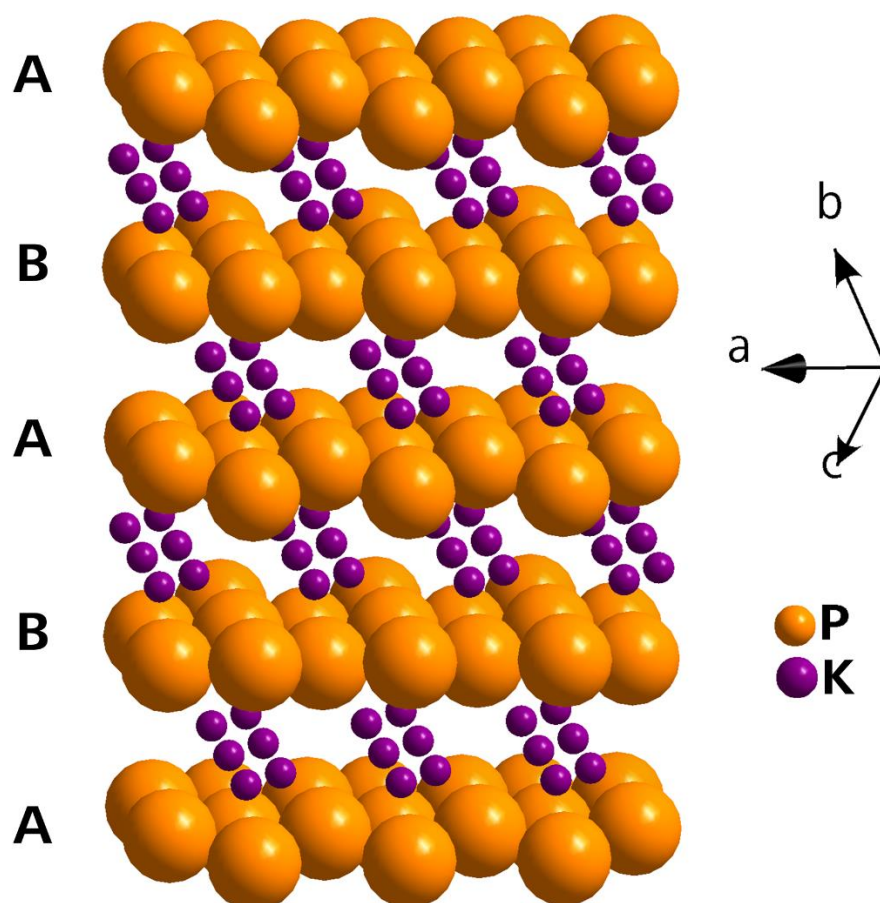
Figure 4.10: Distorted close packed layers of PW^{3-} (only represented by the orange central phosphorous atoms of PW^{3-} and potassium cations (violet) in between. For the sake of clarity EO$_{11}$ chains and crystal water molecules are omitted in this image.

The EO$_{11}$ chain forms a double helix. Five oxygens of the polydental EO$_{11}$ oligomer coordinate towards K$^+$ with distances ranging between 2.35(1) Å - 2.70(1) Å, see **Figure 4.9**. Two of six water molecules also coordinate towards K$^+$ resulting in a pentagonal bipyramidal coordination around K$^+$. This coordination can be compared to the distorted pentagonal bipyramidal coordination of Na3 in PW^{3-} - EO$_5$/EO$_6$ - 3Na crystals, see **section 4.4.4**. Interestingly, EO$_{11}$ is incorporated in PW^{3-} - EO$_{11}$ - K$^+$ - H$^+$ - H$^+$ hybrid crystals - exactly the sum of EO$_5$ and EO$_6$ as incorporated in PW^{3-} - EO$_5$/EO$_6$ - 3Na$^+$ crystals. As a rough estimation the volume of the 7/2 helix of EO$_5$/EO$_6$ in PW^{3-} - EO$_5$/EO$_6$ - 3Na$^+$ crystals and of the double helix of EO$_{11}$ in PW^{3-} – EO$_{11}$ - K$^+$ - H$^+$ - H$^+$ crystals is similar to the volume of the PW^{3-} unit. The lower symmetry (*P*-1 space group in case of PW^{3-} - EO$_{11}$ - K$^+$ - H$^+$ - H$^+$ crystals compared to *P*2$_1$/*c* space group in case of PW^{3-} - EO$_5$/EO$_6$ - 3Na$^+$ crystals) may be explained by a different orientation of the EO$_{11}$ chain which cannot be arranged in a "stretch conformation" as it is the case for a fragmented EO$_{11}$ segment, *i.e.* EO$_5$ and EO$_6$. Note that five EO$_x$ repeating motifs are needed to make a full turn of the helix around K$^+$, whereas in case of PW^{3-} - EO$_5$/EO$_6$ - 3Na$^+$ crystals in average only three EO$_x$ repeating motifs coordinated Na$^+$ observed.

As only EO_{11} is selectively incorporated in the crystal from a polydisperse PEG400 mixture we conclude that EO_x oligomers with $x < 11$ and $x > 11$ remain in the mother liquor.

4.5 Conclusion

It is shown here that the adsorption of POMs on polar surfaces, *e.g.* surfaces covered by EO moieties, does not occur due to a surface effect but it can be generalized to aqueous bulk solutions. Therefore, EO_x oligomers do not have to be located at an interface to promote adsorption of POMs. Scattering techniques (SAXS, SANS) provided a clear evidence of this adsorption in bulk solution whereas NMR informs on the essential role of the internal EO units in the adsorption process. Nano-assemblies consisting of POMs coordinated by loop shaped EO_x oligomers form spontaneously in water by simple mixing of the components. The attractive interactions between PW^{3-} and EO_x oligomers were found to be stronger by increasing the EO_x length, *i.e.* EO_x with $x > 4$, suggesting that multipolar interactions between internal EO units and POM may be at the origin of the self-assembly process.

The screening of the electrostatic repulsions between EO_x-PW^{3-} nano-assemblies promotes the formation of a crystalline material. The loop conformation of EO_x at the POM surface seems to act as a nucleus of the EO_x helix/loop conformation found in the crystal. Therefore, EO_x-PW^{3-} nano-assemblies can be considered as nano-building blocks for the formation of POM-hybrid crystalline materials. Moreover, the structure model obtained for PW^{3-} - EO_5/EO_6 - $3Na^+$ crystals indicates that two oligomers with well-defined length, EO_5 and EO_6, are involved per PW^{3-}. This opens an interesting way for separating oligomers with different polymerization degrees with a high selectively.

The methodology developed here, which is based on the electrostatic screening between pre-formed organic-inorganic EO_x-PW^{3-} nano-assemblies, can be extended to other kind of water soluble oligomers that interact with POMs in solution as shown for composite materials consisting of PW^{3-} – EO_{11} - K^+ - H^+ - H^+, *i.e.* different (mixed) cations, different EO_x chain lengths and different number of ethylene glycol chains (EO_5/EO_6 *vs.* EO_{11}). For example, POMs, PW^{3-} and silicotungstate (SiW^{4-}), have been found previously to also interact with sugar moieties by adsorbing at surfaces (water-micelle or water-air surfaces) covered by sugar based surfactants.[28] Such a general strategy to build hybrid materials which is based on a self-assembly approach in water has the advantages to avoid *(i)* the time consuming multi-step synthesis of organic-inorganic POM building blocks as well as *(ii)* the use of toxic polar solvents, such as acetonitrile or DMSO typically employed to dissolve both POMs and organic building blocks. However, the procedure here only requires that the POM is chemically stable in water. The rational design of new POM hybrid (crystalline) materials with a simple mixing procedure of the components, as exemplified here with EO_x oligomers and PW^{3-}, implies a deep understanding of the molecular interactions leading to the formation of the POM-oligomer nano-assemblies.

This very mild synthesis route developed here opens the possibility to build a whole new class of POM composite materials, which may be interesting for their applications in material science, such as ion or proton conducting materials, electrode based materials, photo-responsive hybrid crystals as well as in catalysis and separation science to selectively precipitate ethylene glycol oligomers with a given number of repeating units from a polydisperse PEG mixture.

4.6 **Bibliography**

[1]   J. J. Borrás-Almenar, E. Coronado, A. Müller, M. Pope, Polyoxometalate Molecular Science, Springer Netherlands, **2012**.

[2]   S. S. Wang, G. Y. Yang, *Chem. Rev.* **2015**, *115*, 4893–4962.

[3]   M. V. Vasylyev, R. Neumann, *J. Am. Chem. Soc.* **2004**, *126*, 884–890.

[4]   A. Dolbecq, E. Dumas, Ddy, C. R. Mayer, P. Mialane, *Chem. Rev.* **2010**, *110*, 6009–6048.

[5]   M.-S. Wang, G. Xu, Z.-J. Zhang, G.-C. Guo, *Chem. Commun.* **2010**, *46*, 361–376.

[6]   R. Prudent, V. Moucadel, B. Laudet, C. Barette, L. Lafanechère, B. Hasenknopf, J. Li, S. Bareyt, E. Lacôte, S. Thorimbert, *Chem. Biol.* **2008**, *15*, 683–692.

[7]   H. K. Yang, Y. X. Cheng, M. M. Su, Y. Xiao, M. B. Hu, W. Wang, Q. Wang, *Bioorganic Med. Chem. Lett.* **2013**, *23*, 1462–1466.

[8]   L. Fu, H. Gao, M. Yan, S. Li, X. Li, Z. Dai, S. Liu, *Small* **2015**, *11*, 2938–2945.

[9]   J. T. Rhule, C. L. Hill, D. a. Judd, R. F. Schinazi, *Chem. Rev.* **1998**, *98*, 327–357.

[10]   C. Zhang, W. Bu, D. Ni, C. Zuo, C. Cheng, Q. Li, L. Zhang, Z. Wang, J. Shi, *J. Am. Chem. Soc.* **2016**, *138*, 8156–8164.

[11]   A. Proust, B. Matt, R. Villanneau, G. Guillemot, P. Gouzerh, G. Izzet, *Chem. Soc. Rev.* **2012**, *41*, 7605.

[12]   D. L. Long, R. Tsunashima, L. Cronin, *Angew. Chem. - Int. Ed.* **2010**, *49*, 1736–1758.

[13]   M. Sadakane, E. Steckhan, *Chem. Rev.* **1998**, *98*, 219–238.

[14]   S. Herrmann, C. Ritchie, C. Streb, *Dalt. Trans.* **2015**, *44*, 7092–7104.

[15]   H. Wang, Y. Yan, B. Li, L. Bi, L. Wu, *Chem. - A Eur. J.* **2011**, *17*, 4273–4282.

[16]   L. Leclercq, A. Mouret, A. Proust, V. Schmitt, P. Bauduin, J. M. Aubry, V. Nardello-Rataj, *Chem. - A Eur. J.* **2012**, *18*, 14352–14358.

[17]   L. Leclercq, A. Mouret, P. Bauduin, V. Nardello-Rataj, *Langmuir* **2014**, *30*, 5386–5393.

[18]   G. Izzet, B. Abécassis, D. Brouri, M. Piot, B. Matt, S. A. Serapian, C. Bo, A. Proust, *J. Am. Chem. Soc.* **2016**, *138*, 5093–5099.

[19]   T. Akutagawa, D. Endo, F. Kudo, S. I. Noro, S. Takeda, L. Cronin, T. Nakamura, *Cryst. Growth Des.* **2008**, *8*, 812–816.

[20]   Y. Wu, R. Shi, Y. L. Wu, J. M. Holcroft, Z. Liu, M. Frasconi, M. R. Wasielewski, H. Li, J. F. Stoddart, *J. Am. Chem. Soc.* **2015**, *137*, 4111–4118.

[21]   S. Liu, D. G. Kurth, B. Bredenkötter, D. Volkmer, *J. Am. Chem. Soc.* **2002**, *124,* 12279–12287.

[22]   S. Liu, D. Volkmer, D. G. Kurth, *J. Clust. Sci.* **2003**, *14,* 405–419.

[23]   N. Joo, S. Renaudineau, G. Delapierre, G. Bidan, L. M. Chamoreau, R. Thouvenot, P. Gouzerh, A. Proust, *Chem. - A Eur. J.* **2010**, *16,* 5043–5051.

[24]   X. Luo, C. Yang, *Phys. Chem. Chem. Phys.* **2011**, *13,* 7892–902.

[25]   R. Zhang, C. Yang, *J. Mater. Chem.* **2008,** *18,* 2691.

[26]   V. Jallet, G. Guillemot, J. Lai, P. Bauduin, V. Nardello-Rataj, A. Proust, *Chem. Commun.* **2014,** *50,* 6610–2.

[27]   S. Landsmann, M. Wessig, M. Schmid, H. Cölfen, S. Polarz, *Angew. Chemie - Int. Ed.* **2012,** *51,* 5995–5999.

[28]   B. Naskar, O. Diat, V. Nardello-Rataj, P. Bauduin, *J. Phys. Chem. C* **2015**, *119,* 20985–20992.

[29]   H. Huang, J. Xu, K. Wei, Y. J. Xu, C. K. K. Choi, M. Zhu, L. Bian, *Macromol. Biosci.* **2016**, *16,* 1019–1026.

[30]   M. W. Tibbitt, K. S. Anseth, *Biotechnol. Bioeng.* **2009,** *103,* 655–663.

[31]   J. Chen, S. K. Spear, J. G. Huddleston, R. D. Rogers, *Green Chem.* **2005,** *7,* 64.

[32]   S. Zalipsky, J. Harris, *ACS Symp. Ser.* **1997,** 1–13.

[33]   S. H. Chung, A. Manthiram, *Adv. Mater.* **2014,** *26,* 7352–7357.

[34]   J. M. Harris, *Poly (Ethylene Glycol) Chemistry: Biotechnical and Biomedical Applications,* Springer Science & Business Media, **2013.**

[35]   W. Ge, Z. Long, X. Cai, Q. Wang, Y. Zhou, Y. Xu, J. Wang, *RSC Adv.* **2014,** *4,* 45816–45822.

[36]   J. Tang, W. Yu, M.-B. Hu, Y. Xiao, X.-G. Wang, L.-J. Ren, P. Zheng, W. Zhu, Y. Chen, W. Wang, *Chempluschem* **2014,** *79,* 1455–1462.

[37]   J. Tang, C. Ma, X.-Y. Li, L.-J. Ren, H. Wu, P. Zheng, W. Wang, *Macromolecules* **2015,** *48,* 2723–2730.

[38]   M. Tsuboi, M. Hibino, N. Mizuno, S. Uchida, *J. Solid State Chem.* **2016,** *234,* 9–14.

[39]   R. Neumann, M. Lissel, *Org. Synth.* **1989,** *2040,* 4607–4610.

[40]   D. Svergun, C. Barberato, M. H. Koch, *J. Appl. Crystallogr.* **1995,** *28,* 768–773.

[41]   O. F. Erdem, D. Michel, *J. Phys. Chem. B* **2005,** *109,* 12054–61.

[42]   J. Wu, Z. Wang, W. Lin, S. Chen, *Acta Biomater.* **2013,** *9,* 6414–6420.

[43]   J. Mohan, *Organic Spectroscopy: Principles and Applications,* Alpha Science International Limited, **2004.**

[44]   R. A. De Graaf, *In Vivo NMR Spectroscopy - 2nd Edition,* Principles and Techniques, John Wiley & Sons Ltd., **2007.**

[45]   J. Dust, Z. Fang, J. M. Harris, *Macromolecules* **1990,** *23,* 3742–3746.

[46]   Y. Takahash, H. Tadokoro, *Macromolecules* **1973,** *6,* 672–675.

[47]   R. Yang, X. R. Yang, D. F. Evans, W. a. Hendrickson, J. Baker, *J. Phys. Chem.* **1990,** *94,* 6123–6125.

[48]   P. Harder, M. Grunze, R. Dahint, G. M. Whitesides, P. E. Laibinis, *J. Phys. Chem. B* **1998,** *102,* 426–436.

[49]   R. D. Walsh, J. M. Smith, T. W. Hanks, W. T. Pennington, *Cryst. Growth Des.* **2012,** *12,* 2759–2768.

[50]   M. L. Alessi, A. I. Norman, S. E. Knowlton, D. L. Ho, S. C. Greer, *Macromolecules* **2005,** *38,* 9333–9340.

[51]   Rigaku Oxford Diffraction, **2017,** CrysAlisPro Version 1.171.39.37b.

[52]   O.V. Dolomanov, L.J. Bourhis, R.J Gildea, J.A.K. Howard, H. J. Puschmann, *Appl. Cryst.* **2009,** *42,* 339-341.

[53]   G.M. Sheldrick, Acta Cryst. A. **2015,** *71* 3-8.

[54]   G.M. Sheldrick, Acta Cryst. C. **2015,** *71,* 3-8.

5   Single crystal to single crystal transformation in a POM based composite crystal

5.1   Preface and Abstract

Several people contributed to the work in this chapter:

- Philipp Schmid and Franziska Kamm contributed with experimental work during a Bachelor thesis.

- Maximilian Röhrl and Simon Stemplinger contributed with experimental work during a research internship.

- Dr. Olivier Diat, Dr. Pierre Bauduin and Prof. Dr. Arno Pfitzner contributed with fruitful discussions and supervised the experimental work.

Abstract: Polyoxometalate-ethylene glycol composite crystals are prepared by the electrostatic screening method upon mixing $H_3PMo_{12}O_{40}$, polydisperse polyethylene glycol 200 (PEG200) and NaCl at ambient conditions. The compound crystallizes in the monoclinic space group $P2_1/c$ with the following parameters: $a = 20.971(5)$ Å, $b = 12.365(1)$ Å, $c = 32.472(6)$ Å, $V = 6081(3)$ Å^3, $\beta = 133.76°$. The structure model consists of one $PMo_{12}O_{40}^{3-}$ anion and two ethylene glycol oligomers with exactly five and six repeating units (EO_5 and EO_6) although PEG200 is a mixture of EO_{3-8}. Both, EO_5 and EO_6 have different functionality and coordinate three sodium cations. Upon irradiation of the crystals with visible light, the $PMo_{12}O_{40}^{3-}$ photocatalyst induces selectively the oxidation of only one terminal hydroxyl function $-CH_2-OH$ of EO_6 to the corresponding aldehyde $-CH=O$ (out of four available $-CH_2-OH$ hydroxyl groups). During this process, *(i)* the crystal colour changes from clear yellowish to black due to the formation of the well-known heteropolyblue-polyoxometalate and *(ii)* the lattice volume decreases continuously.

5.2   Introduction

Single-crystal-to-single-crystal (SCSC) transformations, *i.e.* chemical transformations in the solid-state, are intriguing phenomena as in some cases they enable the synthesis of otherwise inaccessible products.[1] Additionally, the absence of a solvent can have a positive effect on efficiency and selectivity compared to solution reactions. SCSC transformations can be triggered by different stimuli, *e.g.* temperature changes,[2] solvent effects,[3] ion exchange,[4] irradiation,[5,6] the exposition to a gas,[7] mechanochemical forces,[8] or a combination of these.[9] If a SCSC transformation results in a change of the crystal colour, it is of additional interest as this might result in an application in sensor tech-

nology.[10] Reversible SCSC transformations enable further applications, *e.g.* photo switches and optical data storage.[11] Most SCSC transformations are observed in metal-organic frameworks (MOFs) or coordination polymers.[12] Generally, chemical transformations at a molecular level are less common as a specific molecular arrangement and a close proximity of the reactants is necessary for a SCSC. For hybrid compounds containing polyoxometalates (POMs), only few cases of SCSC transformation have been described[13,14] although the unique structural and electronic versatility of POMs - nanometer sized molecular metal-oxide clusters[15] - leads to a vast field of applications of POMs in aqueous solution or biological media, *e.g.* medicine,[16] biology,[17] as photocatalytic active oxidants,[18–20] *etc.* Parallel to this application of POMs solubilized in aqueous solutions, an exhaustive number of findings deal with POM-based materials with magnetic and conducting properties.[21,22] The field of POM-organic hybrids emerged with the goal to build composite materials displaying characteristics between the two original phases or even new properties.[22,23]

Only recently, our group reported a new approach to design POM-organic composite materials: the entropically driven electrostatic screening approach.[24] Therein, the super-chaotropic properties of POMs lead to their adsorption on neutral polar molecules or interfaces in aqueous solution to form soluble POM-organic nano-assemblies in bulk water.[24,25] Screening of repulsive interactions between the $PW_{12}O_{40}^{3-}$ (PW^{3-})-organic nano-assemblies upon the addition of excess salt, *e.g.* NaCl, leads to the formation of crystalline composite materials of these nano-assemblies: in case of $PW_{12}O_{40}^{3-}$ - EO_5/EO_6 - $3Na^+$ composite crystals,[24] two ethylene glycol (EO_x) oligomers $HO-(CH_2-CH_2-O)_x-OH$ (x = 5 and 6) wrap around three sodium cations. Note that in single crystals of $PW_{12}O_{40}^{3-}$ - EO_5/EO_6 - $3Na^+$, this organic EO_5/EO_6 chains are neither covalently nor electrostatically bound to $PW_{12}O_{40}^{3-}$.[24]

The scope of the present work is to investigate if such composite materials synthesized by the method above, called here the "electrostatic screening method" can act as novel functional or stimuli (light, temperature) responsive materials since the organic ethylene glycol moiety and the POM are not linked covalently or electrostatically and as POMs are well-known (photo-)redox active catalysts.[15,18,20] Therefore, we have chosen $H_3PMo_{12}O_{40}$ (H_3PMo) instead of $H_3PW_{12}O_{40}$ (H_3PW) as a POM building block since $PMo_{12}O_{40}^{3-}$ (PMo^{3-}) absorbs visible light whereas PW^{3-} is only UV-active. Thus, the potential application as a visible light responsive material shall be addressed.[15]

Hence, we report here *(i)* the interaction of the $H_3PMo_{12}O_{40}$ Keggin-type POM with EO_x in aqueous solution by means of ^{1}H-nuclear magnetic resonance spectroscopy (^{1}H-NMR).[24] Furthermore, we *(ii)* characterize $PMo_{12}O_{40}^{3-}$- EO_5/EO_6 - $3Na^+$ hybrid crystals obtained by the electrostatic screening method by single crystal X-ray analysis and we *(iii)* show that $PMo_{12}O_{40}^{3-}$- EO_5/EO_6 - $3Na^+$ hybrid crystals are visible light responsive materials.

5.3 Experimental

Materials. Phosphomolybdic acid hydrate ($H_3PMo_{12}O_{40} \cdot 14\ H_2O$, H_3PMo, MW = 2077 g/mol, 99.99% purity), sodium chloride (NaCl, 99.5%), and PEG200 was purchased from Sigma Aldrich. PEG200 means that the average molecular weight of PEG is 200 g/mol, therefore having an average in the size distribution at 4 EO units. This is due to the fact, that PEG polymers consist of mixtures with a distribution of the number of the EO units, for example PEG200 is composed of a mixture of EO_x = 3, 4, 5, 6 EO units. Milli-Q water with a conductivity lower than 10.5 mS/cm and a total organic carbon content of maximal 400 ppb was used.

Sample preparation. Crystals were prepared by the following protocol: an aqueous solution containing 100 mM PEG200 and 100 mM NaCl (solution 1) was cooled down to 4 °C in the refrigerator. A second aqueous solution containing H_3PMo and 100 mM NaCl (solution 2) was also cooled down to 4 °C. Solution 2 was poured gently to solution 1 without stirring and left in the refrigerator for 3 days. The formation of crystals was checked by a microscopic investigation.

NMR. NMR spectra were recorded at room temperature using a Bruker Avance400 (400 MHz for ^1H) NMR spectrometer. All chemical shifts are given in δ-scale as parts per million [ppm] (multiplicity, coupling constant J, number of protons) relative to the solvent residual peak (D_2O) as the internal standard.

EPR spectroscopy. X-band EPR measurements were carried out on a MiniScope MS400 device (Magnettech GmbH) equipped with a rectangular TE102 resonator at a frequency of 9.5 GHz. Spectra were only analysed qualitatively.

IR spectroscopy. IR spectra were recorded on a Varian 670-IR spectrometer with an integrated ATR-unit (Pike Technologies, GladiATR) from 350 cm^{-1} - 4000 cm^{-1}. The Varian Resolutions Pro software was used for data processing.

Single-crystal X-ray diffraction. Diffraction data of suitable single-crystals were collected on a Rigaku Supernova using either Mo-K_α radiation (λ = 0.71073 Å) or Cu-K_α radiation (λ = 1.54184 Å). The diffraction data were corrected for Lorentz- and polarization effects. The CrysAlisPro 1.171.39.37b (Rigaku Oxford Diffraction, 2017) software[26] was used for data reduction and a numerical absorption correction based on gaussian integration over a multifaceted crystal model was performed. The crystal structure was solved with the ShelXT[27] structure solution program using Intrinsic Phasing, and subsequently refined with the ShelXL[28] refinement package using Least Squares minimization both embedded in the Olex2 surface.[29] All non-hydrogen atoms were refined with anisotropic displacement parameters; hydrogen atoms were introduced and refined by a riding model without restraints.

Powder X-Ray diffraction. Powder X-ray diffraction measurements were carried out with a STOE Stadi P diffractometer with monochromatic Cu-$K_{\alpha1}$ radiation (λ = 1.540598 Å, Germanium mono-

chromator, Mython 1K detector). The powdered sample was measured at room temperature between two mylar foils in a *2θ* range from 2 to 90°. The WinXPow software (pattern fitting) was used to process the data.[30]

5.4 Results and Discussion

A concentration of 50 mM PEG200 in aqueous media of H_3PMo provides clear yellowish isotropic solutions at any proportion without the formation of any precipitate visible at the macroscopic level as in case of aqueous mixtures of $H_3PW_{12}O_{40}$ and PEG200.[24]

NMR. As the interaction between PW^{3-} and oligomeric EO_x could be monitored with ^1H-NMR,[24] ^1H-NMR experiments were also performed to probe the electronic change in environment of the EO_x oligomers upon adsorption to PMo^{3-}. ^1H-NMR spectra of 100 mM PEG200 solutions in D_2O were collected for different H_3PMo concentrations (0, 20, 50, 100 mM), see **Figure 5.1**.
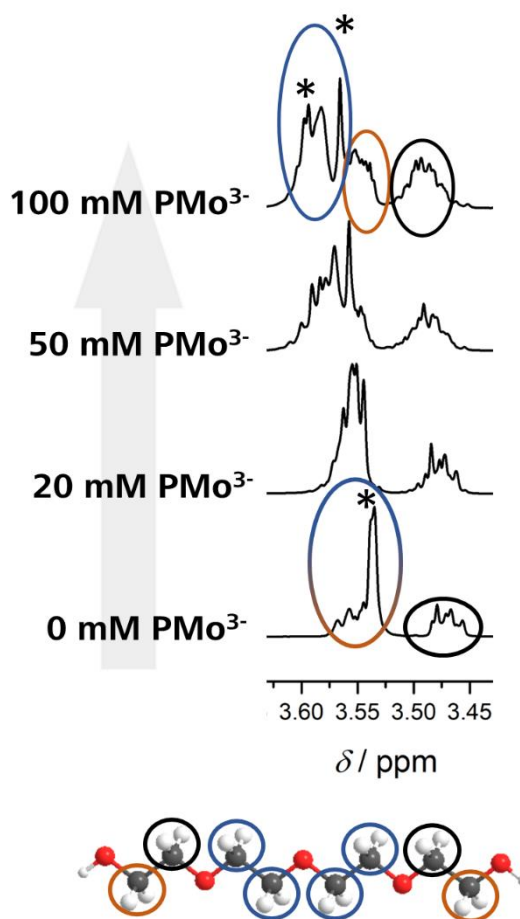
Figure 5.1: NMR resonance signals of 100 mM PEG200 in the presence of 0, 25, 50, and 100 mM PMo^{3-} (from bottom to top). The stars indicate the shift and splitting of the resonance signals stemming from the inner protons upon the addition of H_3PMo. Note that the spectra are normalized to the highest intensity.

The spectrum of pure PEG200 (PEG200 - 0 mM PMo^{3-}) depicts three resonance signals: a multiplet from 3.45 to 3.48 ppm, a multiplet from 3.53 to 3.57 ppm and a sharp singlet at 3.53 ppm (marked with a star *) which overlap. Therefore, a separate integration of the resonance signals is more or less impossible. By considering EO$_4$ (C$_8$O$_5$H$_{18}$) to be the main component of PEG200, hydrogen atoms can be assigned by using Shoolery's rules.[31] The multiplet at 3.53 to 3.57 ppm overlapping with the large singlet at 3.53 ppm is assigned to the -CH$_2$-**CH$_2$**-OH (brown). The large singlet is assigned to the chemically and magnetically equivalent inner -O-**CH$_2$-CH$_2$**-O- groups (blue) and the multiplet from 3.45 to 3.48 ppm is assigned to the methylene group -**CH$_2$**-CH$_2$-OH (black). Upon the addition of H$_3$PMo, the splitting of the multiplet from 3.45 ppm to 3.48 ppm remains almost unchanged, except from the general chemical deep-field shift of the multiplet for all spectra and a slight change in the coupling constants. The presence of higher concentrations of H$_3$PMo (50 and 100 mM H$_3$PMo) leads to a decreasing intensity of the singlet. In addition, a doublet which increases in intensity with increasing H$_3$PMo concentration emerges (marked with two stars). Hence, only the singlet corresponding to the inner hydrogen atoms significantly shifts to the deeper field upon addition of H$_3$PMo. In an aqueous environment internal EO units coordinate towards PMo^{3-} but the more hydrophilic terminal EO units (-CH$_2$-CH$_2$-OH) are not affected by the presence of PMo^{3-}. This conclusion is further supported by the fact that the same splitting and shift of the resonance signals was already observed for PEG200 upon addition of H$_3$PW. Note that the absolute shift of the resonance signals of PEG200 upon the addition of H$_3$PW is larger than in case of H$_3$PMo. Hence, the adsorption of EO$_x$ to PW^{3-} is stronger compared to the adsorption of EO$_x$ to PMo^{3-} due to the larger polarizability of PW^{3-} as already shown.[24,32]

From nano-assemblies in water to crystal formation by screening of electrostatic repulsion. NMR results provide clear evidence that PMo^{3-} interacts with EO$_x$ oligomers in aqueous solution to yield PMo^{3-}-EO$_x$ nano-assemblies. In case of the interaction of PW^{3-} with PEG200 it was found that at concentrations of 50 mM PEG200 and 25 mM PW^{3-}, two EO$_x$ chains adsorb to one PW^{3-} anion. NMR measurements suggest that these EO$_x$ chains adopt a loop shaped conformation. Therein the terminal -OH groups of ethylene glycol remain hydrated and do not interact with PW^{3-}.[24] Screening of repulsive interactions between EO$_x$ - PW^{3-} - EO$_x$ nano-assemblies upon the addition of 100 mM NaCl led to the formation of hybrid crystals containing PW$_{12}$O$_{40}$$^{3-}$ - EO$_5$/EO$_6$ - 3Na$^+$.[24] Hence, the electrostatic screening method is also used here to synthesize transparent, yellow PMo$_{12}$O$_{40}$$^{3-}$ - EO$_5$/EO$_6$ - 3Na$^+$ hybrid crystals. PMo$_{12}$O$_{40}$$^{3-}$ - EO$_5$/EO$_6$ - 3Na$^+$ hybrid crystals are stable in aqueous solution but decompose in dry air.

The crystal colour changes from bright yellow to greenish/black upon irradiation of the crystals with *(i)* sunlight, *(ii)* X-rays or by using *(iii)* a 455 nm 3 W LED, see **Figure 5.3(d)**. A closer inspection of such greenish/black crystals after some time of irradiation showed that only the top-most surface

layer of the crystal was affected by the crystal colour change from yellow to greenish/black, but the crystal core was still yellow. However, this phenomenon is still under investigation.

To investigate the origin of this colour change on a molecular level, a bright yellow single crystal was investigated by means of single-crystal X-ray diffraction. During irradiation of bright yellow crystals with Cu-K_α X-rays, the colour change from bright yellow to greenish/black proceeded even faster than in case of irradiation with sunlight. Upon irradiation with Mo-K_α X-rays, the colour change from bright yellow to greenish/black proceeded much slower as compared to irradiation with sunlight or Cu-K_α X-rays. Hence, a suitable yellow crystal was selected and diffraction intensities were collected on a single source SuperNova diffractometer with Mo-K_α radiation. $PMo_{12}O_{40}^{3-}$ - EO_5/EO_6 - $3Na^+$ hybrid crystals crystallize in the monoclinic space group $P2_1/c$ with $a = 20.980(4)$ Å, $b = 12.361(1)$ Å, $c = 32.472(5)$ Å, $\beta = 133.78(3)$ and $V = 6081(3)$ Å^3. Further parameters are given in **Table 5.1(a)**. Note that crystal water molecules are renounced in the crystal name of $PMo_{12}O_{40}^{3-}$ - EO_5/EO_6 - $3Na^+ \cdot 4\ H_2O$ hybrid crystals hereafter.

Table 5.1: Crystallographic Data for $PMo_{12}O_{40}^{3-}$ - EO_5/EO_6 - $3Na^+ \cdot 4\ H_2O$ hybrid crystals. (a), (b), (c) correspond to different crystals from the same batch.

	(a)	(b)	(c)
	$PMo_{12}O_{40}^{3-}$ - EO_5/EO_6 - $3Na^+ \cdot 4\ H_2O$	$PMo_{12}O_{40}^{3-}$ - EO_5/EO_6 - $3Na^+ \cdot 4\ H_2O$	$PMo_{12}O_{40}^{3-}$ - EO_5/EO_6 - $3Na^+ \cdot 4\ H_2O$ (after 106.4 hours of irradiation)
Sum formula	$C_{22}\ H_{54}\ Na_3\ O_{57}\ P\ Mo_{12}$ *	$C_{22}\ H_{54}\ Na_3\ O_{57}\ P\ Mo_{12}$ *	$C_{22}\ H_{52}\ Na_3\ O_{57}\ P\ Mo_{12}$ *
Molecular weight	2481.87	2481.87	2479.85
Crystal habit at the end of data collection	Yellowish/slightly green block	Greenish/blue block	Deeply blueish/black block
Crystal dimensions / mm^3	$0.487 \times 0.222 \times 0.147$	$0.232 \times 0.181 \times 0.116$	$0.335 \times 0.278 \times 0.205$
Crystal system		monoclinic	
Space group		$P2_1/c$	
a / Å	20.980(4)	20.972(1)	20.877(1)
b / Å	12.361(1)	12.366(1)	12.304(1)
c / Å	32.472(5)	32.417(1)	32.492 (2)
β / °	133.78(3)	133.79(1)	133.679(1)
V / Å^3	6081(3)	6069.3(6)	6036.2(10)
Z	4	4	4
ρ / g cm^{-3}	2.711	2.716	2.729
$F(000)$	4776	4776	4768
μ / mm^{-1}	2.559	2.564	21.327
Absorption corrections		numerical	
Diffractometer		Rigaku Supernova	
X-ray source	Mo-K_a	Mo-K_a	Cu-K_a
λ / Å	0.71073	0.71073	1.54184
T / K	110(3)$^{\#}$	123(1)	128(8)
Index ranges	$-21 \leq h \leq 14, -13 \leq k \leq 11, -33 \leq l \leq 27$	$-27 \leq h \leq 26, -16 \leq k \leq 16, -41 \leq l \leq 44$	$-20 \leq h \leq 25, -12 \leq k \leq 15, -40 \leq l \leq 34$
Reflections collected	13464	40415	38435
Independent reflections	5860; [$R_{int} = 0.0698$, $R_{sigma} = 0.1140$]	14151 [$R_{int} = 0.0337$, $R_{sigma} = 0.0385$]	12023 [$R_{int} = 0.0879$, $R_{sigma} = 0.0616$]
Data/restraints/parameters	5862/0/392	14151/0/1014	12023/0/868
Goodness-of-fit on F^2	1.076	1.067	1.307
R indices [I ≥ 2σ (I)]	$R_1 = 0.1012, wR_2 = 0.2190$	$R_1 = 0.0365, wR_2 = 0.0841$	$R_1 = 0.1017, wR_2 = 0.2942$
R indices [all data]	$R_1 = 0.1490, wR_2 = 0.2619$	$R_1 = 0.0446, wR_2 = 0.0886$	$R_1 = 0.1055, wR_2 = 0.3005$
Completeness / %	58	87	97
Largest diff. peak/hole / eÅ^{-3}	3.04/-2.16	1.51/-1.23	4.53/-2.10
∠(C11 − C12 − O47) / °	103(6)	121.9(8)	117(3)
d(C12 − O47) / Å	1.56(9)	1.236(10)	1.34(4)

* The number of H-atoms changes during the oxidation process which is not reflected in the sum formula since it was in not possible to introduce H-atoms to the bridging oxygen between Na1 and Na2 (O2W) with a riding model in measurements provided in **Table 5.1(a)** and **Table 5.1(c)**.

\# Note that the temperature was adjusted at 110 K (compared to 123 K for the measurements provided in **Table 5.1(b)** and **(c)**) to slow down the SCSC. In case of **Table 5.1(c)** the measurement was also started at 123 K.

Figure 5.2: (a) Structure model of $C_{22} H_{56} Na_3 O_{57} P Mo_{12}$ with the anionic PMo^{3-} unit and the cationic EO_5-EO_6-$3Na^+$ unit. Split positions are not shown in this representation. (b) Distorted close packed layers of PMo^{3-} (represented by the orange central phosphorous atoms of PMo^{3-}) and Na^+ cations (violet) in between. (c) Chains of Na^+ cations between distorted close packed layers of PMo^{3-} projected along [100]. For the sake of clarity, the EO_5/EO_6 chains are omitted in (b) and (c) and Na^+ cations are only displayed for specific layers in (b) and (c).

The structure model consists of one PMo^{3-} anion and three sodium cations entangled by a EO_5 and a EO_6 oligomer, see **Figure 5.2(a)**. Anionic PMo^{3-} anions form distorted close packed layers with an **A** - **B** - **A** - **B** sequence as shown in **Figure 5.2(b)**. Anionic PMo^{3-} anions also form distorted close packed layers along the representation as shown in **Figure 5.2(c)**. Na^+ cations (violet) intercalate in between these distorted close packed layers and form chains see **Figure 5.2(c)**. Four water molecules per structure model are incorporated into the crystal structure. The latter coordinate towards Na^+ and connect Na1 and Na2. Polydentate EO_5/EO_6 oligomers wrap around three Na^+ cations providing the following coordination polyhedra around Na^+ cations: Na1 distorted octahedron, Na2

distorted octahedron, and Na3 distorted pentagonal bipyramid. Note that the compound under discussion is isotypic to $PW_{12}O_{40}^{3-}$ - EO_5/EO_6 - $3Na^+$, see **section 4.4.4** and the unit cell volumes are also almost identical, *i.e.* $V(PMo_{12}O_{40}^{3-}$ - EO_5/EO_6 - $3Na^+) = 6081(3)$ $Å^3$ and $V(PW_{12}O_{40}^{3-}$ - EO_5/EO_6 - $3Na^+) = 6073.6(6)$ $Å^3$.[24]

Since the compound $PMo_{12}O_{40}^{3-}$ - EO_5/EO_6 - $3Na^+$ is isotypic to $PW_{12}O_{40}^{3-}$ - EO_5/EO_6 - $3Na^+$, a more detailed description of the crystal structure is renounced here but can be found elsewhere.[24] Note that the structure model could not be refined anisotropically as the data quality for this measurement was bad due to a very short measurement (20 min).

Photo-induced oxidation reaction. During a longer single-crystal X-ray diffraction experiment on a yellow $PMo_{12}O_{40}^{3-}$ - EO_5/EO_6 - $3Na^+$ crystal a successive crystal colour change with increasing Mo-K_α X-ray irradiation exposition time was observed: the crystal colour changes from transparent yellow to greenish/blue and the lattice parameters of the unit cell *a, b, c* and the unit cell volume *V* decrease, see **Table 5.1(b)**. The single crystal structure analysis revealed that the structure model is nearly identical to the measurement provided in **Table 5.1(a)**, but a special feature is met at the C70 - C71 - O66 fragment, see **Figure 5.3(a) - (c)**. The angle $\angle$(C70 - C71 - O66) = 122(1)°, implies a trigonal planar geometry at C71 for the measurement provided in **Table 5.1(b)** compared to a distorted tetrahedral geometry for the measurement provided in **Table 5.1(a)** $\angle$(C70 - C71 - O66) = 103(8) °. The distance, *d*(C71 - O66) = 1.24(1) Å is significantly shorter compared to the measurement provided in **Table 5.1(a)** where *d*(C71 - O66) = 1.56(12) Å. The atomic positions of the C71 - O66 fragment and the whole PMo^{3-} also change slightly. The refinement of a hydrogen atom to O66 (to yield a hydroxyl group) and the refinement of a second hydrogen atom at C71 was not possible for the measurement provided in **Table 5.1(b)** (the refinement did not converge after several refinement cycles).

Figure 5.3: (a) Zig-zag alignment of PMo^{3-} and EO$_5$/EO$_6$/3Na units in PMo$_{12}$O$_{40}$$^{3-}$ − EO$_5$/EO$_6$ − 3Na$^+$ hybrid crystals; (b) arrangement of a terminal -O-CH$_2$-CH$_2$-OH chain before the oxidation of C71; (c) after oxidation of C71. (d) Successive change of the crystal colour upon irradiation with a 455 nm LED lamp.
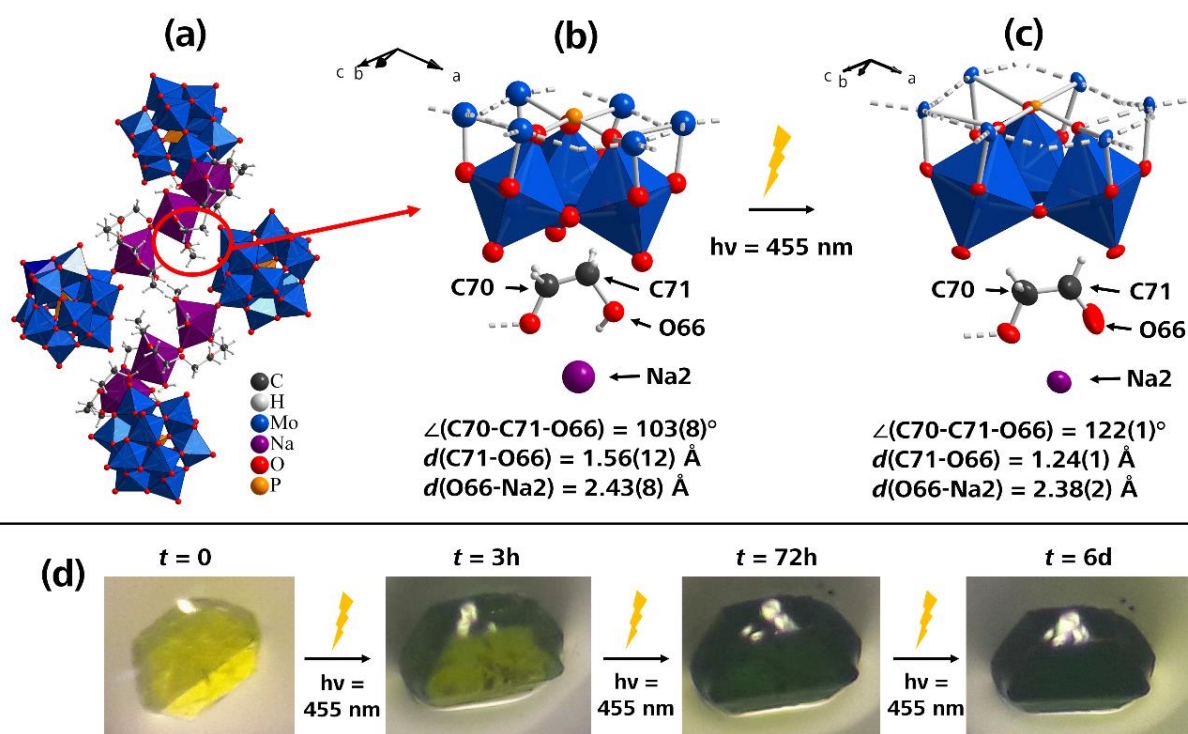
The decrease of the unit cell volume. Irradiation of the crystal for a longer time with softer Cu-K_α X-ray irradiation leads to an even faster crystal colour change from yellow to greenish black with increasing Cu-K_α X-ray irradiation exposition time, see **Figure 5.4(a)**. Hence, one single crystal was irradiated with Cu-K_α X-ray irradiation for in total 112.2 hours. The unit cell volume decreases more or less continuously from V(PMo$_{12}$O$_{40}$$^{3-}$ - EO$_5$/EO$_6$ - 3Na$^+$) = 6081(3) Å^3 to V(PMo$_{12}$O$_{40}$$^{3-}$ - EO$_5$/EO$_6$ - 3Na$^+$) = 6014.3(6) Å^3 (approximately 1 %), see **Figure 5.4(b)**. The unit cell parameters a and b account mainly for the decrease of unit cell volume (20.980(4) Å $\geq a \geq$ 20.854(1) Å; 12.361(1) Å $\geq b \geq$ 12.274(1) Å) since the C71-O66 bond is also located along unit cell parameter a and the slight rearrangement of the C70-C71-O66 fragment occurs along unit cell parameter b. The unit cell parameter c (32.504(2) Å $\geq c \geq$ 32.444(2) Å) decreases less compared to a and b as no rearrangement occurs along unit cell axis c. Note that even after irradiating the single crystal for 112.2 hours with Cu-K_α X-ray irradiation no constant cell volume was reached. Nevertheless, the structure model for a single crystal X-ray experiment after 106.2 hours of irradiation (for refinement parameters see **Table 5.1(c)**) is identical to the structure model of the measurement provided in **Table 5.1(b)**. Hence, longer irradiation with Cu-K_α X-rays to yield the completely oxidized crystal was renounced for time issues as it would only allow to access the final unit cell volume. Note that it is not possible

to refine hydrogen atoms to O2W (bridging oxygen between Na1 and Na2, see **Figure 5.4(c)**) for measurements provided in **Table 5.1(a) and (c)** as the refinement process does not converge.
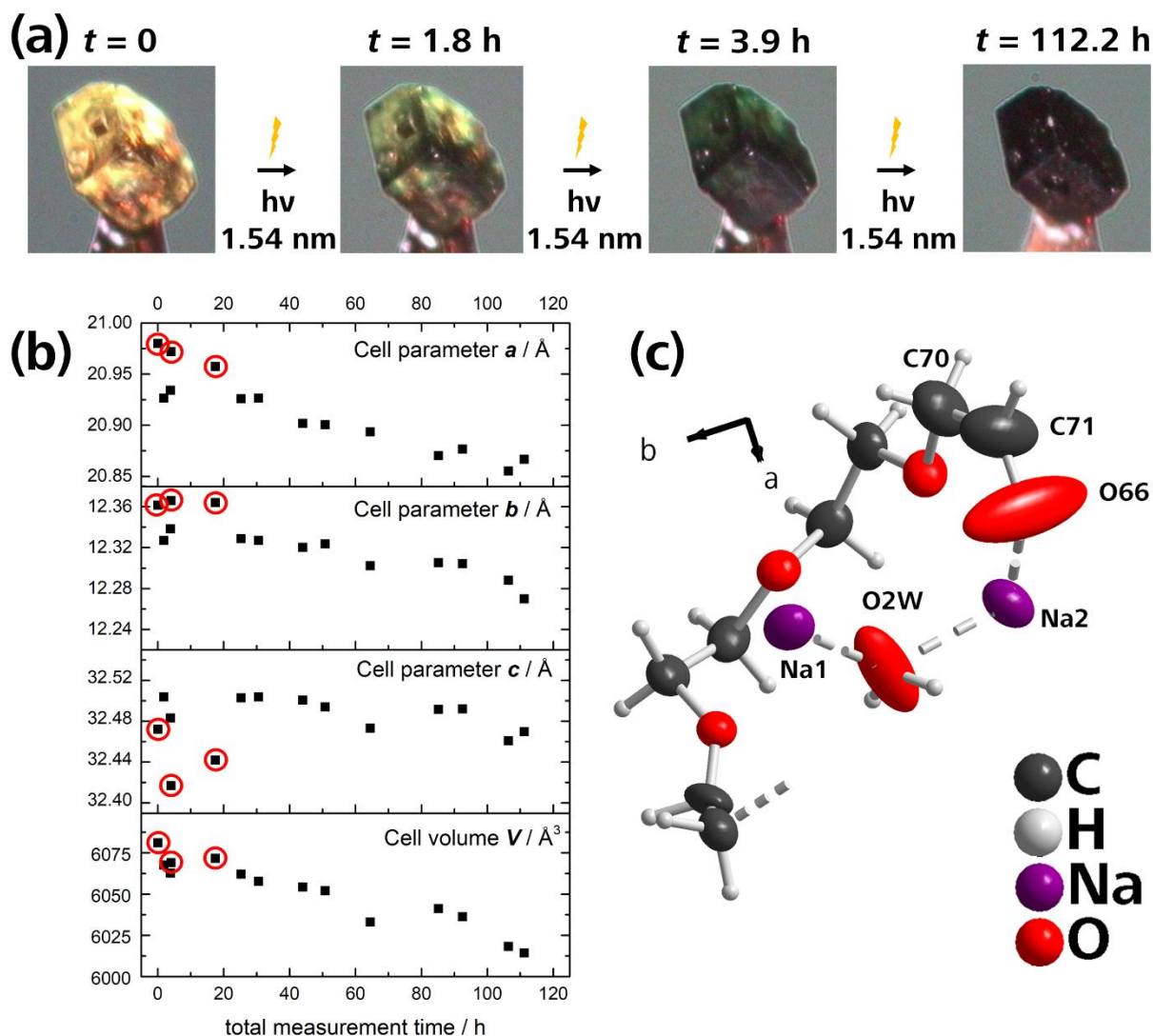
Figure 5.4: (a) Successive change of the crystal colour upon irradiation with a Cu-K_α X-ray radiation (λ = 1.54184 Å). (b) Decrease of the unit cell parameters and unit cell volume of $PMo_{12}O_{40}^{3-}$ - EO_5/EO_6 - $3Na^+$ hybrid crystals as a function of Cu-K_α X-ray irradiation. Note that the standard deviation for a, b, c and V lies within the black points. The unit cell parameters obtained from the single-crystal X-ray measurements presented in **Table 5.1(a) and (b)** and a further measurement with Mo-K_α X-ray radiation at 123 K are also included in this graph (red circles). Note that the y-scaling of all three cell parameters, a, b, c, is equidistant (plotted for $\Delta y(a, b, c)$ = 0.16 Å) to highlight the main decrease of the unit cell parameter a. (c) Excerpt of the structure model projected along [001] demonstrating that the decrease of the unit cell volume occurs along the unit cell axis a.

Comparison of a calculated powder pattern of the structure model with a measured powder pattern. A powder diffraction pattern was calculated from the structure model of the single crystal analysis in **Table 5.1(b)** and was compared to an experimental powder X-ray diffraction pattern of the precipitate obtained by using 50 mM PEG200, 25 mM H_3PMo and 100 mM NaCl, see

Figure 5.5. The precipitate again turned black during the powder X-ray diffraction measurement with Cu-$K_{\alpha1}$ X-ray irradiation. Note that the measured powder pattern could not be indexed and refined. Nevertheless, both diffractograms coincide in most of the reflections but many reflections do not coincide indicating that either *(i)* the structure model is not representative for all crystals or *(ii)* the cell parameters change upon irradiation of the crystals with X-rays. Case *(i)* can be safely neglected as $PMo_{12}O_{40}{}^{3-}$ - EO_5/EO_6 - $3Na^+$ hybrid crystals crystallise isotypic to $PW_{12}O_{40}{}^{3-}$ - EO_5/EO_6 - $3Na^+$ hybrid crystals. In case of $PW_{12}O_{40}{}^{3-}$ - EO_5/EO_6 - $3Na^+$ hybrid crystals a powder diffraction pattern was calculated from the single crystal data and was compared to an experimental pattern of a precipitate formed by 50 mM PEG200, 25 mM H_3PW and 100 mM NaCl (note that these are almost the same experimental conditions as for the preparation of $PMo_{12}O_{40}{}^{3-}$ - EO_5/EO_6 - $3Na^+$ hybrid crystals). Those diffractograms were shown to coincide almost perfectly in most of the reflections indicating that the structure model obtained from single crystal analysis was representative.[24] As single crystal X-ray experiments have already shown that the lattice parameters change continuously upon irradiation with X-rays (and the precipitate also turned greenish black during the powder X-ray diffraction experiment) and the atomic position of the C70-C71-O66 fragment changes, case *(ii)* can explain why the calculated theoretical powder pattern and the measured powder pattern do not coincide perfectly.
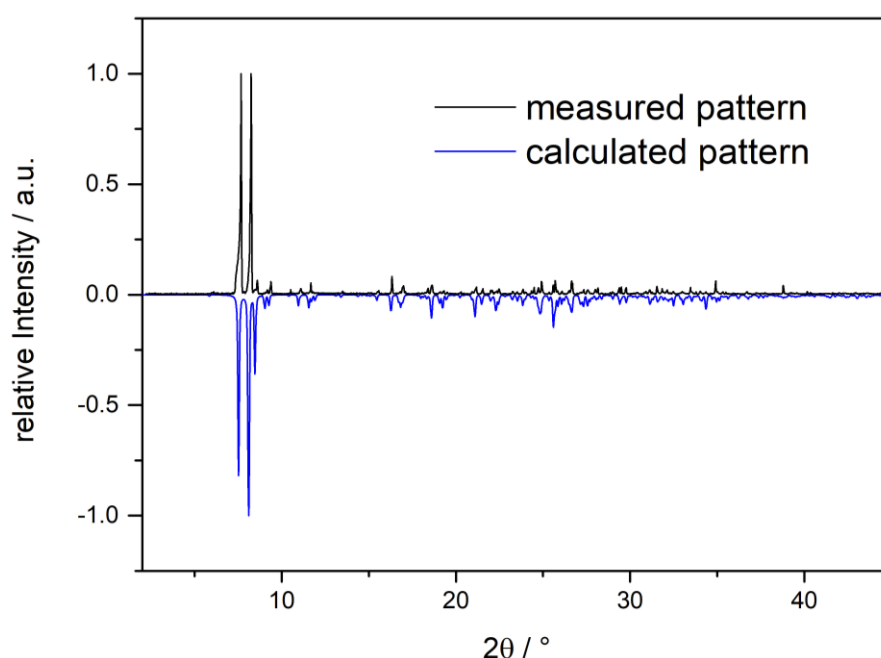
Figure 5.5: Powder diffraction pattern of a $PMo_{12}O_{40}{}^{3-}$ - EO_5/EO_6 - $3Na^+$ powder (top) measured at room temperature with a Cu-$K_{\alpha1}$ radiation (30 min) and a calculated pattern from the structure model (bottom) of the measurement provided in **Table 5.1(b)**.

Infrared Spectroscopy (IR). As the angle $\angle$(C70 - C71 - O66) = 122(1)° implies a trigonal planar geometry at C71 with d(C71 - O66) = 1.24(1) Å - a typical bond length of a C=O double bond[33] - the presence of an aldehyde functional group should also be confirmed by IR spectroscopy. Hence,

some crystals were irradiated for three months with a 50 W halogen light bulb (manufacturer: OSRAM) to induce the oxidation reaction at C71 with UV-VIS light. In **Figure 5.6**, IR spectra of yellow, non-irradiated crystals are compared to IR spectra of deeply greenish/black crystals. In both spectra, absorptions stemming from O-H modes (stretching ν and bending δ modes) of hydroxyl groups of EO_5/EO_6 and of crystal water molecules can be seen from 4000 - 3000 cm^{-1}. Absorptions stemming from C-H modes (stretching ν and bending δ modes) of the EO_x chains and O-H modes (bending δ of H_2O) are located from 1600-1200 cm^{-1}. Absorptions stemming from Mo-oxygen skeletal modes typical for a Keggin ion are located from 1150-650 cm^{-1}: 1070-1060 cm^{-1} (ν(P-O)), 980-965 cm^{-1} (ν(Mo=O)), 900-870 and 850-700 cm^{-1} (ν(Mo-O-Mo)).[34] At 1712 cm^{-1} a small absorption emerges (blue circle in **Figure 5.6**) for irradiated black crystals corresponding to the C=O stretch vibration of an aldehyde. Note that a free carbonyl group shows an absorption at 1750 cm^{-1}: the absorption from the compound under discussion is red-shifted compared to a free carbonyl group as the coordination of the carbonyl group to Na2 should lead to a weakening of the carbonyl bond.[35] The low intensity of the absorption corresponding to the C=O stretch vibration may be deduced to the low overall concentration of the aldehyde in the crystal.
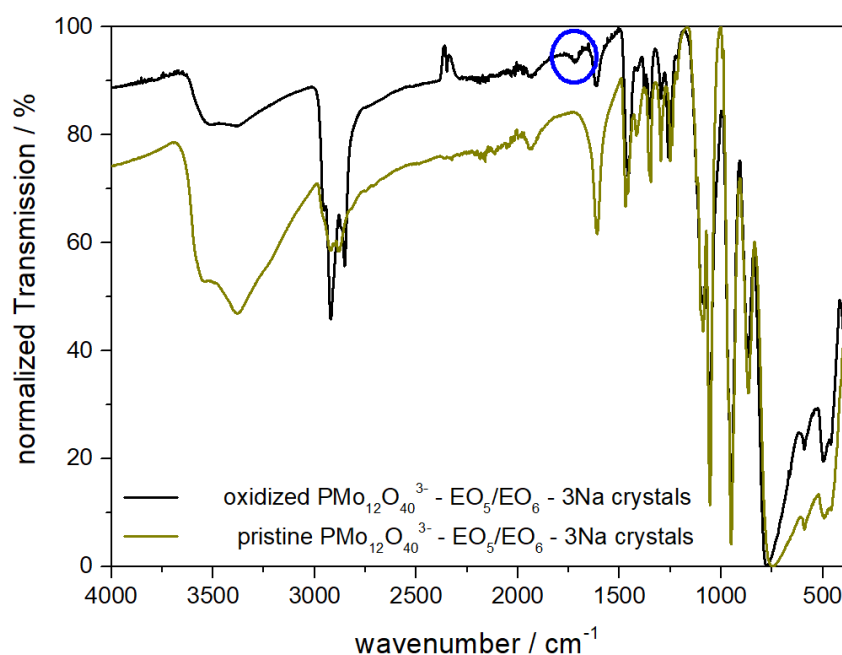
Figure 5.6: Normalized IR spectra $PMo_{12}O_{40}^{3-}$ - EO_5/EO_6 - $3Na^+$ hybrid crystals before 3 months treatment with 50 W halogen light bulb (yellow), and after the LED treatment (black). Note that the black curve represents a normalized IR spectrum of only few crystals (the transmission from 2000 – 2500 cm^{-1} is very low due to a weak detector response).

Electron spin resonance (ESR). ESR spectra were recorded for yellow pristine crystals and deeply black partially oxidised crystals (crystals were irradiated for three months with a 50 Watt halogen light bulb) to *(i)* distinguish if POMs are present in a one-electron or in a two-electron reduced species[15] and *(ii)* to confirm the reduction product, *i.e.* photo-reduced PMo^{4-} or PMo^{5-}, respectively,

see **Figure 5.7**. The ESR signal of solid yellow pristine crystals is not completely flat but rather shows several small oscillations. The ESR signal of solid black oxidised crystals also shows these weak oscillations but additionally a very strong oscillation (g-factor = 1.9498) indicating the presence of unpaired electrons in black $PMo_{12}O_{40}^{3-}$ - EO_5/EO_6 - $3Na^+$ hybrid crystals. The g-factor of 1.9498 indicates that unpaired electrons are not centred on the organic ethylene glycol moiety but on an inorganic moiety indicating the reduction of Mo^{6+} to Mo^{5+}.[36]

Mo^{5+} is known to produce a very strong absorption band in ESR and six weak absorption bands due to hyperfine coupling.[35] Furthermore, this resonance signal is not symmetrical and either suggests *(i)* an anisotropy of the unpaired electron distribution within the PMo^{3-} cluster or *(ii)* the presence of two differently reduced PMo^{x-} clusters, *i.e.* the one-electron PMo^{4-} and two-electron reduced PMo^{5-} cluster. Note that cyclo-voltammetric measurements (CV) are not possible to determine the oxidation potential of photo-excited PMo* clusters in $PMo_{12}O_{40}^{3-}$ - EO_5/EO_6 - $3Na^+$ hybrid crystals in order to distinguish between a one- or a two-electron reduced species as in other cases.[37] This is due to the fact that the oxidation potential is dependent on the *pH*: crystals were prepared with **H₃PMo** whereas in $PMo_{12}O_{40}^{3-}$ - EO_5/EO_6 - $3Na^+$ hybrid crystals PMo^{3-} is present as an isolated cluster with sodium cations as counter ions (and the preparation of Na_3PMo in aqueous solution at *pH* = 7 for investigations in CV is tricky as above *pH* > 2 other fragmented or larger polyoxometalates are formed).
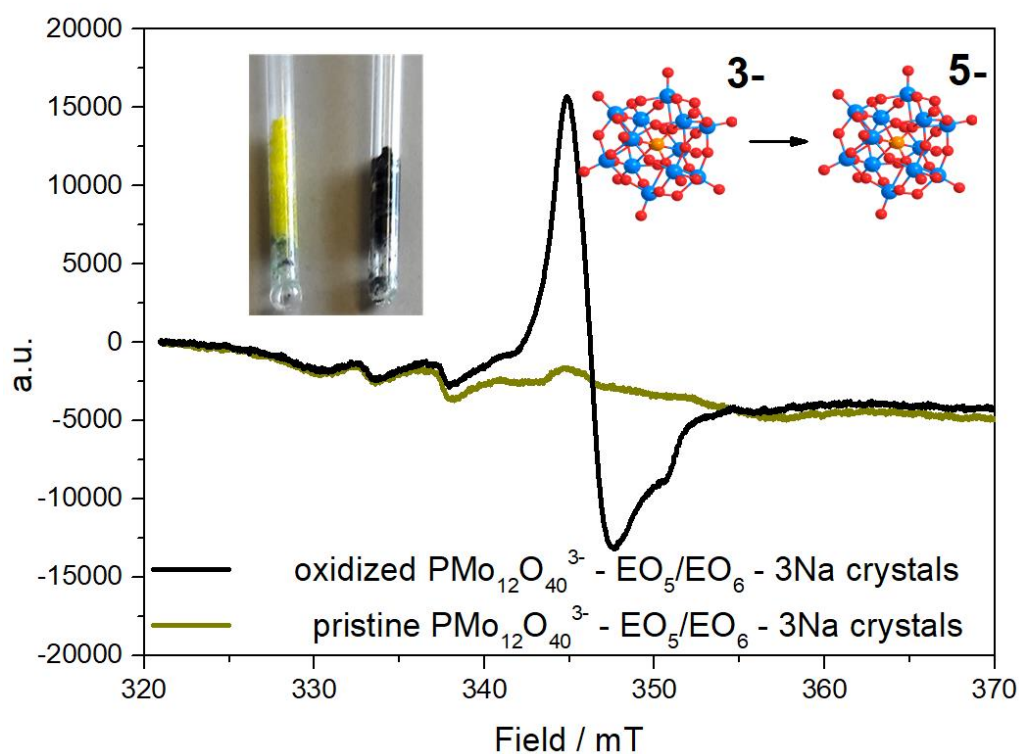
Figure 5.7: ESR spectrum of oxidized crystals and pristine crystals with a successive photo-reduction of PMo^{3-} to PMo^{5-} clusters. The left inset shows samples of yellow pristine crystals and black oxidized crystals.

UV-VIS. Since the greenish/blue colour in POM chemistry is well-known as the one- or two-electron reduced POM heteropolyblue species with large visible light absorptions from 600 – 1000 nm,[15] UV-VIS experiments were performed on few crystals (pristine and oxidized crystals) *solubilized in water,* **Figure 5.8**. No light absorption is observed for non-oxidized $PMo_{12}O_{40}^{3-}$ - EO_5/EO_6 - $3Na^+$ hybrid crystals within 510 – 1000 nm. Two absorption maxima from 450 nm – 1400 nm are observed for black crystals solubilized in H_2O as already expected from the greenish-dark crystal colour. These two absorption maxima are known to be originated by oxygen to metal charge transfers of both terminal and bridging oxygen atoms to molybdenum atoms.[15]
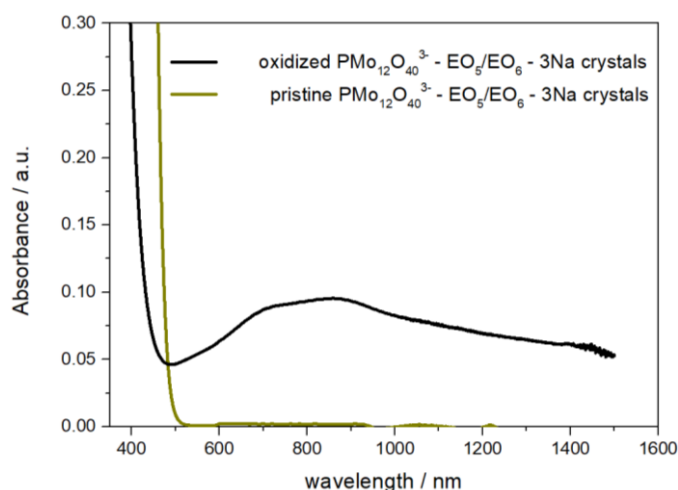
Figure 5.8: UV-VIS spectra of oxidised crystals and not-oxidised crystals with the formation of one- or two-electron reduced PMo^{4-}/PMo^{5-} - heteropolyblue species.

Discussion of the solid-state oxidation. The trigonal planar geometry at C71 in combination with the distance d(C71 - O66) = 1.24(1) Å, - a typical bond length of a C=O double bond [33] - suggests that an aldehyde is present at C71 - O66 and not, as for the measurement provided in **Table 5.1(a)** an alcohol. An aldehyde group can only be present in case of an oxidation reaction of C71 in the solid state. PMo^{3-} is indeed a well-known oxidation- and photocatalyst in solution chemistry mainly owing to its Mo^{6+}, d^0 configuration which makes PMo^{3-} a good electron acceptor. The well-established catalytic solution behaviour of PMo^{3-} can also be transferred to the solid state: PMo^{3-} absorbs incident photons leading to photoexcited PMo^{3-*} clusters. In a second step, these photoexcited PMo^{3-*} clusters oxidise the C71 - alcohol to the corresponding C71 - aldehyde. Since PMo^{3-} absorbs light from the visible spectrum of the light, the oxidation reaction can be triggered with a 455 nm LED lamp. The oxidation reaction can also be triggered and proceeds faster with sunlight (which provides partially UV-light below 400 nm). This is due to the fact that the absorption coefficient of PMo^{3-} for UV light ($\lambda < 400$ nm) is higher than for visible light ($\lambda > 400$ nm), see **Figure 5.8**, and the absorption of photons is more efficient. Additionally, X-rays also promote the oxidation process in the crystal bulk more efficiently as incident photons are not completely absorbed by the yellow crystal on its topmost surface, but can penetrate the whole crystal as implied by *Lambert-*

Beer's law for light absorption. Irradiation of pristine crystals with Cu-K_α X-ray radiation triggers the oxidation reaction more efficiently than irradiation of crystals with Mo-K_α X-ray radiation as the absorption coefficient of pristine yellow crystals is much higher for Cu-K_α X-ray radiation, *i.e.* μ = 21.306 mm^{-1}, than for Mo-K_α X-ray radiation, *i.e.* μ = 2.31 mm^{-1}. As a consequence, more photoexcited PMo^{3-*} clusters are formed being able to oxidize C71.

Furthermore, the shortest distance between an atom of a PMo^{3-} cluster and EO_6 is also found between C71 and a terminal oxygen atom of an adjacent PMo^{3-} cluster as indicated with the red circle in **Figure 5.3a**: d(C71 – terminal oxygen of PMo^{3-}) = 3.12 Å. A short distance PMo^{3-} - C71 facilitates the electron transfer from C71 to a PMo^{3-} cluster during an oxidation reaction. The presence of one or two unpaired electrons in the PMo^{x-} cluster is confirmed by *(i)* the change of the crystal colour from yellow to black due to the subsequent formation of the reduced PMo^{4-}/PMo^{5-} heteropolyblue species[15] and *(ii)* the presence of unpaired electrons at Mo atoms as shown by the intense signal in ESR with a *g*-factor of 1.94.

Note that the deeply coloured heteropolyblue species at the surface of the crystal additionally leads to a lower penetration depth of visible light as it is mostly absorbed at the topmost surface of the crystal. Hence, the reaction rate of the oxidation process in case of visible light should slow down with a more and more intense black-colouring of the crystal.

This oxidation process at C71 and a successive change of the atomic position of O66 is also the reason for the large displacement ellipsoids for O66. Note that it is not possible to localize the two H$^+$ released during the oxidation process in a single-crystal X-ray experiment. Note that this SCSC is irreversible and could not be reverted by exposing the crystals to air (re-oxidation of PMo^{3-} clusters by molecular O_2) or upon passing pure O_2 gas over the crystals.

5.5 Conclusion

$PMo_{12}O_{40}^{3-}$ - EO_5/EO_6 - $3Na^+$ hybrid crystals were obtained by the electrostatic screening method and demonstrated to be visible light responsive. Upon irradiation of $PMo_{12}O_{40}^{3-}$ - EO_5/EO_6 - $3Na^+$ hybrid crystals with visible light/X-rays an irreversible SCSC transformation occurs going along with *(i)* a change of the crystal colour from clear yellow to green and deep black and *(ii)* a decrease in the unit cell volume *V* about 1 % due to a prominent decrease of the unit cell parameters *a* (and partially *b*). During the SCSC, PMo^{3-} induces the oxidation of one terminal hydroxyl group of the EO_6-chain to the corresponding aldehyde. This SCSC transformation allows to selectively oxidize only one terminal alcohol group of in total 4 available alcohol groups of EO_5/EO_6 to the corresponding aldehyde. Note that the selective oxidation of only one alcohol group in an oligomeric mixture of alcohols is nearly impossible in a liquid phase reaction. The high selectivity can only be achieved due to a close proximity of this alcohol to an adjacent PMo^{3-} cluster in the crystalline state.

5.6 Bibliography

[1]   T. Y. Ho, S. M. Huang, J. Y. Wu, K. C. Hsu, K. L. Lu, *Cryst. Growth Des.* **2015**, *15*, 4266–4271.

[2]   T. Taniguchi, H. Sugiyama, H. Uekusa, M. Shiro, T. Asahi, H. Koshima, *Nat. Commun.* **2018**, *9*, 538.

[3]   X. Feng, *Inorg. Chem. Commun.* **2017**, *86*, 249–252.

[4]   Y. Noori, K. Akhbari, *RSC Adv.* **2017**, *7*, 1782–1808.

[5]   R. Samanta, S. Ghosh, R. Devarapalli, C. Malla Reddy, *Chem. Mater.* **2018**, *30*, 577–581.

[6]   M. Servalli, M. Solar, N. Trapp, M. Wörle, A. D. Schlüter, *Cryst. Growth Des.* **2017**, *17*, 3419-3432.

[7]   X. Tao, D. Ju, T. Zhao, D. Yangyang, G. Zhang, X. Hu, D. Cui, *J. Mater. Chem. A* **2017**, *5*, 24014-24014.

[8]   M. Jin, T. Sumitani, H. Sato, T. Seki, H. Ito, *J. Am. Chem. Soc.* **2018**, *140*, 2875-2879.

[9]   R. J. Marshall, S. L. Griffin, C. Wilson, R. S. Forgan, *J. Am. Chem. Soc.* **2015**, *137*, 9527–9530.

[10]   F.-L. Hu, Y.-X. Shi, H.-H. Chen, J.-P. Lang, *Dalt. Trans.* **2015**, *44*, 18795–18803.

[11]   N. Y. Li, D. Liu, Z. G. Ren, C. Lollar, J. P. Lang, H. C. Zhou, *Inorg. Chem.* **2018**, *57*, 849–856.

[12]   G. K. Kole, J. J. Vittal, *Chem. Soc. Rev.* **2013**, *42*, 1755–1775.

[13]   A. Iturrospe, L. San Felices, S. Reinoso, B. Artetxe, L. Lezama, J. M. Gutiérrez-Zorrilla, *Cryst. Growth Des.* **2014**, *14*, 2318–2328.

[14]   S. Reinoso, B. Artetxe, L. S. Felices, J. M. Gutiérrez-Zorrilla, in *Polyoxometalates Prop. Struct. Synth. (Ed.: A.P. Roberts)*, Nova Science Pub Inc, New York, **2016**, pp. 1–256.

[15]   J. J. Borrás-Almenar, E. Coronado, A. Müller, M. Pope, *Polyoxometalate Molecular Science,* Springer Netherlands, **2012**.

[16]   J. T. Rhule, C. L. Hill, D. a. Judd, R. F. Schinazi, *Chem. Rev.* **1998**, *98*, 327–357.

[17]   B. Hasenknopf, *Front. Biosci.* **2005**, *10*, 275.

[18]   S. Krickl, T. Buchecker, A. U. Meyer, I. Grillo, D. Touraud, P. Bauduin, B. König, A. Pfitzner, W. Kunz, *Phys. Chem. Chem. Phys.* **2017**, *19*, 23773–23780.

[19]   M. Dave, C. Streb, *Dalt. Trans.* **2015**, *44*, 18919-18923.

[20]   B. Schwarz, J. Forster, M. K. Goetz, D. Yücel, C. Berger, T. Jacob, C. Streb, *Angew. Chemie - Int. Ed.* **2016**, *55*, 6329–6333.

[21]   D.-L. Long, E. Burkholder, L. Cronin, *Chem. Soc. Rev.* **2007**, *36*, 105–121.

[22]   D. L. Long, R. Tsunashima, L. Cronin, *Angew. Chemie - Int. Ed.* **2010**, *49*, 1736–1758.

[23]   A. Proust, B. Matt, R. Villanneau, G. Guillemot, P. Gouzerh, G. Izzet, *Chem. Soc. Rev.* **2012**, *41*, 7605.

[24] T. Buchecker, X. LeGoff, B. Naskar, A. Pfitzner, O. Diat, P. Bauduin, *Chem. - A Eur. J.* **2017**, *23*, 8434–8442.

[25] B. Naskar, O. Diat, V. Nardello-Rataj, P. Bauduin, *J. Phys. Chem. C* **2015**, *119*, 20985–20992.

[26] Rigaku Oxford Diffraction, **2017**, CrysAlisPro Version 1.171.39.37b.

[27] G. M. Sheldrick, *Acta Crystallogr. Sect. A* **2015**, *71*, 3–8.

[28] G. M. Sheldrick, *Acta Crystallogr. Sect. C* **2015**, *71*, 3–8.

[29] O. V. Dolomanov, L. J. Bourhis, R. J. Gildea, J. A. K. Howard, H. Puschmann, *J. Appl. Crystallogr.* **2009**, *42*, 339–341.

[30] WinXPOW, **2011**, Stoe & Cie GmbH, Version 3.0.2.1.

[31] J. Shoolery, *A Basic Guide to NMR*, Extra Byte, Palo Alto, **1972**.

[32] T. Buchecker, P. Schmid, S. Renaudineau, O. Diat, A. Proust, A. Pfitzner, P. Bauduin, *Chem. Commun.* **2018**, *54*, 1833–1836.

[33] Vollhardt, K. Peter C. *"The Carbonyl Group (17.2)." Organic chemistry structure and function. 5th ed*. Vol. 1. New York: W.H. Freeman, **2007**.

[34] D. Barats-Damatov, L. J. W. Shimon, Y. Feldman, T. Bendikov, R. Neumann, *Inorg. Chem.* **2015**, *54*, 628–634.

[35] B. C. Smith, *Spectroscopy* **2017**, *32*, 31–36.

[36] W. R. Hagen, *Dalt. Trans.* **2006**, *37*, 4415-4434.

[37] B. Rausch, M. D. Symes, G. Chisholm, L. Cronin, *Science.* **2014**, *345*, 1326–1330.

6 The Self-assembly of short chain PNIPAM with Keggin Polyoxometalates

6.1 Preface and Abstract

Several people contributed to the work in this chapter:

- Philipp Schmid contributed with experimental work during a Bachelor thesis.
- Dr. Isabelle Grillo, Dr. Sylvain Prévost, Dr. Thomas Zinn and Dr. Daniel Clemens helped as beamline scientists with SAXS and SANS measurements at ILL, ESRF and HZB, respectively.
- Dr. Markus Drechsler helped recording cryo-TEM measurements at the centre for microscopy in Bayreuth.
- Florian Buchecker, Sebastian Krickl, Alban Jonchère and Dr. Pierre Bauduin contributed with experimental work during a three-day run at ESRF, Grenoble.
- Dr. Olivier Diat, Dr. Pierre Bauduin and Prof. Dr. Arno Pfitzner contributed with fruitful discussions and supervised the experimental work.

The following chapter contains the section "Supporting Information". Additional results and graphs are provided in the Supporting Information (SI) supporting conclusions drawn in the chapter.

Abstract: We show here for the first time that short chain poly-(*N*-isopropylacrylamide) PNIPAM, one of the most famous thermo-responsive polymer, self-assemble in water into *(i)* discrete nm-globules and *(ii)* micrometric sheets with nm-thickness upon the addition of the well-known Keggin-type polyoxometalate (POMs), *e.g.* $H_3PW_{12}O_{40}$ (PW^{3-}). The structures of these supramolecular assemblies were revealed by combining small-angle-X-ray and neutron scattering (SAXS/SANS) and cryo-transmission electron microscopy (cryo-TEM). The type of self-assembly is controlled by the $PW_{12}O_{40}^{3-}$ (PW^{3-}) concentration: at low PW^{3-} concentrations, PW^{3-} adsorbs on fully extended PNIPAM chains to form globules consisting of homogeneously distributed PW^{3-} in PNIPAM droplets of several nm in size. Upon further addition of PW^{3-}, a phase transition from globules to micrometric sheets is observed for PNIPAMs with sufficiently long chains, typically above 22 repeating units. The thickness of the sheets, ranging from 4 to 12 nm can be easily controlled by varying the PNIPAM chain length, here from 44 to 88 repeating units. The PNIPAM sheets are electrostatically stabilized by two monolayers of PW^{3-} adsorbed on each side of the sheets. The shortest PNIPAM chain, with 18 repeating units, led to globular PNIPAM/PW^{3-} aggregates with 5 − 20 nm size but not to sheets. The PW^{3-}/PNIPAM self-assembly arises from non-specific interactions, *i.e.* it is an entropically driven process associated to the partial dehydration of PW^{3-} and of the PNIPAM. This process is related to the general propensity of POMs to adsorb on hydrated surfaces. This effect, known as super-chaotropy, was also highlighted by the significant increase in the lower critical solubilization temperature (LCST)

of PNIPAM observed upon addition of PW^{3-} in the mM range. The influence of the POM structure on the globule and sheet formation was also investigated, by substituting PW^{3-} by H$_4$SiW$_{12}$O$_{40}$ (SiW^{4-}) or H$_3$PMo$_{12}$O$_{40}$ (PMo^{3-}) to get a deeper understanding of the role of electrostatics and polarizability effects on the PNIPAM self-assembly process. The control of POM/PNIPAM nanostructures leads to a self-encapsulating process of biologically active POMs - super-chaotropic nano-ions - with thermosensitive polymers and opens therefore new opportunities in drug delivery formulation systems.

6.2 Introduction

Poly-(N-isopropylacrylamide) (PNIPAM), one of the most studied thermo-responsive polymer, undergoes a liquid-liquid phase separation in aqueous solutions above its lower critical solution temperature (LCST) around 33°C.[1,2] During this process, single PNIPAM polymers undergo a conformational change form a hydrated "swollen" extended conformation to a dehydrated "shrunk" globular conformation concomitant with a reduction of the volume of PNIPAM.[2,3] As the LCST of PNIPAM appears close to body temperature PNIPAM polymers find several applications in *(i)* biotechnology where *e.g.* the LCST is exploited in the bio-separation of proteins conjugated with PNIPAM or in *(ii)* (surface-) functionalization of materials to grant them thermo-responsiveness.[4] PNIPAM is also *(iii)* a simple model polymer for the cold denaturation of proteins in aqueous solution, as PNIPAM has secondary amide side groups reminiscent of the polyamide backbone of proteins.[4,5] Such *in vitro* and *in vivo* applications of PNIPAM require a deep understanding of the conformational and solution behaviour of PNIPAM in the presence of NaCl.[4,6–14] The most comprehensive studies on the effect of salt, chain length and end group polarity on the LCST and solubility of PNIPAM in water have been carried out by the group of P.S. Cremer.[11,12,15,16] Although Du *et al.* stressed by virtue of molecular dynamics (MD)-simulations that PNIPAM interacts predominantly with cations,[6] Fuentes *et al.* showed by combining MD-simulations and experiments that for anions/cations with identical size, shape and valence, the affinity of anions and cations for interfaces is intrinsically different with anions providing a substantially stronger impact on PNIPAM than cations.[7] Cremer *et al.* also focused on the interaction of PNIPAM with sodium salts of different anions. They illustrated that anions interact with the PNIPAM polymer via three pathways: *(i)* anions can polarize water molecules that are involved in hydrogen bonding with the amide bond, *(ii)* anions can interfere with the hydrophobic hydration of the macromolecule by increasing the surface tension of the cavity surrounding the hydrophobic aliphatic backbone and the isopropyl groups and *(iii)* anions may bind directly to the polyamide group. They claimed that *(i)* and *(ii)* lead to a decrease of the water solubility of PNIPAM (called salting-out, *i.e.* lowering the LCST of PNIPAM) whereas *(iii)* leads to an increase of the water solubility of PNIPAM (called salting in, *i.e.* increasing the LCST of PNIPAM). Cremer *et al.* concluded that the ability of an anion to lower the LCST follows the well-known Hofmeister series of anions[17] implying that kosmotropic anions (small anions with high charge density) are strongly

salting-out whereas chaotropic anions (large anions with low charge density, typically SCN⁻ or I⁻) are salting-in by adsorbing on the PNIPAM chains.[15]

Recently, it was shown that POMs, anionic nano-sized molecular metal-oxide clusters, are by far more chaotropic than classical chaotropic anions (*e.g.* I⁻ or SCN⁻), due to their large size, low charge density and delocalized charges. POMs were classified within the Hofmeister series as super-chaotropes due to their extremely strong increase in the clouding temperature of non-ionic polyethoxylated surfactants, typically between 10-40 °C compared to around 2-3 °C for SCN⁻ for salt concentrations in the mM range.[18–20] The super-chaotropic behaviour of POMs is related to their strong propensity to adsorb on hydrated neutral surfaces, *e.g.* on non-ionic surfactant micelles surface made of polyethoxylated or sugar-based surfactants,[18,20] on the water/air interface covered by the latter non-ionic surfactants,[18] on polyethylene glycol (EO$_x$ or PEG) oligomers[19] or cyclodextrines.[18–23] It was shown that the strong adsorption of super-chaotropes on hydrated surfaces is an entropically driven process associated to the release of many water molecules to the water bulk phase, arising from the partial dehydration of the surface and of the super-chaotropes upon surface adsorption.[18,24] As for specific ion effects, the super-chaotropic effect emerges from non-specific interactions and results from competing ion-water/water-surface interactions.[15,25] It is noteworthy that the super-chaotropic behaviour is not only restricted to POMs but can apparently be generalized to nanometric anionic species with a low charge density, such as anionic borane clusters.[24,26]
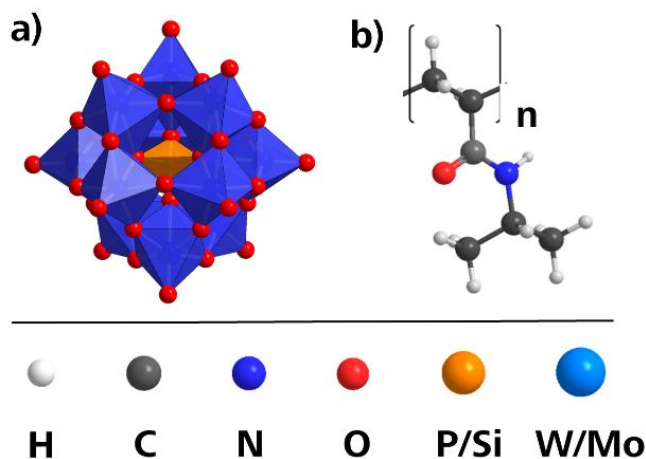
Figure 6.1: Structure of (a) an *α*-Keggin-type POM, (b) the poly-*N*-isopropylacrylamide (PNIPAM) repeating motive.

Here, we investigate the super-chaotropic effect of Keggin type polyoxometalates, *α*-H$_3$PW$_{12}$O$_{40}$ (H$_3$PW), *α*-H$_3$PMo$_{12}$O$_{40}$ (H$_3$PMo) and *α*-H$_4$SiW$_{12}$O$_{40}$ (H$_4$SiW), towards short chain PNIPAM polymers (PNIPAM2000, 5000, 7000, 10000 with averagely 18, 44, 62 and 88 repeating units, respectively), see **Figure 6.1**. The focus was first laid on the interaction of PW$_{12}$O$_{40}$$^{3-}$ (PW^{3-}) with PNIPAM10000 and the effect of the POM charge/structure (PW^{3-}/SiW^{4-}/PMo^{3-}) with PNIPAMx000 (x = 2, 5, 7, 10) was discussed afterwards. To the best of my knowledge (non-specific) interactions between POMs

and PNIPAM as well as the self-assembly of PNIPAM to well-defined nano-structures were not reported in the literature so far. The covalent coupling of PNIPAM to POMs has been explored recently to induce self-assembly, thermo- and salt-sensitivity to POMs.[27] Here, the adsorption and self-assembly process of PNIPAM/POM at the mesoscale was followed by small-angle-X-ray-scattering (SAXS) and small-angle neutron scattering (SANS) in combination with cryo-transmission electron microscopy (cryo-TEM). The interaction of POMs with PNIPAM in water by the evolution of the LCST upon addition of POMs and by differential scanning calorimetry (DSC) measurements was further investigated.

6.3 Experimental

Materials. Phosphotungstic acid hydrate ($H_3PW_{12}O_{40} \cdot 14\ H_2O$, H_3PW, MW = 2898 g/mol, 99.995% purity), phosphomolybdic acid hydrate ($H_3PMo_{12}O_{40} \cdot 9\ H_2O$, H_3PMo, MW = 1825 g/mol, 99.9 % purity) and silicomolybdic acid hydrate ($H_4SiW_{12}O_{40} \cdot 28\ H_2O$, H_4SiW, MW = 3031 g/mol, 99.99% purity) were purchased from Sigma Aldrich. Sodium chloride (NaCl, 99.5%), PNIPAMx000 (x = 2, 5, 7, 10) terminated with CH_3- and $-S-CH_2-CH_2-COOH$ were purchased from Sigma Aldrich. PNIPAM2000 provides in average 17 repeating units, PNIPAM5000 43 repeating units, PNIPAM7000 61 repeating units and PNIPAM10000 88 repeating units. Milli-Q water was used with a conductivity lower than 10.5 µS/cm and a total organic carbon content of max. 400 ppb.

SAXS. SAXS/WAXS experiments were performed at the TRUSAXS beamline (ID02) at the ESRF in Grenoble, France. The instrument uses a pinhole collimated monochromatic incident beam with a wavelength λ = 0.0995 nm (12.46 keV). The SAXS detector (Rayonix MX-170HS) was set to a sample-to-detector distance of 1.2 m and WAXS data is simultaneously recorded with a Rayonix LX-170HS detector placed in air 14 cm away from the sample. This setting allows to cover a broad Q-range from 0.006 nm⁻¹ to 6.5 nm⁻¹ with $q = 4\pi/\lambda\ \sin(\theta)$, the scattering vector defined by the scattering angle 2θ. The magnitude of the q vector for the WAXS was calibrated with the Bragg-refletions of a Para Bromo Benzoic Acid (PBBA) standard. The flux of the incident X-ray beam was 6x10¹² photons/s. Samples were contained in quartz capillaries with a diameter of 2.0 mm and a wall thick-ness of 0.01 mm. Measured 2D scattering patterns were normalized to absolute scale after instrument specific corrections and azimuthally averaged to obtain the scattered intensity as a function of q. The normalized cumulative background of water, sample cell and instrument were subtracted to obtain I(q). Note that the beam polarization was not taken into account during the data reduction.

SANS. SANS spectra were recorded at the V16-TOF beamline at the HZB Berlin. The q-range from 0.6 nm⁻¹ to 7 nm⁻¹ was accessed which corresponds to sizes from around 0.9 to 10.5 nm in real space. All spectra were corrected from instrumental background and empty cell and from the inco-

herent scattering, mainly due to hydrogen atoms of PNIPAM. The small contribution of PW^{3-} (constant scattering over the whole q-range) was also subtracted. The scattered intensity was calibrated with water and therefore data are shown in absolute values (mm^{-1}).

LCST measurements. Solutions containing 1 mM and 2 mM PNIPAMx000 (x = 2, 5, 7, 10), respectively, and a distinct amount of POM were placed into a thermostat (Thermomix_1460, B.Braun Melsungen AG) and were heated from 24 °C to 60 °C with a rate of 0.5 °Cmin^{-1}. The LCST was detected by visual inspection with an uncertainty of $\pm$ 1 °C. Solutions containing PNIPAM/POM sheets are tainted with a larger error as the LCST "smears" over a temperature range of at least 5 °C (as indicated with the large error bars) and is not sharp as it is the case for PNIPAM solutions in the absence of POM. In such cases the LCST was determined as the point, where an advanced turbidity of the solutions was recognizable by the naked eye.

DSC measurements. Differential scanning calorimetry was performed by using a DSC30 (Mettler) in a two-cycle mode, at a heating rate of 7 °Cmin^{-1} from 25 to 60 °C. Approximately 60 mg of the fluid sample were sealed in aluminium pans. Measurements were performed by continuously flushing the instrument with nitrogen to avoid contamination with moisture.

IR measurements. FT-IR spectra were recorded in the range of 4000 – 400 cm^{-1} using a Varian 670 FT-IR spectrometer with a PIKE GladiATR extension.

NMR measurements. All NMR spectra were measured at room temperature using a Bruker Avance 400 (400 MHz for ^{1}H) NMR spectrometer. All chemical shifts are reported in δ-scale as parts per million [ppm] relative to the solvent residual peak (D_2O) as the internal standard.

SLS. Static light scattering experiments were performed using a temperature controlled CGS-3 goniometer system from ALV (Langen, Germany) equipped with an ALV-7004/FAST Multiple Tau digital correlator and a vertically polarized 22 mW HeNe laser (wavelength λ = 632.8 nm). Before starting the measurement, all samples were filtered into dust-free cylindrical light scattering cells (10 mm outer diameter) using a 0.2 µm PTFE membrane filter. The sealed measurement cells could be placed directly into the measurement apparatus. Measurements were performed for scattering angles of 45 – 135° after thermostating to 25 ± 0.1 °C.

TEM. TEM micrographs were recorded with a Zeiss CEM 902 electron microscope operated at 200 kV. The machine was equipped with an in-column energy filter. For cryo-TEM studies, a drop (~2 mL) of the aqueous PNIPAM solution (c(PNIPAM) = 1 mM) was placed on a lacey carbon-coated copper TEM grid (200 mesh, Science Services), where most of the liquid was removed with blotting paper, leaving a thin film stretched over the grid holes. The specimens were shock vitrified by rapid immersion into liquid ethane in a temperature-controlled freezing unit (Zeiss Cryobox, Zeiss NTS GmbH) and cooled to approximately 90 K. The temperature was monitored and kept constant in the chamber during all of the preparation steps. After freezing the specimens, they were inserted

into a cryo-transfer holder (CT3500, Gatan) and transferred to a Zeiss EM922 OMEGA EFTEM instrument. Examinations were carried out at temperatures around 90 K. The microscope was operated at an acceleration voltage of 200 kV. Zero-loss filtered images (DE 1/40 eV) were taken under reduced dose conditions. All images were registered digitally by a bottommounted CCD camera system (Ultrascan 1000, Gatan), combined, and processed with a digital imaging processing system (Gatan Digital Micrograph 3.9 for GMS 1.4). Evaluation of the respective length scales of the structures was achieved by measuring 50-100 different spots within the sample with the UTHSCSA ImageTool V. 3.00.

6.4 Results and Discussion

The addition of small quantities of H_3PW (typically $c(H_3PW) < 5$ mM) to a solution containing 1 mM PNIPAM10000 yield transparent and colorless solutions. The addition of higher concentrations of H_3PW (typically $c(H_3PW) > 5$-10 mM) to aqueous solutions of 1 mM PNIPAM10000 yields blueish solutions and after a while these solutions undergo a liquid-liquid phase separation, see **Figure S 6-1**, (1 min – 1 day, the higher the H_3PW concentration the faster the separation).

Combined SAXS/SANS scattering experiments were performed to extract information on the interaction of PW^{3-} with PNIPAM10000 on the mesoscale. The accessible q-range in SAXS (SANS) was 0.1 - 10 nm^{-1} (0.05 - 3 nm^{-1}) which enables to detect scattering objects with a size of 0.6 - 60 nm (2 - 120 nm). Combined SAXS/SANS scattering experiments highlight the adsorption of PW^{3-} on PNIPAM polymers with both contrasts: SAXS highlights the adsorption of PW^{3-} on PNIPAM from the "PW^{3-} point of view" due to its high electron density and provides information on the self-assembly of PW^{3-}. SANS highlights the adsorption of PW^{3-} on PNIPAM from the "PNIPAM point of view". As the neutron scattering length density (SLD) of PW^{3-} is very close to D_2O (and as PW^{3-} provides a low constant scattering over the whole q-range in SANS) SANS experiments yield information on the aggregation of PNIPAM polymers.
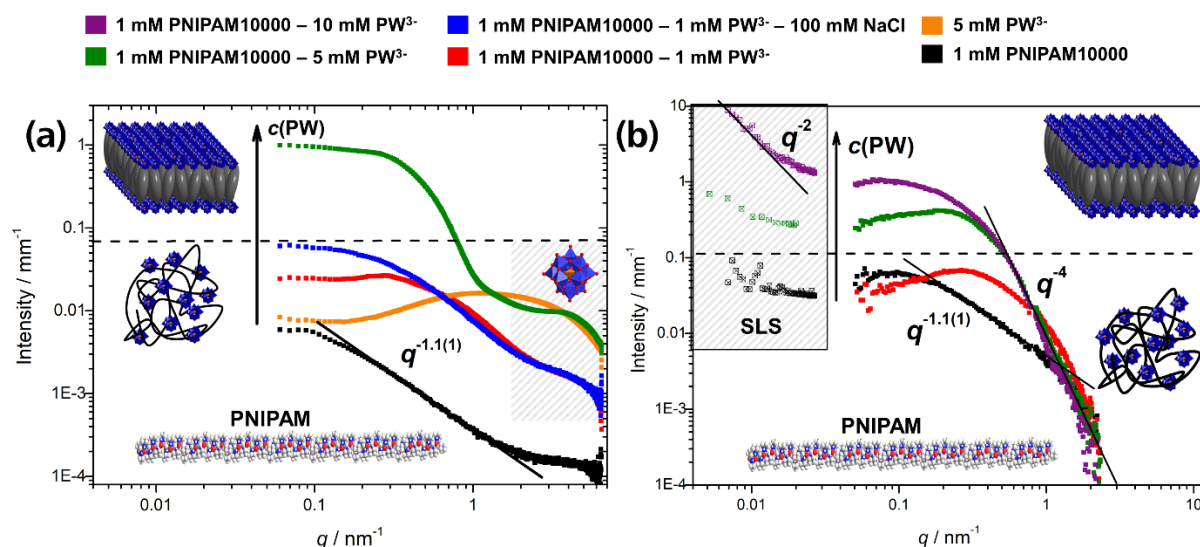
Figure 6.2: (a) SAXS spectra of 1 mM PNIPAM10000, 5 mM PW^{3-} and mixtures of 1 mM PNIPAM with PW^{3-}. (b) SANS spectra of 1 mM PNIPAM10000 in the presence of different concentrations of PW^{3-}. The inset shows the SLS spectra. Note the q^{-2} dependency for $q < 0.02$ nm^{-1} of 1 mM PNIPAM10000 - 10 mM PW^{3-}.

SAXS, see Figure 6.2. The absolute scattered intensity of PINPAM10000 in SAXS is very low due to its low SLD difference to H$_2$O. 1 mM PNIPAM10000 provides a $q^{-1.1(1)}$ decay of the scattered intensity in the q-range of 0.2 - 1 nm^{-1}. 5 mM PW^{3-} in H$_2$O provides a scattering signature for spherical scattering objects with a radius of 0.45 nm, *i.e.* the hard sphere radius of PW^{3-}.[18] The depression of the scattered intensity for 5 mM PW^{3-} for $q < 0.8$ nm^{-1} accounts for the electrostatic repulsion between the PW^{3-} anions. SAXS spectra of mixtures of PNIPAM10000 - PW^{3-} show excess scattering compared to their individual components within the q-range of 0.06 - 2 nm^{-1}, implying the aggregation of PW^{3-} in the presence of PNIPAM10000 polymers. The decrease of the excess scattered intensity of 1 mM PNIPAM10000 - 1 mM PW^{3-} for $q < 0.2$ nm^{-1} implies repulsion between the scattering objects. This repulsion is electrostatic in nature as this electrostatic repulsion can be screened upon the addition of 100 mM NaCl indicated by an increase of the scattered intensity of 1 mM PNIPAM10000 - 1 mM PW^{3-} - 100 mM NaCl for $q < 0.7$ nm^{-1}. The mixture PNIPAM10000 - 5 mM PW^{3-} provides large excess scattering for $q < 1$ nm^{-1} compared to a solution containing only 5 mM PW^{3-}.

SANS and SLS, see Figure 6.2. The scattering signature of 1 mM PNIPAM10000 in D$_2$O is very similar to its scattering signature observed in SAXS following a $q^{-1.1(1)}$ decay for $0.2 < q < 1$ nm^{-1}. Note that the scattering intensity decays with $q^{-1.0}$ when the scattered intensity of D$_2$O is not subtracted. The addition of 1 mM PW^{3-} to 1 mM PNIPAM10000 does not lead to an increase of the overall scattered intensity, but to an increase of the scattered intensity for $0.2 < q < 2$ nm^{-1} and to a decrease in the scattered intensity for $q < 0.2$ nm^{-1} indicating repulsion between uncharged PNIPAM10000 polymers and a conformational change of the PNIPAM10000 polymers from a rather

extended conformation to a rather globular conformation. The addition of 5 mM PW^{3-} to 1 mM PNIPAM10000 leads to an increase of the overall scattered intensity, again with repulsive interactions between the scattering objects as indicated by the depression of the scattered intensity for q < 0.3 nm^{-1}. A mixture of 1 mM PNIPAM10000 - 10 mM PW^{3-} provides excess scattering compared to their individual spectra within the q-range of 0.05 - 2 nm^{-1}. For q > 1 nm^{-1} a q^{-4} dependency of the scattered intensity is observed indicating a sharp interface between the scattering object and the surrounding medium. A SLS measurement on a mixture of PNIPAM10000 - 10 mM PW^{3-} provides a scattering signature following a q^{-2} dependency in the very low q-range implying the presence of planar 2D objects such as sheets, see inset of **Figure 6.2**. Note that samples containing 1 mM PNIPAM10000 - 0/1/5 mM PW^{3-} provide an almost constant (low) scattering signal in SLS.
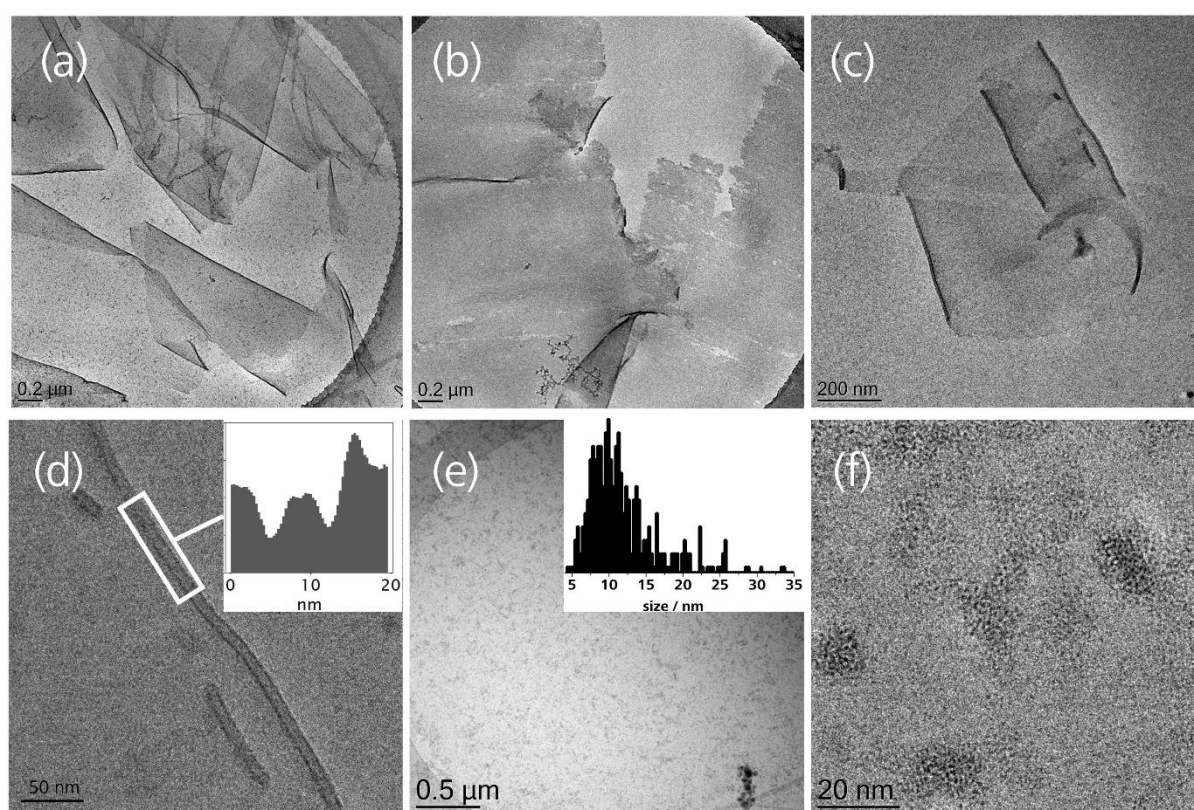
Figure 6.3: Cryo-TEM micrographs of mixtures containing 1 mM PNIPAM10000 and various concentrations of PW^{3-}: (a) PNIPAM10000/PW^{3-} sheets formed by a mixture of 1 mM PNIPAM10000 - 5 mM PW^{3-}; (b) disrupted sheet formed by a mixture of 1 mM PNIPAM10000 - 5 mM PW^{3-}; (c) wrapped sheet formed by a mixture of 1 mM PNIPAM10000 - 5 mM PW^{3-}; (d) inset of wrapped sheet depicted in (c), the electron density excess (width = 1.5 nm) at the edges of the sheet is clearly discernible, see inset which depicts the pixel grey-scale integration averaged over the complete white rectangle; (e) PNIPAM10000/PW^{3-} globules formed in the presence of 5 mM PW^{3-} and 100 mM NaCl with a maximum of the size distribution around 10 nm; (f) inset of PNIPAM/PW^{3-} globules depicted in (e), the dark black dots have an average size of 1 nm and correspond to a single PW^{3-} cluster. The dark edges in the corners of the micrographs (a), (b) and (e) correspond to the cryo-TEM-grid.

Cryo-TEM. Cryo-TEM micrographs were recorded to gain further information on the supramolecular assemblies formed by mixtures of PNIPAM/PW^{3-}. The contrast of objects only formed by PNIPAM against water would be very weak due to its low electron density. The contrast of domains which are rich in PW^{3-}, however, provide a strong electronic contrast due to the high electron density of PW^{3-}. No objects with a significant electronic contrast against water were detected for samples containing either only PW^{3-} (for 5 mM PW^{3-}) or PNIPAM (for 1 mM PNIPAM10000). For mixtures of PW^{3-} and PNIPAM with c(PW^{3-}) < 1 mM, no objects with a significant contrast could be detected. Micrographs reveal the presence of extended sheets for a mixture containing 1 mM PNIPAM10000 and 5 mM PW^{3-}, **Figure 6.3(a)**. These nano-sheets are labile as also disrupted nano-sheets can be observed, see **Figure 6.3(b)**. It should be noted that the rupture of the nano-sheets might be deduced to the harsh conditions during the preparation of the samples for cryo-TEM, see Experimental section. **Figure 6.3(b)** also suggests that the nano-sheets consist of distinct sub-units. **Figure 6.3(c)** depicts a doubly involuted nano-sheet with large lateral dimensions (> µm). **Figure 6.3(d)** – an inset of the upper right part of **Figure 6.3(c)** – reveals that the thickness of the sheets is homogeneous (12 nm). An averaged integration of the pixels (integration over the entire length of the white rectangle from left to right) in **Figure 6.3(d)**) yields an electron density profile with a schematic structure **IOI** (**I** = high electron density and **O** = low electron density). The width of **I** is 1-2 nm and the width of **O** is approximately 5-7 nm. Remember that the diameter of PW^{3-} is approximately 1 nm. Cryo-TEM micrographs of a solution containing 1 mM PNIPAM10000 - 5 mM PW^{3-} - 100 mM NaCl, depict many small, globular domains, see **Figure 6.3(e)**. The size distribution of these globular objects has a maximum at 10 nm, see **Figure 6.3(e)** and **Figure 6.3(f)**. These globular objects are stubbed by small black dots with a high electron contrast with an average diameter of 1 nm, *i.e.* PW^{3-}, see **Figure 6.3(f)**.

Temperature dependence of the LCST. As PNIPAM is most famous for its thermo-responsive behaviour, the LCST of PNIPAM is plotted as a function of the PW^{3-} concentration, see **Figure 6.4(a)**. The addition of PW^{3-} to a solution containing 1 mM PNIPAM10000 leads first to a strong increase of the LCST for c(PW^{3-}) < 2 mM, until it reaches a plateau and then decreases again for c(PW^{3-}) > 3.5 mM. It should be mentioned that the determination of the LCST by visual inspection is not straightforward as the LCST of PNIPAM does not occur at a definite point in the presence of PW^{3-} and is not concomitant with a clear liquid-liquid phase transition (as in the absence of any additives) but rather "smears" over a large temperature range. In case of samples with a blueish appearance, see **Figure 6.4(a)** insets, the CP is not clearly defined and an advanced turbidity was considered as the LCST. Note that the LCST maximum of PNIPAM10000 at c(PW^{3-}) = 2 mM coincides with the onset of the large excess scattering in SAXS and SANS. Cryo-TEM micrographs were also recorded for a solution containing 1 mM PNIPAM10000 - 5 mM PW^{3-} that was prepared at 50 °C (100 %

humidity) and frozen in liquid ethane instantaneously. The micrographs depict long (> μm), worm like objects reminiscent of "involuted sheets" with approximately 30 nm diameter see **Figure 6.4(b)**. The picture of involuted sheets is further supported by the fact that parts of these worm like objects are not completely involuted and similar to sheets as found for samples containing 1 mM PNIPAM10000 - 5 mM PW^{3-} prepared at 25 °C. Note that the contrast of these involuted sheets is relatively high suggesting a high electron density, *i.e.* PW^{3-}, in these involuted sheets.
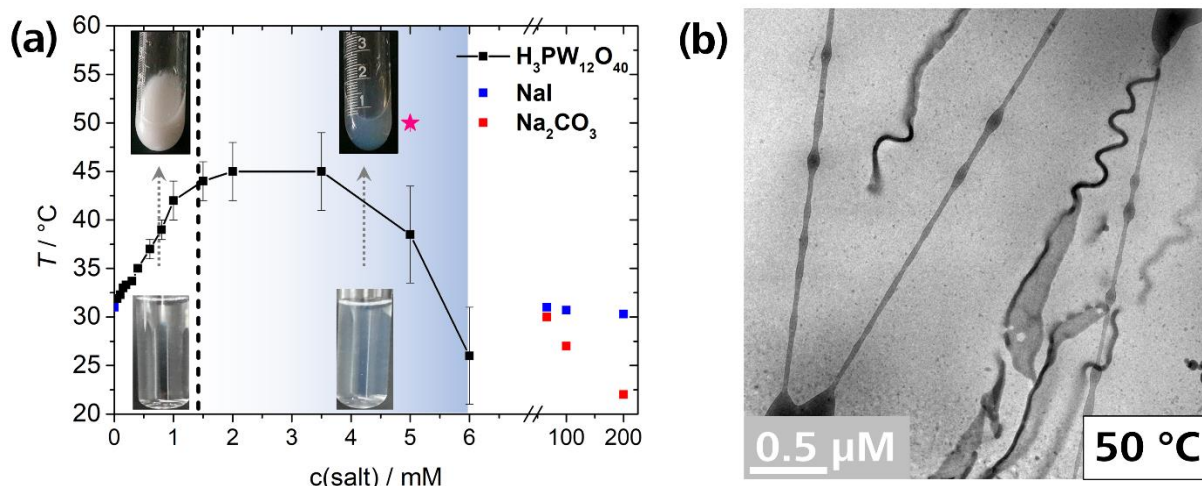
Figure 6.4: (a) LCST of PNIPAM10000 plotted as a function of PW^{3-} from 0 to 6 mM and as a function of c(NaI) and c(Na$_2$CO$_3$). Error bars represent the error of the LCST by detection with visual inspection. The insets depict the LCST transitions from a solution containing 1 mM PNIPAM10000 - 1 mM PW^{3-} and from a blueish solution containing 1 mM PNIPAM10000 - 5 mM PW^{3-}, respectively. The blueish shaded region in the graph indicates that solutions containing 1 mM PNIPAM10000 - x mM PW^{3-} (3 < x < 6) become more and more blueish. (b) Cryo-TEM micrograph of a solution containing 1 mM PNIPAM10000 - 5 mM PW^{3-} prepared at 50 °C, see pink star in (a). The light grey stripes correspond to the TEM-sample grid and the worm-like involuted sheets stem from PNIPAM/PW^{3-} assemblies.

Furthermore, DSC thermograms were recorded. In contrast to all measurements above, 2 mM PNIPAM10000 instead of 1 mM PNIPAM10000 were necessary for DSC measurements to ensure a sufficiently large signal to noise ratio. **Figure S 6-2** depicts the effect of PW^{3-} on a 2 mM PNIPAM10000 solution. Two major features are observed: *(i)* a shift of the exothermic peak to higher temperatures confirming a significantly elevated LSCT and *(ii)* the exothermic peak becomes smaller and broader.

Non-specific interactions. IR measurements were performed for PNIPAM2000 and PNIPAM10000 and their mixtures with PW^{3-}. These measurements did not provide further hints on specific interactions between PW^{3-} and PNIPAM at given (low) concentrations. Remember that no specific interactions were previously observed between PW^{3-} and non-ionic micelles or in the formation of POM-cyclodextrin host-guest complexes.[22,23,28] Furthermore, ^{1}H-NMR experiments on PNIPAM10000 and

their mixtures did not yield any further information on specific interactions between the PNIPAM polymer and PW^{3-}, see **Figure S 6-3**.

The variation of the PNIPAM chain length. The addition of small quantities of POMs, PW^{3-} (typically $c(PW^{3-}) <$ 7-10 mM) to solutions containing 1 mM PNIPAMx000 (x = 2, 5, 7, 10), yields transparent colourless solutions. The addition of higher concentrations of PW^{3-}/PMo^{3-} (typically $c(PW^{3-}) >$ 5-10 mM) to aqueous solutions of 1 mM PNIPAMx000 (x = 2, 5, 7, 10) yields blueish solutions and after a while the solutions undergo a liquid-liquid phase separation, see **Figure S 6-1**, (1 min − 1 day, the higher the PW^{3-} concentration the faster the separation).

To further explore the *(i)* strong interaction between PNIPAM and PW^{3-} and the *(ii)* internal structure of the supramolecular assemblies, SAXS measurements were performed and cryo-TEM micrographs were recorded for solutions containing 1 mM PNIPAMx000 (x = 2, 5, 7) in presence of PW^{3-} (0 < $c(PW^{3-}) <$ 10 mM). SAXS scattering patterns of solutions containing PNIPAMx000 (x = 5, 7) and PW^{3-} are very similar to the scattering patterns of solutions containing 1 mM PNIPAM10000 and PW^{3-}, see **Figure S 6-4**, **Figure S 6-5** and **Figure S 6-6**: for $c(PW^{3-}) <$ 2-3 mM large excess scattering of PNIPAM-PW^{3-} mixtures is observed compared to their individual components within the q-range of 0.06 - 2 nm^{-1}, implying also the aggregation of PW^{3-} on PNIPAMx000 (x = 5, 7) polymers. The decrease of the excess scattered intensity of 1 mM PNIPAMx000 (x = 5, 7) - 1 mM PW^{3-} for $q <$ 0.2 nm^{-1} indicates electrostatic repulsion between the scattering objects that can be screened upon the addition of 100 mM NaCl (indicated by an increase of the scattered intensity of 1 mM PNIPAMx000 (x = 5, 7) - 1 mM PW^{3-} - 100 mM NaCl for $q <$ 0.7 nm^{-1}). The large excess scattering for $q <$ 1 nm^{-1} in case of mixtures containing 1 mM PNIPAMx000 (x = 5, 7) and $c(PW^{3-}) >$ 2-3 mM indicates the presence of large objects. Indeed, cryo-TEM micrographs reveal again the presence of sheets for $c(PW^{3-}) >$ 5 mM. The **IOI** sheet structure of PNIPAMx000 (x = 5, 7) sheets is less prominent compared to PNIPAM10000-PW^{3-} sheets but can nevertheless be seen: the thickness of **I** is again 1-2 nm, whereas the thickness of **O** is 2.5-3 nm, see **Figure 6.5**. Sheets formed by PNIPAM7000 − 5 mM PW^{3-} are 5-7 nm thick but the separate thickness of **I** and **O** could not be determined unambiguously although a clear electron density excess is present at the edges of the sheets, see **Figure 6.5**. Note that the rupture of the sheets in some cases may be deduced to the harsh conditions during the freezing procedure of the cryo-TEM samples. In case of PNIPAM2000, the situation is somewhat different: the scattering spectra of PNIPAM2000 and PW^{3-} also show the same large excess scattering of PNIPAM-PW^{3-} mixtures ($c(PW^{3-}) >$ 2.4 mM) compared to their individual components within the q-range of 0.06-2 nm^{-1}, implying also the aggregation of PW^{3-} on PNIPAM2000, see **Figure S 6-4**. But Cryo-TEM micrographs reveal the presence of globular objects with a diameter from 6 − 30 nm with a maximum of the particle diameter around 10 nm. These globular objects are studded with black dots with an average diameter of 1 nm, *i.e.* the PW^{3-}, see **Figure S 6-7**.
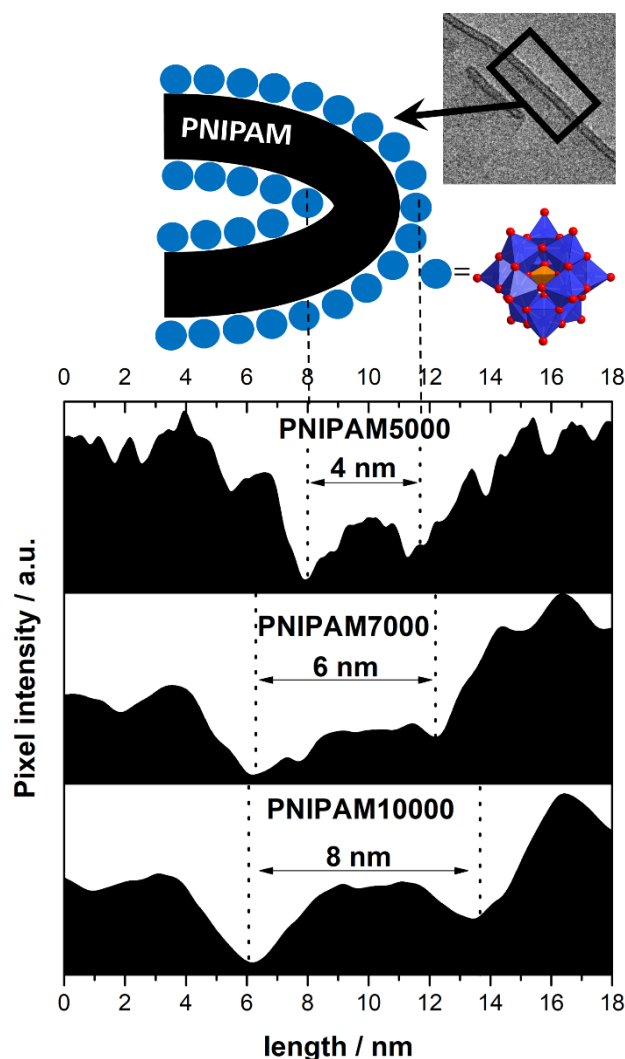
Figure 6.5: Electron density profiles of averaged integrations of involuted PW^{3-}-PNIPAMx000-PW^{3-} sheets (x = 5, 7, 10).

The variation of the POM. The impact of the POM nature, *i.e.* the POM polarizability ($H_3PW_{12}O_{40}$ *vs.* $H_3PMo_{12}O_{40}$) and the POM charge ($H_3PW_{12}O_{40}$ vs. $H_4SiW_{12}O_{40}$) was also investigated by SAXS and cryo-TEM. SAXS spectra of PNIPAM10000 - PMo^{3-} mixtures are very similar to those of PNIPAM10000 - PW^{3-} except of the lower scattered intensity due to the lower SLD of PMo^{3-} compared to PW^{3-}, see **Figure S 6-8**. Cryo-TEM also shows the formation of PMo^{3-}/PNIPAM10000/PMo^{3-} sheets. The scattering spectra of PNIPAM10000 - SiW^{4-}, however, are different: for $c(SiW^{4-}) < 3$ mM excess scattering for 1 $nm^{-1} < q < 3$ nm^{-1} is observed compared to their individual components, see **Figure S 6-9**. The decrease of the scattered intensity for $q < 1$ nm^{-1} indicates strong repulsion between the scattering objects. In contrast to the scattering spectra of PNIPAM10000 - PW^{3-} where a strong increase of the scattered intensity is observed for $c(PW^{3-}) > 3$ mM this excess scattering is not observed for PNIPAM10000 - SiW^{4-} mixtures. Furthermore, SLS measurements do not indicate the presence of large objects for $c(SiW^{4-}) < 10$ mM.

Discussion

The SAXS and SANS scattering patterns of 1 mM PNIPAM10000 (a $q^{-1.1(1)}$ decay in the q-range of 0.2 - 2 nm^{-1} with a stable I($q \to 0$) around 0.2 nm^{-1}) suggest that PNIPAM is in an extended conformation (similar to a rod). This is in agreement with MD simulations performed by Du $et\ al.$, who showed that PNIPAM is present in an extended conformation in an aqueous environment below its LCST.[6] It is further supported by the fact that the length of a fully extended PNIPAM10000 polymer with 88 repeating units is around 25 nm which is in the same order of magnitude as the stable I($q \to 0$) for $q <$ 0.2 nm^{-1}. The forward scattered intensity of 1 mM PNIPAM10000 in SANS for I($q \to 0$) is evaluated by assuming the scattering of isotopically distributed objects as:

Equation (1): $$I(q \to 0) = nV^2(\Delta\rho)^2$$

with n being the concentration of the scattering objects, V their Volume, and $\Delta\rho$ the scattering length density difference between D_2O and the scattering objects. **Equation (1)** can be expanded with

Equation (2): $$I(q \to 0) = c(\text{PNIPAM1000}) \cdot N_{agg} \cdot V^2_{\text{PNIPAM10000}} \cdot (\rho_{D2O} - \rho_{\text{PNIPAM10000}})^2$$

where c(PNIPAM10000) is the PNIPAM10000 number concentration, N_{agg} the aggregation number of PNIPAM10000 polymers, $V^2_{\text{PNIPAM10000}}$ the molecular volume of PNIPAM10000 and ρ the scattering length densities of D_2O and PNIPAM10000. The N_{agg} value of 1 mM PNIPAM in D_2O obtained by this calculation is 1.4 and corresponds to an averaged aggregation number with an error estimated to be at least 0.5. Only averaged N_{agg} values can be estimated as the PNIPAM polymer can be present as a mixture of non-aggregated and aggregated oligomers. Hence, at 1 mM, PNIPAM10000 is present in a mostly monomeric non-aggregated configuration. The large excess scattering in SAXS and SANS confirm an interaction between PW^{3-}/PNIPAM10000 concomitant with the formation of supramolecular assemblies which increase with increasing PW^{3-} concentration. In a supramolecular assembly formed by 1 mM PNIPAM10000 - 1 mM PW^{3-} approximately 17 correlated PW^{3-} anions are present in a supramolecular assembly. This is indicated by the increase of the scattered intensity by a factor of 17 in SAXS (the PNIPAM polymer is not supposed to contribute significantly to the scattered intensity), see **Figure S 6-10**. The PW^{3-}-PW^{3-} average distance within the PW^{3-}/PNIPAM assemblies is 1.05 nm indicated by a correlation peak as obtained by dividing the scattering curve of 1 mM PNIPAM10000 – 1 mM PW^{3-} by the spherical formfactor $P(q)$ of PW^{3-}, see **Figure S 6-10**. Hence, PW^{3-} is almost packed densely in globular assemblies formed by 1 mM PNIPAM10000 and 1 mM PW^{3-}. Note at this point that no correlation peak is obtained for supramolecular assemblies

formed by PNIPAM10000 and SiW indicating that a dense packing of SiW on PNIPAM10000 at 1 mM PNIPAM10000 - 1 mM H_4SiW is not possible, see **Figure S 6-10**. Interestingly, the absolute scattered intensity in SANS does not increase for the same sample 1 mM PNIPAM10000 - 1 mM PW^{3-} compared to 1 mM PNIPAM10000 as the absolute scattered intensity is modulated by a structure factor. The strong structure factor of 1 mM PNIPAM10000 - 1 mM PW^{3-} in SANS - indicated by a decrease in the low q ($q < 0.3nm^{-1}$) - implies repulsive interactions between the scattering objects. This may be deduced to PNIPAM10000 polymers which become charged negatively upon adsorption of PW^{3-} anions. The inter-assembly structure factor was obtained by dividing the SAXS scattering curve of 1 mM PNIPAM10000 - 1 mM PW^{3-} - 100 mM NaCl by the SAXS scattering curve of 1 mM PNIPAM10000 - 1 mM PW^{3-}. The inter-assembly structure factor was then applied to the SANS scattering curve of 1 mM PNIPAM10000 - 1 mM PW^{3-} to yield a SANS scattering curve which is corrected by the inter-assembly S(q). The I($q{\rightarrow}0$) analysis of such a curve leads to an averaged aggregation number of PNIPAM10000 of 3.

In a rough estimation, the scattering signatures of 1 mM PNIPAM10000 – 1 mM PW^{3-} in SANS and 1 mM PNIPAM10000 - 1 mM PW^{3-} - 100 mM NaCl are reminiscent of the scattering signatures of a spherical scattering object with a radius of approximately 5-7 nm as obtained by a Guinier fit, see **Figure S 6-11**. Considering the molecular volume of three PNIPAM10000 molecules ($V_m = 3 \cdot 1.5x10^{-26}$ m³), a spherical dense packing of three PNIPAM10000 polymers with approximately 17 PW^{3-} at 1 mM PNIPAM10000 - 1 mM PW^{3-} leads to a sphere with a radius of 1.5 nm. At a first glance, this may be contradictory to the spherical radius of PNIPAM10000 obtained from SANS measurements (6-7 nm), but PNIPAM10000 is well known to be highly hydrated and each PNIPAM10000 polymer is considered to contain $\sim$ 70–80% of water inside its hydrodynamic volume.[29] Taking into account the volume of hydration water, the radius of PNIPAM/PW^{3-} globules is 5 nm. The only conclusion drawn from this rough approximation is that PNIPAM10000 undergoes a conformational change from a rod-like extended conformation to a globule like dense conformation upon the addition of PW^{3-}. Combining the considerations from SAXS and SANS measurements we conclude that in a sample containing 1 mM PNIPAM10000 - 1 mM PW^{3-} PNIPAM/PW^{3-} globules with a radius of 5 nm are present, see **Figure 6.6**.
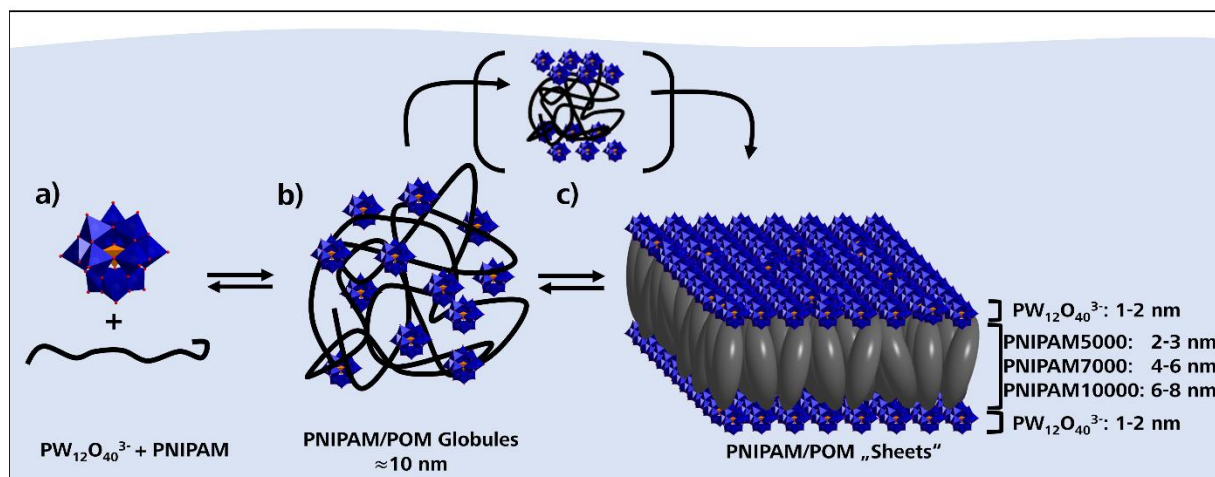
Figure 6.6: Cartoon illustration of the proposed mechanism of forming the PNIPAM/PW^{3-} globules and POM/PNIPAM sheets. PW^{3-}, which is densely packed in the globules, should rearrange to the surface of PNIPAM to be incorporated in the lamellar **IOI** sheet structure.

In contrast to the supramolecular assembly of 1 mM PNIPAM10000 - 1 mM PW^{3-}, where approximately three PNIPAM polymers aggregate, the large excess scattering of 1 mM PNIPAM10000 – 5/10 mM PW^{3-} in SANS indicates that the supramolecular assemblies consist not only of three PNIPAM10000 polymers decorated with several PW^{3-} anions, but more aggregated PNIPAM polymers. For a sample containing 1 mM PNIPAM10000 – 10 mM PW^{3-}, an average aggregation number of 25 aggregated PNIPAM polymers is found. Note that these are only averaged aggregation numbers where both, unaggregated as well as aggregated PNIPAM polymers contribute to the scattering signal. The PW^{3-}-PW^{3-} average distance within the PW^{3-}/PNIPAM assemblies formed in a solution containing 1 mM PNIPAM10000 – 5 mM PW^{3-} is 1.00 – 1.03 nm indicated by a correlation peak as obtained by dividing the scattering curve of 1 mM PNIPAM10000 – 1 mM PW^{3-} by the formfactor *P(q)* of PW^{3-}, see **Figure S 6-12**. Hence, PW^{3-} is also packed densely in the 2D layer of the sheets formed by 1 mM PNIPAM10000 and 5 mM PW^{3-}. Both samples, 1 mM PNIPAM10000 – 5/10 mM PW^{3-}, show a q^{-4} decay of the scattered intensity in the Porod region for $q > 0.6$ nm^{-1} corresponding to a sharp interface between the scattering object and the surrounding medium.

This nanoscopic phase separation of PNIPAM10000 and water is also consistent with the objects detected on the cryo-TEM micrographs: self-assembled PNIPAM10000 molecules are stabilized in a 2D sheet by a monolayer of PW^{3-} at the H$_2$O/PNIPAM10000 interface (PW^{3-}/PNIPAM10000/PW^{3-}) as indicated by a large electron density excess at the edges of the sheets, see **Figure 6.6**. Analogous to PW^{3-}/PNIPAM10000/ PW^{3-} sheets with an unambiguous **IOI** structure, PW^{3-}/PNIPAM7000/PW^{3-} and PW^{3-}/PNIPAM5000/PW^{3-} sheets also clearly show an electron density excess at both sides of the sheets. Interestingly, the width of **I** is again 1-2 nm, *i.e.* the thickness of a layer composed by disordered PW^{3-}, and the thickness of **O** is 2-3 nm in case of PNIPAM5000 nano-sheets, *i.e.* twice the thickness of PNIPAM10000 nano-sheets thereby further supporting the **IOI** structure model, see

Figure 6.5. The addition of NaCl to PW^{3-}/PNIPAM/PW^{3-} nano-sheets leads to a screening of repulsive interactions between PW^{3-} anions.[30] It is assumed that lateral repulsions of PW^{3-} anions at the PNIPAM-H_2O interface should lead to a stabilization of the symmetrical **IOI** arrangement. This screening effect destabilizes the sheets finally resulting in a blast of the sheets to discrete nanometer-sized objects containing PNIPAM10000 and PW^{3-}. Indeed, a dense packing of PW^{3-} anions at an interface is well known, *e.g.* at a H_2O-Ether interface before the famous etherate formation (not published so far). Furthermore, close packed layers of PW^{3-} are also found in case of PW^{3-} - EO_6/EO_5 - $3Na^+$ and PW^{3-} - EO_{11} - K^+-H^+-H^+ hybrid crystals in the solid state, see **chapter 4**. Bera *et al.* further pointed out that for $c(PW^{3-}) > 47.7$ mM a mixture of non-associated PW^{3-} monomers and associated randomly percolated PW^{3-} monomers is present in bulk solution.[31] Furthermore, they found that the structure of an aggregated PW^{3-} layer near the H_2O-air interface is reminiscent of the solid-state crystal structure of PW^{3-} in which PW^{3-} anions are connected by Zundel ions.[32] This transition may also be made here between close packed layers of PW^{3-} in PW^{3-} - EO_6/EO_5 - $3Na^+$ and PW^{3-} - EO_{11} - K^+-H^+-H^+ hybrid crystals and in PW^{3-}/PNIPAM/PW^{3-} nano-sheets. Hence, we assume that in *(i)* the globular assemblies and *(ii)* at the surface of the PW^{3-}/PNIPAM/PW^{3-} nano-sheets we may meet the case of Bera *et al.* Interestingly, PNIPAM2000 does not form sheets with PW^{3-} at any concentrations but rather large globular PNIPAM2000/PW^{3-} objects are formed for $c(PW^{3-}) > 2.4$ mM. Apparently, 18 repeating units of PNIPAM2000 are too few to counterbalance the repulsive interactions of the two opposite PW^{3-} layers stabilizing the **IOI** structure model. Note that Bera *et al.* also found out that Zundel ions stabilizing aggregated POMs at an H_2O/air interface and in the solid state of PW^{3-} align parallel to the interface. Hence, POMs on the surface of PNIPAM sheets may be packed densely only in a monolayer and lateral repulsive interactions can be screened by parallelly aligned Zundel ions that may be present at the interfacial PW^{3-} monolayer. But the small thickness of the PNIPAM layer with a low permittivity may be too small to screen the repulsive interactions between the two PW^{3-} layers.

The LCST maximum of PNIPAM10000 at $c(PW^{3-}) = 3$ mM coincides with the onset of the large excess scattering in SAXS and SANS. The adsorption of PW^{3-} on a PNIPAM10000 polymer and the subsequent formation of PW^{3-}/PNIPAM10000 globules leads to an increase of the LCST, *i.e.* an increase of the solubility of PNIPAM. This is reasonable as the PNIPAM polymer becomes charged upon the adsorption of PW^{3-} as it is the case in the adsorption of POMs on the micellar surface of C_8EO_4 micelles.[20] At this point it is worth to mention that the LCST increase of PNIPAM10000 by PW^{3-} is more pronounced than for a classical chaotropic anion, *e.g.* I^-, highlighting again PW^{3-}'s super-chaotropic nature. When PNIPAM is heated in pure water, the phase transition occurs as a sharp transition due to the cooperative collapse of long segments, and eventually the complete PNIPAM polymer.[33] PW^{3-} interferes with the cooperative collapse of the PNIPAM chain: the higher the salt concentration, the less cooperative the collapse process as already proposed by Schild and Tirrell for

the adsorption of SCN⁻ on PNIPAM.[33] This fact also explains the observation made in DSC measurements: a shift of the exothermic peak to higher temperatures which itself becomes gradually smaller and broader. The length of unperturbed PNIPAM10000 segments decreases upon the adsorption of PW^{3-} resulting in a decreasing peak height and an increasing peak width. However, the addition of $c(PW^{3-}) > 3$ mM leads to a significantly decreased LCST of the PNIPAM10000 polymer. It should be stressed at this point that the term LCST is here not unambiguous: the transition of POMs from being salting in (increasing the LCST) to being salting out (decreasing the LCST) is here concomitant with the formation of the **IOI** supramolecular assembly including a nanoscopic phase separation of PNIPAM10000. The latter becomes a macroscopic phase separation/segregation when large sheets (> µm) are present for $c(PW^{3-}) > 7$ mM. It is questionable if the term LCST is even applicable when PNIPAM10000 self-assemble in sheets. The PNIPAM10000 polymer may already be referred to as "salted out", due to the fact that most of the PNIPAM10000 polymers are not solubilized in bulk water for $c(PW^{3-}) > 3$ mM and despite the fact that the solution is macroscopically homogeneous and clear. Nevertheless, upon heating a solution containing PW^{3-}/PNIPAM10000 sheets above its "LCST", the blueish solution becomes milky and more turbid. Cryo-TEM micro-graphs reveal that the sheets wrap up to form worms-like architectures with a significantly decreased volume. This involution and shrinkage process indicates that PNIPAM10000 is still partially hydrated within the sheets – otherwise the temperature increase would not affect the sheet-structure (further dehydration process). The partial hydration of PNIPAM in the PNIPAM/PW^{3-} globules is further confirmed by DSC measurements due to the presence of an exothermic peak observed during the heating cycle that decreases with increasing PW^{3-} concentration. Hence, increasing the temperature leads to a less efficient hydration of PNIPAM polymers within the sheets. Water molecules still partially hydrating the PNIPAM polymers are expelled leading to a macroscopic phase separation. It is worth to remark that PW^{3-} anions can be confined in these worm-like cylindrical structure. Interestingly, Cremer *et al.* also found a two-step phase transition of PNIPAM beyond a certain concentration of kosmotrope, *e.g.* for $c(Na_2SO_4) > 130$ mM: the lower-temperature phase transition corresponds to the dehydration of the amide group through a polarization effect of the anions and the higher-temperature phase transition corresponds to the removal of the weakly bound hydration waters from the back-bone and isopropyl side chain during polymer folding. The adsorption of super-chaotropic POMs on PNIPAM may also lead to a two-step dehydration process of PNIPAM: *(i)* a first partial dehydration of PNIPAM upon the adsorption of POMs and *(ii)* a second full dehydration upon heating above PNIPAM's LCST. The LCST maxima of PNIPAM*x*000 (*x* = 2, 5, 7, 10) as a function of PW^{3-} behave similar to the LCST maximum of PNIPAM10000 as a function of PW^{3-} and are plotted in **Figure S 6-13**. Note, that no direct relation between number of repeating units of PNIPAM to the number of PW^{3-} and its impact on the LCST of PNIPAM could be found, see **Table S 6.1**.

6.5 Conclusion

Common polyoxometalates, $H_3PW_{12}O_{40}$, $H_3PMo_{12}O_{40}$ and $H_4SiW_{12}O_{40}$ interact strongly with short chain PNIPAM polymers (PNIPAMx000, with x = 2, 5, 7, 10) with strong consequences for its thermo-responsive behaviour. The reason for an adsorption of anionic POMs on uncharged PNIPAM is the result of a subtle balance between partial dehydration of both the PNIPAM oligomer and highly polarizable POM anions and an associated gain of entropy. The adsorption of PW^{3-} on PNIPAM leads first to the formation POM-PNIPAM globular objects and eventually to the formation of stimuli responsive (salt and temperature stimulus) PW^{3-}/PNIPAM/PW^{3-} and PMo^{3-}/PNIPAM/PMo^{3-} nano-sheets via self-assembly of PNIPAMx000 (x = 5, 7, 10). Threefold negatively charged POM anions (PW^{3-} and PMo^{3-}) accumulate at the PNIPAM/H_2O interface as *(i)* the anion charge cannot be fully confined within an aliphatic surrounding and *(ii)* POMs partially remain hydrated. These 2D nanocomposite sheets are not chemically linked by physically linked and their thickness can be tuned by the PNIPAM chain length. The driving force for the nanoscopic phase separation of PNIPAM is considered to be the result of a change in the hydration state of PNIPAM due to the partial dehydration during the adsorption process of PW^{3-}. Note that in case of the interaction of PW^{3-} with short EO$_x$ oligomers no globular structure but discrete nano-assemblies were formed, see **chapter 4.4**. The formation of PW^{3-}/PNIPAM/PW^{3-} nano-sheets with the 2D dense packing of PW^{3-} may also be compared to the layered arrangement of PW^{3-} in PW^{3-} - EO_6/EO_5 - 3 Na^+ and PW^{3-} - EO_{11} - K^+-H^+-H^+ hybrid crystals in the solid state, see **chapter 4.** Hence, PW^{3-}/PNIPAM/PW^{3-} nano-sheets may be considered as soft materials resulting from POMs' specific effects on hydrated oligomers in aqueous solution and the preferential layered 2D arrangement of PW^{3-} in the solid state.

6.6 Bibliography

[1]   M. Heskins, J. E. Guillet, J. Macromol. *Sci. Part A - Chem.* **1968,** *2,* 1441–1455.

[2]   A. Halperin, M. Kröger, F. M. Winnik, *Angew. Chemie - Int. Ed.* **2015,** *54,* 15342–15367.

[3]   B. Hammouda, D. Jia, H. Cheng, *Open Access J. Sci. Technol.* **2015,** *3,* 1–8.

[4]   Y. Cho, Y. Zhang, T. Christensen, L. B. Sagle, A. Chilkoti, P. S. Cremer, *J. Phys. Chem. B* **2008,** *112*, 13765–13771.

[5]   E. I. Tiktopulo, V. N. Uversky, V. B. Lushchik, S. I. Klenin, V. E. Bychkova, O. B. Ptitsyn, *Macromolecules* **1995**, *28*, 7519–7524.

[6]   H. Du, R. Wickramasinghe, X. Qian, *J. Phys. Chem. B* **2010**, *114*, 16594–16604.

[7]   L. Pérez-Fuentes, C. Drummond, J. Faraudo, D. Bastos-González, *Soft Matter* **2015**, *11*, 5077–5086.

[8]   S. Zajforoushan Moghaddam, E. Thormann, *Langmuir* **2017**, *33*, 4806–4815.

[9]   A. Pica, G. Graziano, *Phys. Chem. Chem. Phys.* **2015**, *17*, 27750–27757.

[10]   Y. Zhang, P. S. Cremer, *Curr. Opin. Chem. Biol.* **2006**, *10*, 658–663.

[11]   S. Furyk, Y. Zhang, D. Ortiz-Acosta, P. S. Cremer, D. E. Bergbreiter, *J. Polym. Sci. Part A Polym. Chem.* **2006**, *44*, 1492–1501.

[12]   Y. Zhang, S. Furyk, L. B. Sagle, Y. Cho, D. E. Bergbreiter, P. S. Cremer, *J. Phys. Chem. C* **2007**, *111*, 8916–8924.

[13]   H. I. Okur, J. Hladílková, K. B. Rembert, Y. Cho, J. Heyda, J. Dzubiella, P. S. Cremer, P. Jungwirth, *J. Phys. Chem. B* **2017**, *121*, 1997–2014.

[14]   J. Heyda, J. Dzubiella, *J. Phys. Chem. B* **2014**, *118*, 10979–10988.

[15]   Y. Zhang, S. Furyk, D. E. Bergbreiter, P. S. Cremer, *J. Am. Chem. Soc.* **2005,** *127*, 14505–14510.

[16]   X. Chen, T. Yang, S. Kataoka, P. S. Cremer, *J. Am. Chem. Soc.* **2007**, *129*, 12272–12279.

[17]   F. Hofmeister, *Arch. Exp. Pathol. Par.* **1888,** *24,* 1-30

[18]   B. Naskar, O. Diat, V. Nardello-Rataj, P. Bauduin, *J. Phys. Chem. C* **2015**, *119*, 20985–20992.

[19]   T. Buchecker, X. LeGoff, B. Naskar, A. Pfitzner, O. Diat, P. Bauduin, *Chem. - A Eur. J.* **2017**, *23*, 8434–8442.

[20]   T. Buchecker, P. Schmid, S. Renaudineau, O. Diat, A. Proust, A. Pfitzner, P. Bauduin, *Chem. Commun.* **2018**, *54*, 1833–1836.

[21]   D. Kobayashi, H. Nakahara, O. Shibata, K. Unoura, H. Nabika, *J. Phys. Chem. C* **2017**, *121*, 12895–12902.

[22]   M. A. Moussawi, M. Haouas, S. Floquet, W. E. Shepard, P. A. Abramov, M. N. Sokolov, V. P. Fedin, S. Cordier, A. Ponchel, E. Monflier, et al., *J. Am. Chem. Soc.* **2017**, *139*, 14376–14379.

[23]   M. A. Moussawi, N. Leclerc-Laronze, S. Floquet, P. A. Abramov, M. N. Sokolov, S. Cordier, A. Ponchel, E. Monflier, H. Bricout, D. Landy, et al., *J. Am. Chem. Soc.* **2017**, *139*, 12793–12803.

[24]   K. I. Assaf, M. S. Ural, F. Pan, T. Georgiev, S. Simova, K. Rissanen, D. Gabel, W. M. Nau, *Angew. Chemie - Int. Ed.* **2015**, *54*, 6852–6856.

[25]   E. Leontidis, M. Christoforou, C. Georgiou, T. Delclos, *Curr. Opin. Colloid Interface Sci.* **2014**, *19,* 2–8.

[26]   P. A. Chetcuti, P. Moser, G. Rihs, *Organometallics* **1991**, *10*, 2895–2897.

[27]   J. Zhou, P. Yin, X. Chen, L. Hu, T. Liu, *Chem. Commun.* **2015**, *51*, 15982–15985.

[28]   B. Naskar, O. Diat, V. Nardello-Rataj, P. Bauduin, *J. Phys. Chem. C* **2015**, *119*, 20985-20992.

[29]   G. Zhang, C. Wu, *Adv. Polym. Sci.* **2006**, *195,* 101–176.

[30]   A. Malinenko, A. Jonchère, L. Girard, S. Parrès-Maynadié, O. Diat, P. Bauduin, *Langmuir* **2018**, *34,* 2026–2038.

[31]   M. K. Bera, B. Qiao, S. Seifert, B. P. Burton-Pye, M. Olvera De La Cruz, M. R. Antonio, *J. Phys. Chem. C* **2016**, *120,* 1317–1327.

[32]   M. K. Bera, M. R. Antonio, *ChemistrySelect* **2016**, *1*, 2107–2112.

[33]   H. G. Schild, D. A. Tirrell, *J. Phys. Chem.* **1990**, *94*, 4352–4356.

6.7   Supporting Information
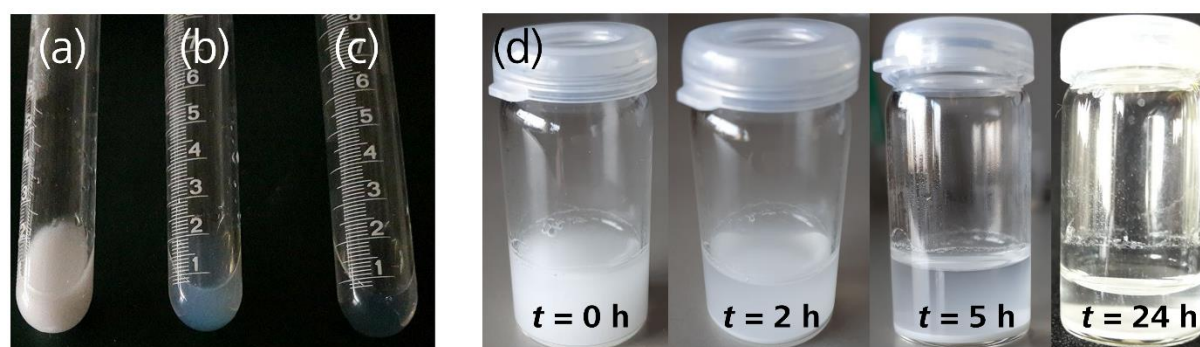
Figure S 6-1: (a) Liquid-liquid phase separation of a solution containing 1 mM PNIPAM10000. The addition of small quantities of PW^{3-} (typically c(PW^{3-}) < 7-10 mM) to solutions containing 1 mM PNIPAMx000 (x = 2, 5, 7, 10), yield transparent solutions, see (c). The addition of higher concentrations of PW^{3-} (typically c(PW^{3-}) > 5-10 mM) to aqueous solutions of 1 mM PNIPAMx000 (x = 2, 5, 7, 10) yields blueish solutions, see (b). (d) After a while, the solutions undergo a liquid-liquid phase separation, see phase separation monitored at a 1 mM PNIPAM10000 – 10 mM PW^{3-} solution directly after mixing - after 2 hours - after 5 hours and after one day.
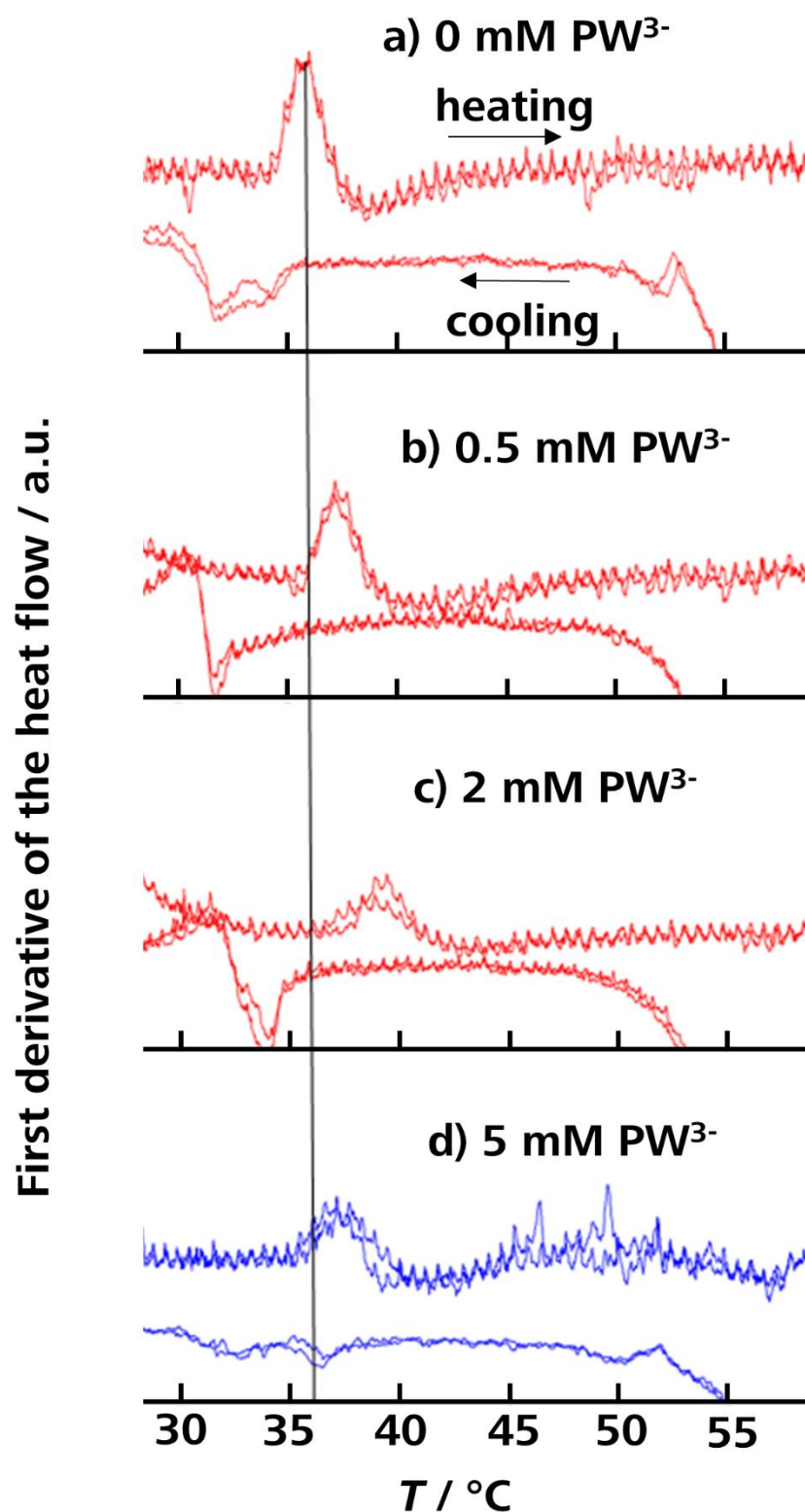
Figure S 6-2: DSC thermograms obtained during heating a) a pure PNIPAM10000 (2 wt%, *i.e.* 2 mM) solution. 2 wt% PNIPAM10000 instead of 1 wt% PNIPAM10000 were necessary for DSC measurements to ensure a sufficiently large signal to noise ratio. (b)-(d) show the effect of PW^{3-} on a PNIPAM10000 (2 wt%) solution. Two major features are observed: *(i)* a shift of the exothermic peak to higher temperatures confirming a significantly elevated LSCT and *(ii)* the exothermic peak becomes smaller and broader.

Measurements were performed on a Perkin Elmer DSC8000 from 20 to 60 °C with a heating rate of 7.5 °C per minute (a screening of the heating rate was performed from 1 °C/min to 10 °C/min and 7.5 °C/min turned out to be best compromise between a distinct exothermic peak and the least offset to the "real" PNIPAM phase transition temperature). Two cycles were recorded to check reproducibility; not the raw data is depicted, but the fist derivative of the heat flow is depicted since the released heat is only subtle. The measurements are normalized to the mass which was in the sample container, so the absolute released heat can be compared. The exothermic peak (corresponding to the liquid-liquid phase separation of PNIPAM and H_2O at around 35 °C) could only be observed for c(PNIPAM10000) $\geq$ 2 mM. In contrast to all measurements shown in the manuscript, 2 mM PNIPAM10000 instead of 1 mM PNIPAM10000 were necessary for DSC measurements to ensure a sufficiently high signal to noise ratio. Solutions contained the following amount of PW^{3-}:

- Solution (a): 2 mM PNIPAM10000 – 0 mM PW^{3-} (homogeneous and transparent at room temperature)
- Solution (b): 2 mM PNIPAM10000 – 0.5 mM PW^{3-} (homogeneous and transparent at room temperature)
- Solution (c): 2 mM PNIPAM10000 – 2 mM PW^{3-} (homogeneous and transparent at room temperature)
- Solution (d): 2 mM PNIPAM10000 – 5 mM PW^{3-} (**not** homogeneous but ***two-phasic*** at room temperature)

Two major features of the DSC peaks upon the addition of PW^{3-} are observed: *(i)* a shift of the exothermic peak to higher temperatures confirming a significantly elevated LSCT and *(ii)* a decrease and broadening of the exothermic peak. The exothermic peak corresponding to the liquid-liquid phase separation of PNIPAM and H_2O is slightly shifted from 33 °C (visual observation) to 36 °C due to the fast heating rate of 7.5 °C/min. Upon addition of PW^{3-}, the exothermic peak is slightly shifted to higher temperatures (40 °C for 2 mM PW^{3-}) and the absolute amount of released heat decreases upon the addition of PW^{3-}.
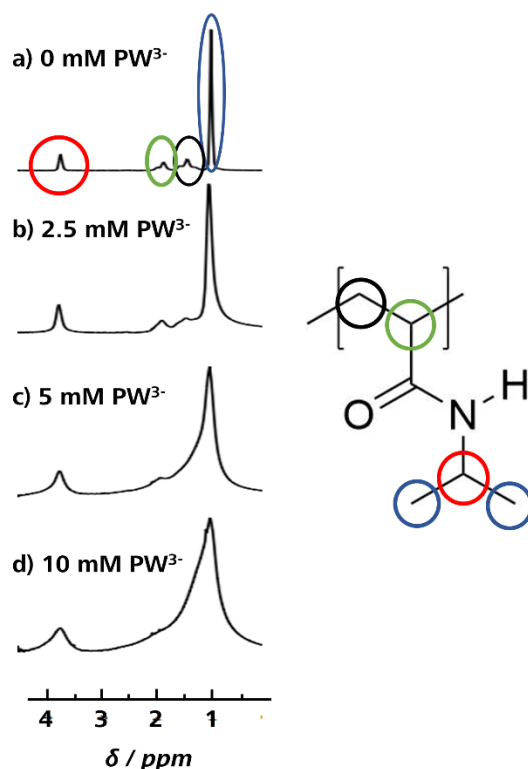
Figure S 6-3: NMR resonance signals of 1 mM PNIPAM10000 in the presence of 0, 2.5, 5, and 10 mM PW^{3-} (from top to bottom and qualitative assignment of the hydrogen atoms of the repeating unit to the resonance signals. Note that the spectra are normalized according to intensity of the most intense peak.

All resonance signals are assigned to hydrogen atoms of the PNIPAM polymer, see **Figure S 6-3**. The proton of the amide group could not be detected. Three major changes of the PNIPAM resonance signals are observed upon the addition of PW^{3-}: *(i)* the overall intensity decreases upon the addition of PW^{3-} (not shown), *(ii)* the half width of all signals becomes broader. Furthermore, *(iii)* the resonance signal of the isopropyl group overlays the resonance signal of the $-CH_2-CH-$ backbone. The decrease of the overall intensity is due to the acidity of the solutions containing PW^{3-}, which is a well-known effect leading to a faster exchange of protons. The increase of the half width of resonance signals is due to (slower molecular motions of the PNIPAM macromolecules due to a more viscous solution or) strong interactions between the PW^{3-} anion and the hydrogen atoms of PNIPAM which makes the relaxation of the magnetic moment more efficient. This leads to shorter relaxation times t_{rel} (Halfwidth $=1/(\pi \cdot t_{rel})$). The line broadening of the isopropyl-signal can be explained by a restricted mobility of the hydrogen atoms.
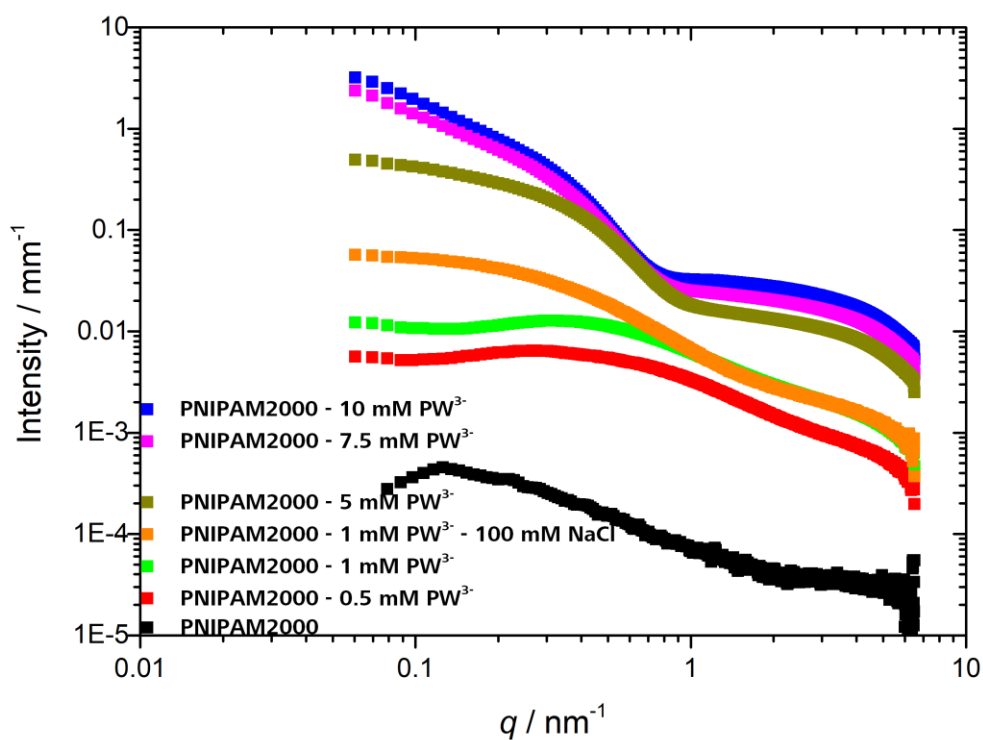
Figure S 6-4: SAXS spectra of mixtures of 1 mM PNIPAM2000 and PW^{3-}.
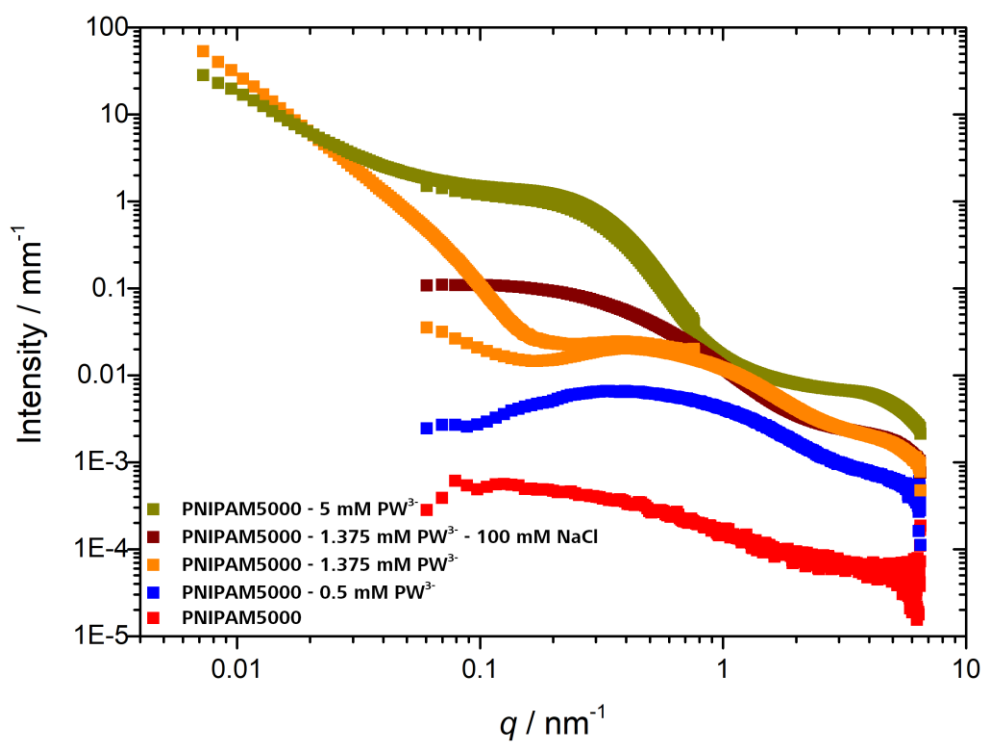
Figure S 6-5: SAXS spectra of mixtures of 1 mM PNIPAM5000 and PW^{3-}.
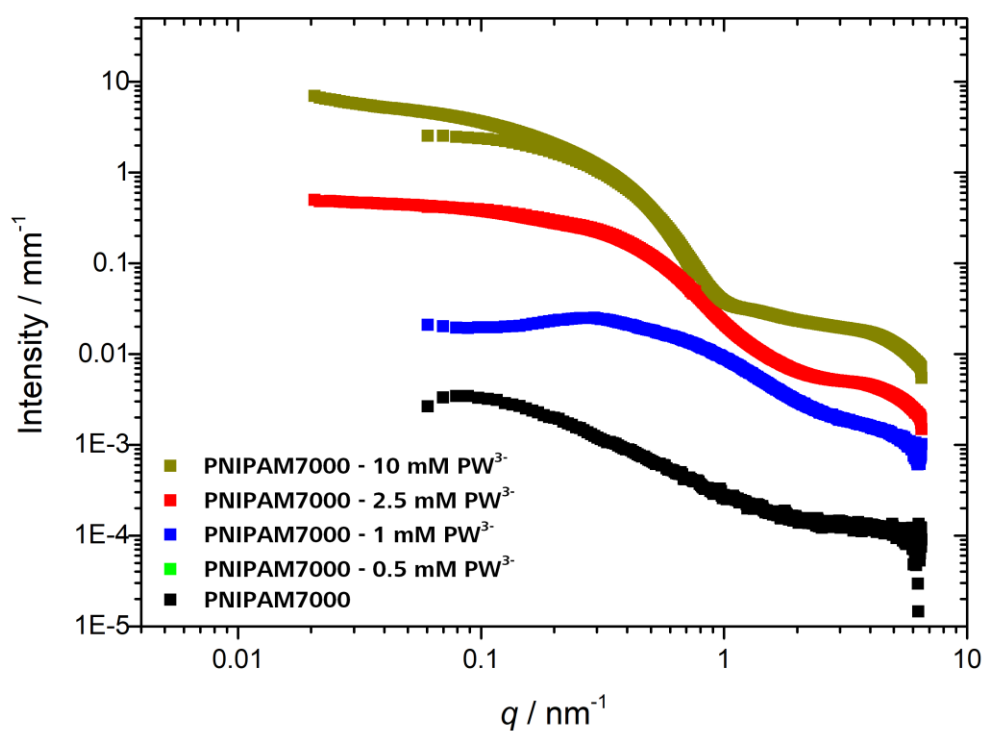
Figure S 6-6: SAXS spectra of mixtures of 1 mM PNIPAM7000 and PW^{3-}.
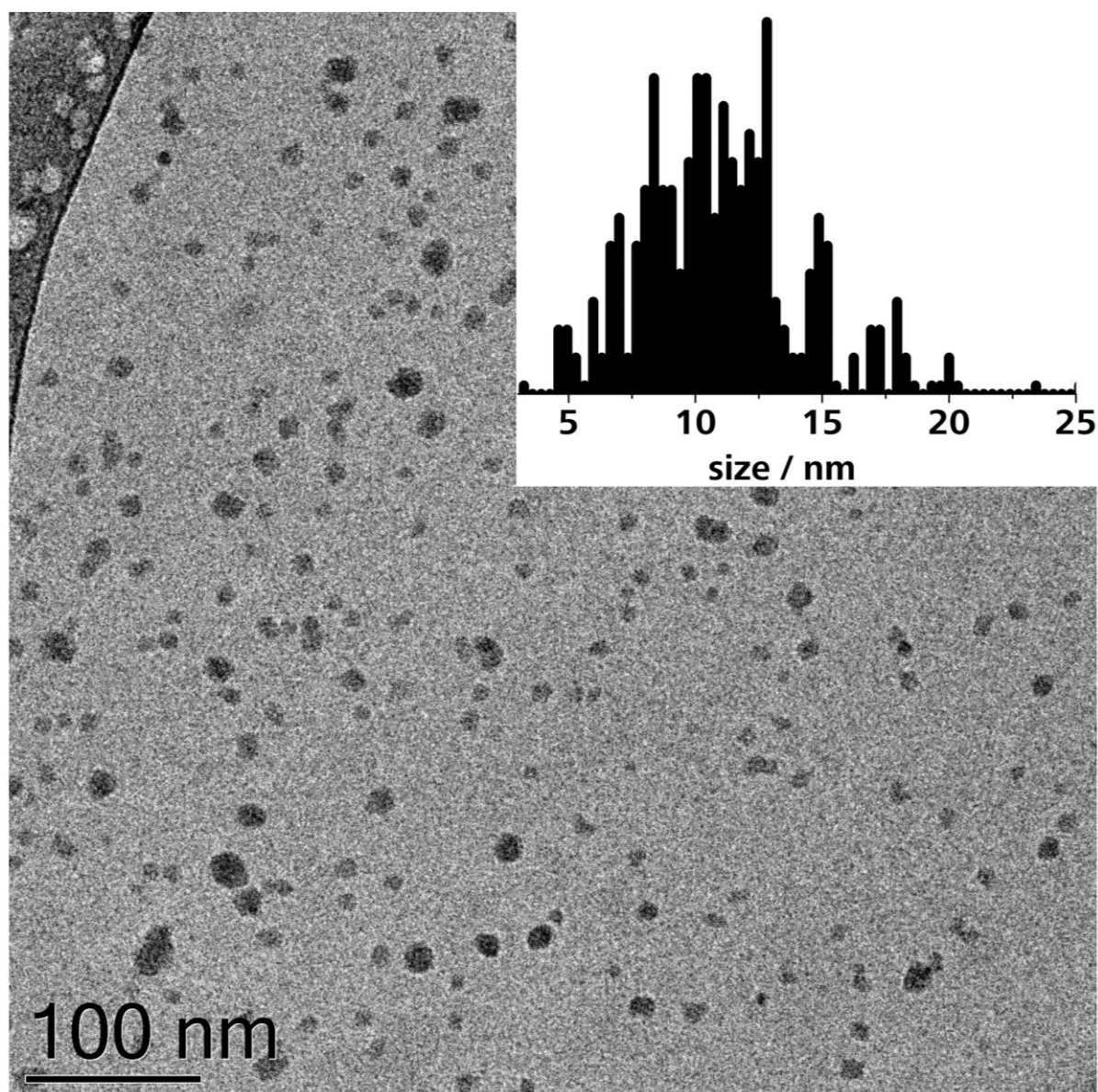
Figure S 6-7: Cryo-TEM micrograph of a mixture of 1 mM PNIPAM2000 and 5 mM PW^{3-}. PW^{3-}/PNIPAM2000 globular objects have a maximum of the size distribution at 10-11 nm. The size of the particles was measured using the ImageJ software (version 1.52d).
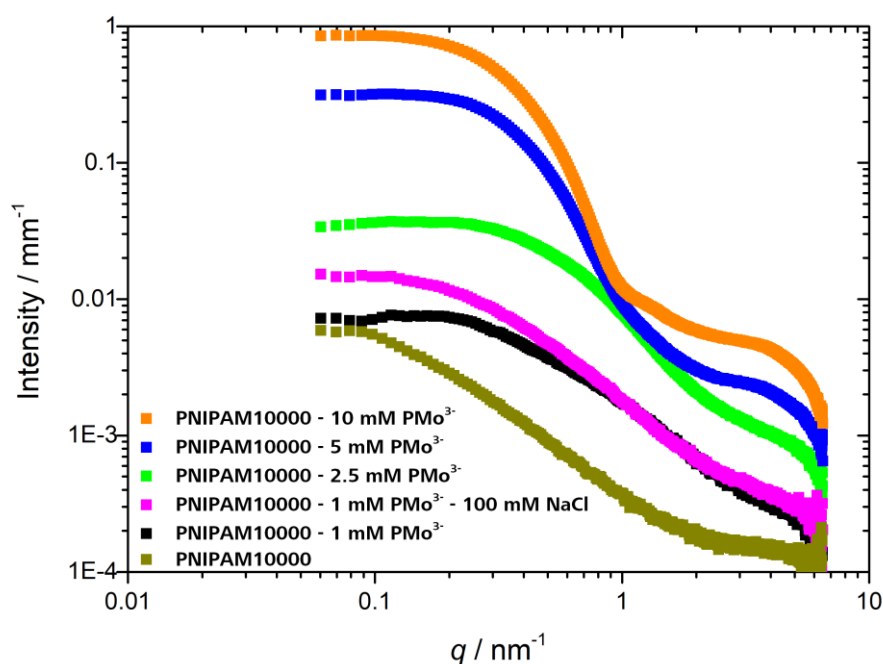
Figure S 6-8: SAXS spectra of 1 mM PNIPAM10000, PMo^{3-} and mixtures of 1 mM PNIPAM10000 with PMo^{3-}.
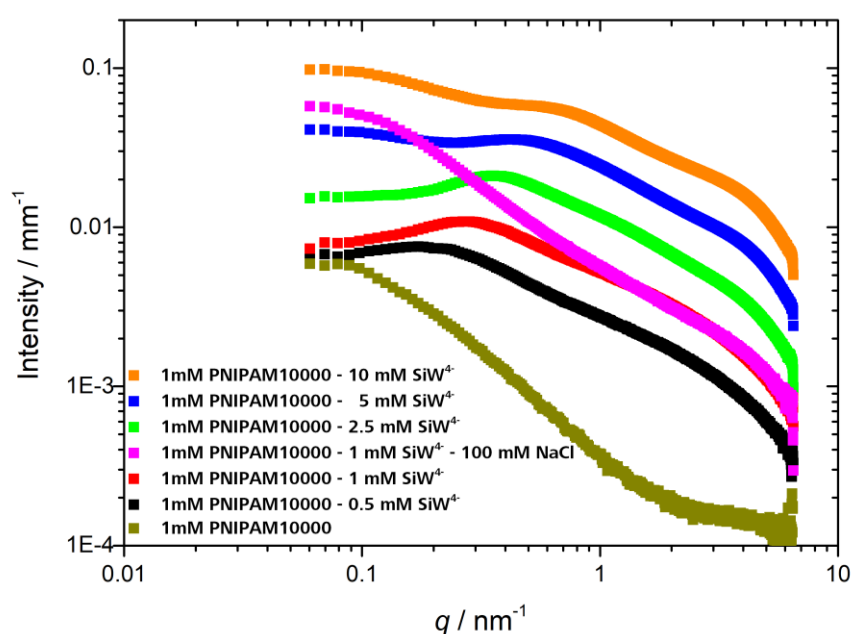
Figure S 6-9: SAXS spectra of mixtures of 1 mM PNIPAM10000, SiW^{4-} and mixtures of 1 mM PNIPAM10000 with SiW^{4-}.
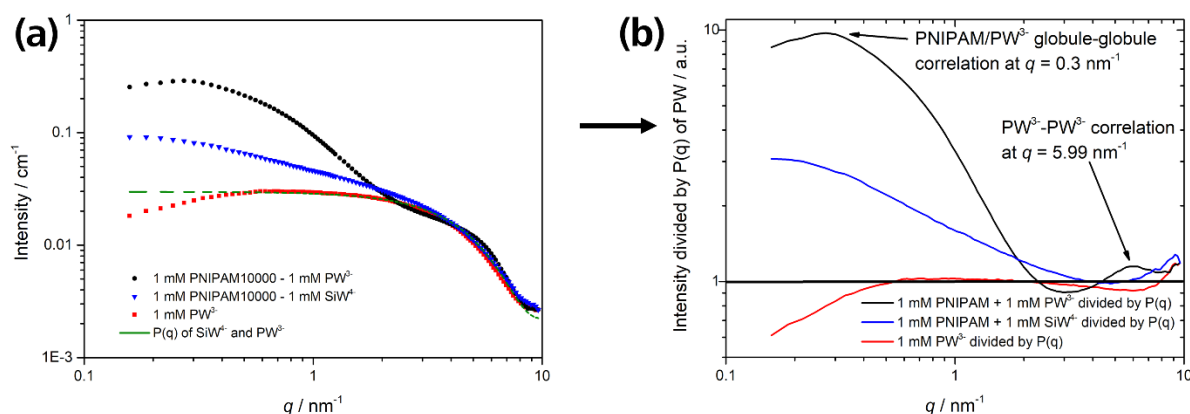
Figure S 6-10: (a) Scattering curves of 1 mM PW^{3-} and mixtures of 1 mM PNIPAM10000 - 1 mM PW^{3-} and 1 mM PNIPAM10000 – 1 mM SiW^{4-}. The green curve represents the *P(q)* of SiW^{4-} and PW^{3-} which is considered to be equal for both. (b) *S(q)* of 1 mM PW^{3-}, 1 mM PNIPAM10000 - 1 mM PW^{3-} and 1 mM PNIPAM10000 - 1 mM SiW^{4-} obtained by dividing the scattering curves by the *P(q)* of PW^{3-}/SiW^{4-}. The PW^{3-}-PW^{3-} average distance within the PW^{3-}/PNIPAM assemblies is 1.05 nm indicated by a correlation peak at q = 5.99 nm^{-1}. Hence, PW^{3-} is packed densely in globular assemblies formed by 1 mM PNIPAM10000 and 1 mM PW^{3-}. No correlation peak is obtained for supramolecular assemblies formed by PNIPAM10000 and SiW^{4-} indicating that a dense packing of SiW^{4-} is not possible.
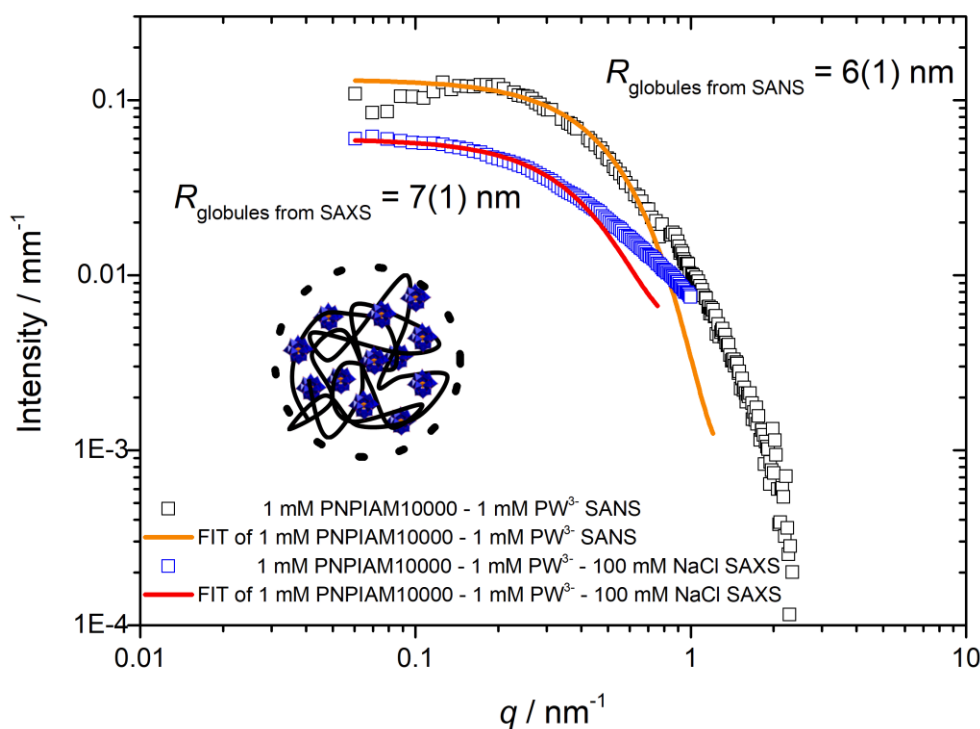
Figure S 6-11: Guinier fits of the SAXS spectrum of 1 mM PNIPAM10000 - 1 mM PW^{3-} - 100 mM NaCl and of the SANS spectrum of 1 mM PNIPAM10000 - 1 mM PW^{3-} corrected by the inter - globule *S(q)*.
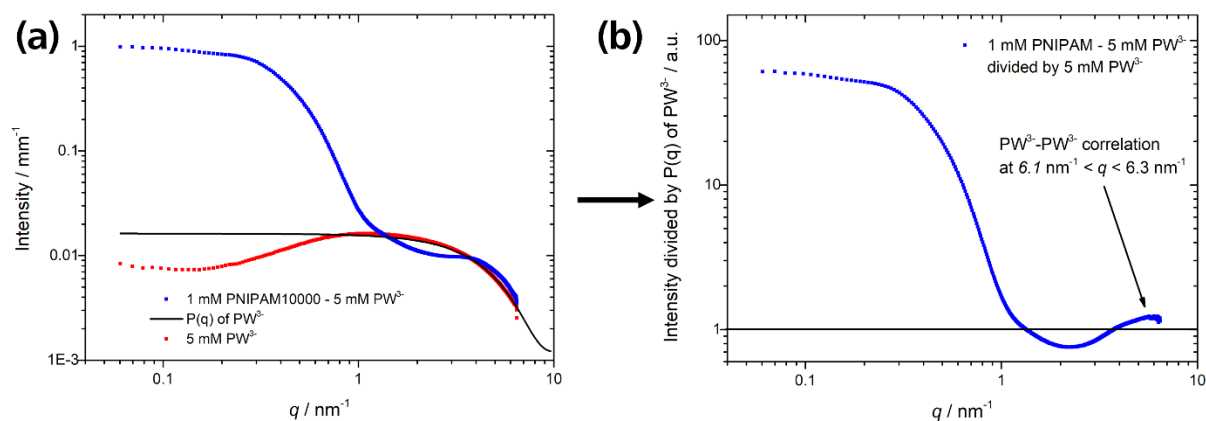
Figure S 6-12: (a) Scattering curves of 5 mM PW^{3-} and a mixture of 1 mM PNIPAM10000 - 5 mM PW^{3-}. The black line represents the $P(q)$ of PW^{3-}. (b) The $S(q)$ of 1 mM PNIPAM10000 - 5 mM PW^{3-} is obtained by dividing the scattering curve by the formfactor $P(q)$ of PW^{3-}. The PW^{3-}-PW^{3-} average distance within the PW^{3-}/PNIPAM assemblies is $1.00 - 1.03$ nm indicated by a correlation peak at $6.1 < q < 6.3$ nm^{-1}. Hence, PW^{3-} is packed densely in the 2D layer of the sheets formed by 1 mM PNIPAM10000 and 5 mM PW^{3-}.
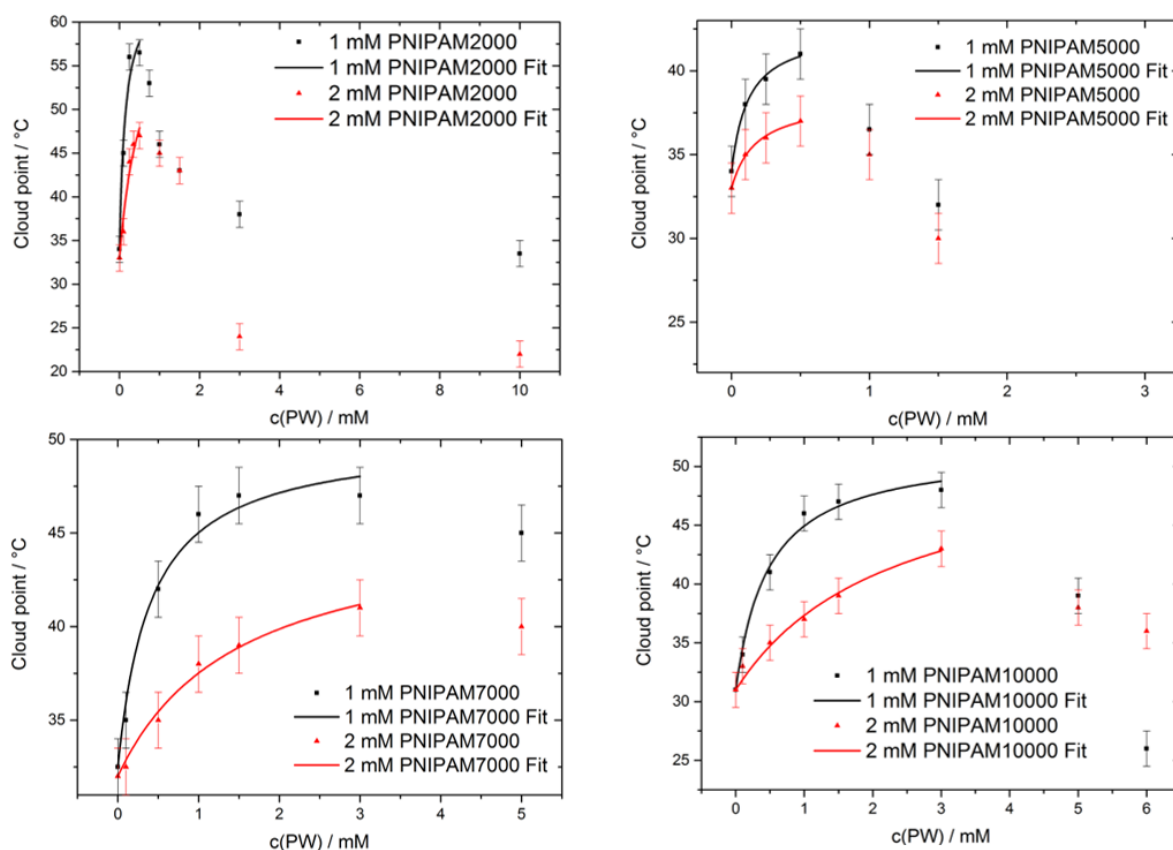
Figure S 6-13: LCST of PNIPAMx000 (x = 2, 5, 7, 10) plotted as a function of *(i)* the PNIPAMx000 (x = 2, 5, 7, 10) concentration, *i.e.* 1 mM or 2 mM, and *(ii)* as a function of $c(PW^{3-})$ from 0 to 6 mM. Error bars represent the error of the LCST by detection with visual inspection.

Table S 6.1: Comprehension of parameters extracted from the CP increase in **Figure S 6-13**. The curves were fitted with the following equation: LCST = LCST(PNIPAM) + (B_{max}•K_A•c(PW^{3-})) / (1 + K_A•c(PW^{3-})).[20] No direct relation between number of repeating units of PNIPAM to the number of PW^{3-} and its impact on the LCST of PNIPAM could be found.

	PNIPAM2000		PNIPAM5000		PNIPAM7000		PNIPAM10000	
	1 mM	2 mM	1 mM	2 mM	1 mM	2 mM	1 mM	2 mM
Repeating units per PNIPAM	18		44		62		88	
length of fully extended PNIPAM / nm	5		11		16		23	
Thickness of sheets / nm	-		5-6		6-7		8-9	
LCST$_{max}$ / °C	56.5	47	41	37	47	41	48	43
$c_{LCSTmax}$(PW^{3-}) / mM	0.42	0.42	0.5	0.5	2.25	3	3	3
B_{max} / °C	30.7	31.2	8.5	5.34	17.6	13.7	20.6	20.8
K_A / mM^{-1}	6.9	1.8	8.3	5.6	2.4	0.7	2.1	0.4
(Monomer$_{PNIPAM}$)/PW^{3-} at LCST$_{max}$	43	86	88	176	28	41	29	59

7 Structuring of Hydrotropes in water

7.1 Preface and Abstract

This chapter was published in the peer-reviewed Journal *Physical Chemistry Chemical Physics (PCCP)* of the publisher Royal Society of Chemistry (DOI: 10.1039/C6CP06696H, this is also where the electronic supplementary information (ESI) can be found).

Thomas Buchecker and Sebastian Krickl contributed equally to the experimental work and to the writing of the manuscript:

- Dynamic light scattering was performed by Sebastian Krickl

- Small-and-wide-angle-X-ray-scattering was performed by Thomas Buchecker

- Conductivity measurements were performed by Thomas Buchecker, Sebastian Krickl and Robert Winkler

- Recording of phase diagrams and optical density measurements: performed by Sebastian Krickl and Robert Winkler

- Small-angle-neutron-scattering was performed by Thomas Buchecker and Dr. Isabelle Grillo

- Data analysis and writing of the paper was performed by Thomas Buchecker and Sebastian Krickl

- Dr. Pierre Bauduin, Dr. Didier Touraud. Prof. Dr. Arno Pfitzner and Prof. Dr. Werner Kunz contributed with fruitful discussions and supervised the experimental work and improved the manuscript (MS)

Abstract: In the present chapter, the pre-structuring of binary mixtures of hydrotropes and H_2O is linked to the solubilisation of poorly water miscible compounds. We have chosen a series of short-chain alcohols as hydrotropes and benzyl alcohol, limonene and a hydrophobic azo-dye (Disperse Red 13) as organic compounds to be dissolved. Very weak pre-structuring is found for ethanol/H_2O and 2-propanol/H_2O mixtures. Pre-structuring is most developed for binary 1-propanol/H_2O and *tert*-butanol/H_2O mixtures and supports the model of a bicontinuity of alcohol-rich and water-rich domains as already postulated by Anisimov *et al.* Such a pre-structuring leads to a high solubilisation power for poorly water miscible components (limonene and Disperse Red, characterized by high octanol/water partition coefficients, log(P) values of 4.5 and 4.85), whereas very weak pre-structuring leads to a high solubilisation power for slightly water miscible components (benzyl alcohol). This difference in solubilisation power can be linked to *(i)* the formation of mesoscale structures in case of ethanol and 2-propanol and to *(ii)* the extension of pre-structures in case of 1-propanol and *tert*-butanol. Three different solubilisation mechanisms could be identified: bulk solubilisation, interface solubilisation and the combination of both. These supramolecular structures in binary and ternary

systems were investigated by small angle X-ray and neutron scattering, dynamic light scattering and conductivity measurements (in the presence of small amount of salt).
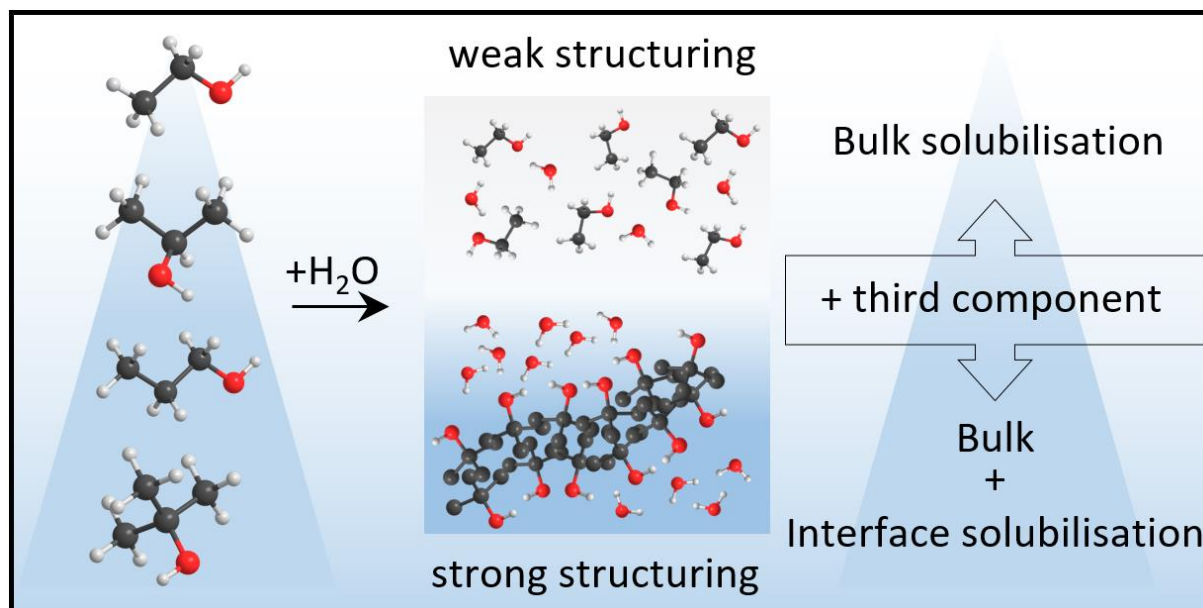
Figure 7.1: TOC illustrating the different modes of solubilisation of a ternary compound in (un-) structured binary solvents

7.2 Introduction

Ternary systems comprising a short chain amphiphilic molecule (hydrotrope) and two immiscible liquids, with both of them being fully miscible with the hydrotrope, are considered as powerful solubilisation media[1–3] and exhibit anomalies concerning enzymatic reactions[4,5] and vapour pressures.[6] The existence of well-defined mesoscale inhomogeneities in macroscopically transparent solutions was shown to be responsible for such unexpected behaviour. Such mesoscale inhomogeneities and compartmentation phenomena of oil-rich and water-rich domains are comparable to the micro-domains observed in water/oil/surfactant ternary systems (direct-, bicontinuous- and reverse-microemulsions) as shown by scattering techniques, molecular dynamics simulations (MD simulations) and conductivity measurements.[7–9] Only recently, Zemb *et al.* provided an extended Dejaguin-Landau-Verwey-Overbeek theory (DLVO) as a general explanation for the existence and thermodynamic stability of such surfactant-free microemulsions (SFME). This extended DLVO theory describes the subtle balance between entropy, *i.e.* homogenous mixing of the three components, and enthalpy, *i.e.* hydrophobic effects between two immiscible fluids causing micellar-like aggregation.[10]

Hydrotropes play a major role in the mesoscale solubilisation phenomena of SFME. The concept of hydrotropy, defined by C. Neuberg in 1916,[11] outlines the capability of short chain amphiphilic molecules to solubilize hydrophobic compounds in a hydrophilic solvent. In SFME showing the compartmentation of hydrophilic and hydrophobic domains, the hydrotrope accumulates mostly at the

interface between water-rich and oil-rich domains as deduced from contrast variation experiments with small angle neutron scattering (SANS) and MD simulations. The interface between the oil- and water-rich domains is usually considered as some sort of highly flexible film in dynamic exchange with the surrounding medium.[7,12]

When using hydrotropes, as in the case of SFME, the solubilisation of hydrophobic compounds in water is only significant at higher hydrotrope concentrations, typically above c(hydrotrope) > 0.2-0.5 M, which may be compared to surfactants for which solubilisation appears above the critical micellar concentration c(surfactant), which is typically > 10^{-5}-10^{-2} M. As a rule of thumb, the solubilisation by hydrotropes starts in the concentration range (c > 1 M), where the average distance between hydrotrope molecules become smaller or in the order of the molecular size (~ 1 nm), encouraging molecular contact between hydrotrope molecules (cluster formation) and between hydrotrope and the hydrophobic component to be dissolved.[13]

In contrast to surfactants, the amphiphilic character of hydrotropes is usually considered to be not enough pronounced to promote micellisation or self-aggregation of the hydrotrope itself in water.[13] Nevertheless, some hydrotropes, such as *tert*-butanol, are known to form clusters in water and thus produce heterogeneities in the sub-nanometer (molecular) or nanometer range.[14–17] Only recently, the group of Shimizu *et al.* developed an approach to describe hydrotropic solubilisation theoretically.[18–21] This approach derived from pure statistical thermodynamics uses the exact Kirkwood Buff theory to describe cooperative phenomena in hydrotropic solubilisation such as *(i)* the sudden onset of solubilisation of hydrophobic compounds in H_2O (commonly referred to as MHC) or *(ii)* solubility saturation of hydrophobic compounds at high hydrotrope concentrations. In a nutshell, they consider hydrotropic solubilisation to be the result of a subtle balance between solute-hydrotrope interaction and hydtrotrope-hydrotrope interaction. In other studies, the authors argued that strong hydrotrope-hydrotrope interactions resulting in a pre-structuring of the hydrotrope in H_2O, diminish the solubilisation efficiency of solutes.[22,23] As we will show here, things are even more complex.

Already a vast number of publications have focussed on the microscopic inhomogeneities of short chain alcohols in H_2O.[24–39] The microscopic structuring in these binary mixtures is mostly attributed to the hydrophobic hydration of non-polar aliphatic chains of the alcohols and a highly dynamic network of hydrogen bonds between alcohols and H_2O.[15] Anomalies concerning permittivity, surface tension, self-diffusion coefficients, structuring, etc. are most pronounced for *tert*-butanol-H_2O mixtures as *tert*-butanol provides the largest aliphatic chain among fully water-miscible alcohols.[29–38,40,41]

The goal of this work is to link such molecular inhomogeneities in binary alcohol/H_2O mixtures to the mesoscale solubilisation of a third hydrophobic component, called "third component" hereafter. To establish this link, it is essential to understand the origin of the compartmentation of water- and oil-rich domains in the ternary systems. Three questions are essential in this context:

(i)   Do the pre-structuring and microscopic inhomogeneities of the hydrotrope in the binary system alcohol/H_2O have an influence on the structuring of the ternary system?

(ii)   Is the structuring in SFME caused by the hydrotrope or by a third, (more) hydrophobic component?

(iii)   Does the mesoscale solubilisation mechanism of the third, hydrophobic component depend on its hydrophobicity?

Hence, it is necessary to understand the structuring of short chain alcohols in water as a function of increasing aliphatic moiety of the alcohol. We extend the pioneering studies by M. Anisimov and M. Sédlak on the mesoscale solubilisation of a third component in pre-structured binary mixtures *tert*-butanol/H_2O[14,17,42] to the homologous series of alcohols and to other hydrophobic compounds. To this purpose, we investigate the structuring of ethanol (EtOH), 1-propanol (NPA), 2-propanol (IPA) and *tert*-butanol (TBA) in water with conductivity measurements and scattering techniques. The structuring in the binary alcohol/H_2O mixtures is related to its impact on the mesoscale solubilisation of a third hydrophobic component, *i.e.* benzyl alcohol, limonene and an azo dye, Disperse Red 13 (DR-13). As we will show, the observed differences in solubility are the consequence of different solubilisation mechanisms.

7.3 Experimental

Materials. Ethanol (purity $\geq$ 99.8%), acetone ($\geq$ 99.5%), 2-propanol ($\geq$ 99.8%), 1-pentanol ($\geq$ 99%), (R)-(+)-limonene (97%, ee: 98%), dodecane ($\geq$ 99%) and Disperse Red 13 (DR-13, dye content 95%) were purchased from Sigma-Aldrich (Steinheim, Germany). Sodium bromide ($\geq$ 99.99%), 1-propanol ($\geq$ 99.5%), benzyl alcohol ($\geq$ 99%) were purchased from Merck (Darmstadt, Germany) and tert-butanol ($\geq$ 99%) from Carl Roth (Karlsruhe, Germany). Sodium dodecyl sulfate (SDS, $\geq$ 99%) was purchased from Applichem (Darmstadt, Germany).

All chemicals were used without further purification. Aqueous solutions were prepared using deionized water with a resistivity of 18 MΩ·cm.

DLS. DLS spectra were recorded using a temperature controlled CGS-3 goniometer system from ALV (Langen, Germany) equipped with an ALV-7004/FAST Multiple Tau digital correlator and a vertical-polarized 22-mW HeNe laser (wavelength λ = 632.8 nm). Before starting the measurement, all samples were filtered into dust-free cylindrical light scattering cells (10 mm outer diameter) using a 0.2 µm PTFE membrane filter. The sealed measurement cells could be directly placed into the measurement apparatus. Measurements were performed at a scattering angle of 90° after thermostating to 25 ± 0.1 °C. Data points were collected for 300 s. Aggregates in SFME are usually highly fluctuating and of no well-defined shape. Hence, we renounced calculations of the exact hydrodynamic

radii. Instead, the DLS spectra were evaluated qualitatively with regard to their correlation coefficient and their lag time and an estimate of the size of the microscopic inhomogeneities is provided. (As a rule of thumb, it was assumed that a higher intercept of the correlation function for small lag times and larger lag times of the correlation function represent the more time-stable and more pronounced structuring inside the solution.)

SAXS. See chapter 4.3

Conductivity. Conductivity measurements were carried out in a thermostated measurement cell (25 ± 0.2 °C) under permanent stirring using a low-frequency WTW inoLab Cond 730 conductivity meter connected with a WTW TetraCon 325 electrode (Weilheim, Germany). 20 g of each sample (pure hydrotrope or hydrotrope/benzyl alcohol mixtures of different mass fractions) was filled in the measurement cell and successively diluted with pure water. Each sample contained in addition 0.2 wt% sodium bromide to ensure a sufficient amount of charge carriers, which did not noticeably affect the microstructure or the miscibility gap present in the phase diagram. In cases where sodium bromide did not dissolve completely, a small amount of water was added to the pure hydrotrope or hydrotrope/benzyl alcohol mixture before the measurement was started. In addition, conductivity measurements of a classical SDS based microemulsion system were carried out for comparison. For this purpose, a mixture of SDS, 1-pentanol, dodecane and water was used as a starting solution with 9 wt% water, a mass ration of SDS to 1-pentanol of 1 : 2 and a mass ration of oil to total surfactant of 21 : 79. The conductivity curve was determined as described above.

UV-VIS. The solubilisation of DR-13 in different hydrotrope/water mixtures was determined by optical density (OD) measurements via UV-Vis measurements. Saturated solutions of DR-13 in hydrotrope/water mixtures of different mass fractions were prepared. For this purpose, an excess of DR-13 was added to the mixtures. After equilibrating the solutions under intense stirring for 7 days, excess dye was removed by filtration using a 0.2 μm PTFE membrane filter. OD measurements were carried out at $\lambda = 525$ nm in 10 mm path length cells using a Lambda 18 UV-Vis spectrometer from Perkin Elmer (Waltham, USA). Samples with an absorbance higher than 1 were diluted with an appropriate amount of acetone before the measurement. The initial absorbance was calculated by using the respective dilution factor. In addition, a standard curve of DR-13 in acetone was measured to further calculate the amount of DR-13 dissolved by a given amount of hydrotrope.

7.4 Results and Discussion

7.4.1 Binary mixtures

Scattering experiments. In order to get a first insight into the structuring of binary mixtures alcohol/water, DLS measurements were performed. Correlation functions obtained by DLS measurements are shown in **Figure 7.2**.
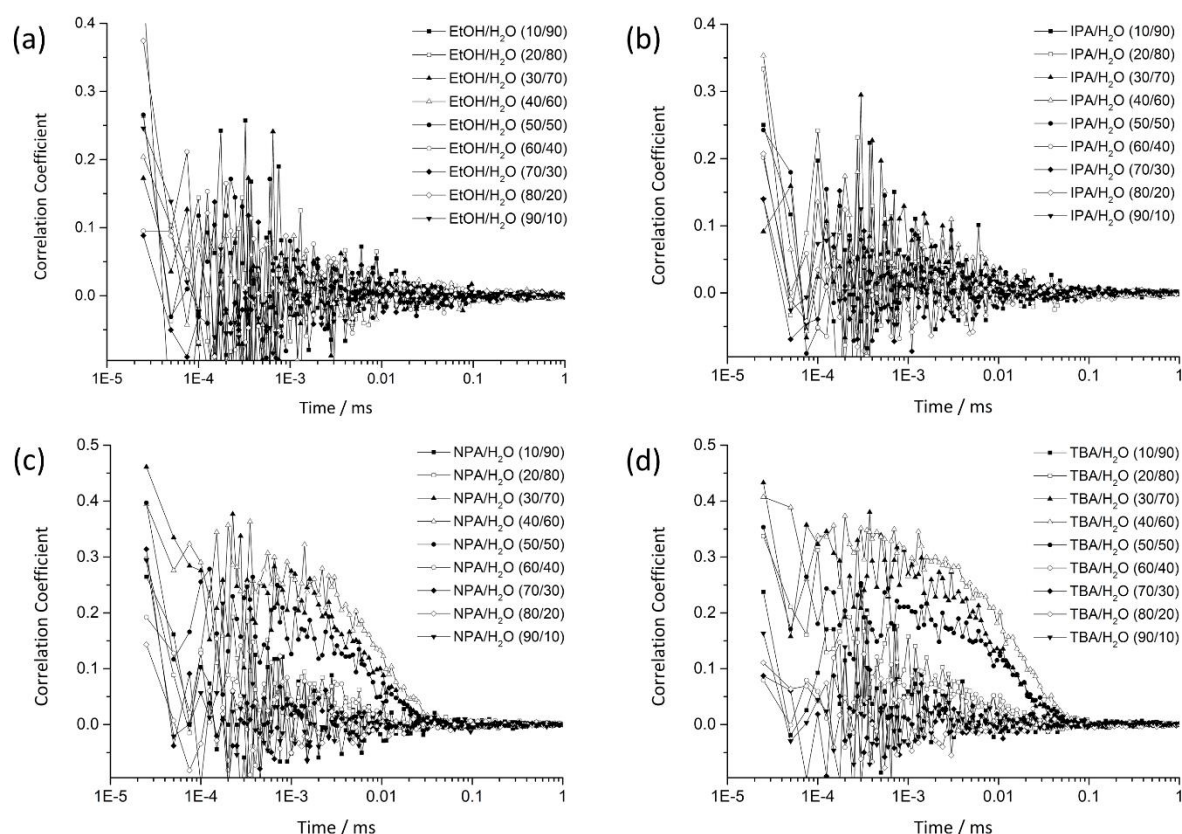
Figure 7.2: Self-correlation functions obtained by DLS measurements at 25 °C for the binary systems (a) EtOH/H$_2$O, (b) IPA, (c) NPA and (d) TBA. The symbols refer to different mass ratios of alcohol to H$_2$O.

EtOH and IPA do not show significant correlations over the whole miscibility range, whereas correlations exist in the NPA/water and TBA/water systems indicating the presence of fluctuating structures. Correlation functions are most pronounced for concentrations ranging from 30 to 50 wt% in NPA and in TBA. The decays in the autocorrelation function for TBA/H$_2$O mixtures appear at longer lag times compared to the system NPA/H$_2$O. This indicates that the fluctuating structures are larger, with lower diffusion coefficients, in the TBA/water mixtures than in the NPA/water system. No correlation functions were measured for EtOH/H$_2$O and IPA/H$_2$O mixtures in the whole concentration range. Nevertheless, it is well known that in EtOH/H$_2$O mixtures cluster formation and inhomogeneous mixing are observed.[24–27] However, these types of structuring appearing at the small molecular scale would produce too fast fluctuations, *i.e.* with high diffusion coefficients, in EtOH/H$_2$O and IPA/H$_2$O systems to be detectable by DLS. As the DLS auto-correlation functions are most pronounced for TBA/water mixtures, additional SWAXS and one particular SANS measurement were performed for this system, see **Figure 7.3** and Figure S1 in the ESI.
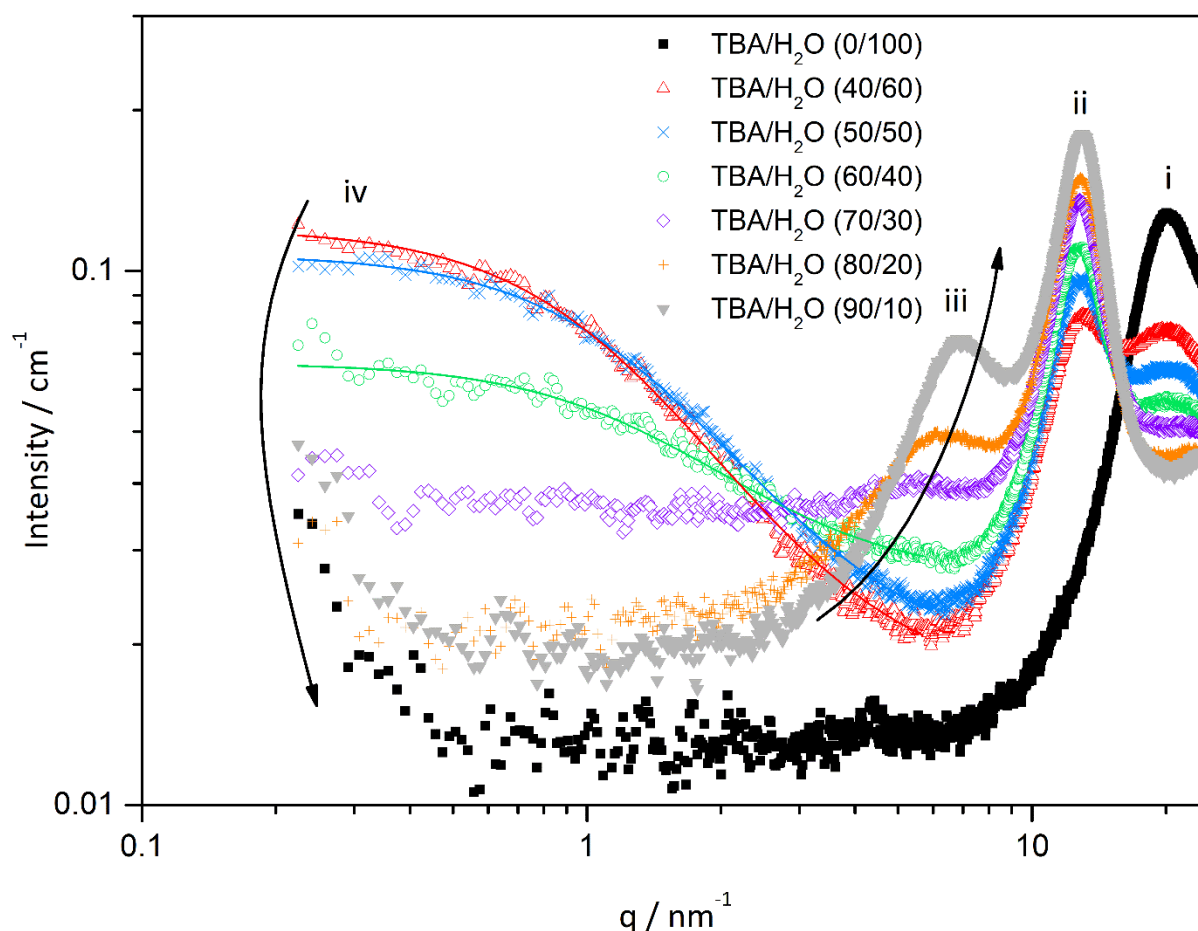
Figure 7.3: SWAXS spectra of the binary mixture TBA/H_2O. Symbols indicate the different mass ratios of TBA to H_2O. Points *(i-iv)* denote the different features found in the spectra.

Four features can be observed in SAXS spectra, assigned to *(i-iv)*. A correlation peak *(i)* is observed at 20 nm^{-1}, originating mainly from the O-O pair correlations in the H-bonding network of H_2O. This peak does not significantly shift in position and decreases in intensity as the amount of water decreases.

Another correlation peak *(ii)* is found at 10.5 nm^{-1}, corresponding to the pair correlations between aliphatic chains. This peak also does not overcome any shift in position and its intensity depends on the TBA concentration. For TBA concentrations above 70 wt%, a correlation peak *(iii)* emerges at 5-7 nm^{-1}, which corresponds to average distances between 0.9 and 1.3 nm. This peak can be attributed to the pair-correlations between hydroxyl groups of TBA as its intensity increases with the TBA content. The peak *(iii)* shifts to lower *q* - values with increasing water concentration indicating a swelling of the H-bond network, formed by the TBA hydroxyl groups, by the added water. Furthermore *(iv)*, a significant excess of scattering is observed in the low-*q* range (*q* < 5 nm^{-1}) for 40, 50 and 60 wt% of TBA with a maximum I(*q*→0) intensity for 40 wt%. It has been noticed that the low-*q* scattering is only observed in the absence of a correlation peak of the alcohol -OH groups *(iii)*. The existence of low *q*-scattering in small angle scattering experiments indicates the existence of a meso-structured system.[10,12] Curves exhibiting low *q*-scattering were fitted with an Ornstein-

Zernike (OZ) formalism to determine the correlation length of different compositions. Correlation lengths of 0.6 nm (60/40 TBA/H_2O), 0.7 nm (50/50 TBA/H_2O) and 0.8 nm (40/60 TBA/H_2O) were found. The scattered intensity is rather constant for $q < 1$ nm^{-1} indicating the presence of structures/inhomogeneities with a size around 6 nm.

SANS measurements on one particular composition, *i.e.* 40/60 TBA/D_2O, confirm the results obtained by SWAXS, see Figure S1. The existence of low scattering again indicates the presence of a structured system. Fitting the curve with an OZ fit yields a correlation length of 0.7 nm, which is approximately the same as obtained for SWAXS for this composition (0.8 nm). The slight difference of the correlation length obtained from SWAXS and SANS can be ascribed to the different scattering contrasts of SWAXS and SANS. Therefore, SWAXS and SANS experiments support results obtained by DLS: the existence of a structured system in the binary mixture TBA/H_2O with microscopic inhomogeneities in the order of 4-6 nm. The structuring is most pronounced between 30 and 50 wt% of TBA. To further investigate the structuring of binary mixtures alcohols/H_2O, conductivity measurements were performed.

Conductivity measurements. Conductivity measurements provide detailed information on the mobility of charge carriers and yield insight to the structuring of a system for example for surfactant-stabilised microemulsions.[43,46,47] Conductivity measurements in surfactant-stabilised microemulsions are a well-known and common method to distinguish between regions of O/W, W/O and bicontinuous microemulsions.[9,43] The results of conductivity measurements as a function of the alcohol/H_2O mass and mole fraction, respectively, are depicted in **Figure 7.4**. All curves show a more or less pronounced increase for low water content. With increasing water content, a maximum is reached before the conductivity decreases again due to excessive dilution of the present charge carriers. The slope of increase in conductivity and sharpness of the maximum is rising in the following order: TBA > NPA $\approx$ IPA > EtOH.

Conductivity was also measured for a classical SDS-based microemulsion, see **Figure 7.4c**.[43] Such systems show a flat rise at low water content, followed by a change in slope passing over into a strong linear increase of conductivity (point T1 in **Figure 7.4c**) with increasing water content. After this linear increase, the slope of the curve starts to decrease again (point T2) and passes a maximum (point T3). For structured solutions – as it is the case for microemulsions – these changes in conductivity are explained by transitions between O/W, bicontinuous, and W/O microemulsions. A W/O microemulsion is present for low water content and causes a low conductivity. With increasing water content, percolation of water droplets is observed, causing the formation of conducting water channels by merging water droplets, which leads to a significant change in the slope (Point T1). Further, point T2 marks the transition to an oil-rich bicontinuous microemulsion. A subsequent transition to a water-rich bicontinuous microemulsion is observed upon addition of H_2O. The maximum of conductivity represents the presence of an extended water-rich bicontinuous phase (Point T3).

For very high water contents ($x > 0.9$), a O/W microemulsion is formed and dilution effects prevail, causing conductivities to decrease.
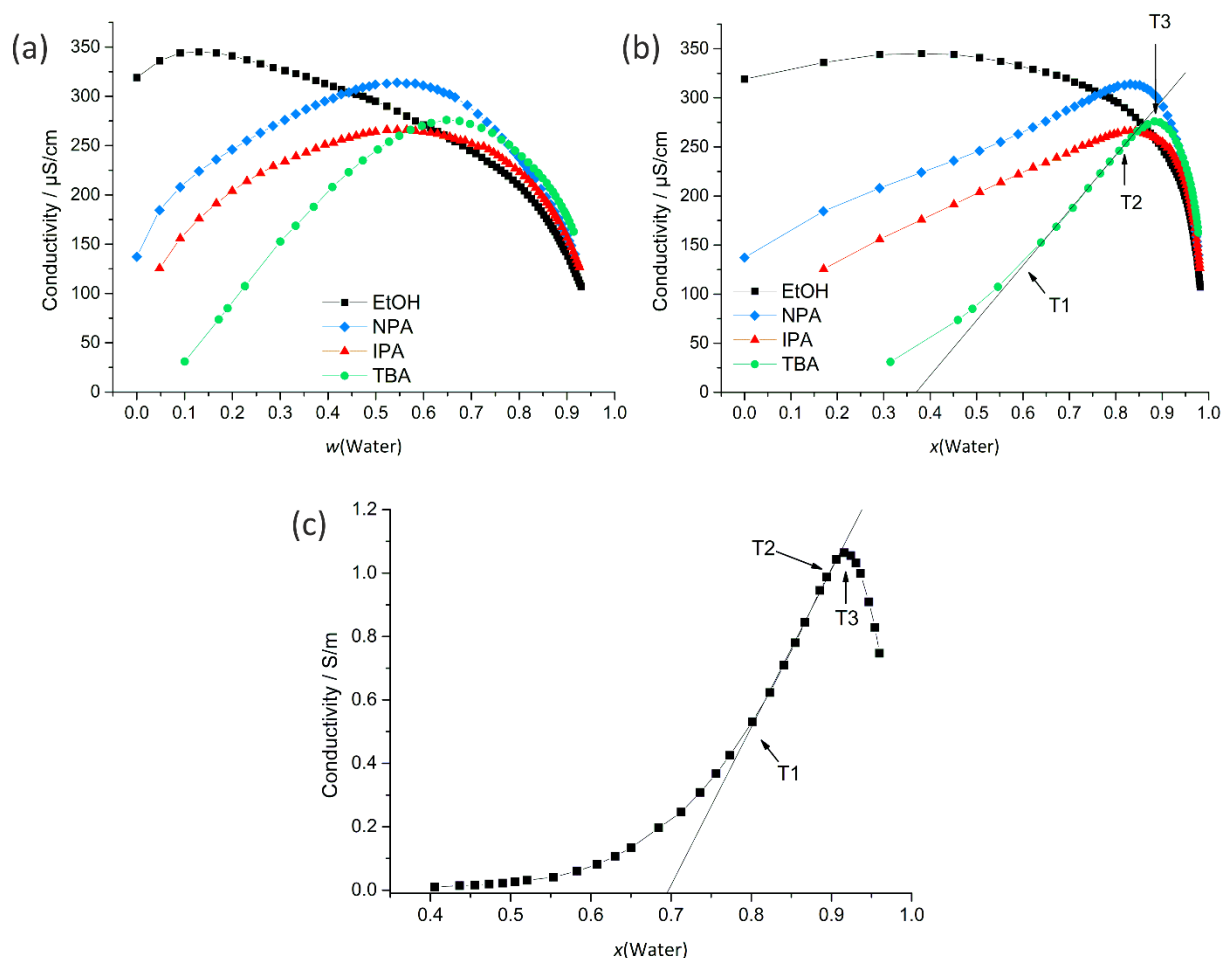
Figure 7.4: Conductivity measurements at 25 °C for binary mixtures of H_2O and EtOH/IPA/NPA/TBA plotted in (a) weight and (b) mole fractions of H_2O. In order to ensure measurable conductivities, 0.2 wt% of NaBr were dissolved in the pure alcohol phase for EtOH, NPA and IPA and in a 10 wt% (H_2O) for the TBA binary system. (c) Conductivities measured at 25 °C for the system H_2O, SDS, 1-pentanol, dodecane. Point T1 marks the point of transition to percolative behaviour of W/O microemulsions and points T2 and T3 mark the transitions from W/O to oil-rich and to water-rich bicontinuous microemulsions.

Comparison of the conductivity curve of this SDS system with the curves of TBA and NPA (**Figure 7.4b** and **c**) shows many similarities regarding the range of increase, the percolation behaviour and the decrease in conductivity for high water contents. The maximum of conductivity for NPA/H_2O lies in a range of approx. 75-90 mol% water content and for TBA of approx. 85-95 mol% water content. This maximum of conductivity coincides with the highest correlation coefficients in DLS and the strongest signal in low q of SWAXS. It is also well known for TBA/H_2O that the binary mixture displays two eutectics, one of them being located at 94 mol% H_2O, which also coincides with the

range of maximum of conductivity.[48] It was found that thermodynamic anomalies and inhomogeneous mixing are most pronounced for this composition even at temperatures above the deep eutectic temperature. The presence of a percolation threshold around 40 mol% H_2O in case of TBA and the conductivity behaviour, see points T1, T2, T3 in **Figure 7.4b**, similar to the SDS system lead to the conclusion that the structuring TBA/H_2O is similar to the structuring of H_2O/SDS/1-Pentanol/Dodecane. Therefore, we propose the presence of a bicontinuity of water-rich and TBA-rich domains, as already suggested by the research group of Anisimov *et al.* for the ternary system H_2O/TBA/propylene oxide, based on MD simulations and the observation of mesoscale inhomogeneities.[42] However, conductivity measurements here suggest the formation of a bicontinuous phase already in the binary mixture TBA/H_2O. Apparently, this bicontinuous structuring behaviour is not only restricted to TBA, but is also observable for aqueous NPA mixtures, as suggested by DLS measurements, although to a much smaller extent.

The conductivity curve of EtOH differs strongly from the conductivity curves of IPA, NPA TBA and SDS regarding the ranges of increase, decrease and the position of the maximum. The small conductivity increase for low water contents might be explained by an enhanced ion dissociation as well as a higher electrophoretic mobility in aqueous media. For increasing water content, the conductivity decrease can be explained by excessive dilution of the charge carriers. Therefore, it is assumed that microscopic inhomogeneities in case of EtOH are very weak and cannot be detected in detail by conductivity measurements.

The conductivity of IPA is in between the conductivities of EtOH and NPA indicating a progressive structuring with increasing aliphatic chain length. Therefore, EtOH/H_2O is a good example of a weakly structured system and TBA/H_2O is a representative binary mixture of a system with pronounced structuring.

7.4.2 Ternary mixtures

Solubilisation power of the hydrotropes for benzyl alcohol, limonene and DR-13. As discussed in the preceding section, scattering and conductivity experiments of the binary mixtures reveal a trend of progressive structuring in the investigated series of fully water miscible alcohols: EtOH < IPA < NPA < TBA.

In the next step, three different hydrophobic compounds were dissolved in binary mixtures alcohol/H_2O, *i.e.* benzyl alcohol, limonene and DR-13. The difference between these compounds is their miscibility with water. Benzyl alcohol is slightly miscible with H_2O. Limonene, as well as DR-13, are poorly water miscible compounds. The realms of solubility in case of benzyl alcohol and limonene and the OD as a measure of the solubility of DR-13 are shown in the ternary phase diagrams in **Figure 7.5**.[49,50] The solubilisation power of the alcohols in case of benzyl alcohol decreases in the following order: EtOH > IPA > NPA ≈ TBA, while phase diagrams with NPA and TBA are very similar. The solubilisation power of the alcohols in case of limonene gradually increases in the following

order: EtOH < IPA < NPA < TBA. Its miscibility with H_2O is very poor (less than in case of benzyl alcohol) and therefore the two-phase region is larger than in the case of benzyl alcohol. The solubility of limonene in TBA/H_2O starts to increase significantly at $x(TBA) = 10$ mol% (see Point T3 in **Figure 7.5**) and at $x(TBA) > 40$ mol% the miscibility gap is closed. Furthermore, and most important, the hydrotrope efficiency for the solubilisation of limonene is reversed compared to the solubilisation efficiency of the regarded alcohols for benzyl alcohol.
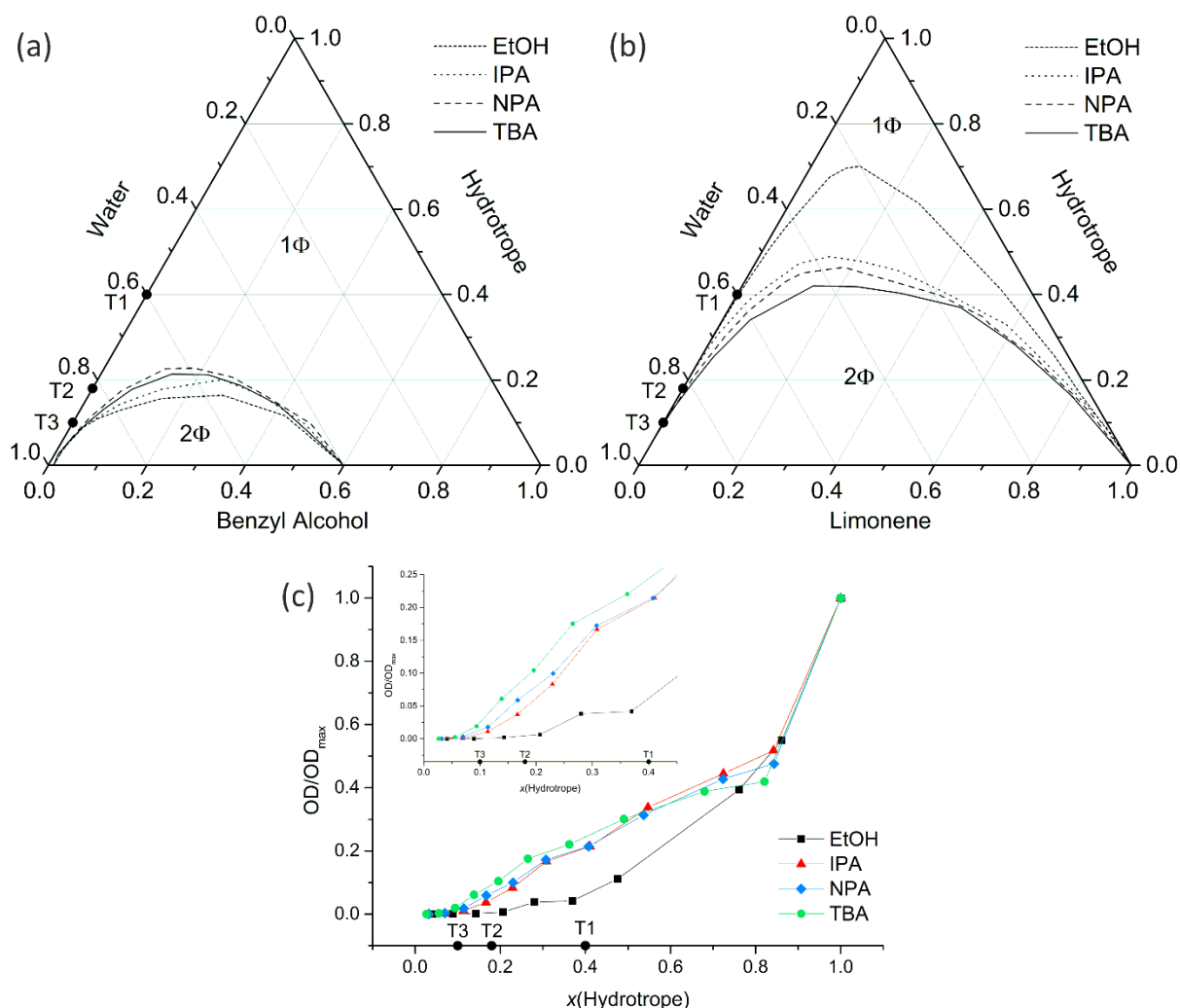
Figure 7.5: Ternary phase diagrams for the systems (a) H_2O/hydrotrope/benzyl alcohol and (b) H_2O/hydrotrope/limonene provided in mol%. (c) shows the results of the OD measurements of DR-13 in H_2O/hydrotrope mixtures given in mole fractions of hydrotrope. ODs were divided by the OD value from the corresponding neat hydrotrope (OD_{max}). T1, T2 and T3 mark the transition points of the binary system TBA/H_2O in mole fractions as determined in Figure 7.4**b.**

In case of the solubilisation of DR-13, the dissolved amount of DR-13 increases in the following order: EtOH $\ll$ IPA < NPA < TBA for hydrotrope contents x(hydrotrope) < 0.4. For hydrotrope contents x(hydrotrope) > 0.4 the situation is different. Note that in case of the solubilisation of DR-13 in TBA/H_2O, the solubility starts to increase at point T3 (remember: maximum of the water-rich

bicontinuous phase in TBA/H_2O). After point T3, the solubility of DR-13 increases linearly up to point T1, where the slope of the solubility of DR-13 in TBA diminishes. All in all, the solubilisation power of the alcohols for DR-13 follows the same trend as for limonene. However, comparing the results of DR-13 solubilisation to the solubilisation of benzyl alcohol and limonene, there are huge differences regarding the absolute amounts of dissolved hydrophobic compound.

Discussion of the solubilisation mechanisms in ternary systems. As for the binary systems, conductivity measurements were performed for several monophasic compositions of the ternary system H_2O/alcohol/benzyl alcohol, see **Figure 7.6**.
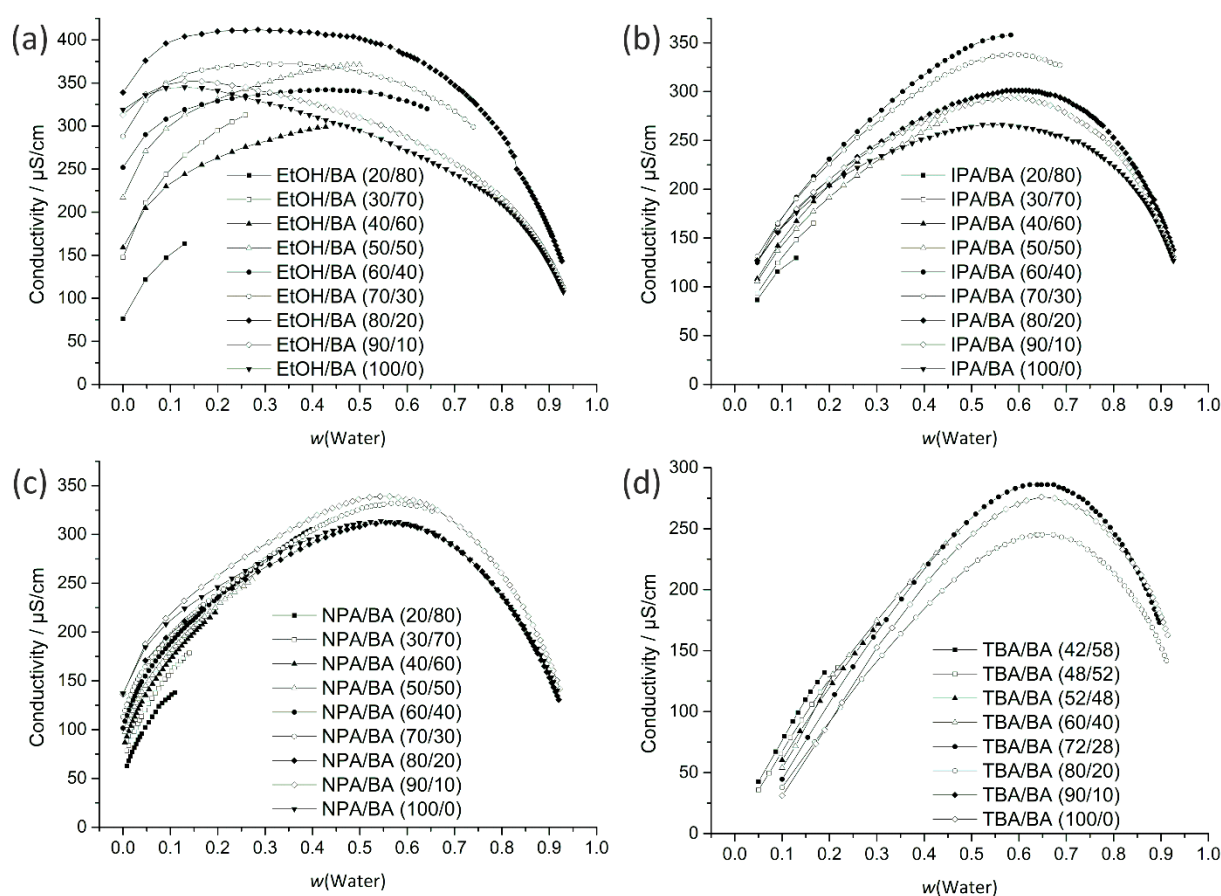
Figure 7.6: Conductivity measurements at 25 °C for ternary mixtures of H_2O/hydrotrope/benzyl alcohol plotted in weight fractions of H_2O. (The measurements were performed by diluting a binary mixture hydrotrope/benzyl alcohol with H_2O. The symbols refer to different mass ratios of hydrotrope to benzyl alcohol (BA) in the binary starting mixture hydrotrope/benzyl alcohol before diluting with H_2O.
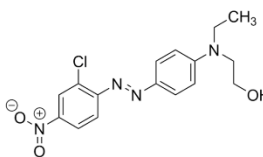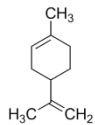
In these experiments, alcohol/benzyl alcohol mixtures of different compositions, expressed here in mass percent of water, and in the presence of 0.2 wt% of NaBr were titrated with pure water. Conductivities for H_2O/EtOH/benzyl alcohol differ strongly from the conductivity curves obtained for H_2O/IPA/benzyl alcohol, H_2O/NPA/benzyl alcohol and H_2O/TBA/benzyl alcohol. For systems containing NPA, IPA and TBA, the shapes of the curves do not significantly deviate for ternary systems

H_2O/alcohol/benzyl alcohol from those of the binary system alcohol/H_2O. The decrease of the initial conductivity for $w(H_2O) = 0$ only in case of increasing EtOH/benzyl alcohol ratio can be explained by a higher charge mobility and enhanced ion dissociation. For EtOH and IPA, no or very weak structuring is observed for their binary mixtures with H_2O. The addition of benzyl alcohol and limonene, respectively, induces the formation of a well-ordered system.[2,6] Hydrophobic hydration and agglomeration causes the hydrophobic compound to form clusters with accumulating the hydrotrope mostly at the interface between the benzyl alcohol clusters and the water-rich domain. Consequently, the solubility of the hydrophobic compound is enhanced with increasing hydrotrope concentration. This is in perfect agreement with the ideas forwarded recently.[22,23,51]

However, in contrast to weakly structured EtOH/H_2O and IPA/H_2O, the situation is completely different for binary pre-structured TBA/H_2O and NPA/H_2O systems. As a bicontinuous structure is already given, the structure is not induced by the third component, but by the hydrotrope itself. Due to the formation of a bicontinuous system, an aliphatic-rich domain as well as a water-rich domain and a large area of interface is created.

In such a case of a pre-structured binary hydrotrope-water system, three possible solubilisation pathways are possible: *(i)* solubilisation in the water-rich bulk phase (appears only for highly polar solutes which are not considered here), *(ii)* solubilisation in the aliphatic-rich bulk phase and *(iii)* solubilisation within the interfacial film between the aliphatic and water-rich pseudo-bulk phases, see **Figure 7.7**.

Solute	log(P)	Solubilisation mechanism	Solubilisation efficiency			
			EtOH/H_2O	IPA/H_2O	NPA/H_2O	TBA/H_2O
Benzyl alcohol	1.1	bulk + interface				
DR-13	4.85	interface + (bulk)				
Limonene	4.5	bulk				

Figure 7.7: Schematic overview of the different solubilisation mechanisms and efficiencies of benzyl alcohol, DR-13 and limonene in binary water/alcohol mixtures. Octanol/water partition coefficients *log(P)* were taken from [54–56].

The aliphatic-rich bulk-like pseudo-phase permits the incorporation of large amounts of hydrophobic components. This is confirmed by the solubilisation power of the hydrotropes in case of limonene, where TBA shows the highest solubilisation power and EtOH the lowest solubilisation power.

Further indications are conductivity measurements for ternary systems H_2O/alcohol/benzyl alcohol, where the absolute conductivity of NPA and TBA is maintained, indicating the retention of the pre-structures.

The SANS spectrum on one exemplary composition of a ternary mixture D_2O/TBA/benzyl alcohol (60/32/8 wt%) was compared to a SANS measurement of a binary TBA/H_2O mixture (40/60 wt%) to further support this fact, see Figure S1. The substitution of TBA by benzyl alcohol leads to a large increase of the scattered intensity. Analyzing the correlation length of these curves (0.8 nm for the binary mixture and 2.1 nm for the ternary mixture) indicates an enlargement of the correlation length of the TBA/benzyl alcohol aliphatic rich phase. This implies that benzyl alcohol and certainly also TBA is "driven" towards the aliphatic rich continuum which is "blown up" and causes an increase of the correlation length. Therefore, the structure is reinforced by the addition of benzyl alcohol.

However, in case of benzyl alcohol, the situation is somehow different to the case of limonene, as it contains a hydroxyl group in addition to the aliphatic moiety. This leads us to the assumption that benzyl alcohol is not only dissolved within the aliphatic-rich continuum, due to its low water miscibility, but may accumulate also at the interfacial film, similar to a co-surfactant. Another indicator is the fact that TBA provides the lowest solubilisation power for benzyl alcohol in the series of EtOH, IPA and NPA. In EtOH/H_2O mixtures, benzyl alcohol induces the formation of mesoscale structures, whereas in case of TBA/H_2O mixtures, it intercalates into the given pre-structure. As soon as the given pre-structure is completely "swollen up" and the interfacial film is saturated, further addition of benzyl alcohol causes the system to collapse and to form two phases.

In case of the solubilisation of DR-13, the situation is again different from both the limonene and the benzyl alcohol solubilisation, since DR-13 bears polar functional groups and an aromatic backbone much larger than that of benzyl alcohol. The solubilisation power of the hydrotropes in case of DR-13 follows the same series as for limonene. However, a closer look at the amount of dissolved DR-13 per amount of hydrotrope reveals a huge difference of the order of several orders of magnitude. Furthermore, DR-13 is assumed to be not capable to induce micro-structuring, as the overall solubility in H_2O and H_2O/hydrotrope is too low. Therefore, the solubility in EtOH/H_2O is very low. However, as the solubility increases with progressive structuring of H_2O/hydrotrope, we assume that the difference in solubility is based on a completely different solubilisation mechanism as compared to limonene. Instead of a bulk solubilisation within a hydrophobic mesoscale pseudo-phase, we suppose DR-13 to be mostly dissolved within the interfacial film of the two pseudo-bulk phases. This assumption is in good accordance with all observations, because an interfacial film provides much less space than a bulky pseudo-phase for the solubilisation of DR-13. The solubility of DR-13 in TBA/H_2O mixtures starts to increase at point T3 representing the maximum of the water-rich bicontinuous phase, see **Figure 7.4b, c**. Beginning from T1 (representing the percolation threshold)

the solubilisation power of TBA/H_2O diminishes compared to the region T3-T1. It is assumed that the interface of pre-structured binary alcohol/H_2O mixtures is rapidly saturated for low concentrations of DR-13. The further increase of the solubilisation of DR-13 for higher TBA contents (x(TBA) > 0.4) may be ascribed to bulk solubilisation due to saturation of the interface. Hence, DR-13 may preferentially solubilise at the interface in highly structured regimes of TBA 0.1 < x(TBA) < 0.4, passing over to a more bulk like solubilisation mechanism for higher TBA contents. A more detailed analysis of the curve shapes clarifies these findings even better. A second-order differentiation of the fitted curves reveals huge differences in the solvent character of the hydrotrope (see Figure S2). In case of EtOH the curvature of the curve stays always positive over the whole miscibility range whereas there is a negative curvature in the case of TBA in the range of approximately 0.23 < x(TBA) < 0.6. This second order differentiation shows that EtOH possesses a more co-solvent character, whereas TBA shows a hydrotropic behaviour when DR-13 is dissolved. The proposed interfacial solubilisation mechanism is further supported by the fact that DR-13 has a very poor solubility both in pure dodecane and pure water, which both do not provide an interface at all. As a consequence, DR-13 is also scarcely soluble in poorly structured mixtures, such as EtOH/H_2O.

7.5 Conclusion

We investigated the structuring of binary mixtures alcohol/H_2O, where the alcohol is miscible with H_2O at any proportion, *i.e.* EtOH, IPA, NPA and TBA. DLS, SWAXS and conductivity measurements revealed microscopic inhomogeneities in case of NPA/H_2O and TBA/H_2O. As in the case of micellar systems, we infer from conductivity that these microscopic inhomogeneities are similar to direct or reverse micellar solutions (meaning organic aggregates in water or water aggregates in an organic pseudo-phase, respectively) and also, at some concentration ratios, to bicontinuous structuring with rapidly fluctuating water-rich and alcohol-rich domains in equilibrium. In case of EtOH, no significant structuring could be detected with our methods. IPA marks the transition from a weakly structured system in case of EtOH to structured systems in case of NPA and TBA.

It is found that this pre-structuring of a binary alcohol/H_2O system can be pivotal to the mesoscale solubilisation of a third component. In case of unstructured binary EtOH/H_2O and IPA/H_2O, a significant structuring is induced upon the addition of a third poorly water miscible component, *i.e.* limonene and benzyl alcohol. Up to now, this solubilisation mechanism is considered to be dominant and fundamental in SFME, as in case of the well-studied system H_2O/EtOH/1-octanol.[2,7,12,52,53] It was further argued that this structuring induced by the addition of the third, hydrophobic component, is crucial for a pronounced solubilisation power of the hydrotrope.[22,23,51] And indeed, the lower the pre-structuring in the binary hydrotrope-water mixture, the less hydrotrope is required to make benzyl alcohol water-miscible.

However, as we demonstrate here, hydrotropic solubilisation is more complicated. Firstly, it is just the other way around in case of limonene: the more pronounced the pre-structuring in the binary hydrotrope-water mixture, the less hydrotrope is required to make the much more hydrophobic (compared to benzyl alcohol) limonene water-miscible. Secondly, the more pronounced the pre-structuring in the binary hydrotrope-water mixture, the lower is the minimum hydrotropic concentration to dissolve the dye DR-13, a very hydrophobic compound that is nevertheless nearly insoluble in both water and dodecane.

Two different solubilisation mechanisms can explain the hydrotropic solubilisation of very hydrophobic compounds: *(i)* pseudo-bulk solubilisation of hydrophobic compounds in the aliphatic-rich moiety of pre-structured hydrotrope-water mixtures and *(ii)* interface solubilisation of hydrophobic, but still slightly amphiphilic compounds in the interfacial film.

This leads to the conclusion that for solubilising a hydrophobic compound in an aqueous medium, the choice of the alcohol (hydrotrope) depends primarily on the nature of the hydrophobic substance. For more hydrophilic compounds bearing polar functional groups, short-chained alcohols are more favourable, which is in agreement with [22, 23, 51]. In order to solubilise hydrophobic compounds without polar groups, structure-forming hydrotropes like TBA and NPA should be used instead.

At a first glance, our conclusions may appear contradictory to recent statistical thermodynamic considerations of hydrotropy.[19–21] These state that the predominant driving forces of hydrotropic solubilisation are *(i)* solute induced interactions between solute and hydrotrope molecules leading to a solute-hydrotrope association. In contrast *(ii)* pre-structuring of hydrotropes (hydrotrope-hydrotrope interactions) in water is considered to be rather obstructive for a good solubilisation of the solute. Indeed, this holds true for solutes, which are able to interact with the hydrotrope due to the presence of polar functional groups, as it is the case for benzyl alcohol. For this case, our results are in total agreement with results obtained by thermodynamic calculations. However, these statistical thermodynamic studies by Shimizu *et al.* consider almost exclusively hydrotropes with polar functional groups, *e.g.* ester functional groups. Yet, for very hydrophobic substances (as it is the case for limonene), the situation becomes more subtle. In this case, the solute-hydrotrope interactions are expected to be weaker and play no longer the dominant role since there is no functional group to interact with the hydrotrope. Instead, it becomes more important that the highly hydrophobic solute molecules can intercalate into a significantly hydrophobic, aliphatic pseudo-phase (as it is the case for TBA in H_2O), originated by the pre-structuring of the hydrotrope in water. For DR-13, we found a similar trend for its solubility as for the solubilisation of limonene, but based on a different solubilisation mechanism, due to its slightly amphiphilic character. Thus, the solubility depends on the chemical nature of both solute and hydrotrope. Furthermore, we want to emphasize that in addition to a different choice of solutes, the aforementioned studies by Shimizu *et al.* focus in most

of the cases on completely different concentration ranges of solute and hydrotrope. They consider a very low amount of solute in aqueous hydrotrope solutions. (This is important for the validity of the Kirkwood-Buff theory used for statistical thermodynamic calculations in these studies). Thus, our studies provide a more general and molecular-based model concept of hydrotrope solubilisation.

All in all, taking into account the different ways how structuring can be induced and how they influence the involved solubilisation mechanisms, our picture of mesoscale solubilisation in ternary systems becomes more general and more complete now. Microscopic inhomogeneities and compartmentation phenomena in SFME cannot only be induced by the addition of a third hydrophobic component to a binary mixture H_2O/hydrotrope, but can also have their origin in the pre-structuring of binary mixtures alcohol/H_2O.

7.6 Bibliography

[1]   M. L. Klossek, D. Touraud, T. Zemb and W. Kunz, *ChemPhysChem*, **2012,** *13,* 4116–4119.

[2]   M. L. Klossek, D. Touraud and W. Kunz, *Phys. Chem. Chem. Phys.*, **2013,** *15,* 10971–7.

[3]   V. Fischer, J. Marcus, D. Touraud, O. Diat and W. Kunz, *J. Colloid Interface Sci.,* **2015,** *453,* 186–193.

[4]   M. Zoumpanioti, H. Stamatis, V. Papadimitriou and A. Xenakis, *Colloids Surfaces B Biointerfaces*, **2006,** *47,* 1–9.

[5]   Y. L. Khmelnitsky, R. Hilhorst and C. Veeger, *Eur. J. Biochem.,* **1988,** *176,* 265–271.

[6]   J. Marcus, M. L. Klossek, D. Touraud and W. Kunz, *Flavour Fragr. J.*, **2013,** *28,* 294–299.

[7]   S. Schöttl, J. Marcus, O. Diat, D. Touraud, W. Kunz, T. Zemb and D. Horinek, *Chem. Sci.,* **2014,** *5,* 2909–3340.

[8]   P. Bošković, V. Sokol, T. Zemb, D. Touraud and W. Kunz, *J. Phys. Chem. B,* **2015,** *119,* 9933–9939.

[9]   Z. Li, X. Liu, Y. Lian, J. Xie, X. Gao and T. Chang, *World J. Eng.*, **2016,** *13,* 142–148.

[10]   T. Zemb, M. L. Klossek, T. Lopian, J. Marcus, S. Schöttl, D. Horinek, S. Prevost, D. Touraud, O. Diat, S. Marčelja and W. Kunz, *Proc. Natl. Acad. Sci. U. S. A.,* **2016,** *113,* 4260–4265.

[11]   C. Neuberg, *Biochem. Z*, **1916,** *76,* 107–108.

[12]   O. Diat, M. L. Klossek, D. Touraud, B. Deme, I. Grillo, W. Kunz and T. Zemb, *J. Appl. Crystallogr.*, **2013,** *46,* 1665–1669.

[13]   P. Bauduin, A. Renoncourt, A. Kopf, D. Touraud and W. Kunz, *Langmuir*, **2005,** *21,* 6769–6775.

[14]   D. Subramanian and M. Anisimov, *J. Phys. Chem. B*, **2011,** *115,* 9179–9183.

[15]   D. Subramanian, C. T. Boughter, J. B. Klauda, B. Hammouda and M. Anisimov, *Faraday Discuss.*, **2013,** *167,* 217–238.

[16]   M. Sédlak, *J. Phys. Chem. B,* **2006,** *110,* 13976–13984.

[17]   M. Sedlák and D. Rak, *J. Phys. Chem. B,* **2014,** *118,* 2726–2737.

[18]   S. Shimizu and N. Matubayasi, *J. Phys. Chem. B*, **2014,** *118,* 10515–10524.

[19]   S. Shimizu and N. Matubayasi, *J. Phys. Chem. B*, **2014,** *118,* 3922–3930.

[20]   S. Shimizu and N. Matubayasi, *Phys. Chem. Chem. Phys.*, **2016,** *18,* 25621–25628.

[21]   T. W. J. Nicol, N. Matubayasi and S. Shimizu, *Phys. Chem. Chem. Phys.*, **2016,** *18,* 15205–15217.

[22]   J. J. Booth, S. Abbott and S. Shimizu, *J. Phys. Chem. B,* **2012,** *116,* 14915–14921.

[23]   J. J. Booth, M. Omar, S. Abbott and S. Shimizu, *Phys Chem Chem Phys*, **2015,** *17,* 8028–8037.

[24]   S. Dixit, J. Crain, W. C. K. Poon, J. L. Finney and A. K. Soper, *Nature,* **2002**, *416*, 829–832.

[25]   O. Gereben and L. Pusztai, *J. Phys. Chem. B,* **2015,** *119,* 3070–3084.

[26]   A. Ghoufi, F. Artzner and P. Malfreyt, *J. Phys. Chem. B*, **2016,** *120,* 793–802.

[27]   M. L. Tan, B. T. Miller, J. Te, J. R. Cendagorta, B. R. Brooks and T. Ichiye, *J. Chem. Phys.,* **2015,** *142,* 0645011–0645016.

[28]   L. Almásy, G. Jancsó and L. Cser, *Appl. Phys. A Mater. Sci. Process.,* **2002,** *74,* 1376–1378.

[29]   K. Nishikawa, H. Hayashi and T. Iijima, *J. Phys. Chem.,* **1989,** *93,* 6559–6565.

[30]   D. T. Bowron, J. L. Finney and A. K. Soper, *J. Phys. Chem. B,* **1998,** *102,* 3551–3563.

[31]   K. Yoshida, T. Yamaguchi, A. Kovalenko and F. Hirata, *J. Phys. Chem. B,* **2002,** *106,* 5042–5049.

[32]   T. Fukasawa, Y. Tominaga and A. Wakisaka, *J. Phys. Chem. A,* **2004,** *108,* 59–63.

[33]   A. A. Bakulin, M. S. Pshenichnikov, H. J. Bakker and C. Petersen, *J. Phys. Chem. A,* **2011,** *115,* 1821–1829.

[34]   H. A. R. Gazi and R. Biswas, *J. Phys. Chem. A,* **2011,** *115,* 2447–2455.

[35]   B. Kezic and A. Perera, *J. Chem. Phys.,* **2012,** *137,* 5011–5012.

[36]   M. D. Hands and L. V. Slipchenko, *J. Phys. Chem. B,* **2012,** *116,* 2775–2786.

[37]   L. Comez, M. Paolantoni, L. Lupi, P. Sassi, S. Corezzi, A. Morresi and D. Fioretto, *J. Phys. Chem. B,* **2014,** *119,* 9236–9243.

[38]   D. Banik, A. Roy, N. Kundu and N. Sarkar, *J. Phys. Chem. B,* **2015,** *119,* 9905–9919.

[39] S. K. Allison, J. P. Fox, R. Hargreaves and S. P. Bates, *Phys. Rev. B - Condens. Matter Mater. Phys.,* **2005**, *71,* 1–5.

[40] P. G. Kusalik, A. P. Lyubartsev, D. L. Bergman and A. Laaksonen, *J. Phys. Chem. B,* **2000**, *104,* 9526–9532.

[41] M. Tomsic, A. Jamnik, G. Fritz-Popovski, O. Glatter and L. Vladek, *J. Phys. Chem. B,* **2007**, *111,* 1738–1751.

[42] D. Subramanian, J. B. Klauda, P. J. Collings and M. Anisimov, *J. Phys. Chem. B,* **2014**, *118,* 5994–6006.

[43] M. L. Dekker, Clausse M., Rosano H.L., Zradba A., *Microemulsion Systems, Surfactant Science Ser.,* New York, *24th edn.,* **1987**.

[44] C. D. Dewhurst, I. Grillo, D. Honecker, M. Bonnaud, M. Jacques, C. Amrouni, A. Perillo-Marcone, G. Manzin and R. Cubitt, *J. Appl. Crystallogr.,* **2016**, *49,* 1–14.

[45] https://www.ill.eu/instruments-support/computing-for-science/cs-software/all-software/lamp/.

[46] B. Lagourette, J. Peyrelasse, C. Boned and M. Clausse, *Nature,* **1979**, *281,* 60–62.

[47] M. Clausse, J. Peyrelasse, J. Heil, C. Boned and B. Lagourette, *Nature,* **19**81, *293,* 636–638.

[48] D. Subramanian and M. A. Anisimov, *Fluid Phase Equilib.,* **2014**, *362,* 170–176.

[49] A. Arce, A. Marchiaro and A. Soto, *J. Solution Chem.,* **2004**, *33,* 561–569.

[50] H. Li and K. Tamura, *Fluid Phase Equilib.,* **2008**, *263,* 223–230.

[51] W. Kunz, K. Holmberg and T. Zemb, *Curr. Opin. Colloid Interface Sci.,* **2016**, *22,* 99–107.

[52] J. Marcus, D. Touraud, S. Prévost, O. Diat, T. Zemb and W. Kunz, *Phys. Chem. Chem. Phys.,* **2015**, *17,* 32528–32538.

[53] T. Lopian, S. Schöttl, S. Prévost, S. Pellet-Rostaing, D. Horinek, W. Kunz and T. Zemb, *ACS Cent. Sci.,* **2016**, *2,* 467–475.

[54] L. O. Copolovici and Ü. Niinemets, *Chemosphere,* **2005**, *61,* 1390–1400.

[55] Patent: US 2005/0065062, **2005**.

[56] G. G. Briggs, J. Agric. *Food Chem.,* **1981**, *29,* 1050–1059.

8 The impact of hydrotrope structuring on a polyoxometalate catalysed reaction

8.1 Preface and Abstract

This chapter was published in the peer-reviewed Journal *Physical Chemistry Chemical Physics (PCCP)* of the publisher Royal Society of Chemistry (DOI: 10.1039/C7CP02134H, this is also where the electronic supplementary information (ESI) can be found).
Thomas Buchecker and Sebastian Krickl contributed equally to the experimental work and to the writing of the manuscript:

- Dynamic light scattering: performed by Sebastian Krickl
- Small-and-wide-angle-X-ray-scattering: performed by Thomas Buchecker
- Conductivity measurements: performed by Thomas Buchecker, Sebastian Krickl
- Recording of phase diagrams: performed by Sebastian Krickl
- Small-angle-neutron-scattering: performed by Thomas Buchecker and Dr. Isabelle Grillo
- Oxygen solubility measurements: performed by Sebastian Krickl
- Synthesis and investigation of $H_5PMo_{10}V_2O_{40}$ catalyst including its impact on SFME: performed by Thomas Buchecker
- Chemical reactions and GC analysis: performed by Dr. Andreas Meyer, Sebastian Krickl, Thomas Buchecker
- Data analysis and writing of the paper was done by Thomas Buchecker and Sebastian Krickl
- Dr. Pierre Bauduin, Dr. Didier Touraud, Prof. Dr. Burkhard König, Prof. Dr. Arno Pfitzner and Prof. Dr. Werner Kunz contributed with fruitful discussions and supervised the experimental work and improved the manuscript.

Abstract. In this contribution, we *(i)* link the mesoscopic structuring of the binary structured solvent mixture H_2O/*tert*-butanol (TBA) to the kinetics and the efficacy of the oxidation of benzyl alcohol (BA) to the corresponding aldehyde catalysed by $H_5PMo_{10}V_2O_{40}$. We also compare the catalytic efficacy of this reaction in the mesoscopically structured solvent H_2O/TBA to an unstructured (or very weakly structured) solvent H_2O/ethanol (EtOH). In this context, we *(ii)* also give a methodological outline on how to study systematically the catalytic efficacy of chemical reactions as a function of the mesoscale structuring of a binary solvent. We demonstrate that the obtained yields of benzyl aldehyde depend on the type of mesoscopic structuring of the binary solvent H_2O/TBA. An elevated

catalytic performance of at least 100% is found for unstructured binary mixtures H$_2$O/TBA compared to compartmented binary mixtures H$_2$O/TBA. We conclude that compartmentation of both the organic substrate and the catalyst in TBA and water-rich micro phases seems to be unfavorable for the catalytic efficacy.
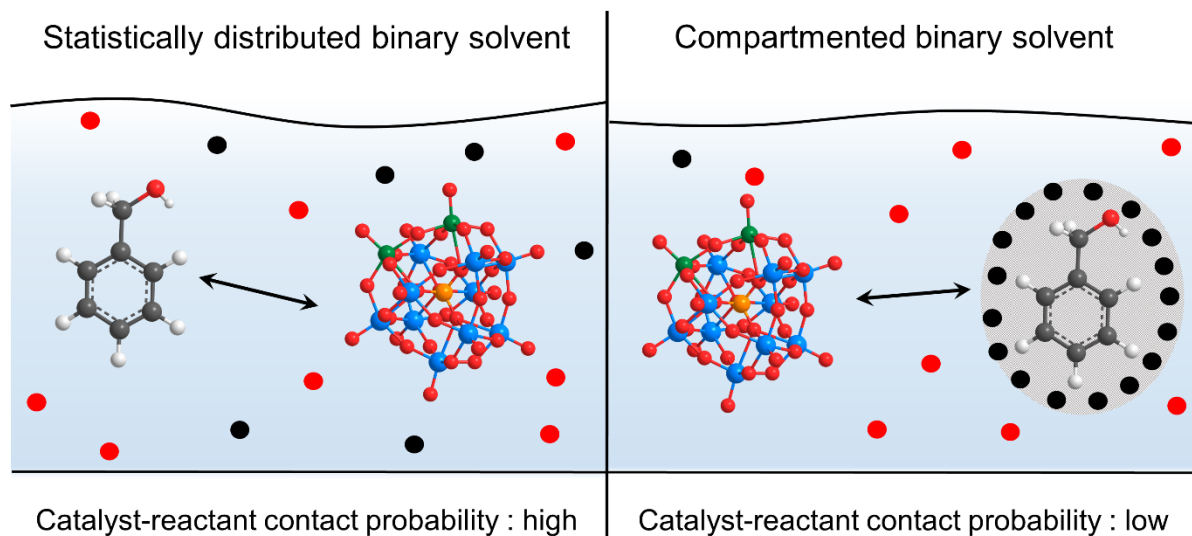
Figure 8.1: TOC illustrating the compartmentation of the POM catalyst and the benzyl alcohol reactant in a compartmented binary solvent. This compartmentation has a huge impact on the catalyst-reactant contact probability and the yield of the oxidation product of benzyl alcohol, *i.e.* benzyl aldehyde.

8.2 Introduction

The focus in synthesis and catalysis is often on the understanding of the reaction mechanism of isolated, *i.e.* molecularly dissolved, reacting molecules. In practice, such a situation can only be realized in gas phase reactions. However, most reactions are carried out in solutions using a neat one-component solvent or a mixture of solvents.[1] It is well known that a change of the solvent and the solvent (-solute) structure leads to large differences in yields and in stereoselectivity of the desired products.[2–4] Up to now, a common method to find the best solvent that leads to preferably high yields and/or the desired stereoselectivity is to screen the reaction in several solvents/solvent mixtures. It is evident that solvent screening inevitably requires considerable and time-consuming efforts. The obtained yields are then usually discussed merely in terms of solvent and solute polarity or polarizability or other molecular parameters. However, mesoscopic organization is often neglected in the context of chemical reactions, but solvent-structuring effects may play an important role in chemical reactivity.

Yet, the origin of solvent induced effects on reactivity of organic compounds is not trivial and comprises plenty of different aspects, like hydration, solvation and hydrophobic effects,[5–7] oligomer formation,[4,8] as well as transport properties like diffusion[9,10] and viscosity.[11] Another important

point is certainly the formation of mesoscale inhomogeneities or surfactant-free microemulsions (SFME) in the case of binary and ternary solvent mixtures, respectively. In recent studies and reviews, it is claimed that chemical reactivity in solutions is not (solely) related to the molecular nature of the solvent, but may also depend on the mesoscopic structuring of the system (solvents + reagents). Slight changes in this subtle solvent organisation may lead to very different reactivity patterns.[2,3]

Recent studies in the field of mesoscale structuring of liquid binary and ternary mixtures unveiled new aspects for the understanding of spontaneous self-assembly and weak interactions in structured liquids.[12–20] Even in macroscopically homogeneous binary mixtures (*e.g.* H_2O/TBA), it was found that compartmentation into hydrophilic and hydrophobic domains can be present with significant consequences for several thermodynamic properties, like vapour pressure, apparent molar volume, viscosity or solubilisation power.[21–23] It should be stressed that these interesting features allow new applications in research and industry.[21,24–26] Nevertheless, studies on the impact of these mesoscale structuring on reactivity are still rare. Although first investigations on structure-reactivity relationships in SFMEs go back to the late 1980s, when Khmelnitsky *et al.* investigated enzymatic reactions in SFME, few researchers continued in this field, mostly due to lacking experimental access to structural information on the microemulsion systems. In these pioneering studies, large differences in the enzymatic activity were found, depending on the composition of the ternary reaction medium consisting of water/2-propanol/n-hexane, and the different enzymatic activities were related to the presence of mesoscale inhomogeneities in the SFME.[27–31] Besides, there is only a small number of studies focusing on the influence of the solvent-, solvent-solute- or solute-structuring on the chemical reactivity patterns.[2–4,6,7,32–35]

Regarding these studies, it sounds reasonable that compartmentation phenomena (such as the mesoscale separation of substrates or of catalyst and substrate) should have a strong impact on chemical reactivity. Consequently, considering all this, in-depth studies of the structure-reactivity relationship between solvent structuring and chemical reactions are essential for a future "tailor-made" experimental design in chemical and biochemical synthesis.
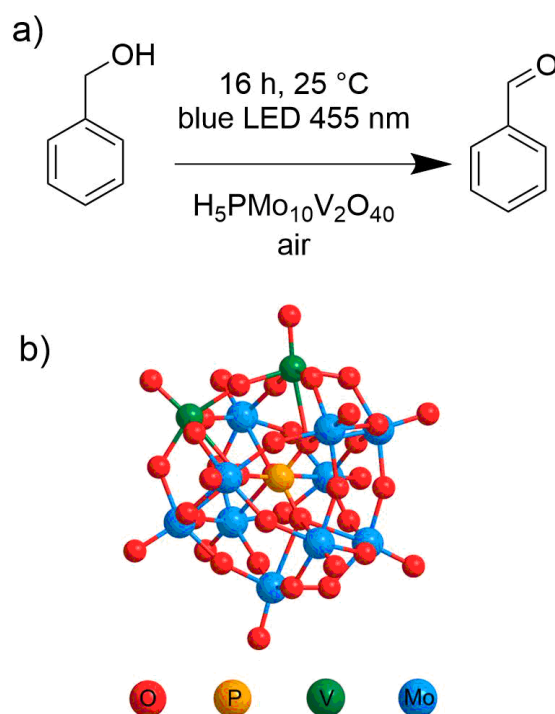
Figure 8.2: a) Catalytic oxidation reaction of benzyl alcohol (BA) to the corresponding aldehyde with the given parameters: 25 °C, 16 h, molecular oxygen as a sacrificial oxidizing agent and a blue LED (455 nm, 1.2 W) to trigger the reaction. b) Structure of the catalyst: α-Keggin type polyoxometalate $PMo_{10}V_2O_{40}^{5-}$ (POM) anion.

In the present contribution, we *(i)* show, with the help of one exemplary reaction, the impact of the mesoscale structuring on the chemical reactivity. For this purpose, we chose the visible light-mediated oxidation of benzyl alcohol (BA), with atmospheric oxygen as terminal oxidizing agent and with a photocatalytic active polyoxometalate $H_5PMo_{10}V_2O_{40}$ (POM), as a simple model reaction, see **Figure 8.2**. Within this context, we also provide *(ii)* a general approach for the investigation of such mesoscale inhomogeneities of binary solvent mixtures and their influence on the chemical reactivity. The reaction provides several advantages: both the light-mediated reaction and all structural investigations are performed at ambient conditions and in the presence of the catalyst. The reaction is only triggered upon irradiation with blue LED light. Oxygen is used as a cheap terminal oxidizing agent to re-oxidize the catalyst and to close the catalytic cycle. Furthermore, oxygen is supposed to have a negligible influence on the solution structure. Two different solvent systems are investigated: binary H_2O/TBA and H_2O/EtOH mixtures. H_2O/TBA is selected, because different regimes of mesoscale structuring can be found similar to surfactant containing solutions (*i.e.* solutions showing inhomogeneities in concentration in the supramolecular range). Depending on the H_2O/TBA ratio unstructured regimes, direct structuring (TBA clusters at low TBA concentration), bicontinuous structuring (for moderate TBA concentrations) and reverse structuring of H_2O in TBA (for high TBA concentrations) are supposed.[23] The type of mesoscale structuring in binary mixtures H_2O/TBA is then correlated with the yield of the oxidation product, *i.e.* benzaldehyde. H_2O/EtOH is chosen as a not

(or very weak) structured solvent mixture generally observed for all H_2O/EtOH ratios (molecular solution).

8.3 Experimental

Chemicals. Sodium bromide ($\geq$ 99.99%), sodium sulphite (95%) and benzyl alcohol ($\geq$ 99%) were purchased from Merck (Darmstadt, Germany) and *tert*-butanol ($\geq$ 99%) from Carl Roth (Karlsruhe, Germany). Ethanol ($\geq$ 99.8%), sodium metavanadate, $NaVO_3$, (99.9%), sodium molybdate, Na_2MoO_4, ($\geq$ 99.5%), sodium hydrogen phosphate, $Na_2HPO_4 \cdot 2\,H_2O$, ($\geq$ 98.5%), benzaldehyde ($\geq$ 99.5%) and cyclohexanone dimethyl ketal (CDK, 99%) were purchased from Sigma-Aldrich (Steinheim, Germany). All chemicals were used without further purification. Aqueous solutions were prepared using deionized water with a resistivity of 18 $M\Omega\cdot$cm.

Synthesis and characterization of the catalyst. The catalyst, $H_5PMo_{10}V_2O_{40}$ (POM), was synthesized according to a literature procedure given by Tsigdinos *et al.*,[36] and dried under vacuum. The product was characterized by IR (characteristic bands of POM: 1052 cm^{-1} (P–O bond), 954 cm^{-1} (terminal M–O), and 877 and 731 cm^{-1} (edge and corner bridging M–O–M).), ^{31}P-NMR (-3.11, -3.29, -3.38, -3.56), ICP-AES (ratio of P:Mo:V (calcd.) found: (1)1.0:(10)9.9:(2)2.0), TGA (8 H_2O), PXRD and compared to literature.[36,37] UV-Vis measurements were carried out at λ = 455 nm in 1 mm path length cells (Hellma 110-QS) using a Lambda 18 UV-Vis spectrometer from Perkin Elmer (Waltham, USA) to determine the molar extinction coefficient of $H_5PMo_{10}V_2O_{40}$ at 455 nm as applied for the catalytic reactions (ε(455 nm) = 1.2·105 L·dm/mol).

SANS. Small-angle neutron scattering (SANS) experiments were performed on the D33 instrument at the Institute Laue-Langevin (ILL), Grenoble, France.[38] The wavelength was set to 6 Å and two sample-to-detector distances 2 m and 5 m with collimation at 5.3 m for both configurations were used to cover a q-range from 0.08 to 0.47 Å^{-1}. A 7x10 mm^2 aperture was placed before the sample. The samples were filled in 1 mm thick Helma cells and thermostated at room temperature using a circulating water bath. The raw data were corrected for the electronic background and empty cell and were normalized on the absolute scale using the attenuated direct beam to calculate the incident flux using the ILL Lamp software.[39] The scattering intensity in cm^{-1} is plotted against the magnitude of q in nm^{-1}, and the curves were fitted with an Ornstein-Zernike (OZ) function: $I(q)$ = $I(0)/(1+\xi^2q^2)$.[18] ξ is a correlation length in nm^{-1}; $I(0)$ is the intensity for q = 0 and takes into account the scattering length density of the different species and volume fraction of each phase. Full fitting of the spectra is out of the scope of this paper.

DLS. DLS spectra were recorded using a temperature controlled CGS-3 goniometer system from ALV (Langen, Germany) equipped with an ALV-7004/FAST Multiple Tau digital correlator and a vertical-polarized 22-mW HeNe laser (wavelength λ = 632.8 nm). Before starting the measurement, all samples were filtered into dust-free cylindrical light scattering cells (10 mm outer diameter) using a

0.2 μm PTFE membrane filter. The sealed measurement cells could be directly placed into the measurement apparatus. Measurements were performed at a scattering angle of 90° after thermostating to 25 ± 0.1 °C. Data points were collected for 300 s. Aggregates in SFME are usually highly fluctuating and of no well-defined shape. Hence, we renounced calculations of the exact hydrodynamic radii. Instead, the DLS spectra were evaluated qualitatively with regard to their correlation coefficient and their lag time and an estimate of the size of the microscopic inhomogeneities is provided. (As a rule of thumb, it was assumed that a higher intercept of the correlation function for small lag times and larger lag times of the correlation function represent the more time-stable and more pronounced structuring inside the solution.)

Conductivity measurements. Conductivity measurements were carried out in a thermostated measurement cell (25 ± 0.2 °C) under permanent stirring using a low-frequency WTW inoLab Cond 730 conductivity meter connected with a WTW TetraCon 325 electrode (Weilheim, Germany). 20 g of each sample (pure hydrotrope or hydrotrope/benzyl alcohol mixtures of different mass fractions) was filled in the measurement cell and successively diluted with pure water. Each sample contained in addition 0.2 wt% sodium bromide to ensure a sufficient amount of charge carriers, which did not noticeably affect the microstructure or the miscibility gap present in the phase diagram. In cases where sodium bromide did not dissolve completely, a small amount of water was added to the pure hydrotrope or hydrotrope/benzyl alcohol mixture before the measurement was started

Oxygen solubility measurements. Measurements of the dissolved oxygen in binary mixtures of H_2O/EtOH and H_2O/TBA were carried out at 23 ± 0.2 °C using a TPS Aqua-D oxygen-meter connected with a TPS ED1 electrode (Brisbane, Australia). A two-point-calibration was performed against air and against a solution of 2 g sodium sulfite in 100 mL water. No corrections were made for the ambient air pressure. Samples (each 10 g) were stirred overnight in closed vials for ideal mixing and equilibration. By doing so, it was ensured that conditions for sample preparation were close to those of the reactivity measurements. Measurements themselves were performed without stirring and values were taken after an equilibration time of 30 min to ensure constant and reproducible results. Note that solutions are not necessarily saturated with oxygen, since conditions of sample preparation were adjusted to those of the reactivity experiments.

Oxidation reaction and GC analysis. Oxidation reactions were performed at 25 °C for monophasic compositions of the ternary system in the presence of 2 mM of $H_5PMo_{10}V_2O_{40}$. Glass vials suited for temperature-controllable blocks were used as sample containers and filled to a height of 1 cm (2 mL). This ensures light absorption of the catalyst to an efficacy of 92%. Samples were irradiated with blue LEDs ($\lambda = 455$ nm, 1.12 W) for 16 h, atmospheric oxygen was used as a sacrificial agent to complete the catalytic cycle. To this purpose, two needles were inserted into the septum-sealed vials to ensure the presence of enough oxygen. The amount of benzyl aldehyde was determined by GC measurements with CDK as internal standard. All oxidation reactions were performed for the

following conditions: *(i)* sample + catalyst + irradiation, *(ii)* sample + catalyst without irradiation, *(iii)* sample without catalyst + irradiation, *(iv)* sample without catalyst and without irradiation. Only in case *(i)*, detectable yields of benzyl aldehyde were obtained. Hence, it is ensured that benzyl alcohol and POM do not undergo a reaction during all structural investigations.

8.4   Results and Discussion

8.4.1   Determination of the reaction conditions and experimental design.

In order to relate the catalytic efficacy of a reaction to its mesoscopic structuring different experimental designs are possible: *(i)* Constant mole fractions of BA in a given solvent mixture or *(ii)* constant molar concentrations of BA in given solvent mixtures. The molar ratio of BA/catalyst has to remain constant (here 50:1) for both to obtain comparable results between the different reaction mixtures.

Constant *(i)* mole fractions provide the advantage of an equal ratio of BA molecules to solvent molecules. Nevertheless, due to a strong difference in the molar volumes of H_2O, TBA and BA, the molar concentration of benzyl alcohol increases with increasing H_2O mole fraction (and decreasing TBA mole fraction). Therefore, a constant mole fraction of BA has the "disadvantage" of a different molar concentration of BA. This, on the other hand, leads to an increasing catalyst concentration to keep the same BA/catalyst ratio of 50:1. Since the adsorption of the incident LED light (according to Beer-Lambert law) is strongly dependent on the concentration of the photocatalyst, solely highly dilute photocatalyst solutions ensure absorption below 99% of the incident light. Hence, only in the dilute region where Beer's law is applicable (usually around 100 µM up to 8 mM, strongly depending on the absorption coefficient of the catalyst, the thickness of the reaction solution, etc.), catalyst concentrations lead to reliable results for reactivity measurements. At higher concentrations, not all $H_5PMo_{10}V_2O_{40}$ catalysts are activated by irradiation, which affects the catalytic efficiency significantly.

In contrast to constant mole fractions of BA, constant concentrations of BA *(ii)* provide the disadvantage of a different molar fraction of benzyl alcohol. Nevertheless, constant concentrations of BA are practically most feasible since the catalyst concentration is kept constant due to a constant BA/catalyst ratio. Hence, the photo-catalyst concentration can be adjusted according to the Beer-Lambert law leading to 90 - 99% absorption of the incident LED light (c(POM) = 2 mM) with a constant BA/POM ratio (in our case to 50:1, *i.e.* c(BA) = 100 mM) for each solvent composition. Such low benzyl alcohol concentrations change the composition of the ternary system only marginally, *c.f.* ternary phase diagram **Figure 8.3a**. It was shown recently that such low BA concentrations enhance the structuring of H_2O/TBA solutions, but do not change the type of structuring of the binary mixture H_2O/TBA.[23] Statistical contact between the catalyst and BA should only be a function of the inherent mesoscopic structuring of the binary solvent H_2O/alcohol.

8.4.2   Influence of the catalyst on the ternary system H_2O/TBA/BA

Next, the location of the catalyst in the reaction mixture and its influence on the structuring of the solution was investigated. In case of no (or very weakly structured) H_2O/EtOH mixtures a homogenous distribution is assumed. For structured mixtures of H_2O/TBA with an inherent interface, the location of the catalyst is important for the catalytic process. For an effective catalysis, the catalyst as well as the organic substrate should be located at a surface/interface to enhance the contact probability of the catalyst and the organic substrate. Here, a polyoxometalate, *i.e.* $H_5PMo_{10}V_2O_{40}$ (POM), was chosen as a suitable catalyst as it *(i)* is highly water soluble, *(ii)* can be applied as photocatalyst and as *(iii)* similar polyoxometalates were recently shown to exhibit a strong propensity to adsorb at neutral soft interfaces covered with electrically neutral functional groups.[40,41] The catalyst was localized in the ternary structured liquid H_2O/TBA/BA by scattering experiments, see **Figure 8.3b**. In contrast to recent experiments, small-angle X-ray scattering (SAXS) could not be used as a technique to investigate the influence of additives on mesoscale structured liquids. POMs provide a strong scattering signal in SAXS due to their high scattering length density superimposing the scattering signal of the mesoscale structured liquid. Hence, SANS was chosen, as the scattering contrast between the POM and the solvent and solute is different. Solutions of POMs in D_2O provide a constant (low) scattering signal in SANS over the whole q-range, as it has a scattering length density close to D_2O and therefore does not produce a significant contrast. Therefore, SANS reflects only the change in the mesoscale structuring of H_2O/TBA/BA upon the addition of POM.
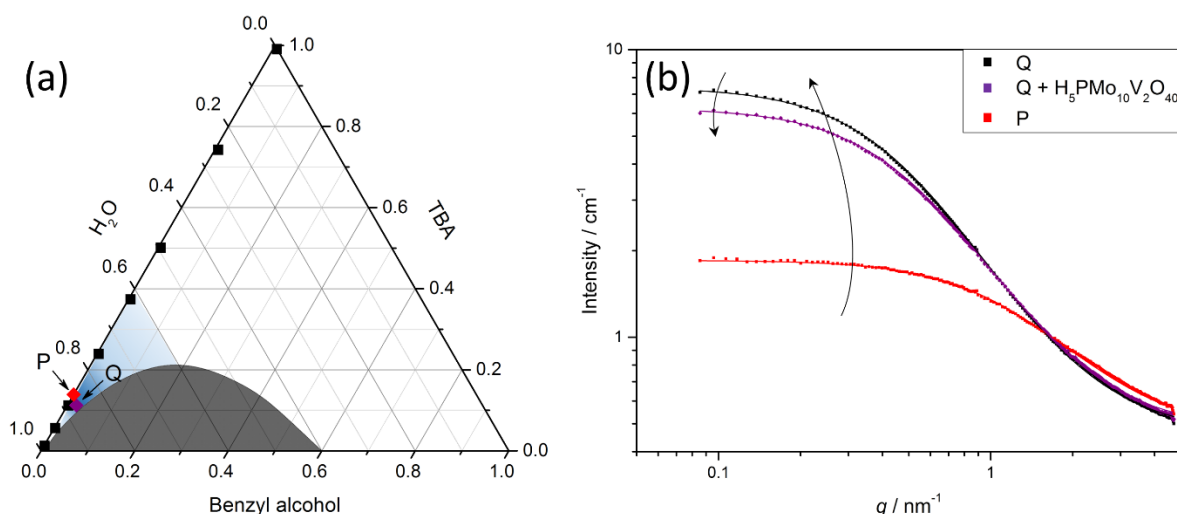
Figure 8.3: Ternary phase diagram of H_2O/TBA/BA at 25 °C provided in mole fractions. The most pronounced structured region of the binary solvent H_2O/TBA is indicated in blue. The black squares in (a) represent the ternary composition of the reaction mixtures. (b) Small-angle-neutron-scattering (SANS) patterns of two compositions at 25 °C indicated in a), *i.e.* compositions P (D_2O/TBA 0.86/0.14) and Q (D_2O/TBA/BA 0.87/0.11/0.02). For composition Q, the catalyst, $c(H_5PMo_{10}V_2O_{40})$ = 2 mM, was added (the same concentration as applied for the catalytic reactions).

Two different compositions (provided in mole fractions) were chosen, *i.e.* point P (D$_2$O/TBA 0.86/0.14) and Q (D$_2$O/TBA/BA 0.87/0.11/0.02), *c.f.* **Figure 8.3**. The binary composition P exhibits strong pre-structuring in the binary system H$_2$O/TBA, which has been previously investigated by SAXS and DLS experiments. Note that the difference between P and Q is only the substitution of TBA by benzyl alcohol. For composition Q, POM was added to ensure a concentration of c(H$_5$PMo$_{10}$V$_2$O$_{40}$) = 2 mM as used in reaction mixtures. The binary mixture D$_2$O/TBA provides a strong scattering signal indicating the presence of a structured binary liquid.[23] The substitution of TBA by BA leads to a strong increase of the scattered intensity. The addition of the POM catalyst to the ternary mixture leads to a decrease in the scattered intensity. As the POM does not produce a contrast, the decrease in the scattered intensity is only due to a change in the mesoscale structure of the TBA-rich pseudo-phase. To obtain qualitative information a correlation length of the nano-domains was obtained from the fitting of the SANS spectra using the Ornstein-Zernike formalism. The correlation length increases from 0.8 nm for the binary D$_2$O/TBA mixture up to 2.1 nm for the ternary D$_2$O/TBA/BA mixture. The correlation length of Q decreases from 2.1 to 1.9 nm in the presence of the POM catalyst.

The increase in the scattered intensity from the binary D$_2$O/TBA to the ternary D2O/TBA/BA mixture indicates a strengthening of the structuring and swelling of the aliphatic (or TBA/BA) rich pseudo-phase. The decrease in the scattered intensity and thus the decreasing correlation length of composition Q in the presence of the POM suggest an adsorption of the catalyst at the interface between the TBA-rich and the water-rich bulk phases and therefore a charging of the interface. The compressibility of the system decreases resulting in a decreasing scattered intensity. The decrease in the correlation length is also a consequence of the lower compressibility of the system: due to repulsive interactions between the domains, smaller aggregates are formed.[16] In an additional experiment, see ESI Fig. S1, the propensity of POM to adsorb at neutral soft interfaces covered with polar functional groups was also confirmed.[40] The adsorption of POM at the surface of non-ionic micelles was indeed proved using SAXS. From SANS and SAXS experiments, we conclude that hydrophilic POMs (fivefold negative charge) should mostly be solubilized in the water-rich pseudo-phase (rather than in the aliphatic-rich pseudo-phase) with a tendency to adsorb at the interface of the ternary structured liquid H$_2$O/TBA/BA.

8.4.3 Reactivity measurements

After clarifying the reaction conditions with a constant BA concentration and a constant H$_5$PMo$_{10}$V$_2$O$_{40}$ concentration, catalytic reactions were performed as a function of the H$_2$O/alcohol solvent ratio at constant BA concentration of 50 mM and 2 mM of POM. Remember that in case of H$_2$O/TBA, the type of mesoscopic structuring depends on the molar ratios (similar to a micellar system as indicated by the conductivity curves of binary solutions H$_2$O/alcohol), see **Figure 8.4a**: for low water contents no structuring, for increasing water content a reverse structuring (water in oil

droplets) is observed followed by a percolation threshold around $x(H_2O) \approx 0.6$ leading to a bicontiuous structuring. For high water contents around $x(H_2O) \approx 0.9$, a direct structuring is proposed followed by an unstructured region for very high water contents $x(H_2O) > 0.95$.[23] Note that reaction conditions (16 h and 25 °C) were chosen to prevent full conversion. Relatively high yields (up to 22%) of benzyl aldehyde are observed for the unstructured region at low water content, see **Figure 8.4a**. In the region where mesoscale inhomogeneities of H_2O/TBA mixtures are found, the yield of benzyl aldehyde decreases to 9-12% for identical reaction times and conditions.

Hence, the yield correlates with the formation and presence of mesoscale inhomogeneities. For low water content ($x(H_2O) < 0.3$), the binary mixture H_2O/TBA can be considered as an ideal solvent mixture, *i.e.* a molecular solution, with a distinct contact probability of POMs and BA. There, the yield of benzyl aldehyde doubles compared to structured regions. When the binary mixture H_2O/TBA starts to form mesoscale structures, the reactivity suddenly decreases. This observation may be the result of the different solubility of POMs and BA in the two pseudo-phases. Since the hydrophilic POMs are mainly dissolved in the water-rich pseudo-phase with a certain affinity to adsorb at interfaces, contact with the hydrophobic BA (mostly solubilized in the TBA-rich pseudo-phase) is reduced. In other words, the solvent compartmentation leads to a different local environment of the reactants, due to their different hydrophilicity/hydrophobicity. The different partition of catalyst and substrate causes a reduced statistical contact of both the catalyst and the substrate and a decrease in the yield of benzyl aldehyde. Accordingly, in case of higher water contents from $x(H_2O) \geq 0.3$, the hydrated POM catalyst and the surrounding water molecules may also be considered as a clathrate like structure. Such clathrate like structures are known to change the activity coefficients of water and the POM catalyst. Hence, in this particular case, a change of the mesoscale structure is also associated with a change in water and POM activity due to the formation of a POM/H_2O clathrate like structure. For very high water contents $x(H_2O) > 0.95$, the absence of mesoscale structure again leads to slightly elevated yields. The difference in absolute yields in the water-rich and TBA-rich unstructured regimes, respectively, may be the consequence of a lower O_2 solubility in the water-rich unstructured regime compared to the TBA-rich unstructured regime, see ESI Fig. S2 (remember that O_2 is the terminal oxidant and completes the catalytic cycle).
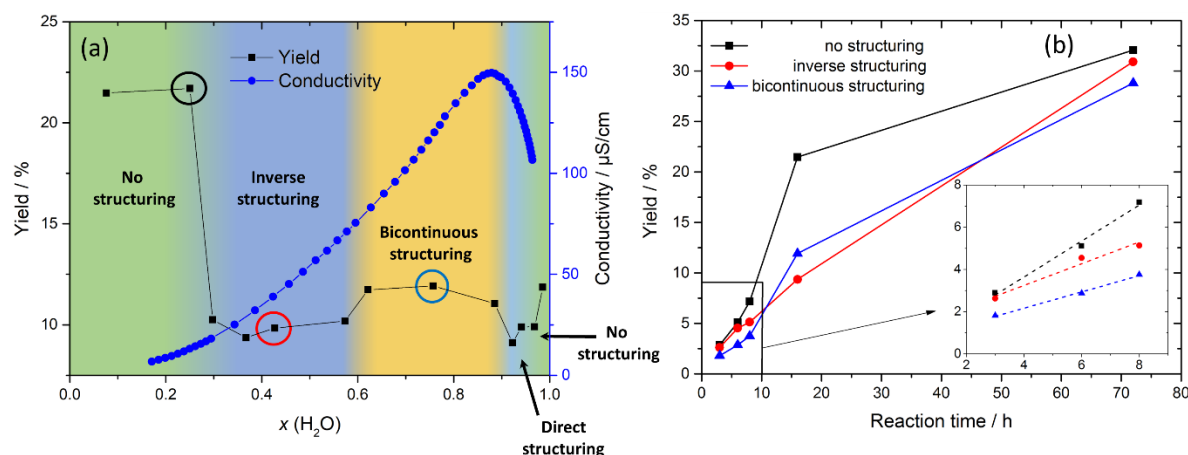
Figure 8.4: (a) Yields of the reaction product, benzyl aldehyde, determined by GC-FID with internal standard (black squares), and conductivity measurements for the binary system H_2O/TBA at 25 °C (blue squares) after 16 h. The amount of water of the binary H_2O/alcohol mixture is given in mole fractions of water $x(H_2O)$. Regions of different morphologies of water/TBA (derived from the conductivity curve) are represented by different colours. (b) Yield of benzyl aldehyde as a function of time for a representative unstructured mixture H_2O/TBA ($x(H_2O)$=0.25), an inversely structured mixture H_2O/TBA ($x(H_2O)$=0.37) and a bicontinuously structured mixture H_2O/TBA ($x(H_2O)$=0.76), as indicated by circles in (a). The inset shows linear fits (dotted lines) for the initial conversion for 3h $\leq t$ $\leq$ 8 h.

Within the structured region, *i.e.* $0.3 < x(H_2O) < 0.95$, the bicontinuous structuring provides a slightly higher yield compared to the direct and reverse structuring of H_2O and TBA suggesting that the extent of interface might have a subtle influence on the obtained yield. However, the slight differences in yield between 9-12% are not significant enough to draw a clear conclusion.

To further investigate the correlation between the mesoscale structuring of the solvent and the chemical reactivity, additional experiments were performed. *(i)* Initial reaction rates were measured for an unstructured, inversely and bicontinuously structured H_2O/TBA mixture and *(ii)* the reaction was carried out for 72 h instead of 16 h. As can be seen by the kinetics experiments, **Figure 8.4b**, initial reaction rates (obtained by linear fitting of data from 3h $\leq t \leq$ 8 h) found for structured H_2O/TBA mixtures (0.48 mmol/(L·h) for bicontinuous and 0.51 mmol/(L·h) for inverse structuring), are significantly lower than the one measured for the unstructured H_2O/TBA mixture (0.85 mmol/(L·h)). The corresponding H_2O/TBA solvent compositions are indicated with circles in **Figure 8.4a** and described in the figure caption. However, after 72 h, differences of the yield of benzyl aldehyde become less significant and almost constant, see ESI Fig. S3. Hence, with increasing reaction time, the correlation between solvent structure and yield becomes more and more blurred until the solvent structure does no longer influence the yield.

Consequently, the influence of solvent structuring should be considered as a kinetic effect on the initial period of the conversion. If solvent structuring is present, compartmentation of the reactants

within the solvent pseudo-phases can retard the chemical reaction. However, with increasing reaction time these compartmentations do no longer play a major role. This can be mainly attributed to the highly fluctuating nature of such mesoscale structures, which do not allow a complete suppression of the reaction. Thus, reaction yields converge with time to a nearly constant value, irrespective of the solvent structuring. It should be mentioned that the presence of solvent compartmentation remains unchanged irrespective of the benzyl aldehyde concentration as shown with DLS experiments, see ESI Fig. S4.

In addition, control experiments were performed *(i)* to compare the reactivity of benzyl alcohol in a mesoscopically structured solvent H_2O/TBA to a mesoscopically unstructured solvent H_2O/EtOH, *(ii)* to exclude side effects of different oxygen solubility in the H_2O/alcohol mixtures and *(iii)* to investigate the repeatability of all the experiments.

In case of the unstructured binary solvent H_2O/EtOH, 6-10% of benzyl aldehyde are obtained, see ESI Fig. S5. The yield slightly decreases with an almost linear dependence with increasing H_2O content. The linear decrease of the benzaldehyde yield with increasing H_2O content may result from different O_2 solubilities in H_2O and EtOH (see ESI Fig. S2). As no (or at least very weak) mesoscopic structuring is present in H_2O/EtOH mixtures, structure induced reactivity changes can be neglected in this case and no steep changes in the yields of benzyl aldehyde are observed by changing the solvent composition.

Furthermore, oxygen solubility measurements (measured for conditions close to those of the reaction) revealed that the oxygen solubility is higher in the alcohol-rich mixtures than in water (see ESI Fig. S2). Although these findings partly explain the higher initial reactivity in the TBA-rich regions, no direct correlation between oxygen solubility and reactivity or oxygen solubility and mesoscale structuring can be derived. It has to be noted that also the location of oxygen within the mesoscale structured solvents should play a major role for the reactivity, since it reoxidizes the catalyst. As the solubility of oxygen increases with increasing alcohol content we can expect that the repartition of O_2 may also be inhomogeneous within the two-pseudo-domains. Consequently, an analogous compartmentation effect of O_2 and the POM catalyst is expected, having strong consequences on the reoxidation of the catalyst. At this point, we also want to emphasize that the re-oxidation of the POM catalyst by O_2 is not the rate determining step. A depletion in oxygen would be indicated by a deeply black coloured solution of POMs (the well-known heteropolyblue species of reduced POMs with additionally incorporated electrons). However, all reaction mixtures were yellowish during all the reactions performed in this study. Hence, it can be ascertained that all reaction mixtures are saturated with oxygen over the whole period.[42]

Effects of viscosity[22,43] on the other hand can be neglected for both systems, since there is no correlation between viscosity and reactivity for neither the H_2O/TBA nor the H_2O/EtOH mixtures (see ESI Fig. S6).

As a last point, the repeatability of the reactions was probed. To this purpose, the reactions at $t =$ 72 h were performed three times under the same conditions for every binary solvent composition H_2O/TBA. The standard deviations of the obtained yields were calculated for each solvent composition. We found standard deviations for the absolute yield ranging from ± 0.7% to ± 3.9% (average value of the standard deviation ± 1.9%) after 72 h, see Fig. S3. We expect the standard deviation at 16 hours to be similar to the standard deviations found for 72 hours. Therefore, we assume an average value of the standard deviation of the yields after 16 hours to be at maximum ± 4% (absolute yield percent), which is small enough not to question our conclusions.

8.5 Conclusion

We present a systematic study of the influence of mesoscale structuring on a simple model photo-catalytic oxidation reaction. We linked the mesoscopic structuring of the binary structured solvent H_2O/TBA to the catalytic efficacy and to the reaction kinetics of the photo-oxidation of benzyl alcohol to the corresponding aldehyde with $H_5PMo_{10}V_2O_{40}$ as catalyst. We also compared the catalytic efficacy of this reaction in the mesoscopically structured solvent H_2O/TBA to the mesoscopically unstructured (or very weakly structured) solvent H_2O/EtOH. SANS and conductivity measurements unveil that the addition of BA and the catalyst, $H_5PMo_{10}V_2O_{40}$, do not significantly affect the mesoscale structuring of such structured systems. Furthermore, SANS studies suggest that the POM catalyst adsorbs at the interface of the structured system.

Reactivity measurements showed that in case of the binary structured solvent H_2O/TBA, the initial formation of benzyl aldehyde strongly depends on the mesoscopic structuring of the binary solvent H_2O/TBA. In H_2O/TBA mixtures, mesoscale structuration was found to be unfavourable for the photo-chemical reactivity, compared to unstructured molecular solutions. We conclude that compartment of both the organic substrate and the catalyst are unfavourable for the catalytic efficacy. These observations are further reflected by initial rate constant measurements for an unstructured, an inversely structured and a bicontinuously structured mixture H_2O/TBA. However, we further showed that the correlation between solvent structure and reaction rates are even more complex. The correlation of solvent structure and yield must be considered as a kinetic effect, which may change with increasing reaction times, where yields equalize over the whole miscibility range of H_2O/TBA. We explain this observation by the highly fluctuating nature of the mesoscale solvent structures.

In case of the unstructured (or very weakly structured) binary solvent H_2O/EtOH, a linear increase of the yield of benzyl aldehyde is observed for increasing EtOH/H_2O ratios. This linear increase is explained by a higher O_2 solubility in alcohol-rich media.

In summary, we demonstrated that the chemical reactivity in solutions is not solely correlated to the molecular properties of the solvent, but that mesoscale structuring of the solvent plays a major role.

Consequently, we suggest reconsidering the general approach of solvent selection for chemical reactions. Mesoscale structuring in solvent mixtures affects the kinetics of chemical reactions and should be considered for optimizing reaction times and reaction conditions.

8.6 Bibliography

[1]   M. B. Smith and J. March, *March's Advanced Organic Chemistry: Reactions, Mechanisms, and Structure*, John Wiley & Sons, Inc., Hoboken, New Jersey, 7th edn., **2013**.

[2]   L. O. Kononov, *RSC Adv.,* **2015**, *5,* 46718–46734.

[3]   G. Cainelli, P. Galletti and D. Giacomini, *Chem. Soc. Rev.,* **2009**, *38,* 990–1001.

[4]   L. O. Kononov, in Advances in Chemistry Research, Nova Science Publishers, Inc., Hauppauge, New York, **2013**, *18,* 143–177.

[5]   Y. L. Khmelnitsky, A. V. Levashov, N. L. Klyachko and K. Martinek, *Enzyme Microb. Technol.,* **1988**, *10,* 710–724.

[6]   R. Breslow, *Acc. Chem. Res.,* **1991**, *24,* 159–164.

[7]   S. Otto and J. B. F. N. Engberts, *Org. Biomol. Chem.,* **2003**, *1,* 2809–2820.

[8]   J. N. Israelachvili, Intermolecular and Surface Forces, Elsevier, Inc., Amsterdam, *3rd edn.,* **2011**.

[9]   D. F. Calef and J. M. Deutch, *Ann. Rev. Phys. Chem.,* **1983,** *34,* 493–524.

[10]   D. S. Achilias, Macromol. *Theory Simulations,* **2007**, *16,* 319–347.

[11]   W. Adam and A. V. Trofimov, *Acc. Chem. Res.,* **2003**, *36,* 571–579.

[12]   O. Diat, M. L. Klossek, D. Touraud, B. Deme, I. Grillo, W. Kunz and T. Zemb, *J. Appl. Crystallogr.,* **2013**, *46,* 1665–1669.

[13]   V. Fischer, J. Marcus, D. Touraud, O. Diat and W. Kunz, *J. Colloid Interface Sci.,* **2015,** *453,* 186–193.

[14]   M. L. Klossek, D. Touraud, T. Zemb and W. Kunz, *ChemPhysChem,* **2012**, *13,* 4116–4119.

[15]   T. Lopian, S. Schöttl, S. Prévost, S. Pellet-Rostaing, D. Horinek, W. Kunz and T. Zemb, *ACS Cent. Sci.,* **2016**, *2,* 467–475.

[16]   J. Marcus, D. Touraud, S. Prévost, O. Diat, T. Zemb and W. Kunz, *Phys. Chem. Chem. Phys.,* **2015**, *17,* 32528–38.

[17]   S. Schöttl, J. Marcus, O. Diat, D. Touraud, W. Kunz, T. Zemb and D. Horinek, *Chem. Sci.,* **2014**, *5,* 2909–3340.

[18]   T. Zemb, M. L. Klossek, T. Lopian, J. Marcus, S. Schöttl, D. Horinek, S. Prevost, D. Touraud, O. Diat, S. Marčelja and W. Kunz, Proc. *Natl. Acad. Sci. U. S. A.,* **2016**, *113,* 4260–4265.

[19]   D. Subramanian and M. A. Anisimov, *Fluid Phase Equilib.,* **2014**, *362,* 170–176.

[20]   M. Sedlák and D. Rak, *J. Phys. Chem. B,* **2014,** *118,* 2726–2737.

[21]   J. Marcus, M. L. Klossek, D. Touraud and W. Kunz, *Flavour Fragr. J.,* **2013,** *28,* 294–299.

[22] P. K. Kipkemboi and A. J. Easteal, *Can. J. Chem.,* **1994**, *72,* 1937–1945.

[23] T. Buchecker, S. Krickl, R. Winkler, I. Grillo, P. Bauduin, D. Touraud, A. Pfitzner and W. Kunz, *Phys. Chem. Chem. Phys.,* **2017**, *19,* 1806–1816.

[24] R. F. Hankel, P. E. Rojas, M. Cano-Sarabia, S. Sala, J. Veciana, A. Braeuer and N. Ventosa, *Chem. Commun.,* **2014**, *50,* 8215–8218.

[25] U. Mohorič, A. Beutner, S. Krickl, D. Touraud, W. Kunz and F.-M. Matysik, *Anal. Bioanal. Chem.,* **2016**, *408,* 8681–8689.

[26] V. Tchakalova, T. Zemb and D. Bencze´di, *Colloids Surfaces A Physicochem. Eng. Asp.,* **2014**, *460,* 414–421.

[27] Y. L. Khmelnitsky, R. Hilhorst and C. Veeger, *Eur. J. Biochem.,* **1988**, *176,* 265–271.

[28] Y. L. Khmelnitsky, A. K. Gladilin, I. N. Neverova, A. V. Levashov and K. Martinek, *Collect. Czech. Chem. Commun.,* **1990**, *55,* 555–563.

[29] Y. L. Khmelnitsky, I. N. Zharinova, I. V. Berezin, A. V. Levashov and K. Martinek, Ann. N. Y. *Acad. Sci.,* **1987**, *501,* 161–164.

[30] Y. L. Khmelnitsky, A. Van Hoek, C. Veeger and A. J. W. G. Visser, *J. Phys. Chem.,* **1989**, *93,* 872–878.

[31] M. Zoumpanioti, H. Stamatis, V. Papadimitriou and A. Xenakis, *Colloids Surfaces B Biointerfaces,* **2006**, *47,* 1–9.

[32] O. A. Kazantsev, D. S. Baruta, K. V. Shirshin, A. P. Sivokhin and D. M. Kamorin, *Russ. J. Phys. Chem. A,* **2010**, *84,* 2071–2076.

[33] O. A. Kazantsev, A. P. Sivokhin, D. S. Baruta, K. V. Shirshin, D. M. Kamorin and A. I. Kvashennikov, *Polym. Sci. Ser. D,* **2011**, *4,* 284–288.

[34] G. B. Manelis, G. V. Lagodzinskaya, A. I. Kazakov, A. V. Chernyak, N. G. Yunda and L. S. Kurochkina, *Russ. Chem. Bull.,* **2013**, *62,* 994–1002.

[35] R. P. Tiger, M. A. Levina, S. G. Entelis and M. A. Andreev, *Kinet. Catal.,* **2002**, *43,* 662–666.

[36] G. A. Tsigdinos and C. J. Hallada, *Inorg. Chem.,* **1968,** *7,* 437–441.

[37] D. Barats-Damatov, L. J. W. Shimon, Y. Feldman, T. Bendikov and R. Neumann, *Inorg. Chem.,* **2015**, *54,* 628–634.

[38] C. D. Dewhurst, I. Grillo, D. Honecker, M. Bonnaud, M. Jacques, C. Amrouni, A. Perillo-Marcone, G. Manzin and R. Cubitt, *J. Appl. Crystallogr.,* **2016**, *49,* 1–14.

[39] https://www.ill.eu/instruments-support/computing-for-science/cs-software/all-software/lamp/.

[40] B. Naskar, O. Diat, V. Nardello-Rataj and P. Bauduin, *J. Phys. Chem. C,* **2015**, *119,* 20985–20992.

[41] T. Buchecker, X. LeGoff, B. Naskar, A. Pfitzner, O. Diat and P. Bauduin, *Chem. - A Eur. J.,* **2017**, *23,* 8434-8442.

[42]   M. T. Pope and A. Müller, *Angew. Chem. Int. Ed. Engl.*, **1991**, *30,* 34–48.

[43]   I. S. Khattab, F. Bandarkar, M. A. A. Fakhree and A. Jouyban, *Korean J. Chem. Eng.,* **2012**, *29,* 812–817.
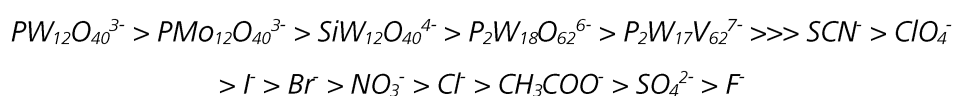
9 Conclusion and Outlook

The first part of this PhD thesis portrayed the interaction between the most common representatives of POMs, *i.e.* Keggin ($PW_{12}O_{40}^{3-}$, $PMo_{12}O_{40}^{3-}$, $SiW_{12}O_{40}^{4-}$, $PMo_{10}V_2O_{40}^{5-}$) and Dawson anions ($H_6P_2W_{18}O_{62}$, $K_6P_2W_{18}O_{62}$ $K_7P_2W_{17}VO_{62}$) with *(i)* self-assembled uncharged interfaces, *(ii)* ethylene glycol oligomers and *(iii)* PNIPAM polymers, called the organic substrates hereafter.

POMs and organic molecules in water. The results of the **chapter 3 *"Polyoxometalates and the Hofmeister series"***, suggest that several features account for the super-chaotropic behaviour of anions: delocalized charges and a large size of the anion, typically at least in the nm range (nano-ions), to provide a high gain of entropy associated with the adsorption process on the organic substrate.[1,2] This high entropic gain during the adsorption process is associated with the release of hydration water molecules from the nano-ion and from the organic substrate to the water bulk phase. The strength of the super-chaotropic behaviour is related to the volume charge density ρ of the anion, *i.e.* the lower the ρ the higher the super-chaotropy of POMs. A stronger anion hydration, due to a higher ρ, leads to a less efficient dehydration (lower entropy gain) during the adsorption process because less water molecules are released.[2] The study suggested that the anion polarizability influences the super-chaotropy of POMs ($PMo_{12}O_{40}^{3-}$ vs. $PW_{12}O_{40}^{3-}$) to a much smaller extent. Note that dispersion forces (originated by a high anion polarizability) were often supposed to be the origin of specific ion effects.[3,4] The low *pH* of aqueous solutions containing the acid form of POMs influences the super-chaotropy of POMs only marginally. This fact contradicts the hypothesis made previously by other authors that the extremely low *pH* of nH^+POM^{n-} (*e.g.* $3H^+PW_{12}O_{40}^{3-}$) causes the formation of oxonium ions at the organic substrate (*e.g.* protonation of the ethylene glycol CH_2-OH^+-CH_2) and the subsequent formation of a contact ion pair between the POM^{n-} and the organic substrate^{n+}.[5,6]

Hence, we are now able to extend the renown Hofmeister series of anions not only to two Keggin type POMs as shown by Naskar *et al.*[1] but also to various POM architectures (spherical Keggin POMs and prolate spheroidal Dawson POMs) with different sizes (1.0 nm diameter for Keggin POMs and 1.2 x 1.0 nm for Dawson POMs), different counter ions (H^+, K^+) and different polarizabilities ($H_3PW_{12}O_{40}$ vs $H_3PMo_{12}O_{40}$):

$$PW_{12}O_{40}^{3-} > PMo_{12}O_{40}^{3-} > SiW_{12}O_{40}^{4-} > P_2W_{18}O_{62}^{6-} > P_2W_{17}V_{62}^{7-} >>> SCN^- > ClO_4^-$$
$$> I^- > Br^- > NO_3^- > Cl^- > CH_3COO^- > SO_4^{2-} > F^-$$

The studies presented in **chapter 4 *"From nano-assemblies in water to crystal formation by electrostatic screening"*** and in **chapter 5 *"Single crystal to single crystal transformation in**

a POM based composite crystal" confirmed that $PW_{12}O_{40}^{3-}$ and $PMo_{12}O_{40}^{3-}$ also interact with the ethylene glycol oligomers in H_2O, *i.e.* the bare hydrophilic head of the C_8EO_4 surfactant studied in **chapter 3 *"Polyoxometalates and the Hofmeister series"***. SAXS and NMR studies revealed that *(i)* only EO_x ($x > 4$) interact with $PW_{12}O_{40}^{3-}$ and *(ii)* only the inner $HO\text{-}CH_2\text{-}CH_2\text{-}$**(O-CH$_2$-CH$_2$-O-CH$_2$-CH$_2$)$_x$**$\text{-}CH_2\text{-}CH_2\text{-}OH$ ether groups are involved in the adsorption of $PW_{12}O_{40}^{3-}$ and $PMo_{12}O_{40}^{3-}$ on EO_x (the terminal $\text{-}CH_2\text{-}CH_2\text{-}OH$ groups are unaffected by the adsorption process). Ether groups are less hydrated than terminal $\text{-}OH$ groups allowing them to be dehydrated more easily. Furthermore, the selective adsorption of $PW_{12}O_{40}^{3-}$ on EO_x with $x > 4$ suggests that *(i)* multipolar interactions play a crucial role in the formation of POM-EO_x assemblies (chelate effect!) and that *(ii)* enough hydration water molecules must be released to the water bulk phase to yield a sufficient entropy gain promoting an adsorption.

> *Hence, the adsorption of POMs on organic molecules and surfaces in water*
> *is an entropically driven, non-specific adsorption process.*

In this context, our conclusions are also an extension of Collins' concept of matching water affinities, observed between two oppositely charged particles (ions) and the conclusion of Leontidis *et al.* of a general ion-lipid competition for hydration water and the conclusions drawn by Schwierz *et al.* and Horinek *et al.*:

> *The experimental findings of the present thesis allow to extend these con-*
> *cepts to the interaction of polyoxometalates with uncharged but hy-*
> *drated/polar molecules or surfaces: both, the POM and the organic substrate*
> *should provide many hydration water molecules that can be dehydrated eas-*
> *ily, i.e. both entities should feature a low free energy of hydration, to form a*
> *"contact ion-organic substrate pair".*

In a next step, it is necessary to investigate if lacunary POMs with an anisotropic charge distribution also influence the CP of an aqueous solution of C_8EO_4. It should be clarified if the super-chaotropy of lacunary POMs is coherent with the extension of the Hofmeister series found for Keggin or Dawson type POMs. It is further necessary to investigate the impact of mono-, di- or tri (Niobium or Vanadium; no lacunary) substituted POMs on the CP of an aqueous solution of C_8EO_4. Such a study should clarify the role of isotropic charge distribution on the super-chaotropy of POMs. An isotropic charge distribution is also a basic requirement for a high ion polarizability which itself is often considered to be necessary to promote an adsorption of POMs on hydrated surfaces.

Functional materials of POMs with ethylene glycol and PNIPAM. As shown in **chapter 4 "From nano-assemblies in water to crystal formation by electrostatic screening",** POMs also

adsorb on single hydrated organic EO_x oligomers in aqueous solution to yield POM-EO_x nano-assemblies which are stabilized by electrostatic repulsion due to the negative charge of POMs. Addition of NaCl, aiming at screening the inter-nano-assemblies repulsions, induces aggregation and formation of hybrid crystalline POM-EO_x-Na materials. This new method to build POM-organic composite materials without covalent or electrostatic grafting of the POM and an organic molecule was called *"the electrostatic screening method"*. The combination of a single-crystal X-ray study with SAXS/SANS and NMR experiments allowed to relate the structure model obtained from the $PW_{12}O_{40}{}^{3-}$ - EO_5/EO_6 - $3Na^+$ single crystals to the structure of the POM-oligomer nano-assemblies solubilized in aqueous solution (EO_x - $PW_{12}O_{40}{}^{3-}$ - EO_x). In **chapter 4.4.5 *The versatility of the "electrostatic screening method"*** it was also shown that this electrostatic screening method is highly versatile by in total three different POM/EO_x composite crystals containing *(i)* different POMs ($H_3PW_{12}O_{40}$ and $H_3PMo_{12}O_{40}$), *(ii)* different EO_x chain lengths (EO_5 + EO_6 and EO_{11}) and *(iii)* different (mixed) counter ions (Na^+ and K^+-H^+-H^+). This versatility is also an onset for the synthesis of several new hybrid materials with different PEG-POM composition and different functionalities as it was shown in the framework of this thesis that it is possible to form a vast variety of PEG-POM hybrid crystals which were not investigated yet. It was also demonstrated that composite crystals formed by the electrostatic screening method display uncharted features: upon irradiation of $PMo_{12}O_{40}{}^{3-}$ - EO_5/EO_6 - $3Na^+$ hybrid crystals with visible light, the $PMo_{12}O_{40}{}^{3-}$ photocatalyst promotes the selective oxidation of only one (out of four available) terminal hydroxyl function -CH_2-OH of EO_6 to the corresponding aldehyde -CH=O in the crystalline state. During this process, the crystal colour changes from clear yellowish to dark black due to the formation of the well-known heteropolyblue-polyoxometalate making these crystals suitable for potential applications in sensor technology. So far, this concept is not fully understood and several open questions should be answered: How extendable is this solid-state oxidation principle? Can it also be observed for hypothetical PMo^{3-} - EO_{11} - K^+-H^+-H^+ crystals? Is a special geometry and a close vicinity of PMo^{3-} and the carbon atom attached to the hydroxyl group required to promote a chemical reaction in the solid state? It could be expected that also other POM-based hybrid materials may be photo-responsive since the "electrostatic screening approach" to produce new functional POM based hybrid materials is highly versatile.

> *Hence, the new versatile "soft" electrostatic screening route allows to access*
> *new functional POM - organic composites featuring uncharted fields of pho-*
> *tochemistry.*

The adsorption of POMs on organic molecules can be generalized to any kinds of weakly hydrated (the term refers to low free energy of hydration) molecules or oligomers as shown for the interaction of PNIPAM with $H_3PW_{12}O_{40}$, $H_3PMo_{12}O_{40}$ and $H_4SiW_{12}O_{40}$. An adsorption of $PW_{12}O_{40}{}^{3-}$ on PNIPAM leads first to the formation $PW_{12}O_{40}{}^{3-}$-PNIPAM globular objects and eventually to the formation of

stimuli responsive (salt and temperature stimulus) $PW_{12}O_{40}^{3-}$/PNIPAM/$PW_{12}O_{40}^{3-}$ and $PMo_{12}O_{40}^{3-}$/PNIPAM/$PMo_{12}O_{40}^{3-}$ trilayer 2D nano-sheets via self-assembly of PNIPAMx000 (x = 5, 7, 10). Again, POM and PNIPAM are not covalently linked in the nanocomposite sheets as it is the case for EO_x and POM in hybrid crystals thereof. A further feature of these self-assembled PNIPAM nano-sheets is that their thickness can be tuned by the PNIPAM chain length. It should be stressed at this point that this is the first study reporting the self-assembly of short chain PNIPAM polymers which is the most studied thermo-sensitive and stimuli responsive polymer.

This study also shows the versatility of **soft** POM based hybrid materials which can be constructed by exploiting the POMs' super-chaotropic effect. It was already shown that $PW_{12}O_{40}^{3-}$ interacts with several other polymers, such as polyvinyl alcohol, polypropylene glycol, serum bovine albumin, *etc*. So far, the supramolecular assemblies formed by these polymers and POMs remain unexplored and should be investigated in the future. An open question which should also be answered is: Why do trivalent POMs ($PMo_{12}O_{40}^{3-}$ and $PW_{12}O_{40}^{3-}$) self-organize preferentially in **2D close packed layers** as observed in case of *(i)* $PW_{12}O_{40}^{3-}$ - EO_5/EO_6 - $3Na^+$ crystals or *(ii)* $PW_{12}O_{40}^{3-}$ - EO_{11} - K^+-H^+-H^+ crystals, or *(iii)* soft $PW_{12}O_{40}^{3-}$/PNIPAM/$PW_{12}O_{40}^{3-}$ and $PMo_{12}O_{40}^{3-}$/PNIPAM/$PMo_{12}O_{40}^{3-}$ trilayer 2D nano-sheets, or *(iv)* in case of the famous etherate formation, *etc.*?

The second part of this PhD thesis dealt with the application of $H_5PMo_{10}V_2O_{40}$ as photocatalyst in two mesoscopically structured ternary solvents H_2O/EtOH/benzyl alcohol and H_2O/*tert*-butanol/benzyl alcohol. The idea was to take advantage of the super-chaotropy of POMs and their adsorption on organic molecules and interfaces in weakly organized binary (or ternary) solvents, *i.e.* to "adhere" the POM photocatalyst on a poorly organized H_2O/benzyl alcohol interface stabilized by alcohol molecules analogous to "micellar catalysis" without surfactants. A close vicinity of $PMo_{10}V_2O_{40}^{5-}$ and benzyl alcohol should then preferably lead to fast reaction rates for the catalytic oxidation of benzyl alcohol to the corresponding benzyl aldehyde. Therefore, several solvent mixtures of H_2O/alcohol were investigated in **chapter 7 "Structuring of Hydrotropes in water"**. We have chosen a series of short-chain alcohols as hydrotropes and benzyl alcohol (among others) to be solubilised. Very weak pre-structuring is found for binary EtOH/H_2O and NPA/H_2O mixtures. Structuring of H_2O/alcohol mixtures is most developed for binary NPA/H_2O and TBA/H_2O mixtures making them a suited binary solvent for the POM catalysed reaction according to the present considerations. Analogous to surfactant containing solutions three different types of mesoscale structuring in TBA/H_2O mixtures were postulated for binary structured TBA/H_2O mixtures: direct (but weakly pronounced) microemulsions, *i.e.* TBA cluster in H_2O, bicontinuous domains and reverse microemulsions, *i.e.* H_2O cluster in TBA. Besides these findings we additionally found that pre-structuring of binary H_2O/TBA mixtures leads to a high solubilisation power for poorly water miscible components compared to non-structured mixtures H_2O/EtOH or H_2O/IPA. This difference in solubilisation power

was linked to *(i)* the formation of mesoscale structures in case of EtOH and IPA and to *(ii)* the extension of pre-structures in case of NPA and TBA. Furthermore, three different solubilisation mechanisms could be identified: bulk solubilisation, interface solubilisation and the combination of both.

In **chapter 8** *"The impact of hydrotrope structuring on a polyoxometalate catalysed reaction"*, the type of mesoscopic structuring of the most structured binary solvent mixture H_2O/*tert*-butanol (TBA) is finally linked to the kinetics and the efficacy of the oxidation of benzyl alcohol to the corresponding aldehyde catalysed by $PMo_{10}V_2O_{40}{}^{5-}$. We demonstrated that the obtained yields of benzyl aldehyde depend on mesoscopic structuring of the binary solvent H_2O/TBA. An elevated catalytic performance of at least 100% is found for unstructured binary mixtures H_2O/TBA compared to compartmented binary mixtures H_2O/TBA. Although SAXS measurements on a solution containing $H_5PMo_{10}V_2O_{40}$ and Brij35 ($C_{12}EO_{23}$) showed that $PMo_{10}V_2O_{40}{}^{5-}$ adsorbs on very hydrophilic surfaces, the adsorption at the interface of highly fluctuating SFMEs (here H_2O/TBA/benzyl alcohol) is indeed very weak. In case of the interaction of $PW_{12}O_{40}{}^{3-}$ with EO_x it was also demonstrated that $PW_{12}O_{40}{}^{3-}$ only interacts with EO_x, with $x > 4$. Hence, an explanation could be that *(i)* the entropic gain due to the dehydration of TBA and benzyl alcohol is too low to promote an adsorption of $PMo_{10}V_2O_{40}{}^{5-}$ on TBA/benzyl alcohol clusters and *(ii)* multipolar interactions of $PMo_{10}V_2O_{40}{}^{5-}$ with TBA and benzyl alcohol molecules are not possible. Hence, we assume that the repartition of $PMo_{10}V_2O_{40}{}^{5-}$ between the water bulk phase and the interface is rather shifted to the water bulk phase leading to a separation of the $PMo_{10}V_2O_{40}{}^{5-}$ photocatalyst and benzyl alcohol. We conclude that compartmentation of both benzyl alcohol and $PMo_{10}V_2O_{40}{}^{5-}$ in TBA and water-rich micro phases seems to be unfavourable for the catalytic efficacy.

> *Hence, the idea of adhering the POM photocatalyst on an ill-defined, highly fluctuating H_2O/benzyl alcohol interface stabilized by tert-butanol molecules analogous to "micellar catalysis" was not possible.*

Nevertheless, the adsorption of POMs on hydrated interfaces or molecules may be used for different catalytic applications since it was shown by Bernadini *et al.* that the catalytic performance of POMs may be completely different when they are adsorbed at interfaces.[7] In their work they highlighted the photochemical oxidation of water and reduction of polyoxometalate anions at diethylether interfaces. Hence, in future investigations the super-chaotropic effect should be exploited to adhere POMs on *(i)* self-assembled nanoscopic interfaces, *e.g.* micellar catalysis, on *(ii)* macroscopic liquid-liquid interfaces, *e.g.* H_2O-ether interfaces, and on *(iii)* coated surfaces of microreactors. Especially *(iii)* is a promising approach since microreactors provide the advantage of a high POM catalyst loading on a hydrophilic surface of the reactor with the possibility to excite POMs photochemically with a higher yield compared to a common batch reaction due to the short penetration depth of light in an aqueous medium.

Bibliography

[1]   B. Naskar, O. Diat, V. Nardello-Rataj, P. Bauduin, *J. Phys. Chem. C* **2015**, *119,* 20985–20992.

[2]   T. Buchecker, P. Schmid, S. Renaudineau, O. Diat, A. Proust, A. Pfitzner, P. Bauduin, *Chem. Commun.* **2018,** *54*, 1833–1836.

[3]   W. Kunz, Specific Ion Effects, *World Scientific*, **2010.**

[4]   B. W. Ninham, V. Yaminsky, *Langmuir* **1997**, *13,* 2097–2108.

[5]   I. P. Alimarin, F. P. Sudakov, V. I. Klitina, *Russ. Chem. Rev.* **1965**, *34,* 574–584.

[6]   E. Dorokhova, I. P. Alimarin, *Russ. Chem. Rev.* **1979**, *48,* 502.

[7]   G. Bernadini, A. G. Wedd, G. Zhao, A. M. Bond, *PNAS* **2012**, *109*, 11552-11557.

DECLARATION

Hiermit versichere ich an Eides statt, dass die vorliegende Arbeit ohne unzulässige Hilfe Dritter und ohne Benutzung anderer als der angegebenen Hilfsmittel angefertigt habe. Die aus Quellen direkt, oder indirekt übernommen Daten und Konzepte sind unter Angabe des Literaturzitats gekennzeichnet. Die Arbeit wurde bisher weder im In- noch im Ausland in gleicher, oder ähnlicher Form einer anderen Prüfungsbehörde vorgelegt. Ich versichere an Eides statt, dass ich nach bestem Wissen die reine Wahrheit gesagt und nichts verschwiegen habe. Über die im § 25 Abs. 5 vorgesehenen Rechtsfolgen habe ich Kenntnis.

_____   _____

Regensburg, June 25, 2018   Thomas Buchecker